

Radio Interferometric Studies of Cool Evolved Stellar Winds

A dissertation submitted to the University of Dublin
for the degree of Doctor of Philosophy

Eamon O'Gorman

Supervisor: Prof. Graham M. Harper
Trinity College Dublin, September 2013

SCHOOL OF PHYSICS
UNIVERSITY OF DUBLIN
TRINITY COLLEGE



Declaration

I declare that this thesis has not been submitted as an exercise for a degree at this or any other university and it is entirely my own work.

I agree to deposit this thesis in the University's open access institutional repository or allow the library to do so on my behalf, subject to Irish Copyright Legislation and Trinity College Library conditions of use and acknowledgement.

Name: Eamon O'Gorman

Signature: **Date:**

Summary

Mass-loss becomes significant for most stars as they approach the end of their lives and become either red giants or red supergiants. This mass-loss, which occurs in the form of a relatively cool and slow-moving wind, can have a significant impact on the evolution of gas and dust in galaxies, on surrounding planets, and indeed on the very evolution of the star itself. Despite the importance of this phenomenon and decades of study, the fundamental mechanisms responsible for producing these winds remain unknown. The main reason for this is due to our lack of understanding of the dynamics and thermodynamics of the stellar outflow environment. Isolated giants and supergiants do not contain the expected additional complexities encountered by binaries, making them ideal targets for understanding the nature of these outflows. Traditionally, observations have provided only limited disk-averaged information about the outflow environments of these stars, making it difficult to infer the outflow properties. However, the latest suite of radio interferometers now have the capability to provide essential spatial information on these outflow environments.

This thesis first presents the results of a radio interferometric study into the dynamics of the two unique flows in the circumstellar environment of the M2 red supergiant, Betelgeuse. The Combined Array for Research in Millimeter-wave Astronomy (CARMA) was used in multiple configurations to observe the CO($J = 2 - 1$) emission line allowing spatial scales as small as $0''.9$ ($\sim 40 R_\star$) to be traced over a $32''$ ($\sim 1500 R_\star$) field of view. The outer flow known as S2, was found to have outflow velocities of -15.4 and $+13.2 \text{ km s}^{-1}$ with respect to the stellar rest frame and extend out to $17''$, while the inner flow known as S1, was found to have outflow velocities of -9.0 and

$+10.6 \text{ km s}^{-1}$ and extend out to between $4 - 6''$. Both flows were found to be inhomogeneous down to the resolution limit, but when azimuthally averaged, their intensity falloff was found to be consistent with an optically thin, spherically symmetric, constant velocity outflow. High resolution multi-epoch centimeter continuum observations of Betelgeuse which probe its inner atmosphere ($< 10 R_\star$) are also presented. The radio flux density is found to vary on time scales of $\lesssim 14$ months at all wavelengths, and again evidence for inhomogeneities in the outflow is found.

Karl G. Jansky Very Large Array (VLA) multi-wavelength centimeter observations of two non-dusty, non-pulsating K spectral-type red giants, Arcturus and Aldebaran, were also analyzed. Detections at 10 cm (3.0 GHz: S-band) and 20 cm (1.5 GHz: L-band) represent the first isolated O-rich luminosity class III red giants to be detected at these long wavelengths. These thermal continuum observations provide a snapshot of the different stellar atmospheric layers and are independent of any long-term variability. The long wavelength data sample Arcturus' outer atmosphere where the wind velocity is approaching its terminal value and the ionization balance is becoming *frozen-in*. For Aldebaran, the data samples its inner atmosphere where the wind is still accelerating. Our data is in conflict with published semi-empirical models based on ultraviolet data. Spectral indices are used to discuss the possible properties of the stellar atmospheres. Evidence for a rapidly cooling wind in the case of Arcturus is found and a new analytical wind model is developed for this star. This model is used as the basis to compute a thermal energy balance of Arcturus' outflow by investigating the various heating and cooling processes that control its thermal structure. The analysis focuses on distances between 1.2 and $10 R_\star$, and includes the wind acceleration zone. We find that a substantial additional heating mechanism is required to maintain the inner thermal structure of the outflow.

*For Mum and Dad,
a constant source of inspiration and guidance.*

Acknowledgements

I am immensely grateful to my supervisor Graham Harper. His enthusiasm, dedication, patience, and encouragement, have been a huge help to me over the past four years. His knowledge and passion for the subject is beyond belief.

I would like to thank Joanna Brown, Alex Brown, and Anita Richards, for their help and advice with the data analysis aspects of this thesis.

I would also like to thank all past and present members of the Astrophysics Research Group. It has been great getting to know everybody and you have made the last four years an unforgettable experience.

A huge thanks to Sarah for proof reading this thesis, to Alex for providing me with a roof over my head during the write-up, and to Claire for keeping me motivated all the way from Brussels. Finally and most importantly, I would like to thank Mum and Dad for everything.

List of Publications

Refereed

1. **O'Gorman, E.**, Harper, G. M., Brown, A., Brown, A., Drake, S., and Richards, A. M. S.
“Multi-wavelength Radio Continuum Emission Studies of Dust-free Red Giants”
The Astronomical Journal, 146, 98 (2013)
2. Richards, A. M. S., Davis, R. J., Decin, L., Etoka, S., Harper, G. M., Lim, J. J., Garrington, S. T., Gray, M. D., McDonald, I., **O'Gorman, E.**, Wittkowski, M.
“e-MERLIN resolves Betelgeuse at wavelength 5 cm”
Monthly Notices of the Royal Astronomical Society Letters, 432, L61 (2013)
3. **O'Gorman, E.**, Harper, G. M., Brown, J. M., Brown, A., Redfield, S., Richter, M. J., and Requena-Torres, M. A.
“CARMA CO($J = 2 - 1$) Observations of the Circumstellar Envelope of Betelgeuse”
The Astronomical Journal, 144, 36 (2012)
4. Sada, P. V., Deming, D., Jennings, D. E., Jackson, B. K., Hamilton, C. M., Fraine, J., Peterson, S. W., Haase, F., Bays, K., Lunsford, A., and **O'Gorman, E.**
“Extrasolar Planet Transits Observed at Kitt Peak National Observatory”
Publications of the Astronomical Society of the Pacific, 124, 212 (2012)

-
5. Sada, P. V., Deming, D., Jackson, B. K., Jennings, D. E., Peterson, S. W., Haase, F., Bays, K., **O'Gorman, E.**, and Lundsford, A.
“Recent Transits of the Super-Earth Exoplanet GJ 1214b”
The Astrophysical Journal Letters, 720, L215 (2010)

Non-refereed

1. **O'Gorman, E.**, & Harper, G. M.
“What is Heating Arcturus’ Wind?”,
Proceedings of the 16th Cambridge Workshop on Cool Stars, Stellar Systems and the Sun. Astronomical Society of the Pacific Conference Series, 448, 691 (2011)

Contents

List of Publications	vii
List of Figures	xiv
List of Tables	xvii
1 Introduction	1
1.1 Motivation for Researching Cool Evolved Stellar Winds	2
1.2 On the Nature of Cool Evolved Stellar Atmospheres	4
1.3 Basic Concepts of Stellar Winds	8
1.4 Stellar Wind Driving Mechanisms Across the H-R Diagram	11
1.4.1 Radiatively Driven Winds	11
1.4.2 Solar Type Winds	12
1.4.3 Cool Evolved Stellar Winds	13
1.5 Red Giant and Red Supergiant Evolution	15
1.5.1 Change in Atmospheric Dynamics	15
1.5.2 Evolutionary Tracks	16
1.6 Radio Emission from Stellar Atmospheres	20
1.7 Radio Emission Mechanisms	22
1.7.1 Thermal Free-free (Bremsstrahlung) Emission	23
1.7.2 Molecular Line Emission	24
1.8 Radio Observations of Stellar Atmospheres	27
1.8.1 Brightness Temperature	28
1.8.2 Brightness Temperature and Flux Density	30
1.8.3 Thermal Free-free Radio Opacity	31
1.8.4 Radio Excess from Stellar Winds	33

CONTENTS

1.8.5	Molecular Emission Lines from Stellar Winds	37
1.9	Thesis Outline	39
2	Introduction to Radio Interferometry	41
2.1	Radio Antenna Fundamentals	42
2.1.1	Properties of a Radio Antenna	42
2.1.2	Antenna Structural Design	45
2.1.3	Antenna Performance Parameters	47
2.2	Radio Antenna Receiving System	49
2.3	Fundamentals of Radio Interferometry	51
2.3.1	Young's Slits	51
2.3.2	The Two-element Interferometer	54
2.3.3	Complex Visibility	57
2.3.4	Coordinate Systems for Imaging	59
2.4	Synthesis Imaging	61
2.4.1	Visibility Sampling	61
2.4.2	Imaging (Making a Dirty Map)	61
2.4.3	Deconvolution (Making a CLEAN map)	64
3	Targets, Instrumentation, and Observations	67
3.1	Betelgeuse	68
3.2	CARMA	72
3.3	CARMA Observations of Betelgeuse	76
3.4	Arcturus and Aldebaran	77
3.5	The Karl G. Jansky Very Large Array	85
3.6	VLA Observations of Arcturus and Aldebaran	89
3.6.1	OSRO and DDT Observations	89
3.6.2	Design of Observations	91
3.7	VLA-Pie Town Observations of Betelgeuse	94
4	Radio Interferometric Data Analysis	98
4.1	Data Examination and Flagging	99
4.2	Calibration	102
4.2.1	Prior Calibration	105

CONTENTS

4.2.2	Bandpass Calibration	107
4.2.3	Gain Calibration	108
4.2.4	Flux Scale Calibration and Application of Solutions	109
4.3	Imaging	110
4.3.1	Imaging the VLA Data	111
4.3.2	Imaging the CARMA Data	113
5	Multi-wavelength Radio Emission Study of Betelgeuse’s Extended Atmosphere	116
5.1	CO molecules in the CSE of Betelgeuse	117
5.2	Adopted Radial Velocity	119
5.3	CARMA CO($J = 2 - 1$) Spectra	121
5.4	Individual Configuration Image Cubes	126
5.5	Multi-configuration Image Cube Inspection	128
5.6	Spatial Extent of S2	130
5.7	Intensity distribution of CO	132
5.8	Spatial Extent of S1	135
5.9	Continuum Flux Densities	136
5.10	Higher CO rotational lines	138
5.11	CARMA CO observations in Context	142
5.12	e-Merlin 5 cm Results	144
5.13	VLA-Pie Town Maps Versus e-MERLIN	148
5.14	Long Term Radio Variability and Thermal Structure	151
5.15	0.7 cm VLA-Pie Town Maps	155
5.16	VLA, VLA-Pie Town, e-MERLIN: Putting it all together	158
6	Multi-wavelength Radio Continuum Emission Studies of Dust-free Red Giants	160
6.1	Why Study Red Giants with the VLA?	161
6.2	Radio Maps	162
6.2.1	α Boo Maps	162
6.2.2	α Tau Maps	165
6.3	Results Versus Previous Observations	166
6.4	Results Versus Existing Models	170

CONTENTS

6.5	Spectral Indices	174
6.6	Analytical Advection Model for α Boo's Wind	181
6.6.1	H II recombination in a stellar outflow	181
6.6.2	Application to α Boo's Wind	184
6.7	Constraining α Tau's Molsphere	187
6.8	Ionized Mass-Loss Rates	189
7	Thermal Energy Balance of Arcturus' Outflow	191
7.1	Motivation for a Thermal Energy Balance	192
7.2	Thermal Model for a Spherically Symmetric Outflow	193
7.3	Cooling Processes	195
7.3.1	Adiabatic Expansion Cooling	195
7.3.2	Radiative Recombination Cooling	195
7.3.3	Lyman-alpha Cooling	197
7.3.4	Other Line Coolants	197
7.4	Heating Mechanisms	200
7.4.1	Photoionization Heating	200
7.4.2	Ambipolar Diffusion Heating	202
7.4.3	Turbulent Heating	203
7.5	Thermal Energy Balance	206
7.6	Discussion	208
8	Conclusions and Future Work	210
8.1	Principle Results	211
8.1.1	Betelgeuse's Extended Atmosphere	211
8.1.2	Dust-free Red Giants	213
8.2	Future Work	215
8.2.1	Probing the S1 flow of Betelgeuse with ALMA	216
8.2.2	Multi-epoch centimeter observations of Betelgeuse	218
8.2.3	Semi-empirical models for Arcturus and Aldebaran	220
8.2.4	Karl G. Jansky VLA Survey of Coronal Evolved Stars	223
8.3	Concluding Remarks	226
A	List of Abbreviations Used in this Thesis.	227

CONTENTS

References	229
-------------------	------------

List of Figures

1.1	The Linsky-Haisch dividing line	5
1.2	<i>HST</i> strong chromospheric lines	7
1.3	Stellar winds across the H-R diagram	12
1.4	Evolutionary tracks of massive stars	17
1.5	Evolution track of a low mass star	18
1.6	Radio H-R diagram	21
1.7	Molecular ladder plot and relative populations	25
1.8	H II region radio spectrum	32
1.9	Schematic for stellar wind radio emission excess	34
1.10	Radio spectral index for Betelgeuse	36
1.11	Theoretical molecular line profiles	38
2.1	Radiation and power pattern of a uniformly illuminated antenna .	44
2.2	Common optical systems used for radio antennas	47
2.3	Block diagram of a superheterodyne receiver	50
2.4	Fringe pattern produced by Young's slits	52
2.5	Visibilities for various source sizes	53
2.6	Simplified schematic diagram of a two-element interferometer . .	55
2.7	Instantaneous point source responses of an interferometer . . .	56
2.8	Interferometric coordinate system	60
2.9	VLA antenna layout and two examples of $u - v$ coverage	62
2.10	The Fourier transform pairs in synthesis imaging	63
3.1	VLA spatially resolved analysis of Betelgeuse	71
3.2	CARMA array configurations used	73

LIST OF FIGURES

3.3	Layout of antenna pads for CARMA	73
3.4	Major components in the signal path for CARMA	75
3.5	<i>IUE</i> Mg II k line and Drake models	82
3.6	Main features of a VLA antenna	87
3.7	Importance of offsetting source from phase center	92
3.8	Overview of a low and high frequency VLA observation	93
4.1	Radio interferometry work flow chart	99
4.2	Examination of a VLA data set	101
4.3	Eliminating RFI from the L band data set	103
4.4	Calibration workflow diagram	105
4.5	Atmospheric opacity at the VLA site	106
4.6	Gain variation as a function of frequency	108
4.7	Example of a well calibrated source	110
4.8	Wide field view of the VLA 20 cm image	112
4.9	Comparing CLEAN to Multi-scale CLEAN	114
5.1	Bernat (1979) CO line profile showing two sharp line cores	118
5.2	Previous CO($J = 2 - 1$) rotational emission line profiles	120
5.3	Radial velocity data and model for α Ori	121
5.4	Spectra for each CARMA configuration	122
5.5	Spectra extracted over various regions	125
5.6	Discrete sources in individual configuration image cubes	127
5.7	Channel maps from the multi-configuration image cube	129
5.8	Geometry of a spherical symmetric flow	131
5.9	S2 radius as a function of channel velocity	132
5.10	Surface brightness vs. projected radius	134
5.11	CARMA maps of the inner S1 flow	136
5.12	CO rotational emission lines from the CSE of Betelgeuse	140
5.13	SiO rotational emission line from the CSE of Betelgeuse	142
5.14	First e-MERLIN results for Betelgeuse	145
5.15	Predicted position of Betelgeuse on 2012 July	147
5.16	1-D model vs. e-MERLIN observations	149
5.17	Radio flux density variation of Betelgeuse between 1996 → 2004 .	152

LIST OF FIGURES

5.18	Atmospheric temperature profile between 1998 – 2013	154
5.19	Pie Town Q band images spanning six years	156
5.20	VLA Q band A-configuration maps of Betelgeuse.	157
6.1	Final VLA multi-wavelength radio maps of α Boo and α Tau . . .	163
6.2	Spectral energy distribution of α Boo	168
6.3	Spectral energy distribution of α Tau	169
6.4	1-D semi-empirical model atmospheres for α Boo and α Tau . . .	171
6.5	Power law fits to the spectra of α Boo and α Tau	176
6.6	Variation of density and temperature coefficients	177
6.7	Predicted effective radius as a function of wavelength	179
6.8	Illustration of how the ionization fraction <i>freezes-in</i>	183
6.9	The temperature dependent recombination rates for hydrogen . .	185
6.10	Hybrid Atmospheric Model which undergoes rapid wind cooling .	187
7.1	Various cooling mechanisms in Arcturus' wind	196
7.2	Summation of all cooling mechanisms	199
7.3	Photoionization cross section values	201
7.4	Example of diverging flux tubes	204
7.5	Main heating mechanisms in Arcturus' wind	206
7.6	Net thermal balance	207
8.1	Simulating ALMA dust observations	217
8.2	Simulating ALMA CO($J = 6 - 5$) observations	217
8.3	MERLIN + “old” VLA image of Betelgeuse	221
8.4	Block diagram for a new semi-empirical model	222
8.5	Ionized stellar mass-loss rate vs. stellar radius	225

List of Tables

1.1	Properties of Main Sequence and Evolved Stars	16
3.1	Physical Properties of α Ori	69
3.2	Properties of the 5 CARMA Array Configurations	74
3.3	CARMA Observations of α Ori	79
3.4	Basic Properties of α Bootis and α Tauri	81
3.5	Improved Performance Parameters of the VLA	86
3.6	Frequency Coverage, Spatial Resolution, and FOV of the VLA	88
3.7	VLA Observations of α Bootis and α Tauri	90
3.8	Multi-wavelength VLA + Pie Town Observations of Betelgeuse . .	96
5.1	CARMA Continuum Fluxes at 230 GHz	138
5.2	Summary of the S1 and S2 Flow Properties	143
6.1	VLA Flux Densities of α Boo and α Tau	164
6.2	Compilation of Previous Radio Observations ($\nu \leq 250$ GHz)	167
6.3	Ionized Mass-loss Rates for α Boo and α Tau	189
7.1	Elemental Abundance in Arcturus's Outflow	198
7.2	Properties of the Strongest Line Coolants	200
8.1	Relevant Capabilities of the VLA and e-MERLIN	219
8.2	Coronal Evolved Star Candidates	224
A.1	List of Abbreviations	227

1

Introduction

The chapter begins by outlining the motivation for studying winds from cool evolved stars, while simultaneously highlighting the problems associated with potential mass-loss mechanisms. The fundamental physics governing these winds along with their physical properties are then discussed. An overview of stellar winds across the Hertzsprung-Russel diagram is then presented, and a description of how stars evolve to become red giants and red supergiants is also included. The second half of this chapter focuses on radio emission from stellar winds. The radio emission mechanisms that are relevant to this thesis are discussed, and the terminology used to study cool evolved stellar winds at radio wavelengths is introduced. The chapter concludes with a brief outline of the remaining chapters within this thesis.

1.1 Motivation for Researching Cool Evolved Stellar Winds

Mass-loss from non-coronal spectral-type K through mid-M evolved stars plays a crucial role in galactic evolution and ultimately provides part of the material required for the next generation of stars and planets. This mass-loss occurs via a cool ($T_e \lesssim 10^4 K$) wind with terminal velocities ($10 \lesssim v_\infty \lesssim 50 \text{ km s}^{-1}$), typically less than the photospheric escape velocity ($v_{\text{esc}} \sim 100 \text{ km s}^{-1}$). The mass-loss rates for red giants¹ are significant, typically $10^{-11} - 10^{-9} M_\odot \text{ yr}^{-1}$, and are even higher for the more short-lived red supergiants (RSGs), typically $10^{-6} - 10^{-4} M_\odot \text{ yr}^{-1}$. This implies that a substantial fraction of the star's initial mass can be dispersed to the interstellar medium (ISM) during these post main sequence evolutionary stages (e.g., Schröder & Sedlmayr, 2001). Mass-loss from these stars is therefore a crucial factor governing stellar evolution (Chiosi & Maeder, 1986), and also in explaining the frequency of supernovae in the galaxy (e.g., van Loon, 2010). Despite the importance of this phenomenon, and decades of study, the specific mechanisms that drive winds from evolved spectral-type K through mid-M stars remain unknown (clearly laid out by Holzer & MacGregor 1985 but still unsolved, e.g., Crowley *et al.* 2009). There is insufficient atomic, molecular, or dust opacity to drive a radiation-driven outflow (Jones, 2008; Zuckerman *et al.*, 1995), and acoustic/pulsation models cannot drive the observed mass-loss rates (Sutmann & Cuntz, 1995). Ultraviolet (UV) and optical observations reveal an absence of significant hot wind plasma, and the winds are thus too cool to be Parker-type thermally-driven flows (e.g., Ayres *et al.*, 1981; Haisch *et al.*, 1980; Linsky & Haisch, 1979).

Magnetic fields are most likely involved in the mass-loss process, although current magnetic models are also unable to explain spectral diagnostics. High signal-to-noise ratio (S/N) *Hubble Space Telescope (HST)* UV spectra have revealed that the 1-D linear Alfvén wave-driven wind models of the 1980s (e.g., Harper 1988; Hartmann & MacGregor 1980) are untenable (Harper *et al.*, 2001). These models predict chromospheres as integral parts of a turbulent, extended,

¹The term *red giant* excludes asymptotic giant branch (AGB) stars throughout this thesis.

1.1 Motivation for Researching Cool Evolved Stellar Winds

and heated wind acceleration zone, but the theoretical line profiles do not agree with the *HST* spectra, (e.g., Judge & Carpenter, 1998). A new generation of theoretical models with outflows driven within diverging magnetic flux tubes have now emerged (Falceta-Gonçalves *et al.*, 2006; Suzuki, 2007) but these too are not yet in agreement with observations (Crowley *et al.*, 2009). Progress in this field continues to be driven by observations which can test existing models and theories, and provide new insights and constraints into the mass-loss problem.

The Advantages of Radio Observations

Understanding the dynamics and thermodynamics of the atmospheres of late-type evolved stars will ultimately lead to a broader understanding of their mass-loss processes. Red supergiants have extended atmospheres which contain a mixture of atoms, ions, molecules, and silicate dust, and are an ideal test bed for ideas and theories of mass-loss. These atmospheres are so extended that the closest red supergiants can be spatially resolved and imaged at centimeter and millimeter-wavelengths, both in continuum and molecular line emission. Such observations can yield direct measurements of the gas excitation temperature, velocity, and atmospheric structure, which can then be used to provide essential constraints on the mass-loss process.

The red giants on the other hand, have less extended atmospheres, which contain little dust and only low abundances of molecules. They currently¹ cannot be spatially resolved at radio wavelengths, but their partially ionized outflows can still be detected at these wavelengths, providing an area-averaged sweep through the atmospheres of these stars. The lack of spatial resolution prevents the direct measurement of the fundamental atmospheric properties. However, point source radio observations can still be compared against existing atmospheric models based on shorter wavelength observations (e.g., models based on optical and UV observations). Radio observations can sample further out in the star's atmosphere than optical and UV observations and can test the validity of, and improve upon existing model atmospheres.

¹ALMA and e-MERLIN will eventually be capable of spatially resolving the atmospheres of red giants.

1.2 On the Nature of Cool Evolved Stellar Atmospheres

The research presented in this thesis attempts to understand the dynamics and thermodynamics of the atmospheres of red giants and RSGs, with the ultimate goal of gaining a deeper understanding of their mass-loss processes. To do so, we utilize the latest suite of radio interferometers which now have the capability of providing spatially resolved sensitive millimeter and centimeter observations of the atmospheres of the closest RSGs, and sensitive multi-wavelength disk-averaged sweeps through the atmospheres of the closest red giants.

1.2 On the Nature of Cool Evolved Stellar Atmospheres

The study of stellar outflows from cool evolved stars began with the discovery of blue-shifted absorption features in strong resonance lines from a number of bright red supergiants (Adams & MacCormack, 1935). They attributed these features to gradually expanding envelopes, even though the expansion velocity was small ($\sim 5 \text{ km s}^{-1}$) and much less than the photospheric escape velocity. Spitzer (1939) analyzed similar data and devised a *fountain model* for the atmospheres of red supergiants. In this model, radiation drives matter upwards from the photosphere until at some height, the ionization state of the matter changes, causing the radiation force to drop so that the matter falls back onto the star. Definitive evidence for mass-loss from cool evolved stars came from Deutsch (1956) who observed a system which is now known to consist of an M5 Ib-II bright giant (i.e., α Her), a G5 giant, and an A9 dwarf (Moravveji *et al.*, 2013). He found that the same blue-shifted absorption features were present in the spectrum of both giants, which were not present in other single G5 giants. This indicated that both stars were enveloped in material which had been emitted from the M5 giant. The inferred expansion velocity at the distance of the G5 giant was sufficient to escape the system, thus confirming that matter was escaping the gravitational potential of the α Her system.

Even though many later studies concluded that evolved late-type stars contained cool ($T_e < 1000 \text{ K}$) extended circumstellar environments (e.g., Bernat & Lambert, 1976; Gehrz & Woolf, 1971; Reimers, 1975; Weymann, 1962), the physical properties of the ouflow between the photosphere and this cool outer environ-

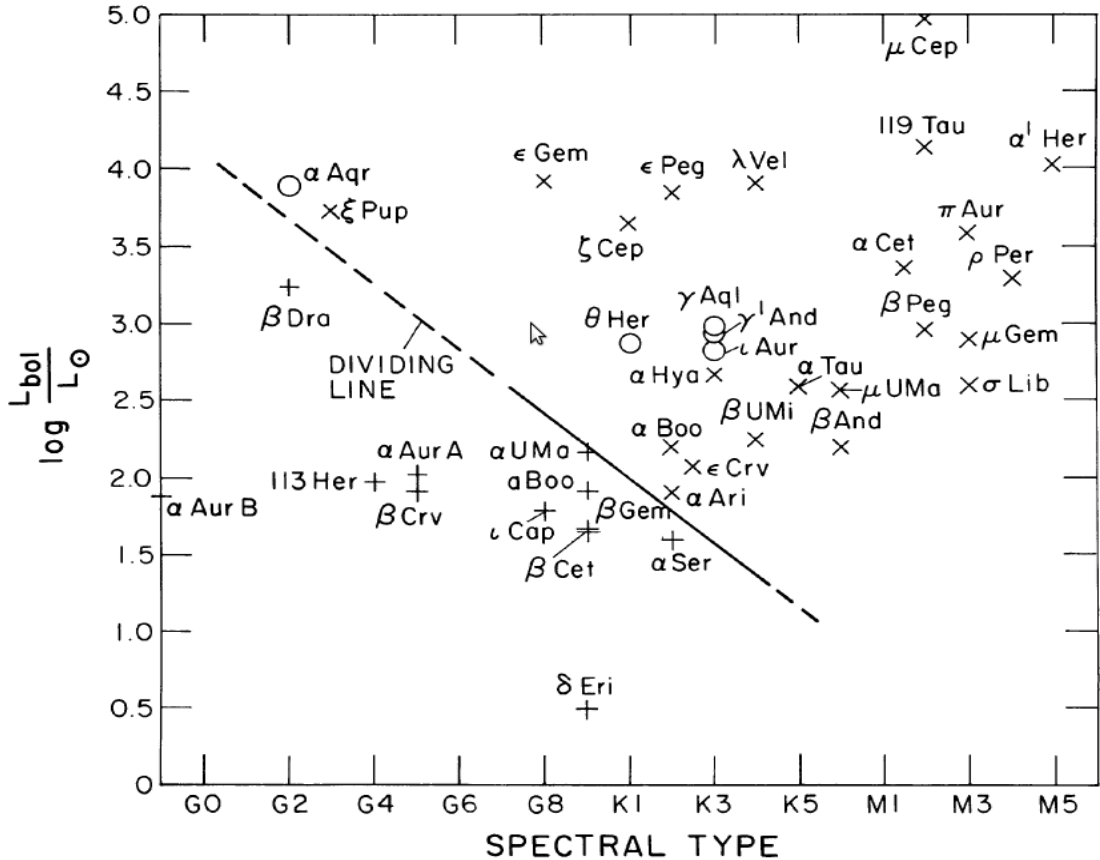


Figure 1.1: A section of the H-R diagram showing the Linsky-Haisch dividing line which was proposed as a sharp division separating coronal (indicated by plus signs) from non-coronal (indicated by crosses) evolved late-type stars. Hybrid atmosphere stars are marked by circles. This figure is taken from Drake & Linsky (1986) who carried out a 6 cm survey of late-type evolved stars.

ment remained unclear. An important discovery in late-type evolved stellar atmospheres resulted from the first UV survey of such stars using the *International Ultraviolet Explorer* (*IUE*; Macchett & Penston, 1978). The survey revealed a “transition region dividing line” in the giant branch of the H-R diagram near spectral type K1 and near spectral type G5 for the brighter giants, which separates these stars based on the properties of their atmospheres (Linsky & Haisch, 1979; Simon *et al.*, 1982). In Figure 1.1 we show the approximate location of this dividing line in the Hertzsprung-Russell (H-R) diagram. Stars blueward of the

1.2 On the Nature of Cool Evolved Stellar Atmospheres

dividing line were found to possess chromospheres and transition regions like the Sun, while stars on the red side were found to possess chromospheres and cool winds. X-ray observations showed that this dividing line extended to coronal emission (Ayres *et al.*, 1981). Around the same time, another class of late-type evolved star emerged which showed signs of possessing both a transition region and a cool wind (e.g., Reimers, 1982). Many of these so-called “hybrid atmosphere” stars now also show evidence for coronal emission, albeit much weaker than on the blue side of the dividing line (e.g., Ayres *et al.*, 1997).

The *HST* allowed the important UV diagnostic transitions (e.g., lines from C II , Fe II , Mg II , and O II) to be observed with superb detail. The photon-scattering wind produces self-reversals in these chromospheric emission lines and revealed that, for the most part, the red giant winds accelerate in a quasi-steady manner and are not the result of ballistic ejecta. This is inferred by the increase of wind scattering absorption velocity with optical depth, and thus height in the wind, as shown in Figure 1.2 (Carpenter *et al.*, 1999). The blue-shifted absorption features, which are indicative of stellar outflows, are also shown in Figure 1.2 for the Mg II and Ca II resonance lines of α Boo (K2 III). For many evolved stars, these disk averaged emission line profiles have also provided crude estimates of atmospheric properties such as the mass-loss rate and terminal velocity, by comparing them to synthetic profiles based on detailed radiative transfer code (e.g., Robinson *et al.*, 1998).

Chromospheres are the manifestation of surface convection and are found almost exclusively in the cool portion of the H-R diagram (Ayres, 2010a). These non-radiatively heated regions of the inner atmosphere are present in the atmospheres of all late-type evolved stars. The isothermal pressure scale height, H_P , is the height in the atmosphere where the pressure drops by a factor of e^{-1} and is given by

$$H_P = \frac{kT_e}{\mu m_{\text{H}} g} \propto \frac{T_e R_*^2}{M_*}. \quad (1.1)$$

Here, k is Boltzmann’s constant, T_e is the electron temperature, R_* is the stellar radius, G is the gravitational constant, M_* is the stellar mass, μ is the mean mass per particle in hydrogen masses, m_{H} is the mass of a hydrogen atom, and g is the gravitational acceleration. The much larger radii of evolved stars means that

1.2 On the Nature of Cool Evolved Stellar Atmospheres

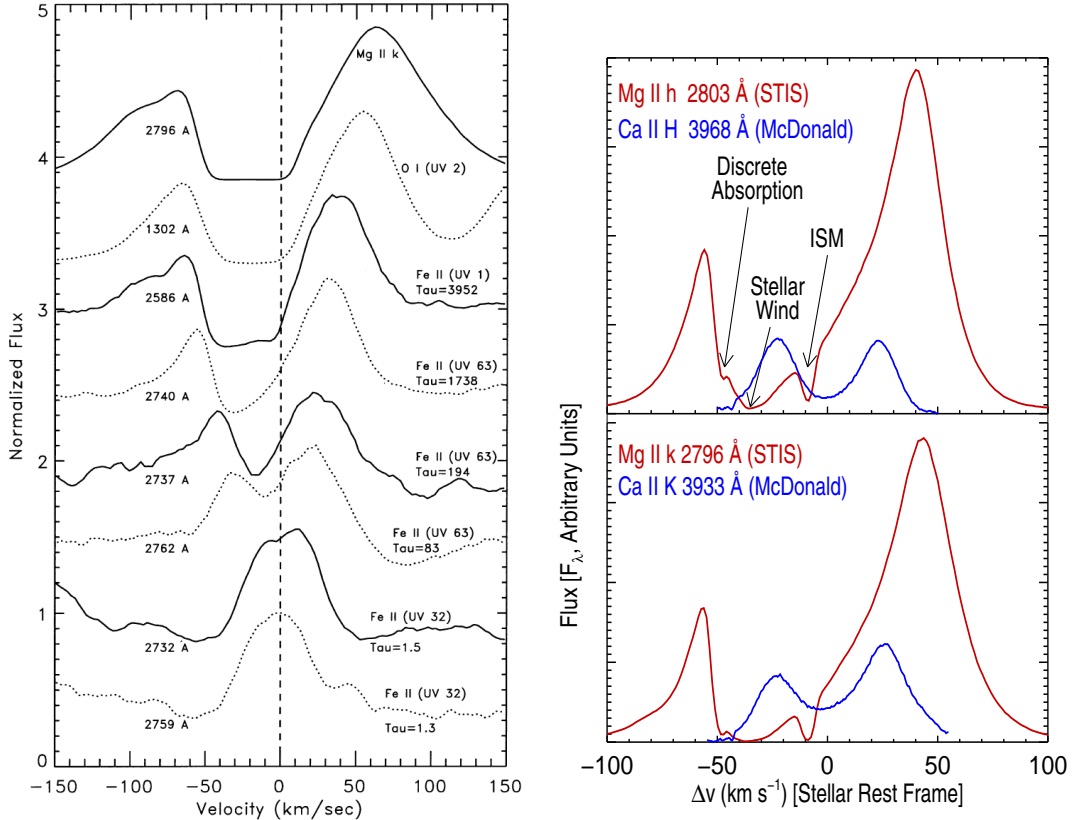


Figure 1.2: *Left:* *HST* Goddard High-Resolution Spectrograph (GHRS) spectra showing the increase of wind scattering absorption velocity with optical depth for strong chromospheric lines (Carpenter *et al.*, 1999). These data were taken for λ Vel (a K5 Ib-II star) and show that it's wind accelerates in a quasi-steady manner. *Right:* The Mg II *h* and *k* and Ca II H and K line profiles of α Boo. For many cool evolved stars, these strong resonant lines have often been compared to synthetic profiles to provide estimates of atmospheric properties. Three absorption components are present in the high S/N *HST* data and originate from the ISM, the stellar wind, and an unknown source.

their *typical* scale height is over two orders of magnitude greater than that of the Sun. For example, a K5 III star with a radius of $40 R_\star$, will have a pressure scale height of $H_P \sim 0.01 R_\star$. It is for this reason that their chromospheres are believed to be much more extended than the Sun's. The red supergiants are now known to have chromospheres which extend out to a few R_\star (Harper *et al.*, 2001; Lim *et al.*, 1998). However, there is still much debate regarding the spatial extent of chromospheres in red giants. Recently, Berio *et al.* (2011) found that β Ceti,

1.3 Basic Concepts of Stellar Winds

a coronal giant, has a chromosphere which may extend out to $\sim 1.5 R_\star$, while Luttermoser *et al.* (1994) found that the chromospheric spatial extent of an M6 giant to be only $\leq 1.05 R_\star$. Determining the spatial extent of chromospheres in red giants is currently an area of active research.

1.3 Basic Concepts of Stellar Winds

The addition of energy above the photosphere is a requirement for a stellar outflow to escape the gravitational potential of a star. This energy input can be either in the form of a heat input (e.g., ambipolar diffusion heating), a momentum input (e.g., radiation pressure on gas species), or a combination of both. The momentum input is described by Newton's second law, $F = dp/dt$, where F is the outward force and p is the momentum. For this reason, the presence of an outward force is usually called momentum deposition, in contrast to energy deposition. The momentum deposition is governed by the momentum equation

$$F = \rho d\mathbf{v}/dt \quad (1.2)$$

where ρ is the mass density, and \mathbf{v} is the velocity vector. In 1-D spherical symmetry, the velocity gradient is

$$\frac{dv(r,t)}{dt} = \frac{\partial v(r,t)}{\partial t} + \frac{\partial v(r,t)}{\partial r} \frac{dr(t)}{dt} = v \frac{dv}{dr} \quad (1.3)$$

where we have assumed a stationary flow. The momentum equation for a flow being acted on by an outward directed force per unit mass, $f = f(r)$, is then

$$v \frac{dv}{dr} = -\frac{1}{\rho} \frac{dP}{dr} - \frac{GM_\star}{r^2} + f \quad (1.4)$$

where P is the pressure and each of these terms have units of cm s^{-2} (e.g., Lamers & Cassinelli, 1999). The term on the left of Equation 1.4 is the acceleration, which is produced by the gas pressure gradient (first term on right), the gravity (second term on right), and other forces which are contained in f . The gas pressure gradient term is directed outwards (positive) because $dP/dr < 0$.

The gas pressure gradient in Equation 1.4 depends on the temperature structure of the outflow, which in turn depends on the heating and cooling. The effects

1.3 Basic Concepts of Stellar Winds

of energy deposition can be expressed via the first law of thermodynamics

$$\frac{du}{dt} = \frac{dq}{dt} - P \left(\frac{d\rho^{-1}}{dt} \right) \quad (1.5)$$

where $u = (3/2)(\mathcal{R}T/\mu)$ is the internal energy of the system per unit mass, q is the net heat gained per unit mass, and the final term is the work done by the gas per unit time per unit mass. The time dependence can be removed using $d/dt = v d/dr$ to give

$$\frac{dq}{dr} = \frac{3}{2} \frac{\mathcal{R}}{\mu} \frac{dT}{dr} + P \frac{d\rho^{-1}}{dr} \quad (1.6)$$

where \mathcal{R} is the gas constant¹. The ideal gas law can be written as

$$\rho = \frac{\mu P}{\mathcal{R} T}. \quad (1.7)$$

Substituting this into the last term in Equation 1.6 gives the desired expression which relates the gas pressure to the heating:

$$\frac{1}{\rho} \frac{dP}{dr} = \frac{5}{2} \frac{\mathcal{R}}{\mu} \frac{dT}{dr} - \frac{dq}{dr}. \quad (1.8)$$

The energy equation for stellar outflows can then be found by replacing the gas pressure term in the momentum equation with an expression which depends on the temperature structure of the outflow and the heating, i.e., combining Equations 1.4 and 1.8:

$$\frac{d}{dr} \left(\frac{v^2}{2} + \frac{5\mathcal{R}T}{2\mu} - \frac{GM_\star}{r} \right) = f(r) + \frac{dq}{dr}. \quad (1.9)$$

The combination of the terms inside the brackets on the left gives the total energy of the system per unit mass, with the first term being the kinetic energy of the flow, the second term being the enthalpy of the gas (the internal kinetic energy plus the capacity to do work), and the third term being the gravitational potential energy. This equation tells us that the change in total energy of the gas as it moves a unit distance outwards from the star, is equal to the momentum input by the force and the heat input.

¹ $\mathcal{R} = 8.3145 \text{ J K}^{-1} \text{ mol}^{-1}$

1.3 Basic Concepts of Stellar Winds

The energy equation in the form of Equation 1.9 is called the *Bernoulli* equation. Integrating the Bernoulli equation gives

$$\begin{aligned} e(r) &= \frac{v^2}{2} + \frac{5\mathcal{R}T}{2\mu} - \frac{GM_\star}{r} \\ &= e(r_0) + W(r) + q(r) \end{aligned} \quad (1.10)$$

which states that the total energy per unit mass, $e(r)$, is equal to the initial energy, $e(r_0)$, at the lower boundary r_0 , plus the energy added to the wind in the form of the work done by the force, $W(r)$, and the heat deposition, $q(r)$. In other words, the total energy added to the wind per unit mass is used to increase the kinetic energy and the enthalpy of the wind, and to lift it out of the gravitational potential well. We can also compare the energy of the wind at the photosphere and at infinity, as described by Lamers (1998). At the photosphere, the total energy is negative and is just the gravitational potential energy, because $v_{\text{esc}} \gg \mathcal{R}T_\star/\mu$ and $v_{\text{esc}} \gg v(R_\star)$, i.e.,

$$e(r_0) \simeq -\frac{GM_\star}{R_\star}. \quad (1.11)$$

At $r \rightarrow \infty$ the potential energy and the enthalpy both go to 0, and so the total energy is the kinetic energy,

$$e(r) \simeq \frac{v_\infty^2}{2}. \quad (1.12)$$

Substituting Equations 1.11 and 1.12 into Equation 1.10 then gives

$$\frac{v_\infty^2}{2} \simeq -\frac{GM_\star}{R_\star} + W(r) + q(r). \quad (1.13)$$

This equation tells us that a wind can only escape the gravitational potential of its star if there is an output force that provides sufficient momentum input or, if there is an energy source that provides sufficient heat input. These momentum and energy inputs are collectively known as wind driving mechanisms and in Section 1.4 we discuss the different mechanisms which occur across the H-R diagram.

1.4 Stellar Wind Driving Mechanisms Across the H-R Diagram

Stellar winds are a ubiquitous phenomenon across almost all of the H-R diagram. The various types of winds found throughout the H-R diagram can be broadly grouped into the three main categories of hot radiatively driven stellar winds, solar-type winds, and cool evolved stellar winds, as shown in Figure 1.3. The cool evolved stellar winds can also be broadly grouped into the two categories of warm hybrid winds, and cool dense winds, as discussed in Section 1.2.

1.4.1 Radiatively Driven Winds

Stars earlier than spectral type \sim A2 emit their peak radiation in the UV, and so it was not until the early UV rocket observations that the presence of strong winds were confirmed from these stars (e.g., Morton, 1967). The broad P Cygni line profiles observed, indicated mass-loss rates as high as $10^{-5} M_{\odot} \text{ yr}^{-1}$ and wind terminal velocities up to 3500 km s^{-1} . Even though the lifetime of these massive hot stars is relatively short at just a few million years, their large mass-loss rates can substantially reduce the original stellar mass by a factor of two or more for the most massive (Owocki, 2004). Indeed, these stars typically end up as Wolf-Rayet (W-R) stars, which often appear to have completely lost their original envelope of hydrogen. These early-type stars do not exhibit the strong sub-surface convection that is present in cool stars, and are therefore not believed to possess coronae. Their winds are therefore expected to remain at temperatures comparable to the star's surface, and so the gas-pressure term in Equation 1.4 is not sufficient to drive their winds. Instead these stars are known to have a high radiative flux (since this scales as the fourth power of the surface temperature), and Castor *et al.* (1975) showed that this flux can accelerate a time-steady wind, by coupling with optically thick atomic lines in regions above the photosphere, where the continuum is optically thin. Therefore, the winds of these stars are effectively driven by the pressure of the star's emitted radiation, and so the dominant term in Equation 1.4 is a radiation pressure term contained within the parameter f .

1.4 Stellar Wind Driving Mechanisms Across the H-R Diagram

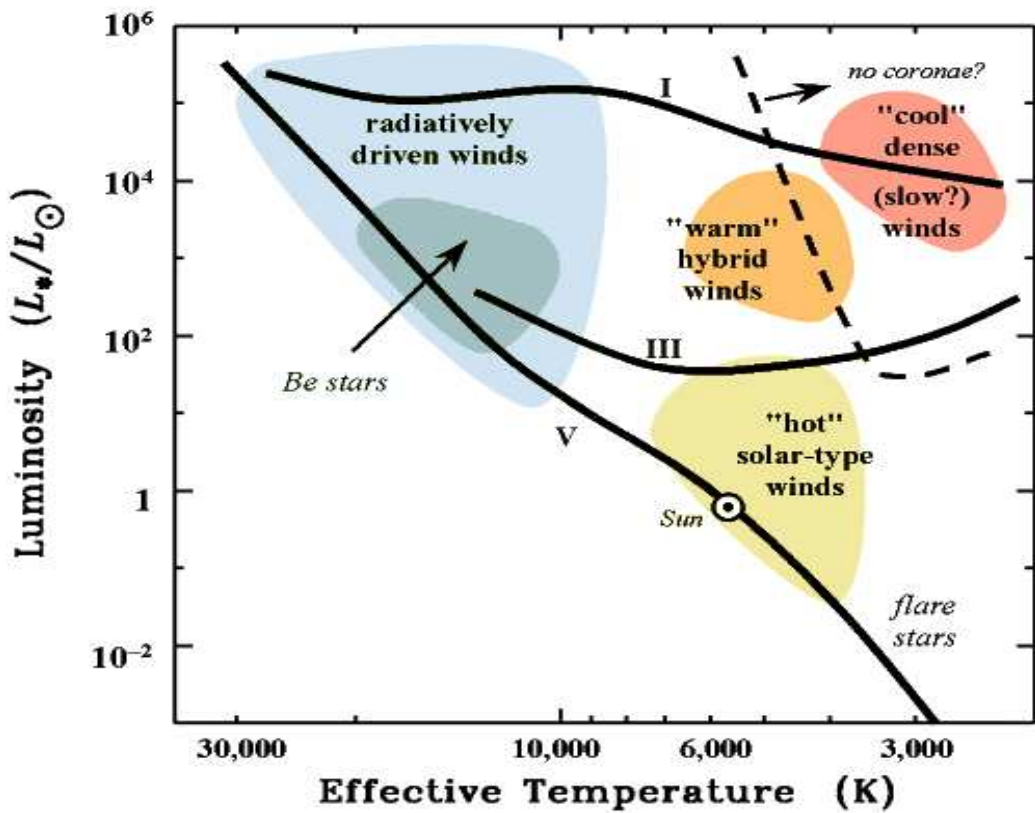


Figure 1.3: Stellar winds across the H-R diagram can be broadly grouped into the three main categories of hot radiatively driven stellar winds (upper left), solar-type winds (center right), and cool evolved stellar winds (upper right). The cool evolved stellar winds can also be broadly grouped into the two categories of warm hybrid winds (orange group) and non-coronal type (red group). *Image credit:* Steven Cranmer.

1.4.2 Solar Type Winds

Our understanding of the wind driving mechanisms for stars with *hot* solar-type winds is mainly based on solar theory and observations. Equation 1.4 was the cornerstone of many early attempts to explain the dynamics of the solar corona. Chapman & Zirin (1957) assumed a static corona (i.e., the acceleration term was zero) and that the pressure gradient was the only outward force (i.e., $f = 0$). Their results were unphysical, however, as they found that the density goes to infinity at large distances, and that the pressure was many orders of magnitude greater than that of the ISM. Parker (1958) assumed that there was a continuous

1.4 Stellar Wind Driving Mechanisms Across the H-R Diagram

isothermal outflow of material from the Sun, caused only by the thermal pressure gradient term in Equation 1.4 (i.e., $f = 0$). He used the mass continuity equation, and the equation of state, to replace the pressure gradient term with a function depending only on velocity. Parker coined the solution to his simple analytical model as the “solar wind” and the predictions his model made for the solar velocity were confirmed shortly afterwards by some of the first space probes (e.g., Neugebauer & Snyder, 1962). The assumptions of a radially expanding and isothermal outflow are not fully accurate in reality, however, and Parker’s solution is an approximate characterization of the observed solar wind.

Coronal winds are generally tenuous, with mass-loss rates being too small to be of evolutionary importance. For example, at the Sun’s current rate of mass-loss, about $10^{-14} M_{\odot} \text{ yr}^{-1}$, its mass would be reduced by only $\sim 0.01\%$ during its main sequence lifespan of 10^{10} yr . Wind velocities are generally high ($200 \rightarrow 800 \text{ km s}^{-1}$), except for the very low gravity stars whose velocities are believed to be less (Drake & Linsky, 1986). Parker (1958) showed that the solar wind is a consequence of the thermal pressure gradient of the hot corona, but the question of which mechanism drives the solar wind is still controversial, i.e., it is not understood how mechanical energy (convection) is transferred above the solar surface. The dissipation of Alfvén waves is a reliable candidate as a primary source of coronal heating (Cranmer & Saar, 2011), although other sources of energy and momentum probably exist (e.g., Parker, 1983, 1988). These waves can transfer energy from the surface convection up to the wind acceleration region because they can travel longer distances due to their incompressible nature (e.g., Hollweg, 1973). The dissipation of these waves then transfer momentum and energy to the gas via a cascade from large to small eddies (Verdini & Velli, 2007). Evolved stars blueward of the Linsky-Haisch dividing line also posses coronae and may share a similar mass-loss mechanism to that of coronal stars on the main sequence.

1.4.3 Cool Evolved Stellar Winds

Cool evolved stars can generally be grouped into three main categories based on their mass and evolutionary status: (1) massive evolved red supergiants, (2) low

1.4 Stellar Wind Driving Mechanisms Across the H-R Diagram

and intermediate mass highly evolved stars ($0.8 - 8 M_{\odot}$) known as asymptotic giant branch (AGB) stars, and (3) low and intermediate mass, less evolved red giant stars. AGB stars lose a significant fraction of their mass through slow, massive winds at a rate of $10^{-8} \rightarrow 10^{-4} M_{\odot} \text{ yr}^{-1}$ (van Loon *et al.*, 2005). This mass-loss occurs as a result of stellar pulsations (Habing, 1996) which levitate material from the stellar surface, followed by the acceleration of dust grains by radiation pressure (Gehrz & Woolf, 1971).

The mass-loss mechanisms operating in red giants and red supergiants remain largely unknown and the theory governing mass-loss in AGB stars is not appropriate (Josselin & Plez, 2007). Red giants and red supergiants have small amplitude variations and so they do not pulsate in a similar manner to AGB stars. Also, significant amounts of dust are only found at large radii for red supergiants (Danchi *et al.*, 1994), while red giants may have little or no dust in their outflows (Jones, 2008). One of the most plausible mass-loss mechanisms for these stars over the past few decades has been the transfer of energy and momentum to the wind by the dissipation of Alfvén waves. Unlike acoustic waves, Alfvén waves have large damping lengths that can transfer energy and momentum to the gas over many stellar radii. Alfvén wave models were originally known to result in high velocity winds, unlike what is observed for cool evolved stars. Hartmann & MacGregor (1980) successfully showed that these observed low outflow velocities and high mass-loss rates could be reproduced if a wave damping mechanism is effective close ($r < 2 R_{\star}$) to the star. Hartmann & Avrett (1984) constructed an Alfvén wave model for the red supergiant Betelgeuse which predicted its wind to have an electron temperature of 8000 K at $4 R_{\star}$ and remaining above 5000 K out to $10 R_{\star}$. However, the radio observations of Lim *et al.* (1998) revealed a much cooler wind (see Chapter 3) in conflict with the models of Hartmann & Avrett (1984). One current school of thought is that giant convection cells may initiate the mass-loss process in red supergiants (e.g., Lim *et al.*, 1998), although currently no model exists to explain how such a mechanism could operate.

1.5 Red Giant and Red Supergiant Evolution

Once a star has exhausted the hydrogen in its core, it evolves from the main sequence where its evolutionary future is dependent mainly on its mass. The vast majority of stars are of either low (i.e., $M_\star \lesssim 3 M_\odot$) to intermediate mass (i.e., $3 \lesssim M_\star \lesssim 8 M_\odot$), and evolve to become red giants, while the rare massive stars (i.e., $M_\star \gtrsim 8 M_\odot$) generally evolve to become red supergiants. The stars studied in this thesis are either low mass or massive stars. These evolved late-type stars contain a condensed core with an extended envelope and have cooler effective temperatures than when on the main sequence. There is currently no consensus in the scientific community on why stars become red giants or red supergiants (e.g., Stancliffe *et al.*, 2009; Sugimoto & Fujimoto, 2000). A common explanation is that the initial expansion is driven by the envelope maintaining thermal equilibrium in response to increasing luminosity from the core. This expansion causes local cooling, allowing heavy elements to recombine, therefore causing an increase in opacity. This increase in opacity traps energy, leading to a runaway expansion that brings the star to the red giant or red supergiant region of the H-R diagram (Renzini *et al.*, 1992). However, Iben (1993) computed evolutionary models for intermediate mass stars with the opacity held constant throughout, and showed that these models still became giants. This meant that opacity was not responsible for the transition to a red giant, apparently in contradiction to Renzini *et al.* (1992).

1.5.1 Change in Atmospheric Dynamics

The expansion of a star's radius as it evolves off the main sequence greatly affects the dynamics of its atmosphere through the change of surface gravity. The decrease in surface gravity causes the pressure scale height to increase, resulting in very extended atmospheres. The mass-loss rate also increases due to the increase in the stellar surface area ($\propto R_\star^2$). In Table 1.1 we describe the typical properties of a 1 and $15 M_\odot$ star, both on the main sequence and as an evolved late-type star. We use these as examples to highlight the changes in the atmospheric dynamics when a star becomes a red giant or red supergiant. For these stars, the massive increase in stellar radius means that the pressure scale height as a fraction of the

1.5 Red Giant and Red Supergiant Evolution

stellar radius, $H_P/R_\star \propto T_{\text{eff}}R_\star$, is ~ 2 orders of magnitude greater than when on the main sequence. There is also a drastic change in the terminal wind velocity, v_∞ . While on the main sequence, hot massive stars have wind velocities that are many times the photospheric escape velocity, v_{esc} , while solar type stars have terminal wind velocities close to v_{esc} . For evolved late-type stars the terminal wind velocity is generally much less than the photospheric escape velocity, signaling that the onset of these winds must be at several stellar radii. The final column in Table 1.1 is a comparison of the integrated mass-loss of these stars while on and off the main sequence. It is clear that during the time, t , spent in these evolved states, these stars lose a significant proportion of their initial mass, i.e., $\sim 30\%$ for massive stars and $\sim 10\%$ for the lower to intermediate mass stars. Such large quantities of mass-loss must have a significant impact on the evolution of the stars themselves and on their surrounding environments.

Table 1.1: Typical properties for main sequence and evolved $1 M_\odot$ and $15 M_\odot$ stars.

Evolutionary Stage ^a	R_\star (R_\odot)	H_P/R_\star	v_∞ (km s $^{-1}$)	v_{esc} (km s $^{-1}$)	t (yr) ^b	\dot{M}_\star (M_\odot yr $^{-1}$)	$t \times \dot{M}_\star$ (M_\odot)
MS F/G	1	10^{-4}	400	600	10^{10}	10^{-14}	10^{-4}
RG	40	10^{-2}	40	100	10^9	10^{-10}	0.1
MS O/B	5	10^{-4}	3000	1000	10^6	10^{-6}	1
RSG	1000	10^{-2}	20	75	5×10^5	10^{-5}	5

^a MS F/G = main sequence spectral type F and G stars. RG = red giant. MS O/B = main sequence spectral type O and B stars. RSG = red supergiant.

^b The lifetimes for the evolutionary phases of the massive star are taken from Stothers & Chin (1969)

1.5.2 Evolutionary Tracks

Once a massive star on the main sequence has exhausted its hydrogen core, it follows a nearly horizontal evolution across the H-R diagram where it usually becomes a helium burning RSG. Examples of these horizontal evolutionary tracks are shown in Figure 1.4 for masses between 9 and $120 M_\odot$. Once the massive blue hydrogen burning stars move off the main sequence, they rapidly evolve across

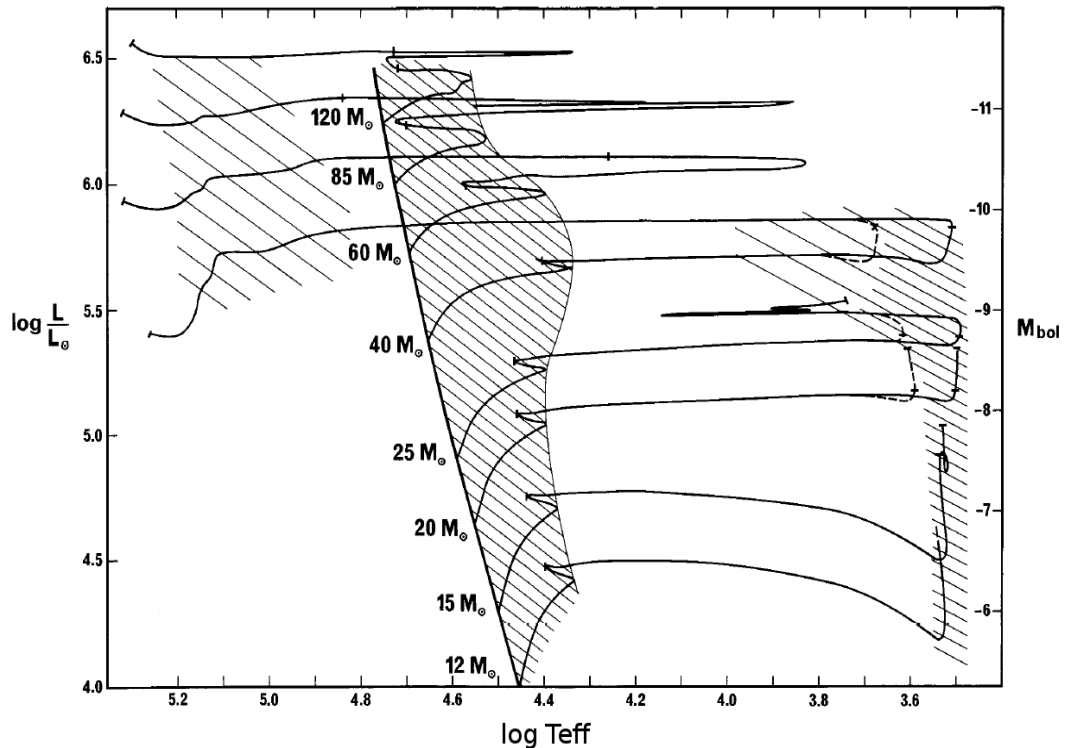


Figure 1.4: Evolutionary tracks of massive stars from Maeder & Meynet (1987). The shaded regions correspond to long-lived evolution phases on the main sequence, and during core He burning as a RSG (at $\log T_{\text{eff}} < 4.0$) or as a W-R star (at $\log T_{\text{eff}} > 4.8$).

the “yellow void” passing through the very short-lived yellow supergiant stage (Levesque, 2010). As these stars evolve, the luminosity remains almost constant because massive stars do not develop degenerate cores and most of the mass is in radiative equilibrium. For stars with main sequence masses $\lesssim 25 M_{\odot}$, like Betelgeuse, the RSG phase is the final stage before ending their lives as hydrogen-rich Type II supernovae. These stars lose a few M_{\odot} during the RSG phase but do not lose enough to remove the whole H-rich envelope. Stars with masses $25 M_{\odot} \lesssim M_{\star} \lesssim 40 M_{\odot}$ lose their H-rich envelope during the RSG stage, turning the star into a W-R star. Finally, stars with $M_{\star} \gtrsim 40 M_{\odot}$ never become RSGs, as their H-rich envelopes are blown off before the RSG stage can be reached.

For low mass stars like Arcturus and Aldebaran, whose masses are $\sim 1 - 2 M_{\star}$,

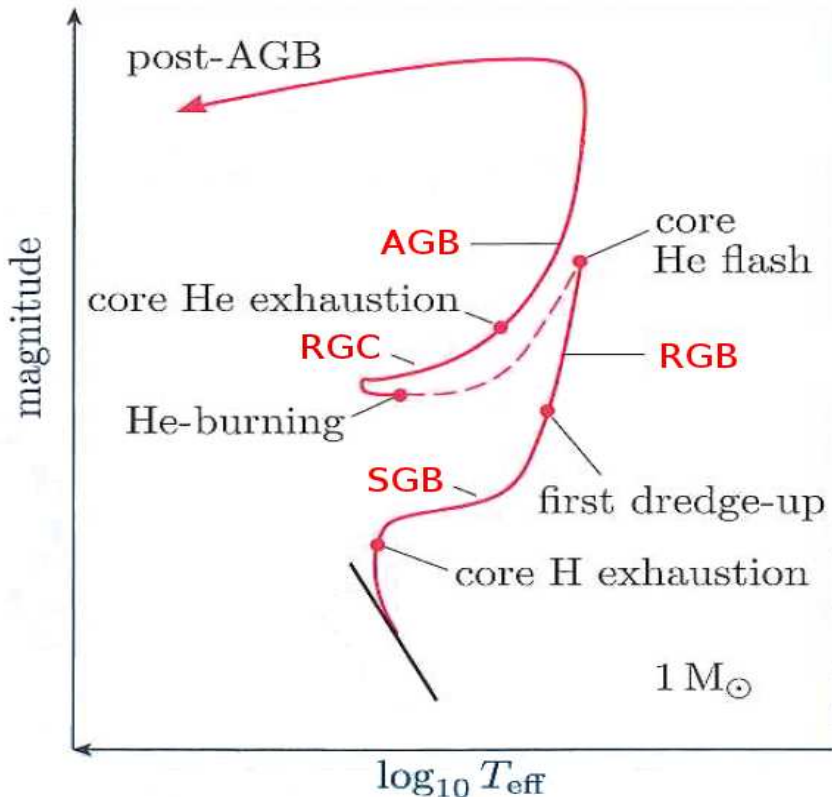


Figure 1.5: Evolutionary track for a $1 M_{\star}$ star. The post main sequence evolution can generally be categorized into four main stages, i.e., the subgiant branch (SGB), the red giant branch (RGB), the red giant clump (RGC), and the asymptotic giant branch (AGB). Figure is adapted from Ryan & Norton (2010).

the post main sequence evolution can generally be categorized into four main stages as shown in Figure 1.5. The following brief summary of these four stages is based on the conclusions of Iben (1967) and Ryan & Norton (2010).

1. The Subgiant Branch (SGB): This stage is the beginning of the period when a star has stopped core hydrogen burning but has not yet begun core helium burning. The core contracts therefore increasing the star's central temperature enough to initiate hydrogen fusion in a shell surrounding the core. The star swells and the effective temperature drops as it moves rapidly across the SGB, resulting in the Hertzsprung Gap.
2. The Red Giant Branch (RGB): As a star moves up the RGB its luminosity

1.5 Red Giant and Red Supergiant Evolution

increases dramatically. The H-burning shell experiences a large gravitational force from the dense contracting core, causing the shell to compress and increase its energy output. A deep convective outer envelope penetrates the inner layers containing the remnants of H-burning resulting in newly synthesized nuclei being transported to the surface. This process is called the “first dredge-up” and the star’s surface $^{12}\text{C}/^{13}\text{C}$ ratio decreases to 5 – 40 (Lambert & Ries, 1981) due to the greater proportion of ^{13}C in C/N-cycled material. At the tip of the RGB, the core finally reaches a sufficiently high temperature to cause helium burning, igniting the triple alpha process. The core begins to expand and the outer layers of the star contract, raising the surface temperature and leading to the output of less shell energy. This leads to a momentary decrease in luminosity and the star moves off the RGB.

3. The Red Giant Clump (RGC): Core helium burning and hydrogen shell burning characterize the RGC. A star’s position on the RGC depends on its initial mass and composition, and also on the amount of mass it has lost during the red giant phase. The pressure increases on the H-burning shell from the contracting envelope above, leading to an overall increase in luminosity. Core He-burning leads to an increasing molecular weight of the gas in the core, causing it to eventually contract. At the end of the RGC phase, all of the helium in the core is exhausted. The core collapses and the temperature rise ignites a shell of He-burning. The star now approaches the asymptotic giant branch.
4. The Asymptotic Giant Branch (AGB): The AGB is marked by a C-O core with two burning shells of He and H. The C-O core continues to grow and contract as the adjacent He shell burns. Stars with $M_\star \gtrsim 4 M_\odot$ will undergo a “second dredge up”, resulting again in the enhancement of the $^{12}\text{C}/^{13}\text{C}$ ratio. With both shells burning, energy is consumed at an ever increasing pace and the star rapidly moves up the AGB while also developing periodic instabilities and generating large mass-loss rates. For stars with masses $\lesssim 8 M_\odot$, their cores never reach high enough temperatures to burn C-O.

1.6 Radio Emission from Stellar Atmospheres

Higher mass stars can continue the process until iron is generated in the core and the evolution has gone as far as it can go.

Traditionally, it has been almost impossible to distinguish between red giants burning helium in the core and those burning only hydrogen in an outer shell. Asteroseismology is now becoming a powerful tool to help probe the internal structures of stars by using their natural oscillation frequencies (Beck *et al.*, 2011), and has recently been used to distinguish between hydrogen and helium burning red giants (Bedding *et al.*, 2011). In this thesis, the term “red giant” refers to evolved low mass stars which have not reached the AGB stage of evolution.

1.6 Radio Emission from Stellar Atmospheres

If we assume the Sun to be a nearly ideal blackbody with temperature $T = 5800\text{ K}$, then at 10 GHz (i.e., 3 cm), its flux density at Earth would be $\sim 10^6\text{ Jy}$. However, at the distance of the nearest star¹ other than the Sun, its flux density would be only $\sim 15\mu\text{Jy}$. Until recently², such a value would have been impossible to detect with even the most powerful radio telescopes. Nevertheless, stars have been detected at radio wavelengths for decades, which tells us immediately that such stars behave differently to the Sun at radio wavelengths. In fact, the discovery that such a huge range of stars emit detectable radio emission was one of the major and unexpected achievements of the old VLA (White, 2000). A sample of the radio detected stars is plotted on a H-R diagram in Figure 1.6, with the filled symbols representing the non-thermal emitters, and the open symbols representing the thermal emitters.

It is clear that the majority of the main sequence and subgaint objects are non-thermal emitters. The only thermal emitters on the main sequence are the massive hot O-B stars which emit free-free radiation from their dense and ionized winds (e.g., Scuderi *et al.*, 1998). Their radio spectrum are generally in good agreement with ionized constant velocity isothermal stellar winds (i.e., $F_\nu \propto \nu^{0.6}$ as discussed in Section 1.8.4). These massive hot stars also emit non-thermal

¹The binary system α Cen AB are the closest stars to the Sun at $\sim 1.3\text{ pc}$.

²The new VLA has the ability to detect such values

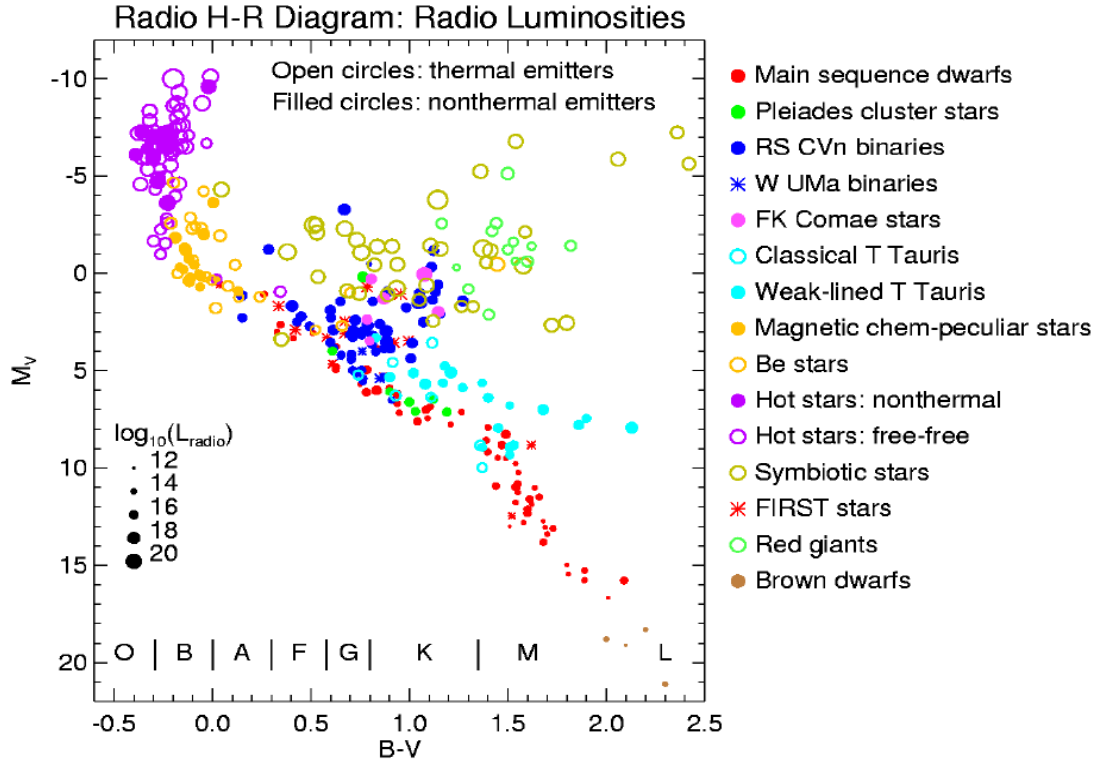


Figure 1.6: Sample of the radio detected stars plotted on a H-R diagram. The filled symbols represent non-thermal emitters while the open symbols represent the thermal emitters. The larger symbols are more radio luminous than the smaller symbols. In general, the sparse thermal emitters are stars with ionized or partially ionized extended stellar atmospheres whose radio emission comes from free-free interactions. Figure from White (2000).

emission, which is believed to be produced by electron shock acceleration in the inhomogeneous wind. The cool region of the main sequence in Figure 1.6 contains red filled dots representing young F, G, K, and M dwarfs. These objects have “non-thermal coronae”, which in addition to thermal populations of electrons at 10^{6-7} K, contain non-thermal populations, which are trapped on closed magnetic field lines and produce strong radio emission. These objects are also flare stars, meaning that they occasionally emit strong optical outbursts. The blue filled circles near the center of the diagram are RS CVn binaries which consist of a late-type giant or subgiant and a close binary companion (Strassmeier *et al.*,

1993). These systems generally rotate fast with typical orbital periods of a few days. Tidal forces between the close components have locked their rotational periods to the orbital period. This fast rotational period in combination with outer convective zones generate intense magnetic activity and subsequent radio emission.

Single (non-binary) cool evolved stars lack the characteristics which make the other stars, described above, radio bright. Even though they have outer convective zones, they rotate too slowly to generate, via an $\alpha - \Omega$ dynamo, the type of magnetic activity which make subgiant binaries and young cool dwarfs strong non-thermal radio emitters. They also lack the intense UV radiation field of the massive hot main sequence stars and their outflows are generally only partially ionized ($n_e/n_H = 10^{-4} - 10^{-1}$). However, their large angular diameters coupled with their relatively large mass-loss rates, means that their partially ionized outflows can be detected at radio wavelengths. Red giants are feeble radio emitters however and up until the work presented in this thesis, only a small number have been detected at one or more radio wavelengths, and these have been modest S/N measurements. On the other hand, a few close-by red supergiants, like Betelgeuse, have mass-loss rates many orders of magnitude greater than the red giants and their partially ionized outflows can be easily detected at multiple radio wavelengths. These red supergiants also contain extended circumstellar envelopes (CSEs) which can be sources of molecular line emission at radio wavelengths.

1.7 Radio Emission Mechanisms

The two radio emission mechanisms which are most relevant in this thesis are thermal bremsstrahlung/free-free emission, and molecular line emission. Both of these emission mechanisms produce incoherent radiation and are discussed in the following sections. Under certain plasma conditions, coherent radiation can be produced due to resonances between particles and some natural wave mode of the plasma, such as Langmuir waves (plasma oscillation) or electron-cyclotron waves. The main characteristic frequencies of the emission from these waves are

the electron plasma frequency

$$\nu_p = \frac{\omega_p}{2\pi} = \left(\frac{n_e e^2}{\pi m_e} \right)^{1/2} \approx 9000 n_e^{1/2} \text{ Hz} \quad (1.14)$$

and the electron-cyclotron frequency

$$\nu_B = \frac{\Omega_B}{2\pi} = \frac{eB}{2\pi m_e c} \approx 2.8B \text{ MHz} \quad (1.15)$$

where n_e is the electron number density with units cm^{-3} , and B is the magnetic field strength with units G [1 Gauss (G) = 1×10^{-4} tesla (T)]. The largest electron densities in the atmospheres of cool evolved stars are typically of the order $n_e \sim 10^9 \text{ cm}^{-3}$ (Judge & Carpenter, 1998), giving a plasma frequency of $\sim 280 \text{ MHz}$. The radio observations discussed in this thesis were all carried out at frequencies $\nu > 1 \text{ GHz}$, well above the plasma frequency, and we can therefore safely make the assumption that the atmospheric refractive index is ~ 1 for cool evolved stars. These stars are also expected to have magnetic field strengths of $\lesssim 10 \text{ G}$ (e.g., Bedecarrax *et al.*, 2013; Sennhauser & Berdyugina, 2011) and so the electron-cyclotron frequency in their atmospheres are expected to be of the order $\nu_B \sim 30 \text{ MHz}$, again well below our observing frequencies. The radio emission from these stars is therefore not expected to be circularly polarized. We now discuss the important radio emission mechanisms in the atmospheres of cool evolved stars.

1.7.1 Thermal Free-free (Bremsstrahlung) Emission

Thermal bremsstrahlung from an ionized or partially ionized plasma is often called free-free emission because it is produced by free electrons which are deflected off ions without being captured. For free-free radio emission, the distant Coulomb interactions of electrons with ions, which cause small angle deflections, are much more important than the rare close encounters and large deflections (Dulk, 1985). The free-free emission, which is the energy radiated per unit volume, per unit time, per unit frequency, is given in Rybicki & Lightman (1979) as:

$$\varepsilon_\nu^{ff} = 6.8 \times 10^{-38} Z^2 n_e n_i T^{-1/2} e^{-h\nu/kT} g_{ff} \text{ erg cm}^{-3} \text{ s}^{-1} \text{ Hz}^{-1}. \quad (1.16)$$

Here, Z is the charge of the ion, n_i is the ion density, and g_{ff} is the free-free Gaunt factor and is a correction factor which is a function of electron energy and frequency of emission. Extensive tables and graphs of g_{ff} exist in the literature (e.g., Karzas & Latter, 1961). The free-free emissivity, which is a fundamental term in the equation of radiative transfer is then

$$j_{\nu}^{ff} = \frac{\varepsilon_{\nu}^{ff}}{4\pi}. \quad (1.17)$$

The free-free radio opacity can then be found from Kirchoff's law and is discussed in Section 1.8.3.

1.7.2 Molecular Line Emission

A diatomic molecule such as CO or SiO, can vibrate (stretch) along the internuclear axis and can also undergo rotational motion around an axis perpendicular to the internuclear axis. The rotational levels of these molecules are designated by a single vibrational quantum number, v , and a rotational quantum number, J . Most of the diatomic molecular lines observed in the radio spectrum are from the rotational levels. These rotational energy levels are approximately those allowed by quantum mechanics for a rigid rotator, i.e., a linear molecule that does not change shape as it rotates. The rotational kinetic energy is

$$E_{\text{rot}} = \frac{I\omega^2}{2} \quad (1.18)$$

where $I = m_r r_0^2$ is the moment of inertia, m_r is the reduced mass, r_0 is the separation of the two masses, and ω is the angular velocity of the rotation. The quantization of angular momentum, L , to integer multiples of \hbar leads to $L = J\hbar$, where $J = 0, 1, 2, \dots$. Equation 1.18 can then be written as

$$E_{\text{rot}}(v, J) = \frac{L^2}{2I} = \frac{J(J+1)\hbar^2}{2I} = \frac{J(J+1)\hbar^2}{2m_r r_0^2} = B_v J(J+1) \quad (1.19)$$

where B_v is the *rotation constant* and is subscripted v because the moment of inertia depends on the vibrational state. $^{12}\text{C}^{16}\text{O}$ and $^{28}\text{Si}^{16}\text{O}$, two molecules studied in this thesis, have rotation constant values of $B_v = 2.766$ and 1.042 K , respectively (Huber & Herzberg, 1979).

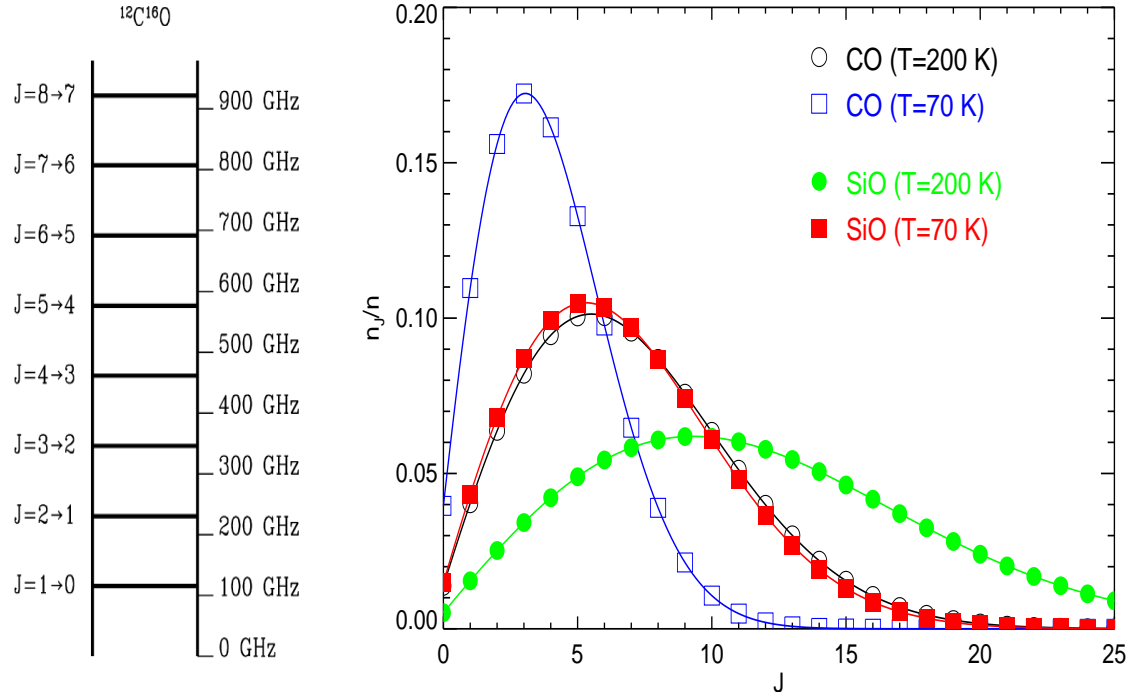


Figure 1.7: *Left:* The radio spectrum of $^{12}\text{C}^{16}\text{O}$ resembles a *ladder* with each step being a harmonic of the fundamental frequency that is determined solely by the moment of inertia. This molecule has a relatively small moment of inertia and therefore has no cm-wavelength lines. *Image Credit:* NRAO’s Essential Radio Astronomy course. *Right:* The relative populations of the rotational levels of $^{12}\text{C}^{16}\text{O}$ and $^{28}\text{Si}^{16}\text{O}$ at temperatures of 70 and 200 K, the excitation temperatures Bernat *et al.* (1979) derived for the two circumstellar outflows of Betelgeuse. At lower temperatures, the distribution of the relative populations of the rotational levels is towards lower J s and is shifted towards higher J s at higher temperatures.

Pure rotational transitions, $J \rightarrow J - 1$, have energy $h\nu = 2B_vJ$. It is straightforward to show that the rotational transitions $J = 1 - 0$ and $J = 2 - 1$ of the CO molecule results in spectral lines at frequency 115.2712 and 230.5424 GHz. A radio spectrum of a particular diatomic molecular species will resemble a *ladder* as shown in Figure 1.7. Each step in the plot are all harmonics of the fundamental frequency that is determined solely by the moment of inertia of that species. As $\nu \propto m^{-1}r_0^{-2}$, large heavy molecules in CSEs may be seen at centimeter wavelengths, but smaller and lighter molecules such as CO and SiO emit only at millimeter wavelengths. Rotational states are usually populated according to

1.7 Radio Emission Mechanisms

Boltzmann's law at densities and temperatures where vibrational levels cannot be excited. In this case the Boltzmann equation can be used to find the relative populations of the levels:

$$\frac{n_J}{n} = \frac{g_J e^{-E_J/kT}}{Z} \quad (1.20)$$

where $n = \sum_J n_J$, and $Z(T)$ is a normalization denominator called the partition function, found by summing over all levels, J ,

$$Z(T) = \sum_J^{\infty} g_J e^{-E_J/kT} \quad (1.21)$$

$$= \sum_{J=0}^{\infty} (2J+1) e^{-B_v J(J+1)/T} \quad (1.22)$$

$$\approx \int_0^{\infty} (2J+1) e^{-B_v J(J+1)/T} dJ = T/B_v. \quad (1.23)$$

where we have replaced the sum over discrete values of J with a continuous integral (Shu, 1991). The relative rotational populations within a given vibrational state are then

$$\frac{n_J(v)}{n(v)} \approx \frac{(2J+1)B_v}{T} e^{-B_v J(J+1)/T}. \quad (1.24)$$

This distribution is plotted in Figure 1.7 for the ground vibrational levels of CO and SiO and shows how the levels are populated with respect to one another at two different temperatures¹. The distribution is such that at low temperatures, the rotational levels are more populated at lower J s, while higher J s become more populated at higher temperatures. Differentiating Equation 1.24 with respect to J gives the most probable occupied rotational state, J_{mp} , as a function of temperature (Rodgers & Glassgold, 1991),

$$J_{\text{mp}} = \sqrt{\frac{T}{2B_v}} - \frac{1}{2}. \quad (1.25)$$

Using the excitation temperatures of the two flows (i.e., S1 and S2) around Betelgeuse from Bernat *et al.* (1979) gives $J_{\text{mp}} = 6$ (S1; $T_{\text{exc}} = 200$ K) and $J_{\text{mp}} = 3$ (S2; $T_{\text{exc}} = 70$ K).

¹These are the expected excitation temperatures of the two CSE flows of Betelgeuse.

1.8 Radio Observations of Stellar Atmospheres

The total flux produced by a transition out of the most probable occupied state, $J_{\text{mp}} \rightarrow J_{\text{mp}} - 1$, will not necessarily be the transition that emits the most flux. To show this, we first note that the emission for any rotational transition is

$$\varepsilon_{J,J-1} = \Delta E_{J,J-1} n_J A_{J,J-1} = \Delta E_{J,J-1} n_H A_{\text{mol}} \frac{n_J}{n_{\text{mol}}} A_{J,J-1} \quad (1.26)$$

where the spontaneous emission coefficient can be written as

$$A_{J,J-1} = 2.14 \times 10^{-7} \frac{J^4}{2J+1} \text{ s}^{-1} \quad (1.27)$$

(Draine, 2011), $\Delta E_{J,J-1} = 2B_v J$, and A_{mol} is the molecular abundance. Therefore, the total flux not only depends on the population of the level but also on the change in energy and the probability of undergoing that transition. The integrated flux is then

$$F(J) \propto \frac{B_v J^5}{T} e^{-J(J+1)B_v/T} \quad (1.28)$$

which can be differentiated with respect to J to find the peak transition that emits the most flux, J_{peak} ,

$$J_{\text{peak}} = \frac{\sqrt{1 + 40T/B_v} - 1}{4}. \quad (1.29)$$

For CO, $J_{\text{peak}} \approx \sqrt{T/1.1}$, which again for the two flows around Betelgeuse gives $J_{\text{peak}} = 13$ (S1; $T_{\text{exc}} = 200$ K) and $J_{\text{peak}} = 8$ (S2; $T_{\text{exc}} = 70$ K).

1.8 Radio Observations of Stellar Atmospheres

In the following sections we present the basic definitions used to describe radio observations of stellar atmospheres. We define the *brightness temperature* which is commonly used in radio astronomy to measure the brightness of a source, along with its relationship to the fundamental quantity measured by a radio telescope, the *flux density*. Focusing on thermal emission, we describe how the flux density varies with frequency when observing both optically thin and optically thick stellar atmospheres, and conclude by discussing how molecular emission line profiles can be studied at radio wavelengths.

1.8.1 Brightness Temperature

In thermodynamic equilibrium the spectral distribution or brightness, B_ν , of the radiation of a black body with temperature T_e is given by the Planck law

$$B_\nu(T_e) = \frac{2h\nu^3}{c^2} \frac{1}{e^{h\nu/kT_e} - 1} \quad (1.30)$$

and has units $\text{erg s}^{-1} \text{cm}^{-1} \text{Hz}^{-1} \text{sr}^{-1}$. One can easily switch to a wavelength form using $B_\nu d\nu = B_\lambda d\lambda$. When $h\nu \ll kT_e$, Equation 1.30 becomes the *Rayleigh-Jeans Law*

$$B_\nu(T_e) = I_\nu(T_e) = \frac{2\nu^2 k T_e}{c^2}. \quad (1.31)$$

This equation does not contain Plank's constant and therefore is the classical limit of the Planck Law. We have also included the specific intensity, I_ν , in Equation 1.31 as it has the same units as the spectral brightness and for blackbody radiation, $I_\nu(T_e) = B_\nu(T_e)$. This equation is valid for all thermal radio sources except in the millimeter or sub-millimeter regime at low temperatures (Rohlfs & Wilson, 1996). In the Rayleigh-Jeans relation, the brightness is strictly proportional to the thermodynamic temperature of the black body. In radio astronomy it is customary to measure the brightness of an object by its *brightness temperature*, T_b . Therefore, the brightness temperature is the temperature at which a blackbody would have to be in order to reproduce the observed brightness of an object at frequency ν and is defined as

$$T_b \equiv \frac{c^2}{2k\nu^2} I_\nu. \quad (1.32)$$

If $h\nu/kT \ll 1$ and if I_ν is emitted by a blackbody, then T_b is the thermodynamic temperature of the source. If other processes are responsible for the emission or if the frequency is so high that Equation 1.31 is not valid, then T_b is different from the thermodynamic temperature of a black body.

The equation of radiative transfer describes the change in specific intensity of a ray along the line of sight in a slab of material of thickness ds

$$\frac{dI_\nu}{ds} = j_\nu - \kappa_\nu I_\nu \quad (1.33)$$

1.8 Radio Observations of Stellar Atmospheres

where j_ν and κ_ν are the emissivity (in $\text{erg s}^{-1} \text{cm}^{-3} \text{Hz}^{-1} \text{sr}^{-1}$) and the absorption-opacity coefficient (in cm^{-1}) of the plasma. In thermodynamic equilibrium, the radiation is in complete equilibrium with its surroundings and the brightness distribution is described by the Planck function

$$\frac{dI_\nu}{ds} = 0, \quad I_\nu = \frac{j_\nu}{\kappa_\nu} = B_\nu(T_e). \quad (1.34)$$

Equation 1.33 can be solved by first defining the optical depth, $d\tau_\nu$, as

$$d\tau_\nu = -\kappa_\nu ds \quad (1.35)$$

and then integrated by parts between 0 to s , and τ to 0, to give

$$I(s) = I(0)e^{-\tau(s)} + \int_{\tau(s)}^0 e^{-\tau} \frac{j_\nu}{\kappa_\nu} d\tau. \quad (1.36)$$

The second term within the integral is known as the source function, S_ν , and this can be taken outside of the integral in the case of a homogeneous source, i.e., one for which both the emissivity and absorption coefficient are constant along the ray path. The solution then to the equation of radiative transfer for a homogeneous source is

$$I_\nu = I_0 e^{-\tau} + \frac{j_\nu}{\kappa_\nu} (1 - e^{-\tau}). \quad (1.37)$$

Using Equations 1.32 and 1.34 one obtains

$$T_b = T_0 e^{-\tau} + T_e (1 - e^{-\tau}). \quad (1.38)$$

This equation assumes thermodynamic equilibrium and so only holds for a thermal source. If T_e is replaced with $T_{\text{n-t}} = h\nu/k$ then this equation becomes valid for a homogeneous non-thermal source, i.e.,

$$T_b = T_0 e^{-\tau} + T_{\text{n-t}} (1 - e^{-\tau}). \quad (1.39)$$

For an isolated thermal source, there are two limiting cases:

$$T_b = T_e \quad (\text{i.e., for optically thick } \tau \gg 1) \quad (1.40)$$

and

$$T_b = \tau T_e \quad (\text{i.e., for optically thin } \tau \ll 1). \quad (1.41)$$

In Equations 1.40 and 1.41, T_e can also be replaced by $T_{\text{n-t}}$ if the radio emission is non-thermal. Also, these equations are only valid if the source is spatially resolved. If the source is unresolved then a lower limit to T_e or $T_{\text{n-t}}$ is found.

1.8.2 Brightness Temperature and Flux Density

The flux density, F_ν , is a fundamental quantity measured by a radio telescope and is usually measured in Janskys (Jy) where $1 \text{ Jy} = 1 \times 10^{-26} \text{ W m}^{-2} \text{ Hz}^{-1}$. The observed flux density measured by the radio telescope is related to the specific intensity by

$$F_\nu = \int_{\Omega} I_\nu d\Omega \quad (1.42)$$

where Ω is the solid angle subtended by the source or the antenna beam. The radio emission from evolved cool stars is almost purely thermal and so Equation 1.42 becomes

$$F_\nu = \frac{\pi R^2}{d^2} \frac{2k\nu^2 T_b}{c^2} \quad (1.43)$$

where R is the radius of the radio emitting region, and we assume that the source is spatially resolved. The angular diameter in radians is $\phi = 2R/d$ and so

$$F_\nu = \frac{\pi k \phi^2 T_b}{2\lambda^2}. \quad (1.44)$$

If ϕ has major and minor axes ϕ_{maj} and ϕ_{min} then (Lim *et al.*, 1998)

$$T_b(K) = 1.96 F_\nu(\text{mJy}) \left(\frac{\lambda}{\text{cm}} \right)^2 \left(\frac{\phi_{\text{min}}}{\text{arcsec}} \frac{\phi_{\text{min}}}{\text{arcsec}} \right)^{-1}. \quad (1.45)$$

Therefore, if an optically thick stellar atmosphere can be spatially resolved at long wavelengths (i.e., ϕ_{maj} and ϕ_{min} can be measured) then the flux density at a particular wavelength gives the brightness temperature and therefore the electron temperature. Unfortunately, the number of stars that can have their atmospheres spatially resolved at radio wavelengths is low due to their relatively small angular diameters. As an example, Betelgeuse has the largest angular diameter of any star other than the Sun in the northern hemisphere, but at 6 cm (i.e., 6 GHz) its

atmosphere is barely resolvable with the VLA in its most extended configuration, which provides a spatial resolution of ~ 330 mas. However, different layers of stellar atmospheres can still be probed, even if the radio emission is unresolved, due to the nature of the free-free radio opacity which is discussed in the next section.

1.8.3 Thermal Free-free Radio Opacity

In Section 1.7.1 we gave an expression for the thermal free-free emissivity of an ionized gas. Kirchoff's law can be used to find the thermal radio free-free opacity (absorption coefficient):

$$\frac{j_{\nu}^{ff}}{\kappa_{\nu}^{ff}} = \frac{2h\nu^3}{c^2} \frac{1}{e^{h\nu/kT} - 1}. \quad (1.46)$$

Using Equation 1.16 and 1.17 provides a value for the free-free radio opacity which is corrected for stimulated emission:

$$\kappa_{\nu}^{ff} = \frac{0.018Z^2 n_e n_i g_{ff}(\nu, T_e)}{T_e^{1.5} \nu^2} \quad \text{cm}^{-1}. \quad (1.47)$$

The Gaunt factor is slightly dependent on temperature and frequency and at cm-wavelengths is given by

$$g_{ff}^{cm} = 11.96 T_e^{0.15} \nu^{-0.1} \quad (1.48)$$

(Altenhoff *et al.*, 1960), while in the sub-millimeter regime it is slightly different

$$g_{ff}^{sub-mm} = 24.10 T_e^{0.26} \nu^{-0.17} \quad (1.49)$$

(Harper *et al.*, 2013; Hummer, 1988). The abundant species in the atmospheres of cool evolved stars are either neutral or single ionized so that $Z = 1$ and $n_e = n_i$. Focusing on centimeter wavelengths, the radio opacity is then

$$\kappa_{\nu}^{ff} = \frac{0.212 n_e^2}{T_e^{1.35} \nu^{2.1}} \quad \text{cm}^{-1}. \quad (1.50)$$

Therefore, the free-free opacity increases towards lower frequencies as $\kappa_{\nu}^{ff} \propto \nu^{-2.1}$ (or longer wavelengths as $\kappa_{\lambda}^{ff} \propto \lambda^{2.1}$). This means that the optical depth, $\tau_{\lambda} = \int \kappa_{\lambda} dr$, also increases towards longer wavelengths implying that the effective

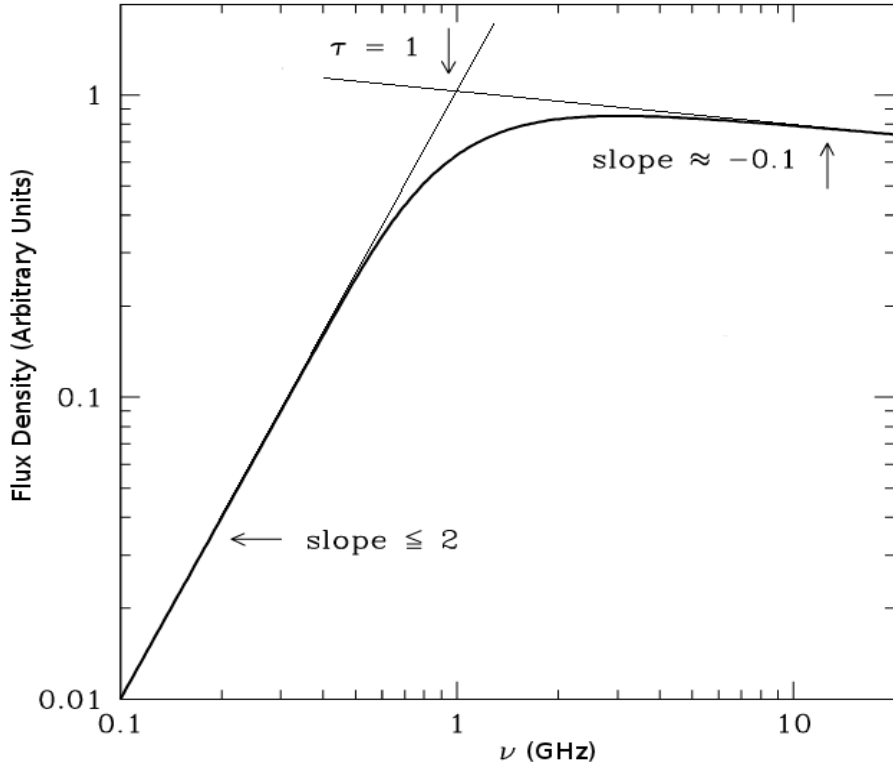


Figure 1.8: The radio spectrum for a hypothetical H II region with no background illuminating source. At long wavelengths the source becomes opaque and has a black body like spectrum with $\alpha = 2$. At short wavelengths where $\tau_\nu \ll 1$, the H II region is almost transparent and $\alpha = -0.1$. Image adapted from NRAO's *Essential Radio Astronomy* course.

radius (i.e., the radius where $\tau_\lambda = \tau_{\text{radial}}$) will increase with longer wavelengths. As a result, different layers of unresolved stellar atmospheres can be probed by observing them at different radio wavelengths.

For thermal radiation, the solution to the equation of radiative transfer (i.e., Equation 1.37) for a plasma with no background source can be written as

$$I_\nu = B_\nu(1 - e^{-\tau}). \quad (1.51)$$

An example of such a source is an isolated H II region. At long enough wavelengths the H II region becomes opaque so that $\tau_\nu \gg 1$. Equation 1.51 then tells us that the spectrum approaches that of a black body with a flux density varying

as $F_\nu \propto \nu^2$. At short wavelengths where $\tau_\nu \ll 1$, the H II region is almost transparent, and the flux density becomes

$$F_\nu \propto \frac{2kT_e\nu^2}{c^2} \tau_\nu \propto \nu^{-0.1}. \quad (1.52)$$

These two scenarios are shown in Figure 1.8 along with the point where these two slopes intersect, which corresponds to the frequency at which $\tau \simeq 1$. When the radio spectrum is plotted on a log-log plot as in Figure 1.8, the spectral slope is referred to as the spectral index, α , and is defined:

$$\alpha = \frac{d \log F_\nu}{d \log \nu}. \quad (1.53)$$

The relatively nearby α Sco binary system (170 ± 29 pc; van Leeuwen 2007), which consists of a M1.5 Iab red supergiant and a B2.5 V star, was observed by Hjellming & Newell (1983) with the old VLA. They found that the massive wind of the red supergiant is ionized around the B2.5 V star creating a H II region. The emission from the H II region had a spectral index of $\alpha = -0.1$, consistent with optically thin emission. The radio excess from the red supergiant was $\alpha = 1.05$, intermediate between that of an isothermal stellar disk emission (i.e., $\alpha = 2$), and an isothermal, constant velocity, and ionization fraction wind whose spectral index is discussed in the following section.

1.8.4 Radio Excess from Stellar Winds

Non-coronal cool evolved stars have partially ionized outflows which emit an excess of continuum emission at long wavelengths. This flux excess is due to thermal free-free emission and is measured relative to the expected photospheric radio flux. If the atmosphere only consisted of a static homogeneous isothermal chromosphere then the radio spectrum would be the summation of the Rayleigh-Jeans tail of the Planck function from the photosphere and the H II spectrum discussed in the previous section. At long wavelengths then, this spectrum would again have a power law of slope $F_\nu \propto \nu^2$. Cool evolved stellar atmospheres cannot in general be described by this simple model because they possess stellar winds which are escaping the gravitational potential of the star and the density thus

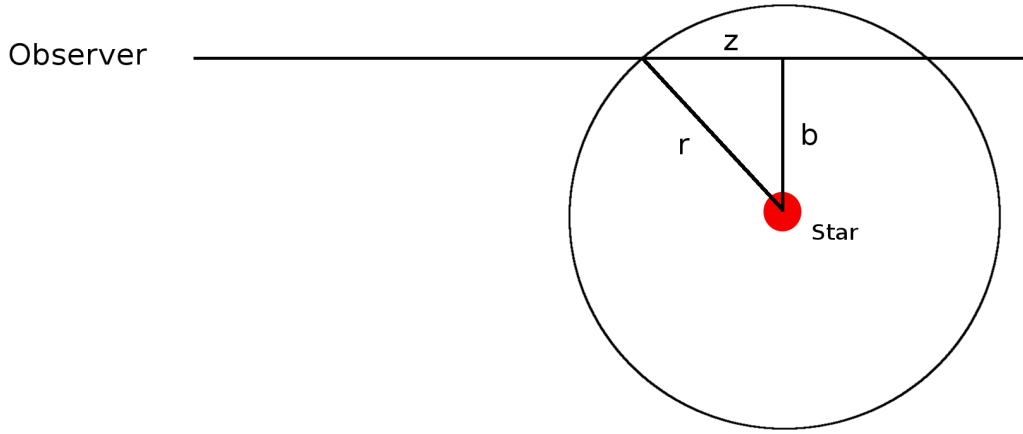


Figure 1.9: In spherical geometry the observer integrates along a ray path in the z direction, with impact parameter, b , to calculate the total optical depth τ_ν , at a frequency ν .

varies with distance from the star. In this section we briefly outline a simple analytical model for the centimeter radio flux for a star with an isothermal, constant velocity, and ionization fraction wind. In Chapter 6 we relax some of these assumptions about the atmosphere's properties to derive a more complete description of the centimeter radio spectrum for these stars.

To calculate the optical depth, we assume spherical geometry and integrate along a ray in the z direction with impact parameter b , as shown in Figure 1.9. The total optical depth at a frequency ν is then

$$\tau_\nu = \int_{-\infty}^{\infty} \kappa_\nu dz \quad (1.54)$$

where the opacity is defined in Equation 1.50. For a constant velocity the electron density is just $n_e(r) = n_e(r_0)(r_0/r)^2$ and so the optical depth can be written as

$$\tau_\nu = \frac{0.212n_e(r_0)^2r_0^4}{T^{1.35}\nu^{2.1}} \int_{\infty}^{\infty} \frac{dz}{(b^2 + z^2)^2}. \quad (1.55)$$

1.8 Radio Observations of Stellar Atmospheres

The solution to this integral is given by (Gradshteyn & Ryzhik, 1994)

$$\int_{-\infty}^{\infty} \frac{dz}{(b^2 + z^2)^{A/2}} = b^{1-A} \sqrt{\pi} \frac{\Gamma(A/2 - 1/2)}{\Gamma(A/2)} \quad (1.56)$$

and so the total optical depth along a ray with impact parameter b is:

$$\tau_{\nu} = \frac{C}{b^3} \quad \text{where} \quad C = \frac{0.333 n_e(r_0)^2 r_0^4}{T^{1.35} \nu^{2.1}}. \quad (1.57)$$

To calculate the flux density we use Equation 1.42 and assume that the source function is given by the Planck function in the Rayleigh-Jeans approximation:

$$F_{\nu} = \frac{2\pi}{d^2} \frac{2\nu^2 k T}{c^2} \int_0^{\infty} (1 - e^{-C/b^3}) b db \quad (1.58)$$

where d is the distance. This integral can be solved using the following expression

$$\int_0^{\infty} y^{v-1} (1 - e^{-uy^p}) dy = \frac{-1}{|p|} u^{-v/p} \Gamma\left(\frac{v}{p}\right) \quad (1.59)$$

which is given in Gradshteyn & Ryzhik (1994). The solution to our integral is then $1.3395 C^{2/3}$ and so the total flux density can be written as

$$F_{\nu} = 2.574 \frac{\pi k}{c^2} \frac{n_e(r_0)^{4/3} r_0^{8/3} T^{0.1} \nu^{0.6}}{d^2}. \quad (1.60)$$

Substituting in the mass continuity equation gives

$$F_{\nu} = 0.277 \frac{k}{c^2 m_H^{4/3}} \frac{\dot{M}^{4/3} T^{0.1} \nu^{0.6}}{\mu^{4/3} v^{4/3} d^2}. \quad (1.61)$$

where \dot{M} is the mass-loss rate. This equation shows that the expected spectral index for an isothermal, constant velocity, and ionization fraction stellar outflow (i.e., a constant property wind) is $\alpha = 0.6$. Equation 1.61 is equivalent to Equation 24 in Panagia & Felli (1975).

The free-free emission from evolved cool stars is weak (usually less than 1 mJy at $\lambda > 3$ cm) and therefore only a handful of these stars have known radio spectral indices at long wavelengths. The small number of such stars whose spectral indices are known have values which are greater than 0.6 (e.g., Drake & Linsky, 1986). Betelgeuse is by far the best studied evolved cool star at radio wavelengths

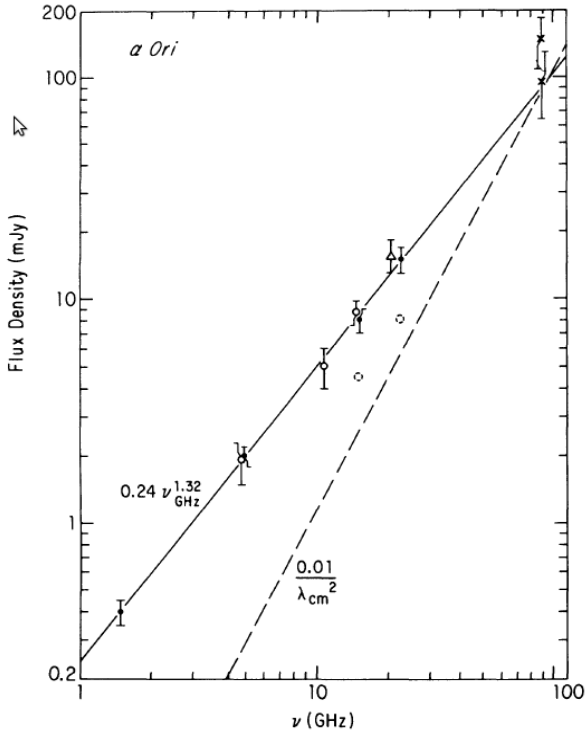


Figure 1.10: Example of a cool evolved star’s radio flux excess, which is a direct result of their ionized atmospheres. Multi-wavelength radio observations of Betelgeuse are plotted along with a best fit power law indicating a spectral index of $\alpha = 1.32$ (Newell & Hjellming, 1982). Even though the observed flux density decreases at longer wavelengths, the excess increases relative to the expected photospheric flux (dashed line).

and its radio spectrum is shown in Figure 1.10 (Newell & Hjellming, 1982). Its spectral index is ~ 1.3 which is significantly larger than 0.6. In Chapter 6 we derive a new version of Equation 1.60 which accounts for a thermal gradient in the outflow, along with flow acceleration. Figure 1.10 is a good example of the radio flux excess which is present for all cool evolved. Even though the observed flux density decreases to longer wavelengths, the excess increases relative to the expected photospheric flux as clearly seen in Figure 1.10.

1.8.5 Molecular Emission Lines from Stellar Winds

The large mass-loss rates of red supergiants along with their low outflow velocities, results in relatively high density winds. This means that these winds are very extended compared to the size of the star itself. The low temperature regime ($T < 1000 K$) of the outer winds (i.e., the CSE) favour the formation of molecules whose emission line profiles have traditionally been studied with single dish radio antennas. As shown in Figure 1.11, these line profiles are generally either flat topped, if the lines are optically thin, or parabolic, if the lines are optically thick. These profile shapes are based on the assumption that the radio antenna is unable to spatially resolve the CSE, which has traditionally been common due to the low resolution of single dish radio antennas. If however, the antenna has the capability to resolve the CSE, then the optically thin line profiles become horned shaped, and the optically thick line profiles become less parabolic, as shown in Figure 1.11. This is due to the fact that the radio antenna does not detect the most extended emission, which has the lowest absolute velocities, and therefore the flux density at the center of the line profile is lower than the rest of the line in the optically thin case.

If these molecular line profiles are observed with a radio interferometer, the appearance of the line can be the same as in Figure 1.11, but the reasons will differ. To explain these reasons, we concentrate on an optically thin emission line. If the emission is unresolved by the interferometer, then as before the profile will be flat topped. However, if the emission is resolved by the interferometer then the profile may take on two different appearances, depending on the *resolving-out scale*¹ of the interferometer. If the emission occurs on scales that are less than the interferometer's resolving-out scale then all emission is recovered and the profile will just have a flat topped appearance. However, if the emission is extended on scales larger than the resolving-out scale, then the interferometer will not detect the material at low absolute velocities (i.e., the most extended material) and the profile will have a horned-shaped appearance - similar to a line profile which has been resolved with a single dish antenna.

¹An interferometer cannot not recover emission on scales larger than this. See Chapter 2.

1.8 Radio Observations of Stellar Atmospheres

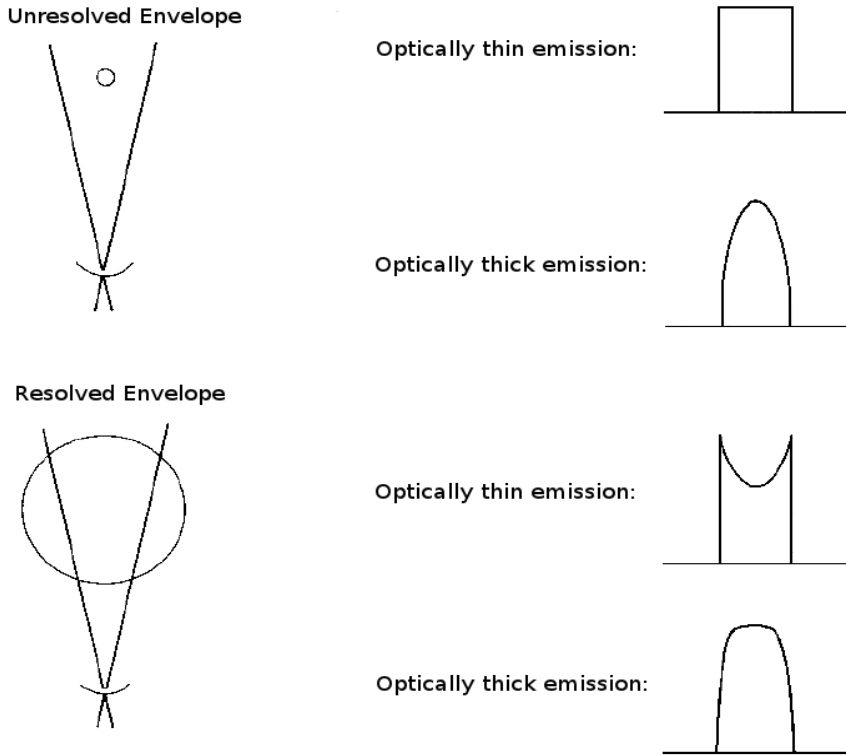


Figure 1.11: Theoretical molecular line profiles of a CSE from a single dish radio antenna. Unresolved line profiles are flat topped for optically thin emission and parabolic for optically thick emission. If the CSE is spatially resolved, the optically thin profile becomes a *horned shaped* line while the optically thick line becomes less parabolic. Figure adapted from Dalgarno & Layzer (1987) with the original permission of H. Olofsson.

Molecular emission lines from red supergiants generally have line widths of the order $20 \rightarrow 50 \text{ km s}^{-1}$, indicative of $10 \rightarrow 25 \text{ km s}^{-1}$ outflows. Even though these velocities are lower than the photospheric escape velocity (generally of the order $50 \rightarrow 100 \text{ km s}^{-1}$), these molecular emission lines are formed in the CSE where the local escape velocity is much lower than at the photosphere and so these lines are indicative of mass-loss.

The most important molecule used in the study of red supergiant outflows is CO, as it can be observed in both O-rich and C-rich stars (Lamers & Cassinelli, 1999). CO is a very stable molecule and can form in the photospheres of very cool

stars and persist far out into the CSE. In typical CSE conditions, the rotational levels in CO are excited via collisions with H atoms and H₂ molecules, and photo-excitation of the vibrational levels by IR photons in a process known as *infrared pumping* (Lamers & Cassinelli, 1999). It is the de-excitation of the rotational transitions of $v = 0$ which produce emission lines at radio (i.e., mm) wavelengths. If collisions are the dominant means of populating the rotational levels (i.e., collisions are more important than infrared pumping) then the distribution over the J levels will be approximately in local thermodynamic equilibrium (LTE) with respect to the gas temperature. If however, infrared pumping is the most efficient means of populating the levels, then the distribution will deviate from LTE.

1.9 Thesis Outline

The main observations used in this thesis were taken at radio wavelengths and utilized the most sensitive radio interferometers available. For this reason, *Chapter 2* is dedicated to introducing the fundamental concepts of radio interferometry. It explains the basic workings of an interferometer and introduces essential radio interferometric terminology including the “complex visibility” and its relation to the sky brightness distribution.

Chapter 3 introduces the three science targets of this thesis; namely, the red supergiant, Betelgeuse, and the red giants, Arcturus and Aldebaran. The properties and capabilities of the radio interferometers used to observe these targets are also described and an overview of the observations is provided.

The radio interferometric data reduction process is outlined in *Chapter 4*. Flowcharts are used to describe the three main steps involved in the analysis of the data; namely, flagging, calibration, and imaging. Examples from the CARMA and VLA data sets are provided at each stage of the data reduction process and the problems specific to data obtained at both short and long wavelengths are discussed.

The results of our millimeter observations of the CSE of Betelgeuse are discussed in detail in *Chapter 5*. The image cubes of the CO($J = 2 - 1$) line and the resulting spectra are presented along with spectra of higher CO rotational

1.9 Thesis Outline

lines. We also present the results of high spatial resolution centimeter continuum observations of the inner atmosphere of Betelgeuse.

Our multi-wavelength centimeter observations of two red giants, Arcturus and Aldebaran, are presented in *Chapter 6*. Previous observations and existing semi-empirical atmospheric models are compared with our high S/N measurements. We discuss the possible physical properties of their stellar atmospheres based on spectral indices and develop a new outer atmospheric model for Arcturus.

Chapter 7 investigates the various heating and cooling processes that control the thermal structure of Arcturus' mass outflow region, using the newly developed atmospheric model. The analysis focuses on the inner region of Arcturus' atmosphere where most of the energy that drives its wind is being deposited.

Chapter 8 presents the main research conclusions and highlights future work which could complement and build on the findings presented in this thesis.

The main analysis and findings of this research are based on newly obtained radio interferometric data from the Combined Array for Research in Millimeter-wave Astronomy (CARMA) and Karl G. Jansky Very Large Array (VLA). These raw data sets were fully reduced by the author. At the end of Chapter 5 we also use archival VLA data which were calibrated by Dr. Alexander Brown¹; and the subsequent imaging and analysis presented in this thesis were carried out by the author. The CO($J = 3 - 2$) line profile presented in 5 was recently obtained from the Submillimeter Array (SMA) and these data were fully reduced by Dr. Joanna Brown².

¹Center for Astrophysics and Space Astronomy, University of Colorado, Boulder, CO 80309-0389, USA

²Harvard-Smithsonian Center for Astrophysics, 60 Garden Street, MS-78, Cambridge, MA 02138, USA

2

Introduction to Radio Interferometry

The low resolution of a single dish radio antenna prevents discrimination against background objects located in the primary beam, so the observed flux density can include unrelated sources. A radio interferometer on the other hand, acts as a spatial filter, enabling separation of the target source from the nearby confusing sources. This chapter introduces the terminology and methods of radio interferometry, an understanding of which is required for subsequent chapters. The fundamental concepts of a radio antenna, which are the basic elements of a radio interferometer, are first discussed along with the radio antenna receiving system. The basic principles of radio interferometry such as the two-element interferometer and the complex visibility are then introduced. The chapter concludes by describing the process of synthesis imaging.

2.1 Radio Antenna Fundamentals

The quality and properties of the final radio image produced from a synthesis array are partially dependent upon the properties of the individual antennas in the array. The most important of such properties are discussed in the following sections and include aperture size, aperture efficiency, pointing accuracy and sidelobe level. We define the radio antenna as the piece of equipment which converts the electromagnetic waves emitted from the observed source into an electrical signal ready to be input into the first low noise amplifier where the signal is at the radio/sky frequency, ν_{RF} . What happens to the signal after this will be discussed in Section 2.2.

2.1.1 Properties of a Radio Antenna

The power gain of a transmitting antenna is a measure of the antenna's capability of converting power into radio waves in a specific direction. In radio astronomy, the receiving counterpart of transmitting power gain is the effective collecting area of an antenna, $A(\nu, \theta, \phi)$, where ν is frequency and θ and ϕ are direction coordinates. An ideal radio antenna would collect all incident radiation from a distant point source and convert it to electrical power. The total spectral power P_ν collected by it would then be a product of its geometric area and the incident spectral power per area, or flux density F_ν . By analogy then, the effective area of a real radio antenna is defined

$$A(\nu, \theta, \phi) = \frac{P_\nu}{F_\nu} = \frac{P}{I(\nu, \theta, \phi)\Delta\nu\Delta\Omega} \quad (2.1)$$

where $I(\nu, \theta, \phi)$ is the source brightness in units $\text{W m}^{-2} \text{ Hz}^{-1} \text{ sr}^{-1}$ that the antenna is pointing at and P is the power (in Watts) received by the antenna in bandwidth $\Delta\nu$ from element $\Delta\Omega$ of solid angle. The normalized antenna reception pattern \mathcal{A} , often referred to as the power pattern due to the duality between receiving and transmitting, is defined as

$$\mathcal{A}(\nu, \theta, \phi) = \frac{A(\nu, \theta, \phi)}{A_0} \quad (2.2)$$

2.1 Radio Antenna Fundamentals

where A_0 (m^2) is often referred to as the effective area of the antenna and is the response at the center of the main lobe of $A(\nu, \theta, \phi)$ [i.e., $A(\nu, 0, 0)$]. Then the beam solid angle, Ω_A , of the primary beam is

$$\Omega_A = \int_{\text{all sky}} \mathcal{A}(\theta, \phi) d\Omega \quad (2.3)$$

and is a measure of the field of view of the antenna.

In the case of an isotropic antenna [i.e., $\mathcal{A}(\nu, \theta, \phi) = 1$], it can be shown that the product of the effective area and the primary beam solid angle is equal to the square of the wavelength (Kraus *et al.*, 1986)

$$A_0 \Omega_A = \lambda^2. \quad (2.4)$$

Ω_A has its maximum possible value of 4π if \mathcal{A} is everywhere equal to 1. This means that the primary antenna can see the whole sky with equal sensitivity. Even though a large field of view is usually desirable in radio astronomy, Equation 2.4 ensures that for any given wavelength, when Ω_A is a maximum, the power received is a minimum and therefore the sensitivity is also at a minimum. To improve sensitivity, one could increase the collecting area of the antenna, but Equation 2.4 then ensures that the field of view must decrease. Thus, when deciding on the primary antenna size in a synthesis array, there is always a trade-off between field of view and sensitivity.

In reality, an antenna cannot radiate isotropically and will radiate preferentially in one or more directions. A Fourier transform relationship exists between the complex voltage distribution of the field, $f(u, v)$, in the aperture of the antenna and the complex far-field voltage radiation pattern, $F(l, m)$, of the antenna (Kraus *et al.*, 1986)

$$F(l, m) = \iint_{\text{aperture}} f(u, v) e^{2\pi i(ul+vm)} du dv \quad (2.5)$$

and

$$f(u, v) = \int_{-\infty}^{\infty} \int_{-\infty}^{\infty} F(l, m) e^{-2\pi i(ul+vm)} dl dm \quad (2.6)$$

where

$$u = \sin\theta \cos\phi \quad \text{and} \quad v = \sin\theta \sin\phi \quad (2.7)$$

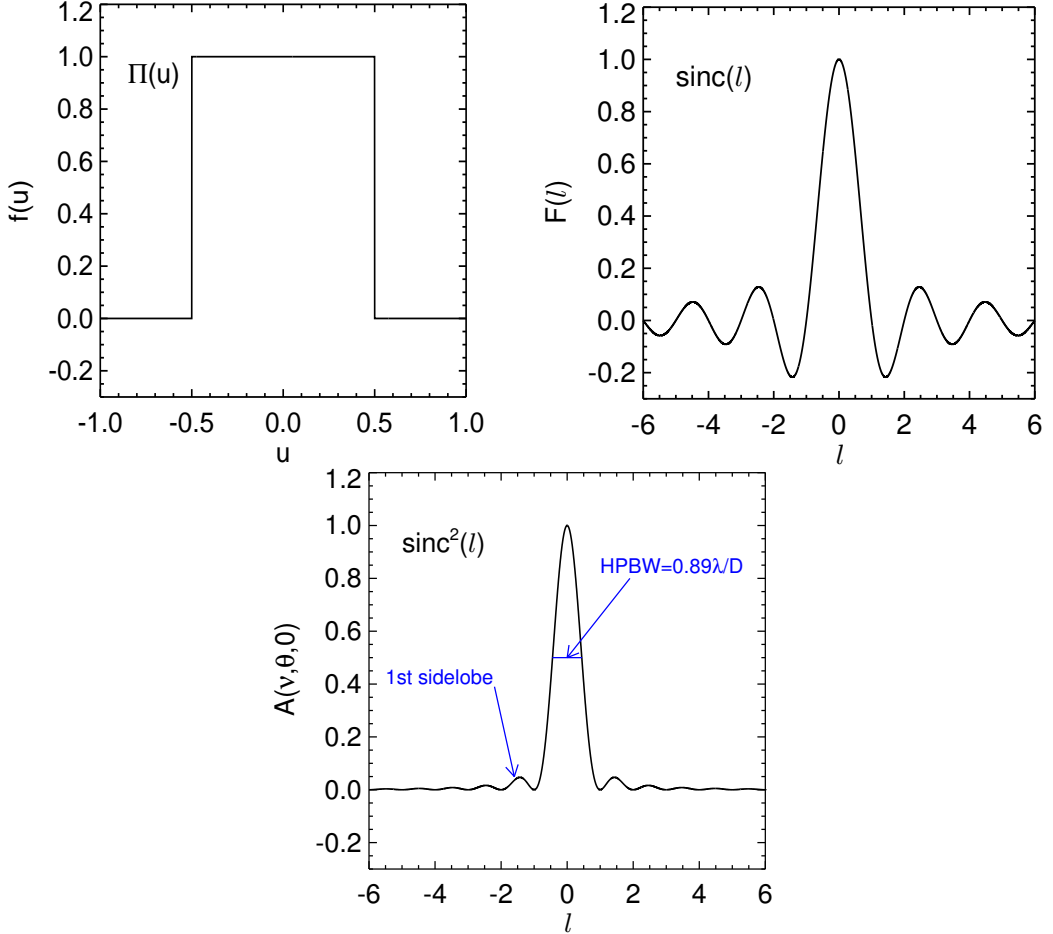


Figure 2.1: Top Left: Uniformly illuminated 1-D aperture $f(u)$. Top Right: The Fourier transform of $f(u)$ gives the antenna radiation pattern in the far-field, $F(l)$. Bottom: The power pattern of the antenna is given by $\mathcal{A} = |F(l)|^2$.

are the antenna coordinates and l and m are their Fourier counterparts. The form of $f(u, v)$ is determined by the manner in which the antenna feed illuminates the aperture. Therefore Equations 2.6 and 2.7 tell us that the radiation pattern in the far-field of a two-dimensional aperture is the two-dimensional Fourier transform of the aperture field illumination. For a uniformly illuminated 1-D aperture shown in Figure 2.1, the radiation pattern in the far-field is the *sinc* function [i.e., $\text{sinc}(x) = \sin(\pi x)/(\pi x)$]. The radiation pattern in the far-field, $F(l, m)$, of such an antenna is related to the antenna power pattern by $\mathcal{A} = |F(l, m)|^2$. This power pattern is known as the Airy pattern if the antenna is uniformly illuminated and

is also shown in Figure 2.1. The central peak of this power pattern is called the main beam while the smaller secondary peaks are called sidelobes. The antenna is maximally sensitive to radiation from the direction of the peak of the beam, but is also slightly sensitive to radiation in the direction of the side lobes. The half-power beamwidth (HPBW) of the main beam θ_{HPBW} is a term commonly used in the literature to describe the field of view of an antenna/interferometer and satisfies

$$\theta_{\text{HPBW}} \propto \frac{\lambda}{D} \quad (2.8)$$

where D is the diameter of the antenna. The constant of proportionality varies slightly with the illumination taper and can be shown to be equal to ~ 0.89 for a uniformly illuminated 1-D aperture, and ~ 1.2 for most single dish radio antennas. When the sky is scanned with a single dish antenna, then this HPBW is the resolution of the resulting map.

2.1.2 Antenna Structural Design

The design of the primary antenna element of an interferometric array will depend on the wavelength range to be observed. In general, dipoles are used for wavelengths longer than ~ 1 m, while reflector antennas are typically used at shorter wavelengths. The reason why the more simple and less expensive dipoles are not used at all wavelengths is given by Equation 2.4. For an isotropic antenna, this equation tells us that the effective area is just

$$A_0 = \frac{\lambda^2}{4\pi}. \quad (2.9)$$

Therefore, at short wavelengths, a non-directional antenna such as a dipole, will have a small effective collecting area, giving it low sensitivity for reception. Thus, dipoles can be used at long wavelengths as they have sufficient collecting area, but cannot be used at shorter wavelengths as an impractical amount would be needed to produce useful collecting areas. Since the interferometric arrays used in this thesis use reflector antennas, the rest of this section will focus on them.

Choice of Antenna Mount. Nearly all interferometric arrays consist of antennas which have altitude over azimuth (alt-azimuth) mounts. These antennas lie

2.1 Radio Antenna Fundamentals

on a horizontal azimuth track on which the antenna can turn in azimuth, and on a horizontal elevation axle about which the antenna can change in zenith angle. The main advantage of such a design is simplicity and thus lower cost. Gravity always acts on the reflector in the same plan, thus reducing the problem of keeping the reflector profile accurate during the duration of an observation. However, sources close to the zenith cannot usually be observed due to the high rate of azimuth rotation required. In addition, the beam rotates with respect to the source for long duration observations, which can affect the dynamic range of total intensity images of very large sources. The other type of mount occasionally used is the equatorial mount. Its polar axis is aligned parallel to the axis of rotation of the Earth and therefore only needs to rotate around the declination axis to observe a source. Furthermore, its beam doesn't have the beam rotation problem encountered by the alt-azimuth design and can track sources close to the zenith. Its major disadvantage and the reason for its scarce usage is the complexity of its design and resulting increased cost.

Choice of Antenna Optics. In Figure 2.2 we show the main optical systems which can be used to feed a large radio reflector. The prime focus system (e.g., used in the Giant Meter Radio Telescope) has the advantage that it can be used at long wavelengths where the use of secondary focus feeds (i.e., sub-reflectors) become impractical. However, access to and space for the feeds and receivers are limited, and sensitivity can be lost due to spillover noise from the ground. The other designs have the advantage of easier access to the feeds and receivers and less spillover noise from the ground. The off-axis Cassegrain (e.g., used in the Very Large Array) also has the advantage of increased frequency capability as many feeds can be located in a circle around the center of the reflector and a slight rotation of the sub-reflector is all that is required to change observing frequency. The receivers and feeds in the Naysmith geometry (e.g., used in the Combined Array for Research in Millimeter wave Astronomy) are located external to the antenna structure. Finally, the offset Cassegrain (e.g., used in the Green Bank Telescope) has no blockage and will have a circular symmetric beam with low sidelobes.

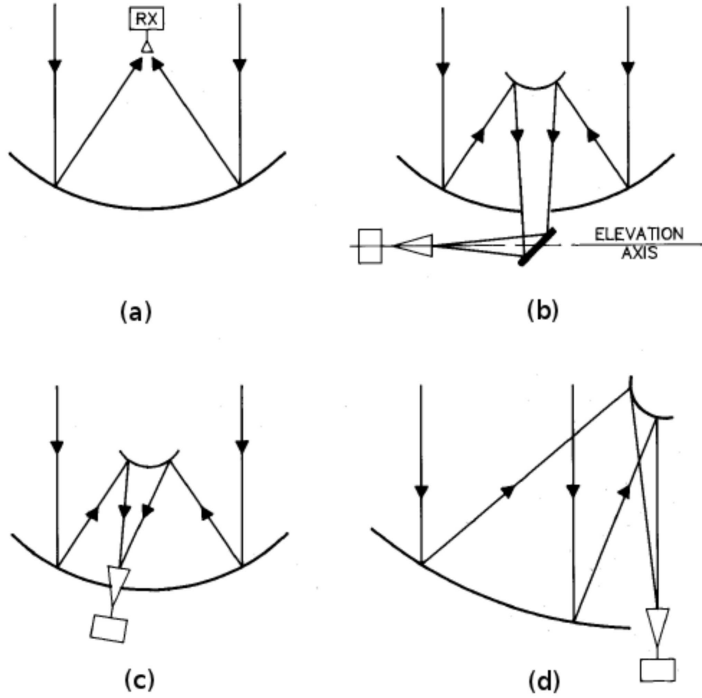


Figure 2.2: Common optical systems used for radio antennas. (a) Prime focus, (b) Naysmith, (c) Off-axis Cassegrain, (d) Offset Cassegrain [Figure adapted from Taylor *et al.* (1999)].

2.1.3 Antenna Performance Parameters

Aperture Efficiency. The geometric collecting area of a parabolic antenna, A_{geo} ($= \pi D^2/4$), is related to the effective area (i.e., the collecting area when pointing directly at a source) via the dimensionless quantity, η ($\eta < 1$), known as the aperture efficiency where

$$\eta = \frac{A_0}{A_{\text{geo}}}. \quad (2.10)$$

The aperture efficiency directly impacts on the sensitivity of the interferometric array and can be defined as the product of a number of different efficiency loss factors,

$$\eta = \eta_{\text{sf}} \eta_{\text{bl}} \eta_{\text{s}} \eta_{\text{t}} \eta_{\text{misc}}. \quad (2.11)$$

The surface efficiency, η_{sf} , accounts for the aperture efficiency loss as a result of reflector profile inaccuracies. Such inaccuracies result in the electric field from

2.1 Radio Antenna Fundamentals

various parts of the aperture not adding together in phase at the feed, leading to a decrease in power. The aperture blockage efficiency, η_{bl} , accounts for the fact that the sub-reflector (or feed) and its support structure result in a reduction in the incident radiation on the antenna. The feed spillover efficiency, η_{bl} , is best understood if the antenna is considered in transmission rather than in reception mode, and is defined as the fraction of power radiated by the feed that is intercepted by the reflector for a prime focus system, or by the sub-reflector for a Cassegrain system. The illumination taper efficiency, η_t , accounts for the fact that the feed pattern does not illuminate the primary reflector uniformly, but illuminates the outer part of the reflector at a lower level than the inner part. Finally, the miscellaneous efficiency losses such as reflector diffraction and feed position phase errors are accounted for in η_{misc} . As an example, the total aperture efficiency of the VLA antennas can vary between 0.65 and 0.2, at 6 and 0.7 cm, respectively.

Pointing Accuracy. The main lobe of an antenna's power pattern will usually not point exactly in the desired direction, due to gravity deformations, wind pressure deformations, and mechanical inaccuracy. The angular offset, $\Delta\theta$, between the actual and desired pointing direction is called the pointing error. Usually, the desirable pointing error of an antenna at the highest operational frequency is $\Delta\theta < \theta_{\text{HPBW}}/20$ (Taylor *et al.*, 1999). With this specification reached, an antenna pointing at a compact source will suffer negligible intensity variations as $\mathcal{A}(\theta_{\text{HPBW}}/20) > 0.99$. However, this pointing error of only $\theta_{\text{HPBW}}/20$ will still have a substantial effect on the accuracy of the outer image. For example, a source located at the half power point will suffer a substantial fractional intensity variation of $2\mathcal{A}(\theta_{\text{HPBW}}/2 + \theta_{\text{HPBW}}/20) \simeq 0.86$. The blind pointing of a VLA antenna is only about $10''$ and can be much worst in daytime, occasionally exceeding $1'$. This means that at Q band (45 GHz; 0.7 cm), which is the highest observing frequency on the VLA, the pointing error is only at best $\theta_{\text{HPBW}}/6$, and at worst $> \theta_{\text{HPBW}}$, meaning that the target may lie outside of the primary beam. To overcome this problem of large antenna pointing errors at high frequencies with the VLA, a technique known as referenced pointing is implemented. This technique will be discussed further in Chapter 3.

2.2 Radio Antenna Receiving System

A radiometer (a radio receiver) is a device used to measure the timed-averaged power of the noise coming from a radio telescope within a well-defined radio frequency (RF) range, $\nu_{\text{RF}} - \Delta\nu_{\text{RF}}/2 \rightarrow \nu_{\text{RF}} + \Delta\nu_{\text{RF}}/2$, where $\Delta\nu_{\text{RF}}$ is the bandwidth of the receiver and $\Delta\nu_{\text{RF}} < \nu_{\text{RF}}$. The simplest radiometer carries out the following tasks:

1. Filters the broadband noise coming from the antenna via a bandpass filter.
2. Multiplies the filtered voltage by itself (i.e., its output voltage is proportional to its input power).
3. Smooths out the rapidly fluctuating output of the detected voltage via a signal averager or integrator.
4. Measures the smoothed voltage.

In practice, radiometers are never as simple as those described above and nearly all practical radiometers are *superheterodyne* receivers which incorporate a number of additional steps to produce an output voltage. The RF front end is the term used to describe all the circuitry between the feed horn and the lower intermediate frequency (IF) stage. The first task of the front end is to amplify the received signal. The radio signals we want to measure are generally very weak, and therefore need to be initially amplified by many orders of magnitude, so they are above the noise level in succeeding stages. However, the front end electronic components produce random electrical noise which will also get amplified by this large factor. Therefore the role of the pre-amplifier is to amplify the incoming signal from the antenna, while adding as little noise as possible. For this reason, the pre-amplifier is called a low noise amplifier (LNA), and are often cooled to very low temperatures to minimize the amount of noise contributed by the components.

The amplified RF signal is then sent through a mixer, which multiplies the RF signal by a sine wave of frequency ν_{LO} , which is generated by a local oscillator (LO), as shown in Figure 2.3. The effect of this is that RF signal is changed

2.2 Radio Antenna Receiving System

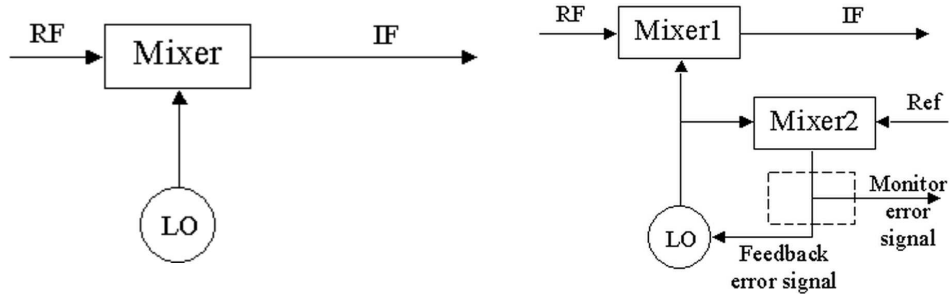


Figure 2.3: *Left:* Block diagram of a simple superheterodyne receiver. The amplified RF signal is mixed with a signal from a local oscillator to convert the signal to the more manageable intermediate frequency. *Right:* For interferometry, a phase lock loop is used to ensure all antennas are locked to the same frequency. *Image Credit:* Prof. Dale E. Gary (New Jersey Institute of Technology).

to a lower frequency which can be more easily handled by the IF amplifier and improves frequency selectivity. Mathematically, the mixer does the following

$$2\sin(2\pi\nu_{\text{LO}}t) \times \sin(2\pi\nu_{\text{RF}}t) = \cos[2\pi(\nu_{\text{LO}} - \nu_{\text{RF}})t] - \cos[2\pi(\nu_{\text{LO}} + \nu_{\text{RF}})t] \quad (2.12)$$

and produces two additional outputs, one at the input signal frequency minus the local oscillator frequency, and one at the sum of these frequencies. The lower of the two outputs called the intermediate frequency (IF) is taken by passing the mixer output through a filter in the IF amplifier. In interferometry, where the signals from two antennas are correlated, it is crucial that the receivers from both antennas are operating at the same frequency, to control the phase difference between them. This is achieved by using a phase lock system, whose block diagram is laid out in Figure 2.3. In this system another mixer compares the LO to a reference frequency, which is the same for all antennas. Any existing phase error results in an error signal that is sent back to the oscillator, so that its frequency can be adjusted to maintain exact frequency tuning. After this, the IF can finally be sent to the radiometer and recorded.

2.3 Fundamentals of Radio Interferometry

The angular resolution, $\Delta\theta$, of a radio antenna is the minimum angular separation which two point sources can have in order to be recognized as separate objects. The *Rayleigh criterion* is the operational defined angular resolution of a filled circular aperture of diameter, D , at the observational wavelength λ and is given as

$$\Delta\theta = 1.22 \frac{\lambda}{D} \text{ rad.} \quad (2.13)$$

The Rayleigh criterion states that two objects are resolved when the first null of the diffraction pattern of one object coincides with the maximum of the diffraction pattern of the other. An immediate consequence of Equation 2.13 is that at large wavelengths, the angular resolution becomes low unless the diameter of the aperture can be increased substantially. In order to achieve modest angular resolution at radio wavelengths with a single radio antenna, the diameter becomes impractically large. Radio interferometry is a technique used in radio astronomy to overcome this problem of low angular resolution at long wavelengths. For example, the world's largest fully steerable radio telescope is the 100 m Robert C. Byrd Green Bank Telescope (GBT), which at 6 cm can achieve an angular resolution of $2.5'$. The VLA on the other hand, in its most extended configuration, can achieve a resolution that is ~ 400 times better than that of the GBT, at the same wavelength.

2.3.1 Young's Slits

The basic principles of interferometry can be understood through Young's double-slit experiment. If coherent radiation emitted from a distant point source propagates through two slits, an illumination pattern composed of bright and dark fringes is observed. The phenomenon is a result of the constructive and destructive interference between the secondary waves produced by the slits. The fringe separation is λ/B , where B is the projected separation of the slits and is called the baseline. The fringe contrast which is historically known as the fringe visibility, V , can be written as

$$|V| = \frac{I_{\max} - I_{\min}}{I_{\max} + I_{\min}} \quad (2.14)$$

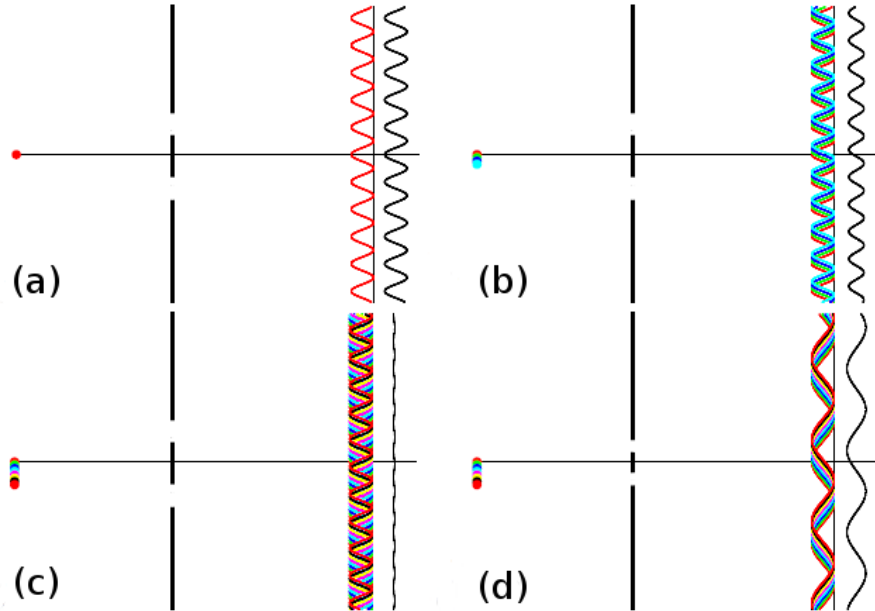


Figure 2.4: The resulting fringe pattern produced by Young's slits under various conditions. The source is shown on the left of the slits in each panel, while the separate fringe patterns (colors) along with the added fringe pattern (black) is shown on the right of the slits. (a) Point source at infinity, (Visibility = 1). Fringes are separated by an angular distance of λ/B . (b) An increase in source size results in a drop in visibility. (c) When the source size is equal to λ/B , the visibility is zero. (d) If the source size remains the same as in (c) and the slit spacing is reduced, then the fringes re-appear. Figure adapted from Jackson (2008).

where I_{\max} and I_{\min} are the maximum and minimum intensity of the fringes, respectively. In other words, the fringe visibility is the fringe amplitude normalized by the sum of the maximum and minimum intensity.

In the simple case shown in Figure 2.4a, the angular size of the source is $\ll \lambda/B$ and the fringe visibility is 1. In interferometry, this equates to the situation in which the source size is smaller than the synthesized beam and only an upper limit of the source size can be obtained (i.e., the source is unresolved). In Figure 2.4b, the angular size of the source is now larger and can be thought of as a sequence of point sources each emitting radiation which is uncorrelated with emission from the others. An angular shift of ϕ , called phase, in the sources position results in a shift in the corresponding fringe pattern by the same angle the other way. The total interference intensity pattern is then just the sum of

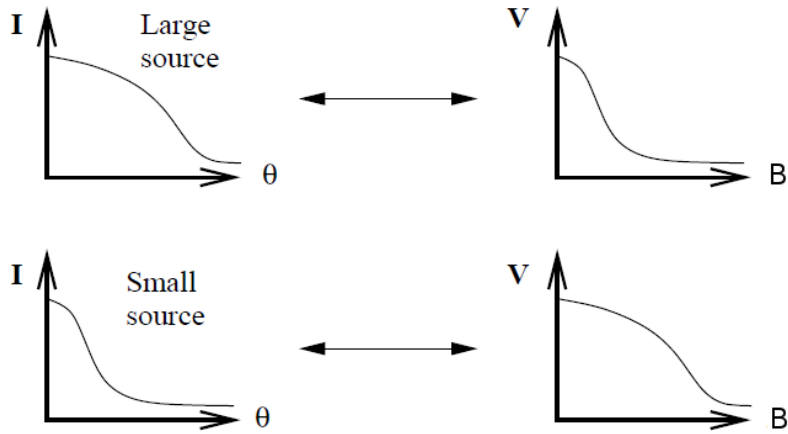


Figure 2.5: *Left column:* Intensity distribution as a function of sky angle for an extended source (top) and for a more compact source (bottom). *Right column:* The corresponding fringe visibility as a function of slit separation or baseline. Figure adapted from Jackson (2008).

these individual patterns and the visibility is reduced. When the extension of the source equals λ/B , the fringes disappear and give a constant illumination pattern. In this case the fringe visibility is zero and the source is completely resolved as shown in Figure 2.4c. Finally, if the source size is the same as that in Figure 2.4c but the slit separation is reduced, then the fringe separation λ/B will again increase as shown in Figure 2.4d. This is because the source now produces much less displacement of the fringe patterns as a fraction of the fringe separation. In interferometry, this result means that extended sources can only be probed with short baselines.

Visibility and phase are often expressed together as the complex visibility $V = |V|e^{i\phi}$, which completely defines a pattern of interference fringes. Young's double-slit experiment demonstrates a fundamental property of interferometry, namely that the contrast of fringes is a function of the geometry of the source. The results of the experiment are summarized in Figure 2.5. The top row shows that a large source (i.e., one whose intensity distribution extends out to a large angle on the sky) has a fringe visibility pattern which falls off quickly as projected baseline length increases. The bottom row shows that for compact sources, the fringe visibility remains high out to large baselines. In the following sections, we

2.3 Fundamentals of Radio Interferometry

will show that the relationship between the sky brightness distribution $I(\theta)$ and the visibility $V(B)$ is a Fourier transform.

2.3.2 The Two-element Interferometer

Interferometers with N antennas can be treated as $N(N - 1)/2$ independent interferometer pairs, so it is worthwhile studying the simplest case of the two-element interferometer. A simplified block diagram of the components of such an interferometer is shown in Figure 2.6. The figure shows two identical antennas separated by a baseline vector, \mathbf{b} , pointing towards a distant radio source in a direction indicated by the unit vector, \mathbf{s} . The plane waves from the distant radio source reach antenna 1 at a time τ_g later than they reach antenna 2. τ_g is called the geometric delay and is given by

$$\tau_g = \frac{\mathbf{b} \cdot \mathbf{s}}{c} = \frac{b \cos \theta}{c} \quad (2.15)$$

where c is the speed of light. If we assume that the interferometer only responds to a very narrow band centered on frequency $\nu = \omega/2\pi$, then the output voltages of antennas 1 and 2 at time t can be written as

$$V_1(t) = V \cos[\omega(t - \tau_g)] \quad \text{and} \quad V_2(t) = V \cos(\omega t) \quad (2.16)$$

where ω is the angular frequency and V is the voltage amplitude. The signals are then passed through a correlator which first multiplies these voltages to give

$$V_1(t)V_2(t) = \frac{V^2}{2} [\cos(2\omega t - \omega\tau_g) + \cos(\omega\tau_g)] \quad (2.17)$$

and then averages them over a time interval Δt which is long enough such that $\Delta t >> (2\omega)^{-1}$ to give the final power output, R :

$$R = \langle V_1(t)V_2(t) \rangle = \frac{V^2}{2} [\cos(\omega\tau_g)]. \quad (2.18)$$

This correlator output is free from uncorrelated noise from the receivers and the atmosphere over the two telescopes, and so variations in receiver gain or atmospheric emission are much less of a problem than for a total-power observation with a single dish.

2.3 Fundamentals of Radio Interferometry

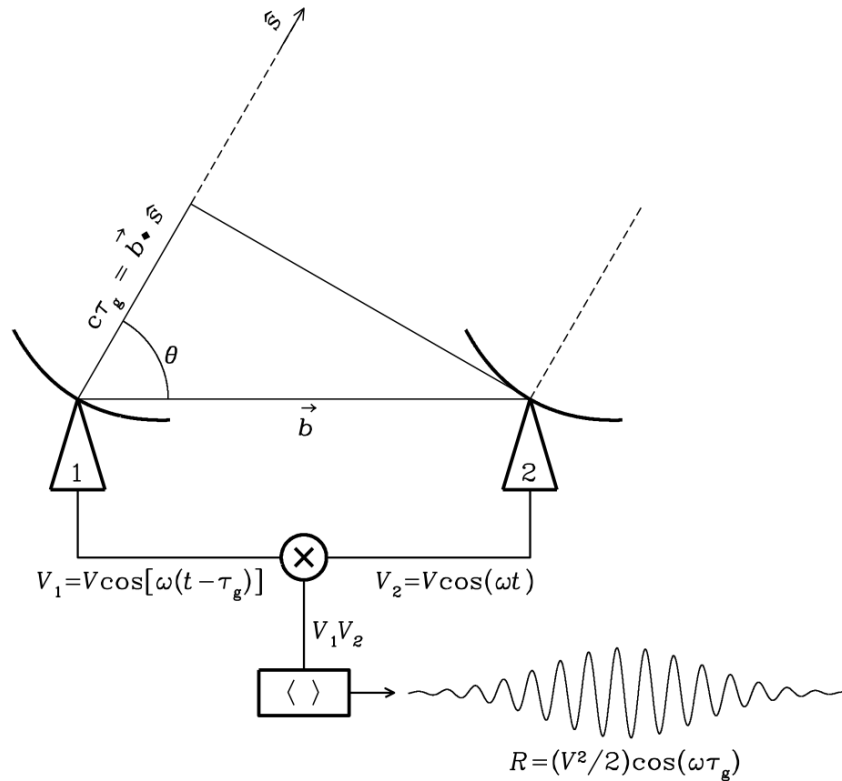


Figure 2.6: Simplified schematic diagram of a two-element interferometer. The correlator multiplies and averages the voltage outputs V_1 and V_2 of the two dishes and yields an output amplitude $V^2/2$ which is proportional to the point-source flux density, F_ν . *Image Credit:* National Radio Astronomy Observatory.

As the Earth rotates, τ_g varies slowly with time and the resultant oscillations in the correlator output voltage represent the motion of the source. These sinusoidal oscillations are called fringes, and the fringe phase is

$$\phi = \omega\tau_g = \frac{\omega b \cos\theta}{c} \quad (2.19)$$

which changes with source direction as follows

$$\frac{d\phi}{d\theta} = \frac{\omega b \sin\theta}{c} = 2\pi \left(\frac{b \sin\theta}{\lambda} \right). \quad (2.20)$$

The fringe phase completes a full period (i.e., $\Delta\phi = 2\pi$) when an angular change

2.3 Fundamentals of Radio Interferometry

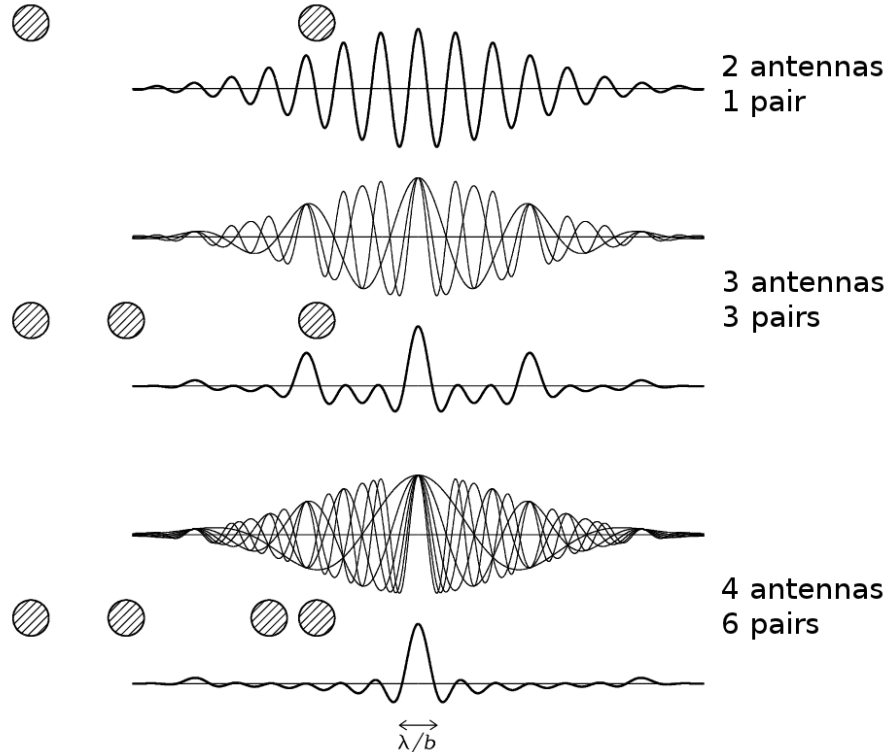


Figure 2.7: The instantaneous point source responses of an interferometer with two, three and four elements is indicated by the thick curves. The individual responses of the three pairs of two-element interferometers of the three-element interferometer and the six pairs of two-element interferometers of the four-element interferometer are plotted as thin curves. The main beam of the four-element interferometer is nearly Gaussian and has a width of $\sim \lambda/B$. This is known as the instantaneous synthesized beam of the interferometer. *Image Credit:* National Radio Astronomy Observatory.

$\Delta\theta = (\lambda/b\sin\theta)$ occurs. This tells us that the fringe phase is an extremely sensitive measure of source position if the projected baseline $b\sin\theta$ is many wavelengths long and is the reason why interferometers can determine the positions of compact radio sources with exquisite accuracy.

If the antennas in an interferometric array are isotropic, then the point-source response of the interferometer would be a sinusoid spanning the entire sky, and the interferometer would be only sensitive to one Fourier component of the sky brightness distribution, having angular period $\lambda/b\sin\theta$. The response of a two-

2.3 Fundamentals of Radio Interferometry

element interferometer R with non-isotropic antennas is this sinusoid, multiplied by the product of the voltage patterns (i.e., defined as $f(u, v)$ in Section 2.1.1) of the individual antennas. If the antennas are identical then this product is the power pattern of the individual antennas called the primary beam. The primary beam is usually a Gaussian that is much wider than the fringe period, as $D \ll b\sin\theta$ (where D is the antenna diameter). The result is that an interferometer with directive antennas responds to a finite range of angular frequencies centered on $b\sin\theta/\lambda$. The instantaneous point source response of an interferometer is known as the synthesized beam and is the point source response obtained by averaging the outputs of all antenna pairs. The synthesized beam of an interferometer is an important quantity as it defines the maximum angular resolution of the instrument. The synthesized beams produced by an interferometer with a various number of antennas arranged in 1-D is shown in Figure 2.7. The figure shows that the synthesized beam can be improved by acquiring more Fourier components (i.e., baselines) and rapidly approaches a Gaussian as N increases. However, sidelobes are still significant and a broad negative “bowl” exists between the main beam and the first sidelobes, due to the absence of short spacings.

Interferometers have a maximum angular scale that be observed effectively. This scale is often referred to as the *resolving-out scale* or *maximum scale*, and is dependent upon the observing wavelength, λ , and the minimum projected baseline, B_{\min} . Emission will be “resolved out” if the observed source contains smoothly varying structures that are larger than this scale. This is an intrinsic property to interferometry and is known as the “missing flux” problem. For any array configuration, emission with angular scales of $\sim \lambda/B_{\min}$ or greater is not reproduced in the maps (Taylor *et al.*, 1999) and this scale is often used as a guide for the resolving-out scale of a specific array configuration.

2.3.3 Complex Visibility

The interferometer output can be expressed in terms of the radio brightness over the sky, which is sometimes also called specific intensity and has units $\text{W m}^{-2} \text{Hz}^{-1} \text{sr}^{-1}$. If the radio brightness of a spatially extended source in the direction of unit vector \mathbf{s} is $I(\mathbf{s})$, then the power output of the two-element interferometer

2.3 Fundamentals of Radio Interferometry

with “cosine” correlator output near frequency $\nu = \omega/2\pi$ is obtained by treating the extended source as the sum of independent point sources:

$$R_c = \int_{\Omega} \mathcal{A}(\mathbf{s}) I_{\nu}(\mathbf{s}) \cos\left(\frac{2\pi\mathbf{b}\cdot\mathbf{s}}{\lambda}\right) d\Omega \quad (2.21)$$

where \mathcal{A} is the normalized antenna reception pattern defined in Section 2.1.1 and we call $\mathcal{A}(\mathbf{s}) I_{\nu}(\mathbf{s})$ the modified brightness distribution. However, the cosine function in the “cosine” correlator output is only sensitive to the even part of the sky brightness distribution, which can be written as the sum of even and odd parts:

$$I(\mathbf{s}) = I_e(\mathbf{s}) + I_o(\mathbf{s}). \quad (2.22)$$

A “sine” correlator whose output is odd, is needed to detect the odd part of $I(\mathbf{s})$ and this is implemented by inserting a 90° phase delay into the signal of one of the antennas to give

$$R_s = \int_{\Omega} \mathcal{A}(\mathbf{s}) I_{\nu}(\mathbf{s}) \sin\left(\frac{2\pi\mathbf{b}\cdot\mathbf{s}}{\lambda}\right) d\Omega \quad (2.23)$$

It is convenient to write the cosines and sines as complex exponentials using the identity

$$e^{i\phi} = \cos(\phi) + i\sin(\phi) \quad (2.24)$$

and so the combination of “cosine” and “sine” correlators is called a “complex” correlator. The term *visibility* was first introduced by Michelson (1890) to describe the relative amplitudes of the optical fringes that he observed. The visibility is a complex quantity in radio astronomy and has dimensions of spectral power flux density ($\text{W m}^{-2} \text{ Hz}^{-1}$). The complex visibility is the response of a two-element interferometer with a complex correlator to an extended source with brightness distribution $I(\mathbf{s})$ and is defined as

$$V \equiv R_c - iR_s = Ae^{-i\phi} \quad (2.25)$$

2.3 Fundamentals of Radio Interferometry

where

$$A = \sqrt{R_c^2 + R_s^2} \quad (2.26)$$

$$\phi = \tan^{-1} \left(\frac{R_s}{R_c} \right). \quad (2.27)$$

This gives the useful relationship between the source brightness, and the response of an interferometer

$$V_\nu(\mathbf{b}) = \int_{\Omega} \mathcal{A}(\mathbf{s}) I_\nu(\mathbf{s}) e^{-2\pi i \nu \mathbf{b} \cdot \mathbf{s}/c} d\Omega \quad (2.28)$$

which under some circumstances, is a 2-D Fourier transform, and allows $I_\nu(\mathbf{s})$ to be recovered from $V_\nu(\mathbf{b})$.

2.3.4 Coordinate Systems for Imaging

The projected baseline has coordinates (u, v, w) in three dimensions shown in Figure 2.8, where w points in the directions of interest, i.e., towards a direction s_0 that becomes the center of the synthesized image. u , v and w are measured in wavelengths (i.e., the components of \mathbf{b}/λ) and have directions towards the East, the North and the phase tracking center, respectively. An arbitrary unit vector \mathbf{s} has components (l, m, n) called direction cosines, where $n = \cos\theta = (1 - l^2 - m^2)^{1/2}$. Using these coordinates, the parameters in Equation 2.28 become

$$\begin{aligned} \frac{\nu \mathbf{b} \cdot \mathbf{s}}{c} &= ul + vm + wn \\ d\Omega &= \frac{dl dm}{n} = \frac{dl dm}{\sqrt{1 - l^2 - m^2}}. \end{aligned} \quad (2.29)$$

Therefore Equation 2.28 can be defined in terms of the coordinate system laid out in Figure 2.8 as

$$V_\nu(u, v, w) = \int_{-\infty}^{\infty} \int_{-\infty}^{\infty} \mathcal{A}_\nu(l, m) I_\nu(l, m) e^{-2\pi i [ul + vm + w(\sqrt{1 - l^2 - m^2})]} \frac{dl dm}{\sqrt{1 - l^2 - m^2}} \quad (2.30)$$

which is not a three-dimensional Fourier transform. This equation becomes a two-dimensional Fourier transform if $w = 0$ which is a good approximation for

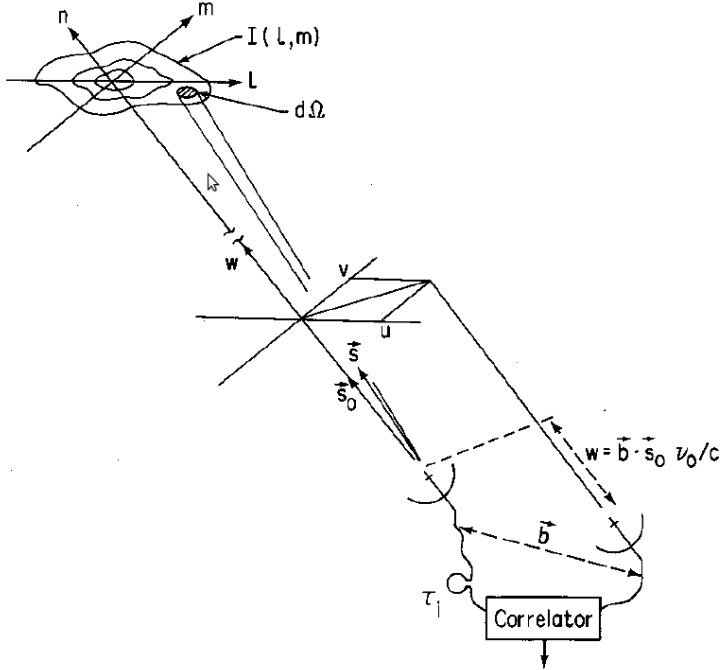


Figure 2.8: The (u, v, w) interferometric coordinate system. l , m , and n are the projections of the unit vector \mathbf{s} onto the u , v , and w axes, respectively. *Image Credit:* Taylor *et al.* (1999).

small field imaging, i.e., when $|l|$ and $|m|$ are small. Thus, for a source in the far field observed with a small FOV, and ignoring the response of the primary beam, the complex visibility is the 2-dimensional Fourier Transform of the sky brightness distribution

$$V_\nu(u, v) = \int_{-\infty}^{\infty} \int_{-\infty}^{\infty} I_\nu(l, m) e^{-2\pi i(ul+vm)} dl dm. \quad (2.31)$$

This Fourier transform relationship is the result of the van Cittert-Zernike theorem (van Cittert, 1934), upon which synthesis imaging is based. Since $I_\nu(l, m)$ is real, $V(u, v)$ is Hermitian [i.e., $V(-u, -v) = V^*(u, v)$] and so one measurement of the sky brightness gives two measurements of the complex visibility. Also, $V(u = 0, v = 0)$ is the integral of $I_\nu(l, m) dldm$, which is the total flux. An interferometer cannot measure this value because it cannot take measurements at $(u = 0, v = 0)$.

2.4 Synthesis Imaging

A synthesis imaging telescope uses the Earth’s rotation to vary the projected baseline coverage, thereby increasing the sampling of the $u - v$ plane. In this section we describe how Earth-rotation aperture synthesis is used to convert the complex visibilities outputted from the correlator to a final radio image of the observed sky.

2.4.1 Visibility Sampling

An example of how a radio interferometer samples the $u - v$ plane is shown in Figure 2.9. The left panel of this figure shows the overhead view of the VLA in its most extended configuration, while the other two panels show the corresponding $u - v$ coverage for different periods of time. We define u and v as the east-west and north-south components of the projected baseline in wavelengths, respectively. As the Earth rotates, the projected baseline of every two-element pair in the array changes, thus sampling a different part of the $u - v$ plane. The middle panel shows that the total $u - v$ coverage of the VLA for a very short duration track (i.e., a *snapshot*) results in a “snowflake” like pattern, with more dense coverage in the direction of the arms of the array due to the larger number of baselines. Most radio interferometers have their own unique array configuration layout and thus produce a different snapshot $u - v$ coverage to that shown in Figure 2.9. Over many hours, the $u - v$ points trace out portions of ellipses and eventually after a full Earth rotation the points can trace out full ellipses as shown in the right panel of Figure 2.9.

2.4.2 Imaging (Making a Dirty Map)

For every sky brightness distribution $I(l, m)$ there exists a continuous complex visibility function, $V(u, v)$, which is its Fourier Transform. An array of antennas will only ever measure a certain set of values of this visibility function where the measured set is called the sampling function $S(u, v)$. This function is zero where no data have been taken. The actual data provided by the array is known

2.4 Synthesis Imaging

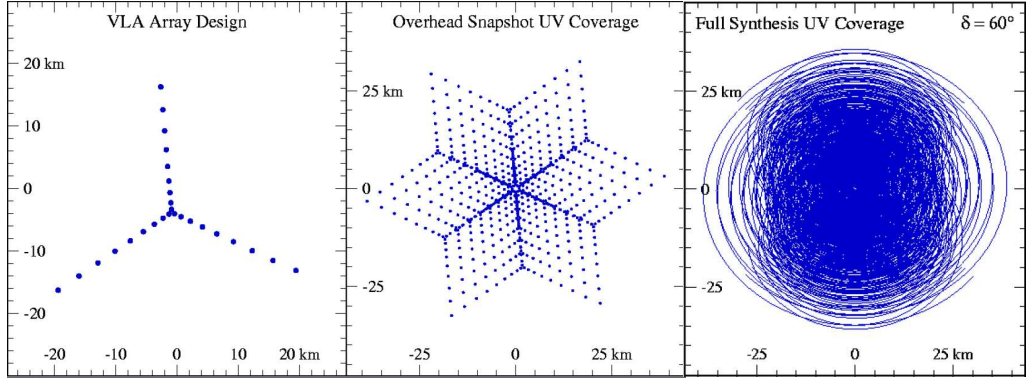


Figure 2.9: *Left:* The VLA in A-configuration is an example of an “Y” shaped array design. *Middle:* The corresponding overhead snapshot $u - v$ coverage results in “snowflake” pattern. *Right:* The corresponding $u - v$ coverage after a 12 hour track of a source at a declination of 60° . Note the more intense $u - v$ coverage in the direction of the three straight arms of the VLA for a snapshot track compared to the more uniform coverage over a longer duration track. *Image Credit:* National Radio Astronomy Observatory.

as the sampled visibility function, $S(u, v)V(u, v)$. If we take the inverse Fourier transform of this function we get what is known as the *dirty image*:

$$I_\nu^D(l, m) = \int_{-\infty}^{\infty} \int_{-\infty}^{\infty} S(u, v)V_\nu(u, v)e^{2\pi i(ul+vm)} du dv \quad (2.32)$$

where we have used $I_\nu(l, m)$ to denote the modified sky brightness $\mathcal{A}(l, m)I_\nu(l, m)$, as the correction for primary beam can be made at the final stage of data processing. Using the convolution theorem, the relationship between the dirty image and the desired intensity distribution $I_\nu(l, m)$ is

$$I_\nu^D(l, m) = I_\nu(l, m) * B(l, m) \quad (2.33)$$

where the asterisk implies convolution and

$$B(l, m) = \int_{-\infty}^{\infty} \int_{-\infty}^{\infty} S(u, v)e^{2\pi i(ul+vm)} du dv \quad (2.34)$$

is the *point spread function* (PSF), or *synthesized beam*, or *dirty beam* (i.e., the inverse Fourier Transform of the sampling function S). Equation 2.33 says that the dirty image, I_ν^D , is the true intensity distribution I_ν , convolved with the

2.4 Synthesis Imaging

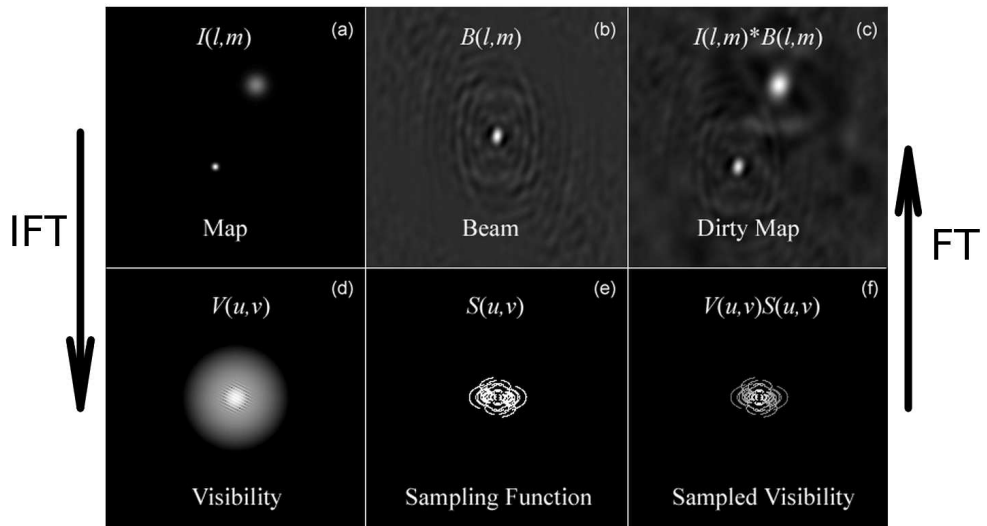


Figure 2.10: The Fourier transform pairs in synthesis imaging. (a) and (d): The true sky brightness and the visibility. (b) and (e): The dirty beam and the sampling function. (c) and (f): The dirty image and the sampled visibility. *Image Credit:* Prof. Dale E. Gary (New Jersey Institute of Technology).

synthesized beam, B .

In Figure 2.10 we graphically summarize what has been said above. The panels in the upper row show the sky plane representations of the true image, the point spread function, and the dirty image, while the panels in the lower row show the corresponding $u - v$ plane representations of the true visibility, the sampling function, and the sampled visibility. In other words, Equation 2.31 is summarized graphically by the relationship between panels (a) and (d), Equation 2.34 by (b) and (e), and Equations 2.32 and 2.33 by (c) and (f).

Before the dirty image is computed, a weighting system is often applied to the visibilities to control the PSF. The two most common types of weighting system used are:

$$D_k = 1, \quad \text{natural weighting} \quad (2.35)$$

$$D_k = \frac{1}{N_s(k)}, \quad \text{uniform weighting} \quad (2.36)$$

where D_k is the weight to be applied to cell k , and $N_s(k)$ is the number of data

samples falling into cell k of characteristic width s . Natural weighting treats all points alike, and gives the best S/N for detecting weak sources. However, it produces a beam with a broad low-level plateau which is undesirable when imaging sources with both large and small scale structure. Uniform weighting produces fewer artifacts in the final map, while keeping the full resolution of the array but gives lower S/N than natural weighting.

The “direct Fourier transform” method can then be used to solve for the dirty image in Equation 2.32. However, if this method is evaluated at every point on a $N \times N$ grid, then the number of multiplications required goes as N^4 . The fast Fourier transform (FFT) algorithm can also be used to solve Equation 2.32 but requires interpolating the data onto a regular grid (i.e., a process known as *gridding*). This method is widely used for large data volumes as it requires only a few times $N^2 \log_2 N$ operations - not $\mathcal{O}(N^4)$, and the total time taken for gridding and FFT is usually a lot less than it would take using the direct Fourier transform method.

2.4.3 Deconvolution (Making a CLEAN map)

In reality, Equation 2.33 contains an additional noise term, n , so that

$$I^D = I * B + n. \quad (2.37)$$

The goal of image reconstruction is to recover I from this equation. Mathematically, one could solve Equation 2.37 by first taking the Fourier transform of both sides, then use the convolution theorem to allow division by the Fourier transform of B , and finally recover I by taking the inverse Fourier transform of both sides to get

$$I = \text{IFT} \left(\frac{\text{FT}(I^D) - \text{FT}(n)}{\text{FT}(B)} \right) \quad (2.38)$$

where FT and IFT represent the Fourier transform and the inverse Fourier transform, respectively. However, there are two main problems associated with solving Equation 2.37 by this method. First, the presence of the noise term means that the division by $\text{FT}(B)$ amplifies the noise and introduces high frequency artifacts

2.4 Synthesis Imaging

into I (Taylor *et al.*, 1999). Also, Equation 2.38 is not unique, because the unmeasured points in the $u - v$ plane could have *any* value without violating the data constraints. The “principle solution” is the one in which all missing $u - v$ measurements are set to zero and gives the dirty image discussed in the previous section. The dirty image is usually not a satisfactory representation of the sky as one would expect a more continuous distribution of visibilities than that provided by the array. The goal of the deconvolution process is to find a method that determines more reasonable values for the unmeasured $u - v$ data. A priori information is the key to choosing *reasonable* values. For example, we know that the Stokes parameter I must be positive and that radio sources generally do not have sidelobe patterns.

The CLEAN algorithm (Cornwell *et al.*, 1999; Högbom, 1974; Schwarz, 1978) is the most widely used technique in radio interferometry to deconvolve the true sky intensity from the dirty beam. It assumes that the radio source can be represented by a number of point sources in an otherwise empty field and a simple iterative process is used to find the strengths and positions of these point sources. The final CLEAN image (i.e., the deconvolved image) is the sum of these point sources convolved with a CLEAN beam, which is usually an elliptical Gaussian of the same size and shape as the inner part of the dirty beam. The CLEAN algorithm obeys the following steps:

1. Find the strength and position of the brightest point in the dirty image. It may also be desirable to search for peaks in specified areas of the image, called CLEAN windows or regions.
2. At this position in the dirty image, subtract the dirty beam multiplied by the peak strength and a damping factor g ($g \leq 1$, usually called the loop gain).
3. Record the position and the subtracted flux in a model.
4. Iterate between (1), (2), and (3) until the peak is below some user specified level. The remainder of the dirty image is now termed the residuals.

2.4 Synthesis Imaging

5. Convolve the accumulated point source model with an idealized CLEAN beam (usually an elliptical gaussian of the same size and shape as the central lobe of the dirty beam).
6. Add the residuals to the image in (5) to create the final CLEAN image.

A problem with CLEAN is that the final CLEANed image is somewhat dependent upon the various control parameters such as CLEAN boxes, the loop gain and the number of CLEAN subtractions. For example, using too high a gain tends to make extended, weak emission undetectable and noisy. This problem is unavoidable, and input values must be chosen on a case by case basis, depending on the source and data quality.

Another deconvolution algorithm used in radio synthesis imaging, albeit less often, is the Maximum Entropy Method (MEM) which operates by minimizing a smoothness function (“entropy”) in an image. To conclude this section, we briefly discuss the practical differences between CLEAN and MEM:

1. CLEAN is nearly always faster than MEM, unless the image contains more than 1 million pixels.
2. MEM images are nearly always smoother than CLEAN images. This is because for CLEAN, what happens at one pixel is not coupled to what happens to its neighbours, while MEM couples pixels together by minimizing the spread in pixel values.
3. CLEAN sometimes makes extended emission look blotchy and may introduce artificial stripes into the image while MEM copes very poorly with point sources in extended emission. (Multi-scale CLEAN which is discussed in Chapter 3 is now becoming a popular choice in the radio community as an alternative deconvolution algorithm for images containing extended emission.)
4. For MEM, it is necessary to know the noise level quite well and it also helps to know the total flux density of the image. Knowledge of these are not required for CLEAN.

3

Targets, Instrumentation, and Observations

Two unique data sets were analyzed as part of this thesis. The first data set was a millimeter interferometric multi-configuration study of Betelgeuse’s circumstellar environment (CSE) at 1.3 mm. In the first half of this chapter we give a detailed introduction to Betelgeuse and discuss our current understanding of the star and its stellar atmosphere. We give a description of the millimeter interferometer CARMA, which we used to study its complex CSE on a number of spatial scales and also describe our observations which spanned ~ 2.5 yr. The second data set consisted of a multi-wavelength centimeter study of two non-dusty red giants, Arcturus and Aldebaran. In the second half of this chapter we give a detailed introduction to both of these stars, including a description of their stellar properties, and their existing atmospheric models which we test against our data in Chapter 6. We give a short description of the VLA, which was the centimeter interferometer we used to study these stars, and describe our VLA observations. Finally, we briefly describe how the Pie Town antenna can be connected to the VLA, and outline our VLA-Pie Town observations of Betelgeuse.

3.1 Betelgeuse

Betelgeuse (α Ori: M2 Iab) is one of a pair¹ of nearest red supergiants ($d = 197 \pm 45$ pc, Harper *et al.* 2008). It has a limb darkened angular diameter of 44.28 ± 0.15 mas² (Haubois *et al.*, 2009) which means that it subtends the largest angular diameter of any star in the northern sky apart from the Sun. It is by far the best studied red supergiant and has been observed with various techniques from the radio to the UV. According to Harper *et al.* (2001), Betelgeuse probably was a runaway star from the star-formation region Ori OB1 (see, e.g., Hoogerwerf *et al.*, 2000), and was a spectral type O9 V star while on the main sequence, where it had a mass of $\sim 20 M_\odot$. The evolutionary models of Meynet & Maeder (2003) suggest that its current mass is $18 M_\odot$ which corresponds to a surface gravity of 0.5 cm s^{-2} (i.e., $2 \times 10^{-5} g_\odot$). Its mass loss is characterized by low velocity outflows ($10 - 17 \text{ km s}^{-1}$) and a mass loss rate of $\sim 3 \times 10^{-6} M_\odot \text{ yr}^{-1}$ (Harper *et al.*, 2001). Like most late-type evolved stars, Betelgeuse's terminal wind velocity v_∞ is smaller than the surface escape speed v_{esc} (values given in Table 3.1). This means that most of the energy and momentum are deposited into its flow within the first few stellar radii.

Betelgeuse has a large rotation period of ~ 17 yr (Uitenbroek *et al.*, 1998), which implies that it is probably experiencing very limited action of a solar-like dynamo. This rotation period is in stark contrast to the equatorial solar rotation rate which is just 24.5 days. Its large radius ($\sim 950 R_\odot$) means that any possible remnant of a strong main sequence magnetic field is likely negligible due to a large dilution factor. In comparison to Sun like stars, its large radius also means that it has a large photospheric scale height ($H_\star \sim 0.01 R_\star$). The expected result of this is the presence of no more than a few giant and stable convection cells in the photosphere Schwarzschild (1975). Such features should enhance the detectability of the magnetic fields generated through a turbulent dynamo (Vögler & Schüssler, 2007). Bedecarrax *et al.* (2013) have recently monitored Betelgeuse over a three year period using high resolution spectropolarimetry, and find a longitudinal magnetic field strength which varies in values ranging from

¹The other being Antares (α Sco: M1.5 Iab + B2.5 V; $d = 170 \pm 29$ pc)

²mas = milliarcsecond

3.1 Betelgeuse

Table 3.1: Physical Properties of α Ori.

Property	Value	Reference
HD Number	39801	...
Spectral Type	M2 Iab	Perryman <i>et al.</i> (1997)
Apparent Magnitude (V)	0.45 ± 0.4	Perryman <i>et al.</i> (1997)
RA (ICRS: ep=J2000)	$05^{\text{h}}55^{\text{m}}10.305^{\text{s}}$	van Leeuwen (2007)
Dec (ICRS: ep=J2000)	$+07^{\circ}24'25.430''$	van Leeuwen (2007)
Proper motion-RA (mas yr $^{-1}$)	27.54	van Leeuwen (2007)
Proper motion-dec (mas yr $^{-1}$)	11.30	van Leeuwen (2007)
π (mas)	5.07 ± 1.1	Harper <i>et al.</i> (2008)
d (pc)	197 ± 45	Harper <i>et al.</i> (2008)
Main Sequence M_{\star} (M_{\odot})	~ 20	Meynet & Maeder (2003)
Main Sequence Spectral Type	O9 V	Harper <i>et al.</i> (2008)
Current M_{\star} (M_{\odot})	~ 18	Meynet & Maeder (2003)
θ_{UD} (mas)	43.33 ± 0.04	Perrin <i>et al.</i> (2004)
θ_{LD} (mas)	44.28 ± 0.15	Haubois <i>et al.</i> (2009)
R_{\star} (R_{\odot})	950	Harper <i>et al.</i> (2008)
T_{eff} (K)	3650	Levesque <i>et al.</i> (2005)
$\log_{10} L_{\star}/L_{\odot}$	5.10 ± 0.22	Harper <i>et al.</i> (2008)
$\log_{10} g_{\star}$ (cm s $^{-2}$)	-0.3	Meynet & Maeder (2003)
Heliocentric v_{rad} (km s $^{-1}$)	20.7 ± 0.4	Harper <i>et al.</i> (2008)
v_{esc} (km s $^{-1}$)	85	...
v_{∞} (km s $^{-1}$)	10, 17	Bernat <i>et al.</i> (1979)
T_{wind} (K)	< 4000	Lim <i>et al.</i> (1998)
\dot{M}_{\star} (M_{\odot} yr $^{-1}$)	3×10^{-6}	Harper <i>et al.</i> (2001)
Photospheric H_{\star} (R_{\star})	0.006	...
[Fe/H]	0.05 ± 0.14	Ramírez <i>et al.</i> (2000)
O/C	2.5	Lambert <i>et al.</i> (1984)
Rotational period (yr)	17	Uitenbroek <i>et al.</i> (1998)
B_{\star} (G)	$-3 \rightarrow +2 \pm 0.5$	Bedecarrax <i>et al.</i> (2013)
Chromosphere Model	...	Harper <i>et al.</i> (2001)
Wind Model	...	Harper <i>et al.</i> (2001)
Outer CSE	...	Rodgers & Glassgold (1991)
$^{12}\text{C}/^{13}\text{C}$	6 ± 1	Harris & Lambert (1984)
$^{16}\text{O}/^{17}\text{O}$	525 ± 250	Harris & Lambert (1984)
$^{16}\text{O}/^{18}\text{O}$	700 ± 300	Harris & Lambert (1984)

3.1 Betelgeuse

-3 ± 0.5 G to $+2 \pm 0.5$ G with temporal changes in the field strength occurring over timescales as short as a few weeks.

Various studies have assumed that Betelgeuse has a warm ($T_e \sim 8000$ K) extended atmosphere where ionized hydrogen dominates the electron density (e.g., Hartmann & Avrett, 1984; Newell & Hjellming, 1982). In fact, high resolution UV photon scattering imaging with the *HST* partially resolved the *hot* chromosphere revealing $6000 - 8000$ K plasma extending to more than $2 R_\star$ (Gilliland & Dupree, 1996). However, Lim *et al.* (1998) spatially resolved Betelgeuse with the ‘old’ VLA at 5 different wavelengths and showed that the mean electron temperature is actually much cooler, i.e., $T_e = 2000 - 4000$ K and extends out to several stellar radii as shown in Figure 3.1. In fact, the mid-IR [Fe II] line studies of Harper *et al.* (2009) suggest that the temperature of the bulk of the plasma where the chromosphere has its largest filling factor is < 2500 K. Therefore, it appears that the hot chromospheric plasma has a small filling factor and co-exists with the much more abundant cool plasma within several stellar radii. Harper *et al.* (2001) constructed a detailed physical model for the inner atmosphere of Betelgeuse which reproduces the radio fluxes of Lim *et al.* (1998) and consists of electron temperature and gas densities as a function of radius.

In comparison to other well studied red supergiants such as VY CMa, Betelgeuse has a modest mass loss rate, a low dust-to-gas ratio of $\sim 5.4 \times 10^{-4}$ (Bowers & Knapp, 1987; Harper *et al.*, 2001), and low molecular abundances (Huggins, 1987; Jewell *et al.*, 1991; Knapp *et al.*, 1980; Lambert & Vanden Bout, 1978). However, it is known to possess a molecular shell known as a MOLsphere above its photosphere (Tsuji, 2000), and recently Verhoelst *et al.* (2006) and Perrin *et al.* (2007) have used the VLTI to establish some of its properties. They find the MOLsphere to have a geometrical thin extent ($\sim 0.1 R_\star$) with a temperature of ~ 1500 K at $\sim 1.4 R_\star$, and contains molecules such as H_2O , SiO , and Al_2O_3 . Notably, they suggest that this molecular layer is where dust nucleation commences in support of a dust-driven wind scenario. However, the existence of Al_2O_3 is disputed by Kamiński *et al.* (2013) who argue that the absence of AlO (which is required to form Al_2O_3) in the photospheric spectrum is puzzling, and verification by independent studies is needed. Indeed recent studies suggest that silicates are not formed inside $\sim 23 R_\star$ (Skinner *et al.*, 1997; Tatebe *et al.*, 2007)

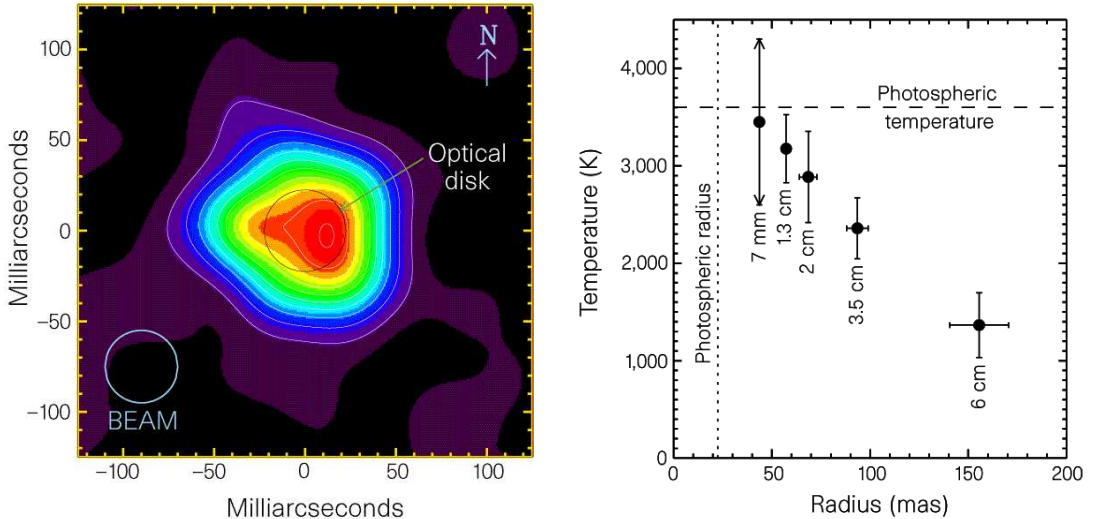


Figure 3.1: Left: The spatially resolved Q band VLA image of Betelgeuse showing asymmetry in its atmosphere. Right: The multi-frequency spatially resolved radio maps revealed that the mean electron temperature profile was lower than expected (Lim *et al.*, 1998).

and so for Betelgeuse, it appears that radiation pressure on dust grains is not the main mechanism driving its mass loss (Harper, 2010).

In the past decade or so, a number of sensitive multi-wavelength studies of Betelgeuse have revealed a complex non-spherically symmetric circumstellar environment. Starting at its surface, a H band interferometric image was reconstructed using data from the Infrared Optical Telescope Array (IOTA) and showed a non-uniform brightness distribution across its surface (Haubois *et al.*, 2009). The data were compared to 3-D hydrodynamical simulations by Chiavassa *et al.* (2010), resulting in the detection of a granulation pattern on the surface. They concluded that the surface contained a large (~ 30 mas) convective cell and a few small to medium scale (5 – 15 mas) convection-related surface structures. Adaptive optics images with the Very Large Telescope (VLT) at $1.04 – 2.17 \mu\text{m}$ revealed an irregular circumstellar envelope at a few R_\star with a few bright plumes extending out to $6 R_\star$ (Kervella *et al.*, 2009). These plumes have been attributed to the action of giant convection cells. Thermal infrared VLT ($\lambda = 8 – 20 \mu\text{m}$) imaging revealed oxygen-rich dust out to $100 R_\star$ ($2.5''$) (Kervella *et al.*, 2011), while Herschel images show a chaotic dust distribution far out in the circumstel-

lar envelope, i.e., beyond $600 R_\star$ (i.e., $> 15''$) (Decin *et al.*, 2012). A conclusion that can be drawn from these studies is the constant presence of inhomogeneities in the circumstellar environment probably play a role in the formation of dust and molecular species. We defer a discussion on previous observations of CO in Betelgeuse's circumstellar environment until Chapter 5.

3.2 CARMA

The Combined Array for Research in Millimeter-wave Astronomy (CARMA) (Bock, 2006) is a millimeter interferometer located at Cedar Flat in eastern California at an elevation of 2200 m. The array consists of nine 6.1 m antennas and six 10.4 m antennas formerly from the Berkeley Illinois Maryland Association (BIMA) and the Owens Valley Radio Observatory (OVRO) arrays respectively, and operates at 85-115 GHz (3 mm) and 215-270 GHz (1.3 mm). Eight additional 3.5 m antennas known as the Sunyaev-Zel'dovich Array (SZA) can also be added to CARMA for continuum observations at 26-36 GHz (1 cm) and 85-115 GHz (3 mm). The different sizes of the CARMA antennas makes it a heterogeneous array with a total collecting area equivalent to a single 32 m dish antenna. Despite some technical difficulties associated with image restoration for a heterogeneous array (e.g., the 15-element CARMA array has 3 different primary beams), there are a number of advantages. Such an array samples shorter $u - v$ spacings directly when the smallest antennas are in a compact configuration. This results in more of the total flux density being recovered and also recovers more of the large scale structure and is the reason why the smaller diameter antennas are usually left in the center of the array as shown in Figure 3.2. It has been shown that a heterogeneous CARMA array produces better image fidelity than a homogeneous array with the same number of antennas and collecting area (Wright, 1999).

CARMA is a reconfigurable array and has 5 different configurations providing baselines ranging between 8 m and 2 km; A configuration being the most extended and E configuration being the most compact. Figure 3.3 gives an overview of how these configurations are achieved at Cedar Flat. As the resolution is set by the array configuration and frequency of observation, we list the various achievable resolutions (i.e., the HPBW of the synthesized beam) for each of CARMA's 5

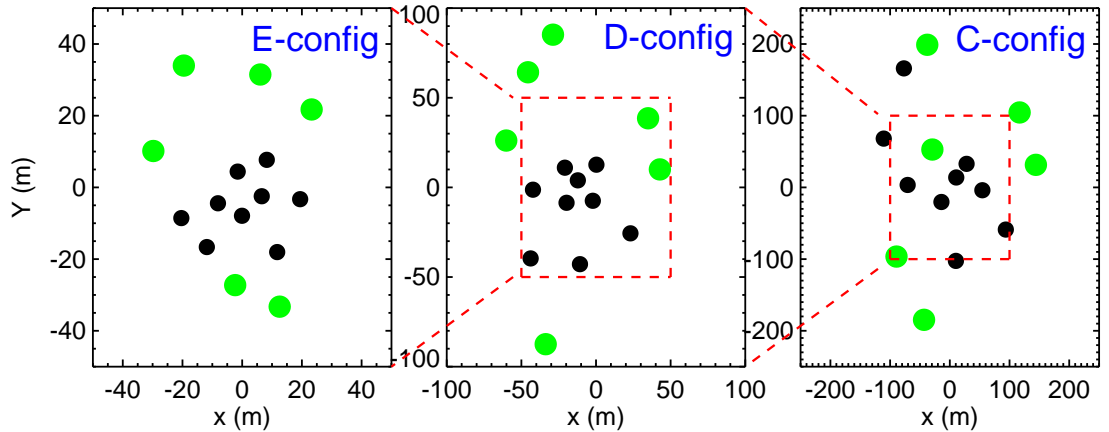


Figure 3.2: The three CARMA array configurations used to study the CSE of Betelgeuse. The most compact CARMA configuration is E configuration (*left*) which has $B_{\max} = 66$ m, D configuration (*middle*) has $B_{\max} = 148$ m, while C configuration (*right*) has $B_{\min} = 370$ m and was the most extended configuration used in our study. The 10.4 m antennas are marked green while the 6.1 m antennas are marked black.

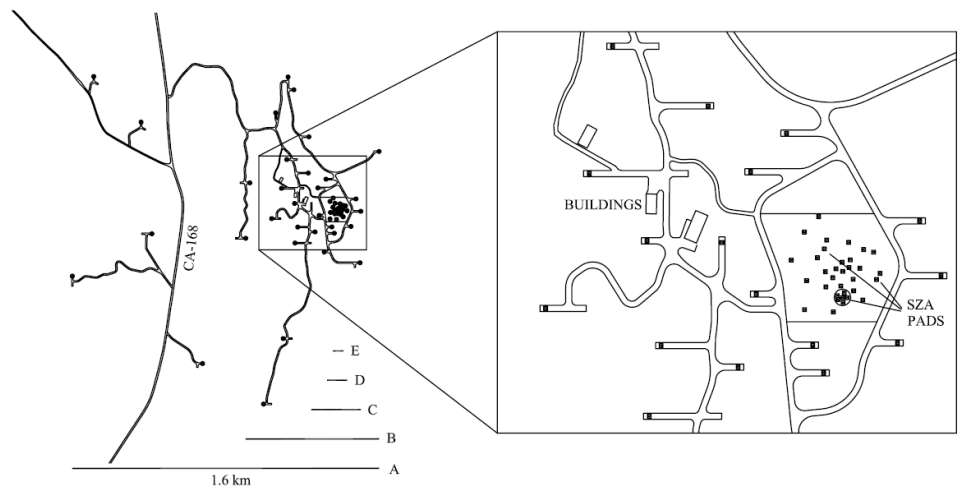


Figure 3.3: The layout of antenna pads for CARMA and a visual of the extent of each configuration (Bock, 2006).

3.2 CARMA

Table 3.2: Properties of the 5 CARMA configurations.

	A	B	C	D	E
B_{\max} (m)	1883	946	370	148	66
B_{\min} (m)	150	82	26	11	8.5
Synthesized Beam θ_{HPBW} (")	0.15	0.38	0.86	2.1	4.4
Largest Angular Scale θ_{LAS} (")	1.1	2.0	6.2	14.6	18.9
6.1 m Primary Beam θ_{HPBW} (")			50 × " (230 GHz/ ν)		
10.4 m Primary Beam θ_{HPBW} (")			30" × (230 GHz/ ν)		

configurations at 230 GHz, in Table 3.2. We also list the largest angular scale that can be imaged at 230 GHz as this is an important property of each configuration, especially when imaging extended emission. This limitation is unique to interferometers and means that structures on angular scales significantly larger than the fringe spacing formed by the shortest baseline are not measured. This information can only be obtained by observing in a smaller array configuration or by using the mosaicing method. The HPBW of the primary beam (i.e., the FOV) at a frequency ν , is $50'' \times (230 \text{ GHz}/\nu)$ for the 6.1 m antennas, and is $30'' \times (230 \text{ GHz}/\nu)$ for the 10.4 m antennas.

The 10.4 meter and 6.1 meter antennas are equipped with circular polarization superconductor-insulator-superconductor (SIS) receivers (Engargiola *et al.*, 2004) for the 1mm band, and single-polarization SIS receivers for the 3 mm band. The tuning ranges of the 1 mm and 3 mm receivers are 215–265 GHz and 85–116 GHz, respectively. Figure 3.4 shows the main components in the signal path through the CARMA system. Upon passing through the atmosphere and antenna Naysmith optics, the RF signal is sent through the cooled low noise double sideband mixer, where it is combined with a local oscillator ν_{LO1} to produce the intermediate frequency ν_{IF} . The ν_{LO1} can be either below or above the ν_{RF} ; known as the upper and lower sidebands, respectively, giving:

$$\nu_{\text{IF}} = \nu_{\text{RF}} \pm \nu_{\text{LO1}}. \quad (3.1)$$

The radio frequency gain $G_{\text{RF}}(\nu_{\text{RF}})$, results from components before this mixer (i.e., the sky and antenna optics) and depends only on the sky frequency. The

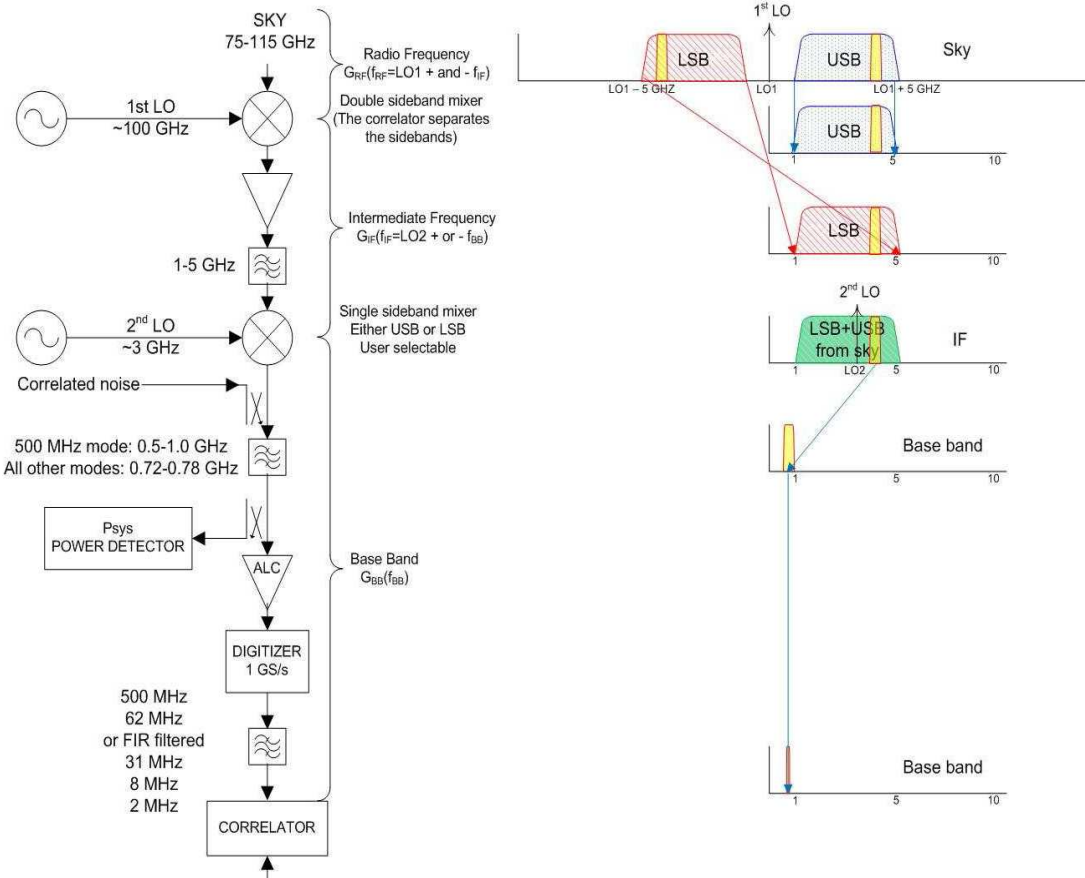


Figure 3.4: Major components in the signal path through the CARMA system (Wei *et al.*, 2008). The RF signal first reaches the cooled double sideband mixer to produce a lower frequency IF signal. Signals in the range from 1 – 5 GHz below and above the first LO show up in the IF. The IF signals pass through amplifiers and attenuators (which reduces the amplitude of the signal) at the antenna before being sent to the control building where it reaches the second mixer. Noise gets injected at the beginning of the chain of baseband components before the analog filters. The ALC amplifier ensures that the digitizers operate at a constant level.

IF signals then pass through amplifiers and attenuators in the antenna, are converted to light and sent along fibers to the control building, where they are then converted back to microwaves, amplified and attenuated further before reaching the second mixer. Even though many of the components in the IF path are common across all bands, the IF gain $G_{IF}(\nu_{IF})$, will vary per band as there are components in the second mixer which are separate for each band. The second

3.3 CARMA Observations of Betelgeuse

mixer is a single sideband mixer and its baseband output contains either the upper sideband signals above the second LO or the lower sideband:

$$\nu_{\text{BB}} = \nu_{\text{IF}} \pm \nu_{\text{LO2}}. \quad (3.2)$$

A noise signal is passed through all of the remaining correlator configuration dependent components and the selectable analog filters are measured by this noise source. The noise source can be used to correct for the baseband response, although it does not include the signal path which precedes the noise source injection (Wright, 2009). The power measurement, P_{sys} , used for the system noise temperature measurement is calculated after the analog filters and before the Automatic Level Control (ALC) amplifier which ensures that the digitizers operate at a constant level.

3.3 CARMA Observations of Betelgeuse

We used CARMA to obtain on-source spectral emission profiles of the rotational transition line $^{12}\text{C}^{16}\text{O}(J = 2-1)$ which has a rest frequency of 230.538 GHz (1.3 mm). Table 3.3 summarizes our complete set of multi-configuration observations¹ which span the period 2007 May - 2009 November. Our first set of observations took place in June 2007 when CARMA was in D configuration providing a spatial resolution of 2.1''. A total of 5 D configuration tracks were carried out and one which took place in 18 May 2007 was excluded from the final analysis due to large levels of noise in the final map, due to poor weather conditions. We obtained five E configuration (the most compact configuration available) tracks during the summer of 2009 which provided a relatively low spatial resolution of 4.4'' but gave the best sensitivity to extended emission. However, only one track was found to be of sufficient quality to be included in the final analysis. Our C configuration observations provided sub-arcsecond resolution at 230 GHz (i.e., 0.9'') and were originally scheduled for December 2008 but were postponed for a full year due to very poor weather conditions at Cedar Flat that season. We obtained a total of 4 usable tracks in C configuration amounting to 8.4 hours

¹The design of the CARMA scheduling blocks were carried out by Dr. Joanna Brown.

on source. The FOV of the individual 10.4 m antennas is $\sim 32''$ at the observed frequency.

CARMA can now take measurements in eight bands, yielding a maximum bandwidth of 4 GHz per sideband. However, back when our data were obtained, the CARMA correlator took measurements in just three separate bands, each having an upper and lower sideband. One band was set to the low resolution 468 MHz bandwidth mode (15 channels of 31.25 MHz each) to observe continuum emission and was centered on the line. The other two bands were configured with 62 MHz and 31 MHz bandwidth across 63 channels (with a resolution of 1.3 km s^{-1} and 0.65 km s^{-1} respectively) and were also centered on the line.

Bandpass and phase calibration were performed using 3C120 and 0530+135. 0532+075 was used as a secondary phase calibrator to determine the quality of the phase transfer from the primary phase calibrator. The observing sequence was to integrate on the primary phase calibrator for ~ 2.5 minutes, the target for ~ 18 minutes, and the secondary phase calibrator for ~ 2.5 minutes. The cycle was repeated for each of the tracks, which lasted between 1.5 hours and 5 hours. Absolute flux calibration was carried out with 0530+135 and 3C120 using the continuously updated CARMA flux catalog to obtain their flux values at each observation.

3.4 Arcturus and Aldebaran

Currently the most detailed spatial information about the atmospheres of K and early M spectral type evolved stars is obtained from eclipsing binaries such as the ζ Aurigae and symbiotic systems (e.g., Wright 1970; Baade *et al.* 1996; Eaton 2008; Crowley *et al.* 2008). Even though these systems offer us the best opportunity to obtain information on the dynamics and thermodynamics at various heights in the evolved star's atmosphere, the very nature of the binary system may introduce further complexities. For example, the orbital separation is often within the wind acceleration region and one could expect flow perturbations to be present (e.g., Chapman 1981). Using the old VLA, Harper *et al.* (2005) find a slow wind acceleration for ζ Aurigae and confirm that its velocity structure is

not typical of single stars with similar spectral types, such as λ Velorum (Carpenter *et al.*, 1999). In order to avoid the assumed additional complexities of a companion, we have selected two single luminosity class III red giants: Arcturus (α Bootis: K2 III) and Aldebaren (α Tauri: K5 III). These nearby red giants have been extensively studied at other wavelengths and their stellar parameters, which are summarized in Table 3.4, are accurately known. These stars are predicted to be point sources at all frequencies between 1 and 50 GHz, in all VLA configurations, so our radio observations measure their total flux density, F_ν . For example, our observations of these stars, which are discussed in Section 3.6, were taken in B configuration, providing a maximum spatial resolution of $\sim 0.14''$ at 45 GHz, which is equivalent to $\sim 7 R_*$ for both stars. The radio emission from these stars at 45 GHz is expected to be chromospheric in origin (Harper *et al.*, 2013), and as the spatial extent of red giant chromospheres is expected to be less than $1.5 R_*$ (Berio *et al.*, 2011), we can be assured that these targets will be unresolved even at the highest VLA frequencies. Moreover, both stars have existing semi-empirical 1-D chromospheric and wind models, which we can directly compare our data against.

Arcturus (α Bootis: K2 III)

Arcturus (α Bootis: K2 III) is the nearest ($d = 11.3 \pm 0.1$ pc, Perryman *et al.* (1997)) and brightest ($V = -0.04$ mag) noncoronal red giant, and is probably the best example of a red giant whose atmosphere can be studied in detail with the VLA. It is the leader of a group of stars that share a similar V space velocity (the component of stellar motion relative to the LSR in the direction of rotation), age (≥ 10 Gyr), and metallicity ($[\text{Fe}/\text{H}] \sim -0.5$, i.e., mildly metal poor), known as the Arcturus moving group (Eggen, 1971). The group has traditionally been regarded as the remains of a dissolved open cluster (e.g., Eggen, 1971, 1996) but it has also been suggested to be the debris of a metal-poor accreted satellite galaxy some billions of years ago (Navarro *et al.*, 2004). Recent analysis of chemical abundances are consistent with the former hypothesis but do not entirely rule out a merger one (Williams *et al.*, 2009). Arcturus is ascending the red giant branch (Abia *et al.*, 2012), and being a single star, its mass is relatively poorly constrained, but is similar to that of the Sun ($0.8 \pm 0.2 M_\odot$ by Kallinger *et al.*,

Table 3.3: CARMA Observations of α Ori between June 2007 and November 2009.

Date	Configuration	Time on Source (hr)	Flux Calibrator	Phase Calibrator	Image Cube Dynamic Range ^a
2007 Jun 18	D	0.9	0530+135	0530+135, 0532+075	22.8
2007 Jun 21	D	3.0	0530+135	0530+135, 0532+075	22.7
2007 Jun 24	D	2.1	0530+135	0530+135, 0532+075	26.1
2007 Jun 25	D	2.4	0530+135	0530+135, 0532+075	30.2
2009 Jul 07	E	3.2	3C120	3C120, 0532+075	30.1
2009 Nov 05	C	1.2	3C120	3C120, 0532+075	17.3
2009 Nov 09	C	3.0	3C120	3C120, 0532+075	27.2
2009 Nov 15	C	1.0	3C120	3C120, 0532+075	17.8
2009 Nov 16	C	3.2	3C120	3C120, 0532+075	32.0
All	C	8.4	43.8
All	D	8.4	31.9
All	Multi-configuration	20.0	52.3

^a The peak emission of the image cube divided by the root mean square of the residual image.

2010). During the last decade there has been a large dispersion in the reported values of Arcturus' effective temperature (i.e., $3850 < T_e < 4630$ K, Griffin, 1996) but it is now generally accepted to be about 4300 K (di Benedetto, 1993; Griffin & Lynas-Gray, 1999). A number of interferometric measurements of the limb-darkened angular diameter of the star are available in the literature with most values agreeing within their uncertainties. The weighted mean value of these values is $\theta_{LD} = 21.06 \pm 0.17$ mas (Ramírez & Allende Prieto, 2011) giving the star a radius of $25.4 \pm 0.3 R_\odot$.

Arcturus is an important target for high spatial and spectral resolution calibration. Thus when the Hipparcos catalog flagged Arcturus as a two component object (Perryman *et al.*, 1997) it caused debate in the community. However, the uncertainties in the Hipparcos data (Soderhjelm & Mignard, 1998) along with a non-detection in both adaptive optics observations (Turner *et al.*, 1999) and sensitive interferometric techniques (Lacour *et al.*, 2008) suggest that Arcturus is single and can still be used as a calibrator. Nevertheless, Lacour *et al.* (2008) still do not rule out the possibility of a planetary companion of a few Jovian masses as suggested by its long period radial velocity variations of ~ 233 days (Brown, 2007; Hatzes & Cochran, 1993). Variations on timescales of a few days are also seen in its radial velocity (Merline, 1999) and photometry (Retter *et al.*, 2003). The photometric amplitude oscillations can vary by up to a percent and may be the manifestation of convection such as large-scale granulation, or solar-like oscillations (Dziembowski *et al.*, 2001).

The first detailed model of the atmosphere of Arcturus was the 1-D time-independent semi-empirical model of Ayres & Linsky (1975) which was based on diagnostics observable from the ground (i.e., Ca II *H* and *K* and the Ca II IR triplet) and early satellite observations of the Mg II *h* and *k* emission lines with the Orbiting Astronomical Observatory 3 (*OAO-3* or *Copernicus*). They were able to calculate temperature and mass column densities for the upper photosphere and chromosphere and estimated the temperature at the top of the chromosphere to be ~ 8000 K. They also found $T_{\min}/T_{\text{eff}} \sim 0.77$, which is similar to that of the Sun. The important *IUE* cool star survey by Linsky & Haisch (1979) placed Arcturus on the right of the dividing line. This meant that its atmosphere showed lines formed at temperatures no hotter than $10,000 - 20,000$ K, suggestive of a

3.4 Arcturus and Aldebaran

Table 3.4: Basic Properties of α Bootis and α Tauri.

Property	α Bootis	α Tauri	Reference
HD Number	124897	29139	...
Spectral Type	K2 III	K5 III	1
App. Mag. (V)	-0.5	0.86v	1
RA (ICRS: ep=J2000)	14 ^h 15 ^m 39.672 ^s	04 ^h 35 ^m 55.239 ^s	2
Dec (ICRS: ep=J2000)	+19°10'56.673"	+16°30'33.489"	2
Proper motion-RA (mas yr ⁻¹)	-1093.39 ± 0.44	63.45 ± 0.84	2
Proper motion-dec (mas yr ⁻¹)	-2000.06 ± 0.39	-188.94 ± 0.65	2
π (mas)	88.83 ± 0.54	48.94 ± 0.77	2
d (pc)	11.3 ± 0.1	20.4 ± 0.3	2
M_* (M_\odot)	0.8 ± 0.2	1.3 ± 0.3	3, 4
θ_{LD} (mas)	21.06 ± 0.17	20.58 ± 0.03	5, 6
R_* (R_\odot)	25.4 ± 0.3	44.2 ± 0.9	...
T_{eff} (K)	4294 ± 30	3970 ± 49	7
L_*/L_\odot	198 ± 3	442 ± 11	...
g_* (cm s ⁻²)	34	18	...
Heliocentric v_{rad} (km s ⁻¹)	+5.19 ± 0.04	+54.11 ± 0.04	8
v_{esc} (km s ⁻¹)	110	106	...
v_∞ (km s ⁻¹)	35 – 40	30	9, 10
T_{wind} (K)	~ 10,000	~ 10,000	9, 10
\dot{M}_* (M_\odot yr ⁻¹)	2×10^{-10}	1.6×10^{-11}	9, 10
Photospheric H_* (R_*)	0.005	0.005	...
Fe/H	-0.5 ± 0.2	-0.15 ± 0.2	11
Rotational period (yr)	2.0 ± 0.2	1.8	12, 13
B_* (G)	0.65 ± 0.26	unknown	14
Chromosphere Model	Drake (1985)	McMurtry (1999)	...
Wind Model	Drake (1985)	Robinson <i>et al.</i> (1998)	...

References.-(1) Perryman *et al.* (1997); (2) van Leeuwen (2007); (3) Kallinger *et al.* (2010); (4) Lebzelter *et al.* (2012) (5) Ramírez & Allende Prieto (2011) (6) Richichi & Roccatagliata (2005); (7) di Benedetto (1993); (8) Massarotti *et al.* (2008); (9) Drake (1985); (10) Robinson *et al.* (1998); (11) Decin *et al.* (2003); (12) Gray *et al.* (2006); (13) Hatzes & Cochran (1993); (14) Sennhauser & Berdyugina (2011)

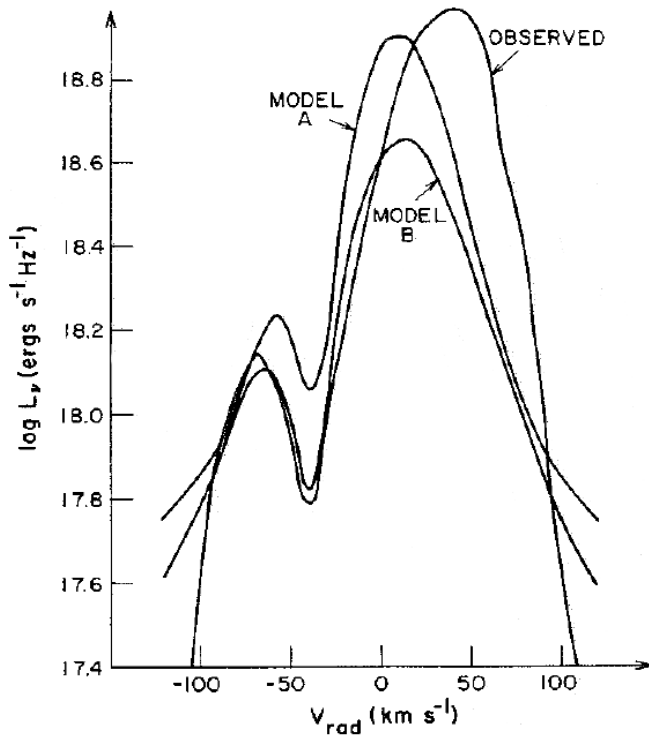


Figure 3.5: *IUE* Mg II *k* line profile for Arcturus over-plotted with the model atmospheres of Drake (1985). The superior resolution and sensitivity of the *HST* profile in Figure 1.2 is probably the main reason for the difference in line profile shapes.

chromosphere only. However, they also developed a hot coronal wind model for the star and found it to be consistent with the absence of a detection of transition region material in the *IUE* spectra; i.e., the high temperature transition region emission line fluxes could be below the detection limit. Drake (1985) developed a semi-empirical chromosphere and wind model for Arcturus based on the Mg II *k* emission line from the *IUE* (see Figure 3.5) and estimated a mass loss rate of $2 \times 10^{-10} M_{\odot}$ yr⁻¹.

Evidence began to emerge that Arcturus actually falls into the class of late type stars known as hybrids when deeply exposed *IUE* echelle spectrograms showed the weak presence of the Si III] $\lambda 1892.0$ feature, indicating the existence of a small amount of plasma at temperatures as hot as 6×10^4 K. Its hybrid status was confirmed when C IV and N V (indicative of temperatures $\sim 1 \times 10^5$

K) were detected with the *HST* STIS, and also with a tentative 3σ X-ray detection made with the Chandra X-Ray Observatory (Ayres *et al.*, 2003). It appears that Arcturus has been able to sustain a modest level of magnetic activity. Three measurements for the mean longitudinal magnetic field (albeit weak: $B = 0.65 \pm 0.26$, 0.43 ± 0.16 , and -0.23 ± 0.20 G) have reportedly been detected on the star via the Zeeman effect (Sennhauser & Berdyugina, 2011), and a magnetic cycle with a period of ≥ 14 years has also been proposed (Brown *et al.*, 2008).

Arcturus appears to have a thermally bifurcated chromosphere which consists of large (i.e., $> 99\%$) amounts of material within the chromosphere that is cooler than the surrounding chromospheric temperature minimum [i.e., a CO-mosphere, Wiedemann *et al.* (1994)]. This suggests that the assumption in current semi-empirical chromospheric models of the *hot* UV emitting material having a filling factor of unity may not be correct. The more recent spectroscopic analysis of CO and H₂O transitions have confirmed the existence of cooler molecular *clouds* in the outer atmosphere of Arcturus (Ryde *et al.*, 2002; Tsuji, 2009).

Aldebaran (α Tauri: K5 III)

At a distance of 20.4 ± 0.3 pc (van Leeuwen, 2007), Aldebaran (α Tauri: K5 III) is a nearby red giant and is one of the most easily recognizable stars from the Northern and most of the Southern Hemisphere. Even though it is almost twice as far away as Arcturus, its larger stellar radius ($R_\star = 44.2 \pm 0.9 R_\odot$) gives it a comparable angular diameter ($\theta_{LD} = 20.58 \pm 0.03$; Richichi & Roccatagliata 2005), and is therefore another excellent candidate for multi-frequency studies with the VLA. Its effective temperature ($T_{\text{eff}} = 3970 \pm 49$ K; di Benedetto 1993) is lower than Arcturus', and it also has a higher mass ($M = 1.3 \pm 0.3 M_\odot$; Lebzelter *et al.* 2012). Using these values for its radius and mass gives a surface gravity of $g_\star = 18$ cm s⁻², about 1500 times lower than the Sun's. The metallicity of Aldebaran is close to solar with $[\text{Fe}/\text{H}] = -0.15 \pm 0.2$ (Decin *et al.*, 2003). Using high spectral resolution data in the H, K, and L bands, Tsuji (2008) derived the carbon, nitrogen, and oxygen abundances in Aldebaran which suggests the mixing of the CN-cycled material in the first dredge-up. A 643 day period in the radial velocity for Aldebaran was reported by Hatzes & Cochran (1993), and Hatzes & Cochran (1998) find evidence to support the hypothesis that this variability

comes from the reflex motion of the central star due to a planetary companion having a mass of $11 M_{\text{Jup}}$, although this has not been confirmed to date.

Aldebaran has been extensively studied at UV wavelengths. Early *IUE* observations placed the star well to the noncoronal side of the Linsky-Haisch dividing line (Linsky & Haisch, 1979). The first chromospheric model of the star was developed in the late 1970s (Kelch *et al.*, 1978) and was based on both optical (mainly Ca II H and K) and UV (Mg II *h* and *k*) emission line profiles. Later, GHRS spectra revealed the presence of significant flux in the C IV resonance lines around 1550 Å (Carpenter & Robinson, 1996), which indicated the presence of some *hot* transition region plasma. In light of the new GHRS findings, a new model of the chromosphere and transition region of Aldebaran was developed, with temperatures reaching up to $T_e \sim 1 \times 10^5$ K as a result of the presence of C IV in the spectrum (McMurry, 1999). Modelling the GHRS optically thick Mg II and O I resonance lines (which show typical stellar wind absorption features), Robinson *et al.* (1998) found evidence for the acceleration of a slow wind and derived a mass-loss rate of $1.6 \times 10^{-11} M_{\odot} \text{ yr}^{-1}$ and a terminal wind velocity of 30 km s⁻¹. FUSE spectra revealed the presence of the coronal proxy O VI 1032 and 1038 Å emission lines (Dupree *et al.*, 2005) although Ayres *et al.* (2003) failed to detect any X-ray emission from the star. Like Arcturus, Aldebaran appears to harbour small levels of magnetic activity.

Wiedemann *et al.* (1994) observed Aldebaran's infrared ro-vibration absorption lines ($v = 2 - 1$) and matched them with synthetic spectra based on a model containing the semi-empirical photosphere of Kelch *et al.* (1978) and the best fitting temperature and column density profiles. Like Arcturus, they found a steady decrease in temperature with height, with the chromospheric temperature being constantly below the temperature minimum ($T_{\min} \sim 2800$ K) of the Kelch model. Again, they explained their results by suggesting the existence of an extra *cool* component with a large (> 99%) filling factor in the outer atmosphere (i.e., a thermally bifurcated CO-mosphere). Recently, Ohnaka observed the CO first overtone lines ($v = 2 - 0$) of Arcturus near 2.3 μm with the Very Large Telescope Interferometer (VLTI) and discovered a CO layer extending out to $2.5 R_{\star} \pm 0.3 R_{\star}$. They were unable to constrain the geometrical thickness of this CO layer from their data but we will show how our VLA radio data can constrain this value in

3.5 The Karl G. Jansky Very Large Array

Chapter 6. H₂O was also confirmed in its MOLsphere when Tsuji (2001) detected a H₂O absorption feature at $\sim 6.6 \mu\text{m}$. A narrow absorbtion feature in the midst of the wind absorption of the GHRS Mg II h and k lines has been interpreted and modelled as a feature of α Tau's wind-ISM interaction region, also known as its astrosphere (Wood *et al.*, 2007).

3.5 The Karl G. Jansky Very Large Array

The NRAO¹ Karl G. Jansky Very Large Array (VLA) is an aperture synthesis radio telescope located on the Plains of San Agustin, New Mexico, USA. At high frequencies (i.e., Q band), it is capable of producing radio images with a spatial resolution greater than that of the *HST*. It is the product of a program to modernize the electronics of the old VLA which had been in operation at the same site since the late 1970's. One of the main upgrades to the VLA is the addition of the Wideband Interferometric Digital Architecture (WIDAR; Carlson 2001) correlator, which allows the digital correlation of very wideband signals. WIDAR digitally filters and splits the data into sub-bands which are then separately cross correlated and integrated before being combined together again to yield the final wideband spectrum. The new WIDAR correlator and its superior bandwidth capability provides the VLA with greater sensitivity, allowing the detection of lower flux density sources than was previously possible with the old VLA. A comparison of the performance parameters of the VLA with those of the old VLA is shown in Table 3.5. The three major new observational abilities of the VLA are:

1. Complete frequency coverage between 1 and 50 GHz, opening up new regions of the electromagnetic spectrum to astronomy.
2. An increase in continuum sensitivity by an order of magnitude at some frequencies, by increasing the bandwidth to 8 GHz per polarization.
3. Process the large bandwidth with a minimum of 16,384 spectral channels per baseline.

3.5 The Karl G. Jansky Very Large Array

Table 3.5: Improved Performance Parameters of the VLA.

Parameter	old VLA	VLA	Improvement Factor
Continuum sensitivity (1σ , 9 hr)	$10 \mu\text{Jy}$	$1 \mu\text{Jy}$	10
Bandwidth per polarization	0.1 GHz	8 GHz	80
Coarsest frequency resolution	50 MHz	2 MHz	25
Finest frequency resolution	381 Hz	0.12 Hz	3180
Channels at max. bandwidth	16	16,384	1024
Maximum number of channels	512	4,194,304	8192

Apart from the addition of more feeds at the center of the reflector, and a refurbishment of all antennas, the structural design of the VLA has not changed during its recent upgrade. As before it consists of 27 fully steerable alt-azimuth antennas arranged along the arms of an upside-down ‘Y’ as shown in Figure 2.9. The array is re-configurable and can vary its resolution by over a factor of ~ 50 through movement of its component antennas along twin railroad tracks. Four standard configurations of antennas along the arms of the array are possible whose scales vary by the ratios 1 : 3.28 : 10.8 : 35.5 from smallest to largest. These are called D, C, B, and A configurations, with A having the longest baselines (~ 36 km) giving the best spatial resolution, but lacking short baselines needed for imaging extended structure. In each configuration, the distance of each antenna from the center of the ‘Y’ is equal to $m^{\ln 2}$ where m is the antenna location number, counting outwards from the center of each arm. With this design, the m 'th station in any configuration coincides with the $2m$ 'th station in the next smaller configuration. This means that only 72 stations are needed to handle all four configurations. Additionally, there are 3 hybrid configurations called DnC, CnB, and BnA, which are well suited for sources with low declination. In these configurations, the North arm antennas are deployed in the next larger configuration than the SE and SW arm antennas, resulting in a more circular synthesized beam for these sources.

Each antenna is 25 m in diameter giving the array a total collecting area equivalent to a single dish of 130 m in diameter. Each antenna has an off-axis

¹The National Radio Astronomy Observatory is a facility of the National Science Foundation operated under cooperative agreement by Associated Universities, Inc.

3.5 The Karl G. Jansky Very Large Array

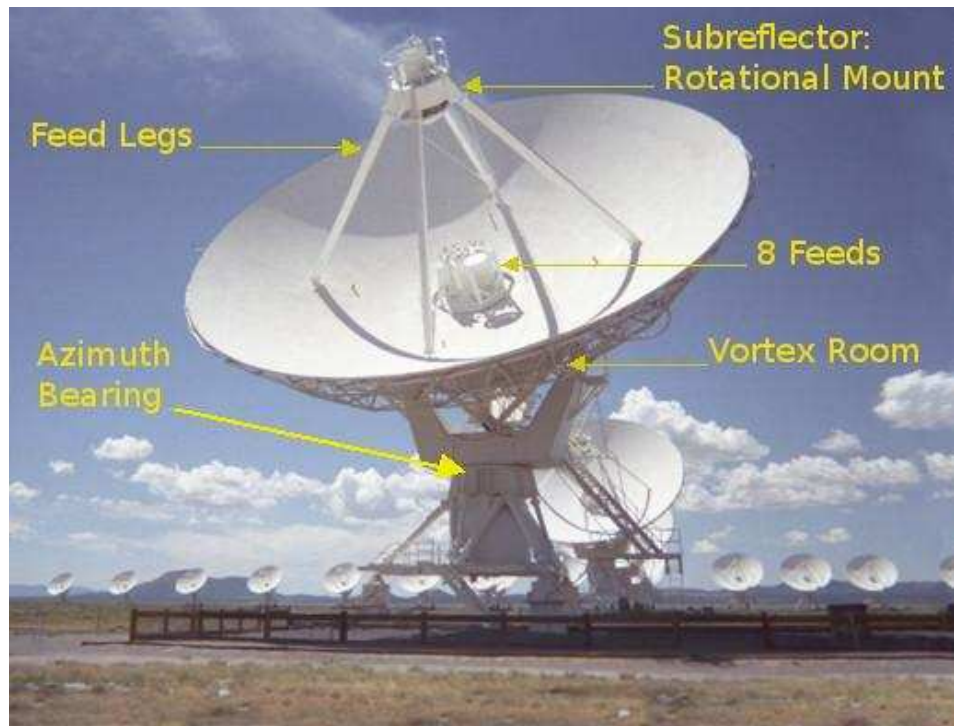


Figure 3.6: Main features of a VLA antenna. The sub-reflector is located at the prime focus on a rotational mount, which is supported by four feed legs. The 8 feeds are located in a ring at the secondary focus. The feeds send the RF signal to the front end located in the vortex room directly beneath the main reflector.
Image Credits: NRAO/AUI.

Cassegrain design with a rotatable sub-reflector at the prime focus of the main reflector and is supported by four feed legs as shown in Figure 3.6. All feeds are located on a feed ring at the Cassegrain focus and the observing feed is changed by rotating the asymmetric sub-reflector about the main reflector axis so that the secondary focal point moves to the desired feed. The standard observing mode for all feeds is circular polarization. RF signals from each feed are sent via a waveguide to the antenna vortex room located directly underneath the main reflector, where they are feed into low noise front ends. The vortex room is temperature controlled and also contains cryogenic cooling systems for the front end, portions of the LO, and IF equipment. IF signals from each antenna are sent by cable to a shielded room where the signals are cross correlated.

3.5 The Karl G. Jansky Very Large Array

Table 3.6: Frequency coverage, spatial resolution, and FOV of the VLA.

	L	S	C	X	Ku	K	Ka	Q
ν (GHz)	1.5	3.0	6.0	10	15	22	33	45
λ (cm)	20	13	6.0	3.0	2.0	1.3	1.0	0.7
ν Range (GHz)	1-2	2-4	4-8	8-12	12-18	18-26.5	26.5-40	40-50
A config: θ_{HPBW} ('')	1.3	0.65	0.33	0.20	0.13	0.089	0.059	0.043
B config: θ_{HPBW} ('')	4.3	2.1	1.0	0.6	0.42	0.28	0.19	0.14
C config: θ_{HPBW} ('')	14	7.0	3.5	2.1	1.4	0.95	0.63	0.47
D config: θ_{HPBW} ('')	46	23	12	7.2	4.6	3.1	2.1	1.5
FOV(')	30	15	7.5	4.5	3.0	2.0	1.4	1.0

All VLA antennas are outfitted with eight receivers providing continuous frequency coverage between 1 and 50 GHz. As shown in Table 3.6, the frequency ranges of 1-2 GHz, 2-4 GHz, 4-8 GHz, 8-12 GHz, 12-18 GHz, 18-26.5 GHz, 26.5-40 GHz, and 40-50 GHz, are commonly referred to as L, S, C, X, Ku, K, Ka, and Q bands, respectively. In addition, the VLA is currently being outfitted with even lower frequency receivers, P band (230 – 470 MHz), and 4 band (54 – 86 MHz) which will operate just above the ionospheric cut-off frequency (~ 10 MHz). The VLA’s spatial resolution is set by the maximum baseline, B_{\max} , and frequency of observation. This means that structures smaller than the diffraction limit ($\theta_{\text{HPBW}} \sim \lambda/B_{\max}$) will be smoothed to the resolution of the array. Table 3.6 also summarizes the maximum resolution for each of the four main configurations at each wavelength. The resolution is defined here as the HPBW of the synthesized beam, using uniform weighting, over a full 12 hour synthesis observation, of a source which passes near the zenith. For completeness, we also give the field of view (FOV) at each observing frequency in Table 3.6, defined as the HPBW of the primary beam, which for the VLA antennas can be approximated using the formula: $\text{FOV}' = 45/\nu_{\text{GHz}}$.

3.6 VLA Observations of Arcturus and Aldebaran

3.6.1 OSRO and DDT Observations

The Open Shared Risk Observing (OSRO) program at the VLA existed during its commissioning phase (i.e., between September 2011 - January 2013) to provide observers with early access to a number of VLA correlator capabilities and observing modes. This represented a considerable improvement over the capabilities of the old VLA correlator as observers were provided with increased bandwidth capability at existing VLA bands, increased spectral resolution capabilities, and access to new spectral bands. In September 2010 our proposal (PI: G. M. Harper, Program ID: 10C-105) to observe two archetypical red giants at multiple frequencies was allocated the requested 15.5 hours of observing time with the VLA as part of NRAO's OSRO Science Program 2010C. A number of observing scripts called scheduling blocks (SBs) were prepared during December 2010 and their duration were each kept to ≤ 2.5 hours to increase their likelihood of being scheduled. The VLA now uses dynamic scheduling for deciding which SBs are executed at any time. This takes into account many factors like the scheduling priority assigned by the time allocation committee, weather constraints, and SB duration. A consequence of dynamic scheduling is that the observer does not know when their observations will occur. In general the chances of observations being scheduled are increased if the duration of the SB is kept short.

Our main set of observations took place in February 2011 while the VLA was in B configuration. All observations were taken in continuum mode and the correlator was set up with two 128 MHz sub-bands centered on the frequencies listed in Table 3.7. Each sub-band had sixty-four channels of width 2 MHz and four polarization products (RR, LL, RL, LR). We obtained all of our requested observations of α Tau in just two days between the 11th and 13th of February 2011, which consisted of Q, Ka, K, X, C, and S band observations of the star. We did not request L band (i.e., 1.5 GHz) observations of α Tau as it was believed that the star would be too faint to be observable at this frequency, with the available bandwidth. There was also insufficient Ku band receivers available at the time

Table 3.7: VLA Observations of α Bootis and α Tauri obtained in February 2011 and July 2012.

Star	Date	Band	ν (GHz)	λ (cm)	Time on Star (hr)	Restoring Beam (" \times ")	Bandwidth (GHz)	Number of Antennas	Phase Calibrator
α Bootis	2011 Feb 22	Q	43.3	0.7	0.3	0.19 \times 0.15	0.256	22	J1357+1919
	2011 Feb 22	Ka	33.6	0.9	0.2	0.25 \times 0.20	0.256	23	J1357+1919
	2011 Feb 22	K	22.5	1.3	0.4	0.35 \times 0.28	0.256	24	J1357+1919
	2011 Feb 11	X	8.5	3.5	0.3	1.14 \times 0.70	0.256	18	J1415+1320
	2011 Feb 11	C	5.0	6.0	0.5	2.02 \times 1.30	0.256	21	J1415+1320
	2011 Feb 13	S	3.1	9.5	1.8	2.57 \times 2.08	0.256	12	J1415+1320
	2012 Jul 19	S	3.0	10.0	0.7	2.82 \times 2.30	2.0	23	J1415+1320
	2012 Jul 20	L	1.5	20.0	1.6	4.46 \times 3.94	1.0	23	J1415+1320
α Tauri	2011 Feb 11	Q	43.3	0.7	0.3	0.18 \times 0.16	0.256	22	J0431+1731
	2011 Feb 11	Ka	33.6	0.9	0.2	0.22 \times 0.20	0.256	19	J0449+1121
	2011 Feb 11	K	22.5	1.3	0.4	0.35 \times 0.31	0.256	21	J0449+1121
	2011 Feb 13	X	8.5	3.5	0.5	0.85 \times 0.78	0.256	25	J0449+1121
	2011 Feb 13	C	5.0	6.0	1.2	1.48 \times 1.32	0.256	21	J0449+1121
	2011 Feb 12	S	3.1	9.5	1.8	2.74 \times 2.02	0.256	11	J0431+2037

3.6 VLA Observations of Arcturus and Aldebaran

to carry out observations at 15 GHz. We obtained Q, Ka, K, X, C, and S band observations of α Boo in eleven days between the 11th and 22nd of February 2011. We also had prepared a 2.5 hour SB for α Boo at L band but this SB was never executed for reasons unknown to the authors and VLA *helpdesk* staff.

For this reason we applied for (and were awarded) 3 additional hours of directors discretionary time (DDT) in early 2012 (PI: E. O’Gorman, Program ID: 12A-472) to observe α Boo at S and L band. We decided to include a short observation at S band to check that the star’s flux density had not significantly changed over that period and so any possible L band detection could be included in the analysis of the main set of data from the previous year. Our DDT observations took place in July 2012 when the VLA was again in B configuration with details given in Table 3.7. The capabilities of the VLA had greatly increased in the ~ 1.5 years since the main set of observations and we now could utilize the full 1 and 2 GHz of bandwidth at L and S band, respectively. The 1-2 GHz and 2-4 GHz frequency ranges were both divided into 16 sub-bands, each with sixty-four channels. The channel width was 2 and 1 MHz for S and L band, respectively, and each sub-band had four polarization products (RR, LL, RL, LR).

3.6.2 Design of Observations¹

In radio interferometry, baseline-dependent additive errors in the visibilities can occasionally lead to artifacts occurring at phase center of the final image (Ekers, 1982). Such errors may be caused by unflagged low level interference picked up by some antennas baselines. An example of this is demonstrated in Figure 3.7 in which two radio images of Betelgeuse at 15 GHz are shown (A. Brown, priv. comm.). The left panel was taken on 2nd February 2002 and shows a 30σ detection of Betelgeuse with low level background noise. The right panel, which was taken two months later on 2nd April 2002, shows a 45σ detection of the star but now also shows a 15σ artifact at phase center. If the target had been observed at phase center in this case, then this artifact would lead to an incorrect flux density measurement for the star. For our VLA observations, both α Boo and α Tau were slightly offset from the phase-center by ~ 5 synthesized beam

¹Both the OSRO and DDT observations were designed by the author.

3.6 VLA Observations of Arcturus and Aldebaran

widths in order to avoid source contamination by these rare but possible phase center artifacts, therefore avoiding spurious detections.

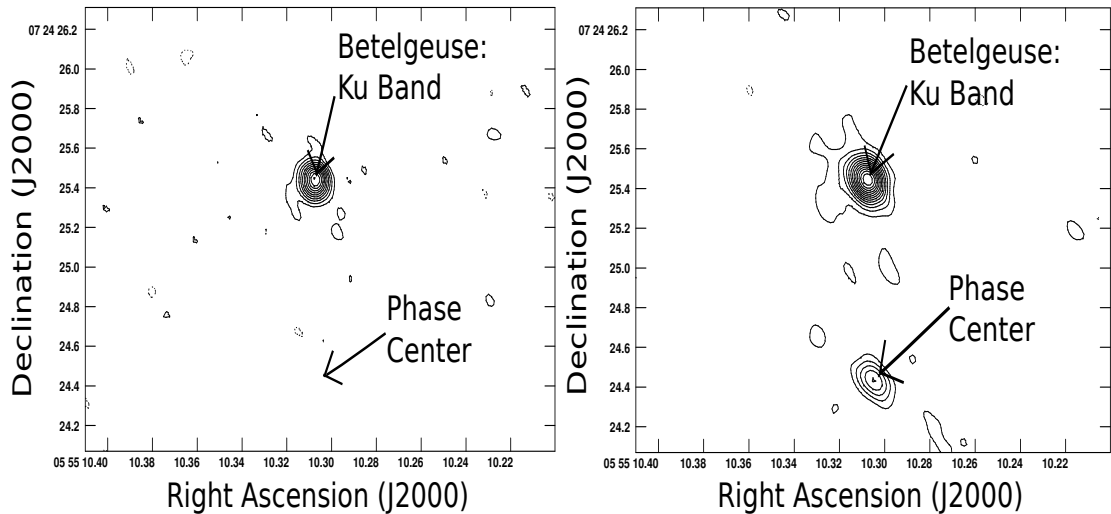


Figure 3.7: An example to highlight the importance of offsetting the source from phase center. *Left:* Old VLA image of Betelgeuse at 15 GHz taken in February 2002 showing no source at the phase center of the image. Contour levels are at $\sigma(-6,-3,3,\dots,30)$ where $\sigma = 84 \mu\text{Jy}$. *Right:* Two months later Betelgeuse was again imaged at 15 GHz but now shows a strong artifact at phase center. Contour levels are at $\sigma(-6,-3,3,\dots,45)$ where $\sigma = 90 \mu\text{Jy}$ (A. Brown, priv. comm.).

A problem at low VLA frequencies (L and S bands) is disturbances in the ionosphere caused by solar activity. At L band, solar flares can be as strong as $1 \times 10^6 \text{ Jy}$ and are a major source of interference, with their effects sometimes being impossible to remove from the data. To avoid such problems, the S and L band SBs were scheduled for night time observing only. The low to intermediate frequency observations (L - X bands) were composed of repeatedly interleaved observations of the target and a nearby phase calibrator with cycle times of 12 minutes; 10 minutes on the target and 2 minutes on the phase calibrator. For α Boo, the point source J1415+1320, which is located 6° away, was used as the phase calibrator at these frequencies. For α Tau, the point source J0449+1121, located 6° away, was used at C and X band, while the brighter J0431+2037, located 4° away, was used at S band due to it being unresolved at this frequency (but is resolved at C and X band). The primary calibration sources 3C286 and 3C138 were observed at the end of all low and intermediate frequency SBs and

3.6 VLA Observations of Arcturus and Aldebaran

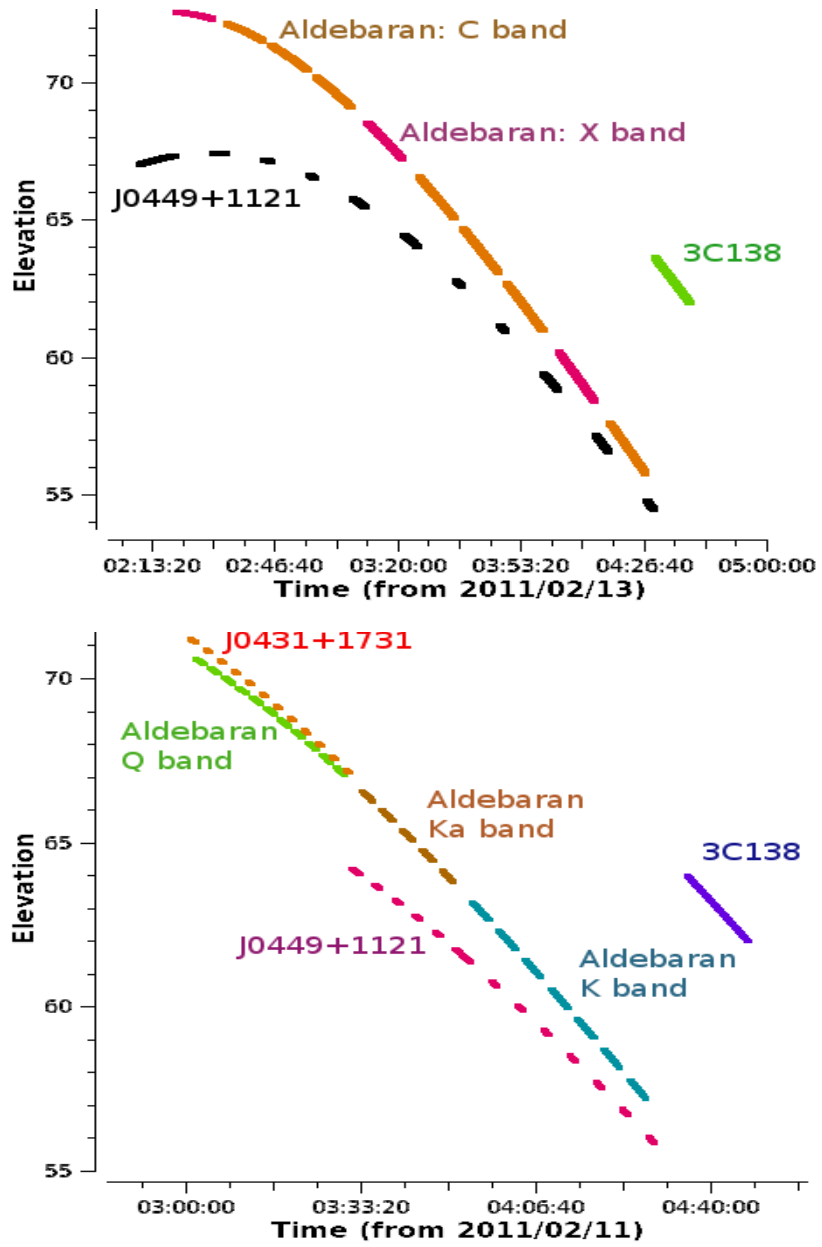


Figure 3.8: Overview of a low and high frequency VLA SB for α Tauri. *Top Panel:* The low frequency observations consisted of interleaved observations of the target and a nearby phase calibrator with cycle times of 12 minutes. The X band observations were interspersed between C band observations to obtain a good spread in $u-v$ coverage. *Bottom Panel:* The high frequency observations had short cycle times to compensate for tropospheric effects. Q band observations were taken first to ensure the best pointing solutions were applied to them.

3.7 VLA-Pie Town Observations of Betelgeuse

were used to measure the bandpass and set the absolute flux for α Boo and α Tau, respectively. The top panel in Figure 3.8 shows a plot of elevation against time for all the sources observed in the SB of the C and X band observations of α Tau. In this SB, observations of α Tau at X band were interspersed between C band observations throughout the track to obtain a good spread in $u-v$ coverage.

At high VLA frequencies (i.e., K, Ka, and Q band) the troposphere can cause major phase variations to incoming radio waves. To reduce this problem, the old VLA used a technique called *fast switching* (Carilli *et al.*, 1996) which reduced the setup overhead and slewing compared to traditional iterating between source and calibrator scans. This overhead is sufficiently reduced with the new VLA and no special fast switching mode is necessary. Instead regular but short duration source-calibrator loops are implemented. As a result, the calibration overheads for high frequency observing are typically considerably larger than for lower frequency observations. For both stars, the total cycle times for the Q, Ka, and K band observations were 160, 230, and 290 s, respectively. These high frequency observations were combined into a single 2 hour SB for each star and commenced with X band reference pointing with solutions being applied on-line. As mentioned in Section 2.1.3, the blind pointing errors of the VLA antennas can occasionally be as large as the HPBW of the primary beam at high frequencies. Thankfully, the pointing can be calibrated for using a technique known as *reference pointing*, whereby a nearby known calibrator is observed in interferometer pointing mode every hour or so. The measured local pointing corrections are then applied to subsequent target observations. Reference pointing can reduce the rms pointing errors to as little as $2''$ if the reference source is with 10° of the target source. After X band pointing the target source was observed at Q band to ensure the best pointing solutions were used, as shown in the lower panel of Figure 3.8 for α Tau.

3.7 VLA-Pie Town Observations of Betelgeuse

As part of our study into Betelgeuse's extended atmosphere we decided to re-visit some archival high spatial resolution VLA data from the early 2000's. This was motivated by the recent findings of Richards *et al.* (2013) who detected two hot

3.7 VLA-Pie Town Observations of Betelgeuse

chromospheric features with the very long baseline interferometer e-MERLIN. The two features, also referred to as “hot spots”, were found to have brightness temperatures well above the mean brightness temperature measured at the same radio wavelength, and were separated from each other by 90 mas. We wanted to see if these features were present at other wavelengths and if so, how they varied over time.

Asymmetries in Betelgeuse’s atmosphere were first detected at radio wavelengths by Lim *et al.* (1998) at 0.7 cm, and subsequently by Morris (2001) at 6 cm by combining old VLA and MERLIN data. To see how these asymmetries evolved with time, a multi-wavelength study¹ into the temporal evolution of Betelgeuse’s atmosphere was carried out with the old VLA over a number of years in the early 2000’s, in its most extended A configuration plus the Pie Town link. This study focused on fitting various models to the visibility data as was done by Lim *et al.* (1998), i.e., the analysis was mainly carried out in the visibility plane. The detection of the two unique hot spots in the e-MERLIN radio maps by Richards *et al.* (2013) inspired us to revisit these data which, because of the addition of the Pie Town link to the VLA, gave spatial resolution comparable to or exceeding that of e-MERLIN at some wavelengths. Our goal was to carry out the analysis in the image plane to make a direct comparison with the findings of Richards *et al.* (2013). In Table 3.8 we summarize this unique data set which consists of almost four years of high resolution multi-wavelength observations of Betelgeuse. To increase our observational time period we also include the short wavelength high resolution (i.e., A configuration) observations of the star from 1998. Betelgeuse was resolved at all wavelengths listed in Table 3.8 except at L band.

The VLA-Pie Town Link

The 25 m antenna located at Pie Town, New Mexico is one of 10 antennas spread across the United States of America which together make up the Very Long Baseline Array (VLBA). It was successfully connected in real time via a 104 km long fiber optic line to the VLA in 1999 and was operational at all old VLA frequencies prior to its upgrade to the Karl G. Jansky VLA. The Pie Town antenna is located

¹These data were carefully flagged and calibrated by Dr. Alexander Brown.

3.7 VLA-Pie Town Observations of Betelgeuse

Table 3.8: Multi-wavelength VLA + Pie Town Observations of Betelgeuse.

Date	Band	λ (cm)	Time on Star (hr)	Restoring Beam (mas)	rms noise (mJy/beam)
2004 Oct 21,30	Q	0.7	1.2	39×26	0.37
	K	1.3	2.6	80×41	0.09
	U	2.0	3.3	121×91	0.08
	X	3.5	3.8	208×126	0.02
	C	6.2	2.9	377×265	0.02
	L	16.7	2.4	1262×889	0.03
2003 Aug 10,12	Q	0.7	0.9	40×27	0.46
	K	1.3	2.6	80×42	0.18
	U	2.0	3.3	119×96	0.10
	X	3.5	3.0	204×139	0.03
	C	6.2	2.8	378×297	0.03
	L	16.7	2.6	1247×931	0.04
2002 Feb 17,18	K	1.3	2.0	82×47	0.14
	U	2.0	2.0	128×90	0.11
	X	3.5	2.1	200×135	0.03
	C	6.2	1.6	372×273	0.3
	L	16.7	1.1	1312×951	0.05
2002 Apr 12,13	K	1.3	2.0	91×59	0.18
	U ^a	2.0	2.0	130×98	0.39
	X	3.5	2.1	224×154	0.03
	C ^b	6.2	1.6	406×295	0.3
	L	16.7	0.9	1397×1146	0.07
2001 Jan 02	K	1.3	6.0	78×42	0.08
2000 Dec 23	Q	0.7	6.0	44×20	0.18
1998 Mar 29,30	Q ^c	0.7	5.3	39×36	0.38
	K ^c	1.3	6.3	114×89	0.25

^a Spurious source seen at phase center of image.

^b The star was not detected in this data set.

^c No Pie Town link was used in this data.

approximately 52 km west of the center of the VLA, effectively doubling its resolution while in A configuration when connected. It is worth noting that the Pie Town link was only functional when the VLA was in A configuration. The extra

3.7 VLA-Pie Town Observations of Betelgeuse

collecting area together with 27 additional baselines also increases the sensitivity of the array. The Pie Town antenna generates IF signals in VLBA format and these are converted, at Pie Town, to a 50 MHz wide VLA signal where they are multiplexed and then modulated onto a single laser before being sent over 104 km of fiber to the VLA. When the signal arrives at the VLA site it is received and converted back into an RF signal. The received RF signal is then amplified and filtered before its is sent on to the backend receiver.

4

Radio Interferometric Data Analysis

The complex visibilities outputted from the correlator of a radio interferometer are far from ideal and many additional steps of processing are required before they can be of scientific use. The imperfection of the synthesis radio telescopes (e.g., surface accuracy, receiver noise, gain stability, etc.), the adjustments to the signal (e.g., filter bandpass, etc.), hardware or software failures, poor atmospheric conditions, and the presence of RFI are some of the many sources of visibility corruption that must be accounted for before they can be Fourier transformed to get the sky brightness distribution. The chapter describes the three main steps involved in reducing any standard radio interferometric data set, namely: data examination and flagging, data calibration, and imaging. In each step we give relevant examples of the data reduction techniques used in O’Gorman *et al.* (2012) and O’Gorman *et al.* (2013). A general work flow chart is given in Figure 4.1 which highlights the standard procedure required to go from raw visibilities to image analysis and summarizes what will be discussed in this chapter.

4.1 Data Examination and Flagging

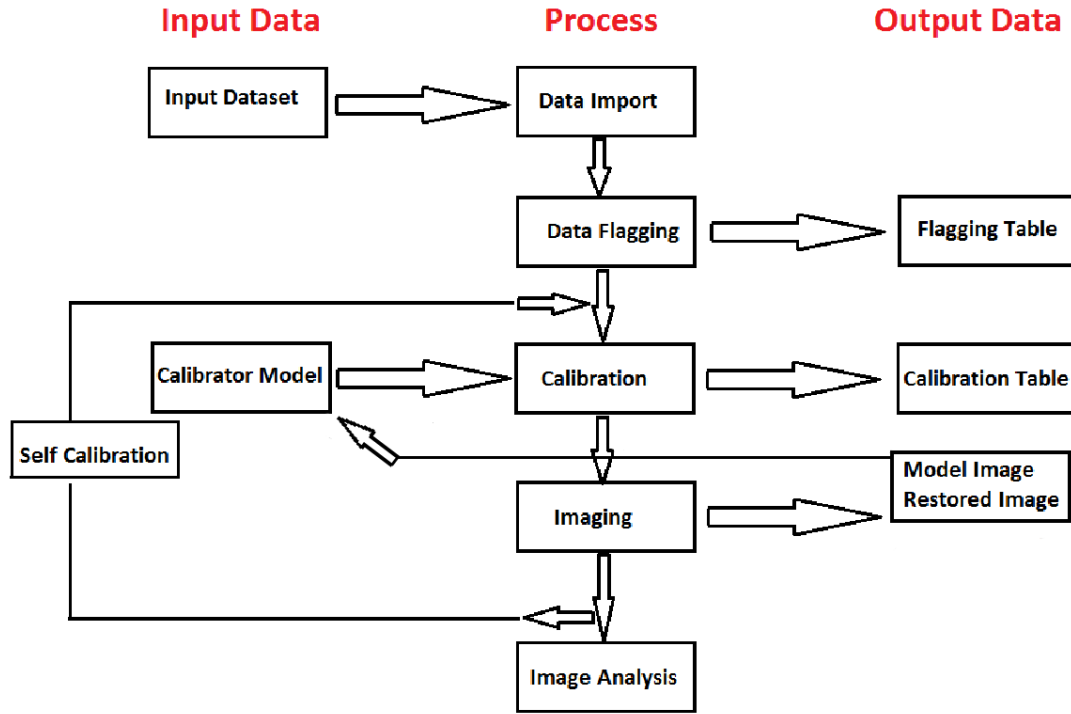


Figure 4.1: Work flow chart highlighting the general procedure required to go from the raw visibilities outputted by the correlator to a final radio image that can be used for scientific analysis. (Image adapted from the CASA cookbook, NRAO)

4.1 Data Examination and Flagging

The Common Astronomy Software Application (CASA; McMullin *et al.*, 2007) package was used to flag, calibrate, and image the main data sets used in this thesis. CASA is operated through a Python interface and uses a suite of astronomical data reduction tools which have been developed to meet the processing requirements of the large data sets from the Karl G. Jansky VLA and ALMA. It can also be used to process data from practically all other modern radio synthesis arrays. For synthesis data to be processed in CASA, it must be in a “measurement set” format. VLA data is easily transferable into this format using the *importevla* task within CASA. CARMA data files however come in *Miriad* format and need to be first converted into Flexible Image Transport System (FITS)

4.1 Data Examination and Flagging

format within the Miriad (Sault *et al.*, 1995) data reduction package. During this process the raw data are smoothed by a Hanning filter (combining adjacent frequency channels with weights 0.25, 0.5, and 0.25) to dampen ringing in the bandpass. Once in FITS format, the data can then be imported into CASA using the *importuvfits* task.

Once the data has successfully been imported into CASA the *listobs* task can be used to get a summary of the data set, allowing the user to make sure the observing track contains the requested sources observed at the correct times. At this point it is also a good idea to check any observing logs which are created on site during the observation by the array operators. These logs contain important information about specific tracks such as non-operational antennas or unavailable receivers, and such data will either need to be treated appropriately during calibration or flagged at this stage. The *plotms* task, which is a GUI-style plotter, can then be used to obtain X-Y plots of the visibility data. A good visual overview of the observation track is obtained by plotting all the source visibility amplitudes as a function of time. Averaging the data over channels or baselines often alerts the user to obvious bad data, which can be manually flagged through the *plotms* interface or through the *flagdata* task. An example of such a plot is shown in Figure 4.2 where the visibility amplitudes of three sources in a 1.3 cm VLA observing track for Aldebaran are displayed against time. The relatively weak target is shown between interleaving scans of the stronger phase calibrator, while the flux calibrator is the scan at the end of the observing track and is the strongest source in this observation. The data can be averaged over channels or baselines to speed up the plotting process. Some relatively low visibility amplitudes can clearly be seen for all scans of the phase calibrator, which can be traced to a single poor performing antenna.

Another important way to represent the data at this stage of the flagging process is to plot the visibility amplitude of each of the sources as a function of $u-v$ distance or baseline length (i.e., $\sqrt{u^2 + v^2}$). The amplitude distribution should be relatively constant as a function of $u-v$ distance for the phase calibrator (i.e., a point source) and will fall off with increasing baseline length if the flux calibrator is resolved. Plotting the data in this format often results in extreme points at certain baselines which can then often be traced back to poorly behaving antennas

4.1 Data Examination and Flagging

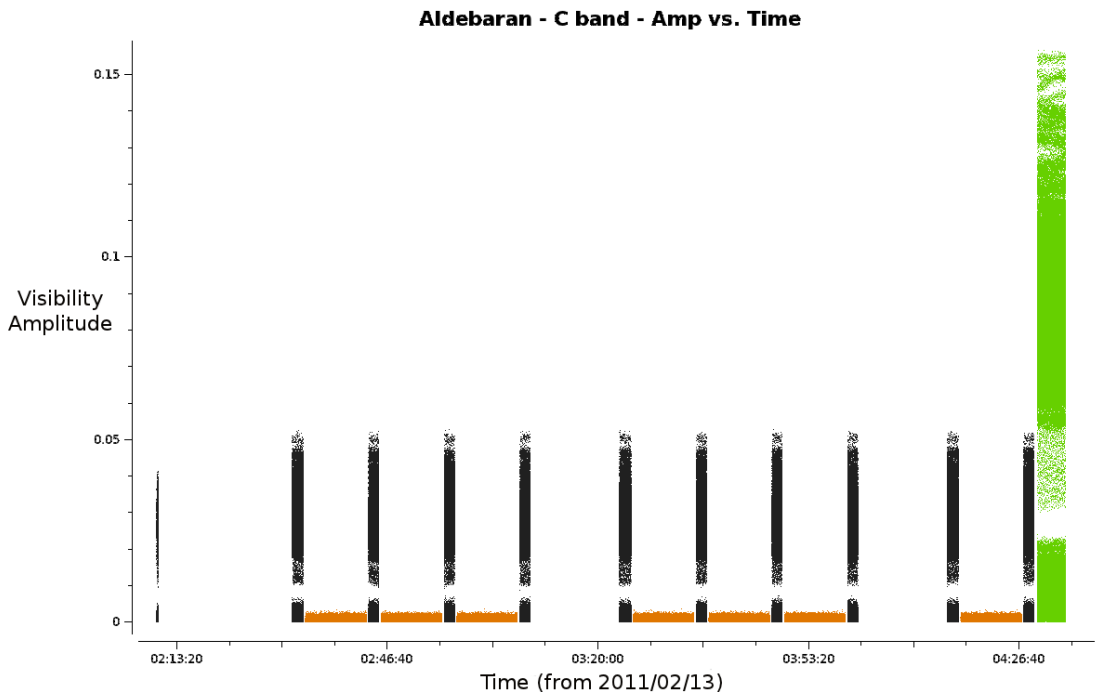


Figure 4.2: Data examination of a 6 cm VLA data set for Aldebaran. A good visual overview of the observation track is obtained by plotting all the source visibility amplitudes as a function of time. Averaging the data over channels or baselines sometimes allow rogue data to stand out. Here the black, orange, and green data points represent the phase calibrator, the science source, and the flux calibrator, respectively. The left most black data points are part of the dummy scan which was subsequently flagged. The low data points of the phase calibrator are data which needs further investigation. The absence of data at certain times represent observations at 3 cm.

or corrupt baselines. There is also some flagging which can be carried out based in part on a priori information. Antennas in very compact configurations can partially block the incoming RF signal to other antennas, which is often referred to as antenna shadowing. This was not a problem in our VLA B configuration observations but some data obtained in the more compact CARMA configurations had to be flagged as a result of this shadowing. At the time when our VLA observations took place, every observing track (i.e., scheduling block) needed to commence with at least a one minute *dummy scan* to facilitate the correlator setup. We subsequently flagged these scans as they contained no useful scientific

data. Other a priori flagging was to remove any visibilities with zero amplitudes and to flag the edge channels in the CARMA data sets. Finally, visual inspection of each scan was carried out to determine if data at the beginning or end of these scans needed to be flagged. This process is often referred to as quacking in radio interferometry analysis.

No RFI was present in any of the CARMA data sets and in any of the VLA data sets at wavelengths $\lesssim 3\text{ cm}$ (i.e., X, K, Ka, and Q bands). For the 2011 long wavelength ($> 3\text{ cm}$) data, the two sub-bands were centered at relatively RFI free regions of the bandpass and only a very small amount of RFI had to be manually flagged. The 2012 wide-band data were taken at 10 and 20 cm (i.e., S and L band) and many of the sub-bands were severely contaminated with RFI, especially at 20 cm. In Figure 4.3 we plot the visibility amplitude of the flux calibrator 3C286 against frequency for the 2012 wide-band data set at 20 cm. The upper panel shows the raw data before any RFI had been removed. Some of the sub-bands were badly contaminated with RFI ($> 90\%$) and had to be completely flagged. The remaining sub-bands were initially Hanning smoothed to suppress Gibbs ringing. This action spreads the single-channel RFI into three channels, but importantly removes the effects of some of the worst RFI from a number of channels and allows as much good data to be retained as possible. The *testautoflag* task was then used to conservatively flag RFI from all sources and any remaining RFI was manually flagged. The final result for the flux calibrator is shown in the bottom panel of Figure 4.3 with only some residual RFI still remaining, particularly between 1 and 1.2 GHz.

4.2 Calibration

The role of calibration is to correct the measured visibilities $V'(u, v)$ to approximate as closely as possible the true visibilities $V(u, v)$. As discussed in Chapter 2, the true visibilities are related to the sky brightness via the Fourier transform:

$$V_{ij}[u_{ij}(t), v_{ij}(t)] = \int A(l, m) I(l, m) \exp[-i2\pi(u_{ij}(t)l + v_{ij}(t)m)] dl dm \quad (4.1)$$

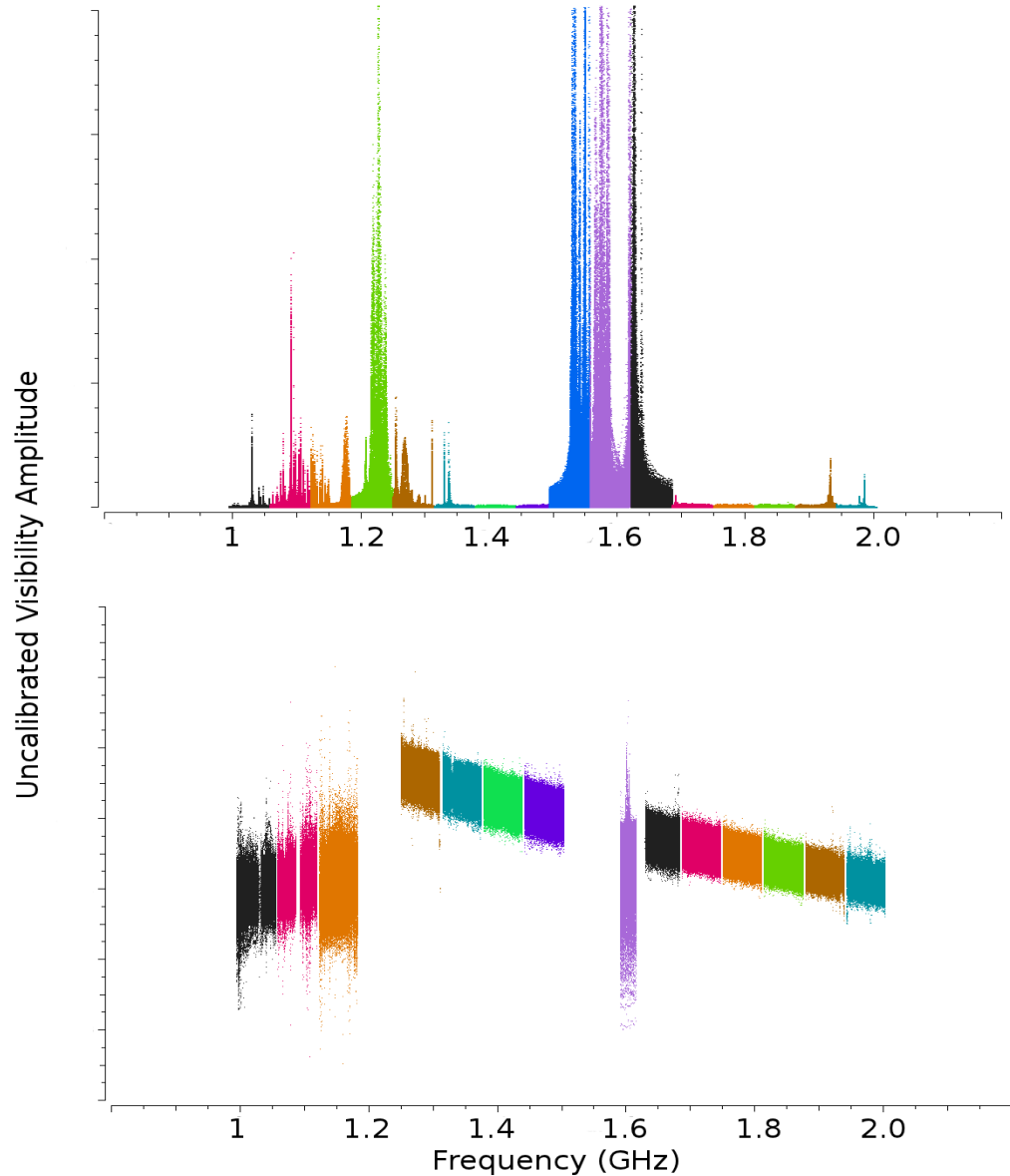


Figure 4.3: Eliminating RFI from the 20 cm wide-band data set. *Top panel:* Raw visibility amplitudes showing the presence of high levels of RFI in many sub-bands. *Bottom panel:* Post flagging visibility amplitudes. Some of the sub-bands were so severely contaminated with RFI that they had to be completely flagged. The data is still uncalibrated at this stage and the gain as a function of frequency is clearly present.

4.2 Calibration

where i, j represent the discrete sampling of the antennas i and j , at time t . The term $u_{ij}(t)l + v_{ij}(t)m$ is the geometric phase difference produced by the geometric path length difference between antenna i and antenna j from the source (or part of) at location (l, m) relative to the phase center. The relationship between the measured visibility and the true visibility on a baseline between antennas i and j may be expressed as

$$V'_{ij} = J_{ij} V_{ij} \quad (4.2)$$

where J_{ij} represents the accumulation of all corruptions affecting baseline ij . This equation is known as the Hamaker-Bregman-Sault Measurement Equation (Hamaker *et al.*, 1996). The most important of the effects contained in J_{ij} are antenna-based and arise from the measurable physical properties of individual antenna elements or the measurable physical conditions in the atmosphere above them. Thus, an array of N antennas forming $N(N - 1)/2$ baselines can usually be adequately calibrated through the determination of only N factors.

For the purpose of the work presented in this thesis, the Measurement Equation can be written as

$$V'_{ij}(u, v, \nu) = b_{ij}(t)[B_i(\nu, t)B_j^*(\nu, t)]g_i(t)g_j(t)V_{ij}(u, v, \nu)e^{i[\theta_i(t) - \theta_j(t)]} \quad (4.3)$$

where

- g_i and θ_i are the amplitude and phase portions of the complex gain. These are usually determined separately in the calibration process and may change over the observation period due to factors such as temperature, atmospheric conditions, etc.
- B_i is the complex bandpass, the instrumental response as a function of frequency, ν , and may also vary over time.
- $b_{ij}(t)$ is the baseline term and is important shortly after a configuration change when antenna positions may not be well known.

The general calibration strategy is then to derive a series of scaling factors from both the phase and flux calibrators, which are then collectively applied to the

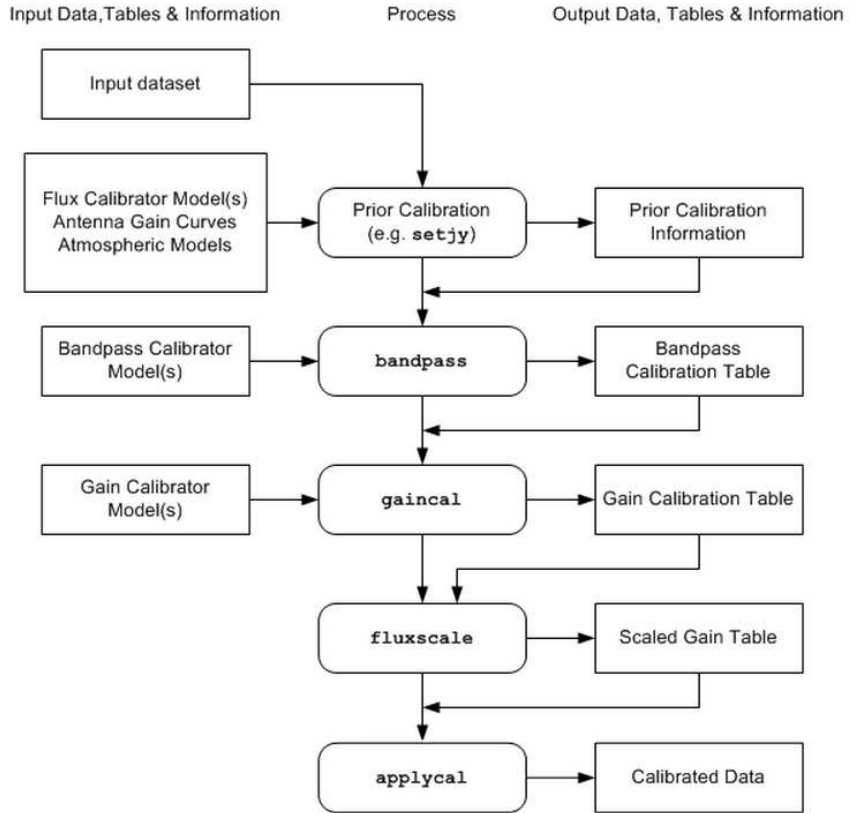


Figure 4.4: A workflow diagram outlining the main steps involved in calibrating radio interferometric data. Each of these steps are discussed in the text in relation to our CARMA and VLA observations (CASA cookbook, NRAO).

science target in the final stage of calibration. A general workflow diagram describing the main steps involved in calibration process are summarized in Figure 4.4. We now discuss each of these steps while placing emphases on our CARMA and VLA data.

4.2.1 Prior Calibration

Our 2011 VLA data were acquired just after an array re-configuration, which meant that the positions of some of the antennas were not accurately known at the time of observations. This resulted in some data points having inaccurate $u - v$ coordinates. During the course of observations in each configuration, the

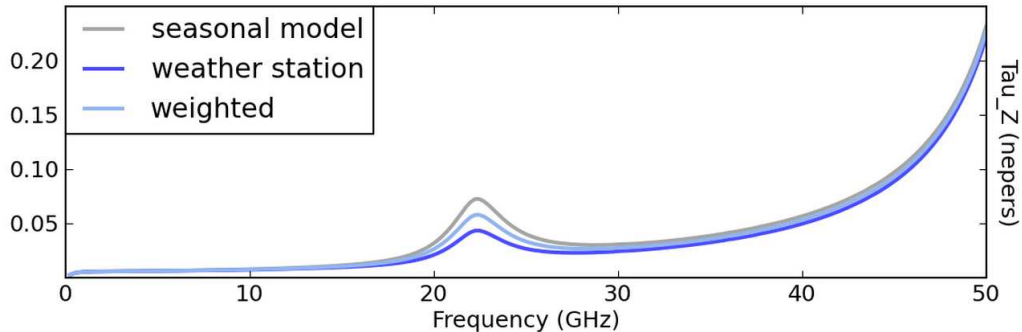


Figure 4.5: Calculation of the atmospheric opacity at the VLA site between 1 – 50 GHz on 2011 February 11. The adjustment values applied to the data were based on the average of a seasonal model and information from the weather station obtained during the observations.

exact position of all antennas become known and so the $u - v$ data could be calibrated to account for the discrepancies in the $u - v$ coordinates. At the VLA site, atmospheric opacities become significant at frequencies $\gtrsim 20$ GHz as shown in Figure 4.5 and so opacity corrections were applied to the high frequency data sets. The adjustment values were based on the average of a seasonal model (based on many years of measurements) and information from the weather station obtained during the observations. For the CARMA data, the opacity at 1.3 mm is measured by a tipper (White, 2009). The tipper reflects radiation from the blank sky at different inclinations onto a radiometer. The voltage from the radiometer can then be plotted against inclination to allow the opacity to be calculated.

The final a priori calibration step is to provide a flux density value to the flux calibrator via CASA’s *setjy* task. The VLA flux calibrators were assigned values using the “Perley-Butler 2010” flux density standard models and with assumed systematic uncertainties of 3% at all frequencies (Perley & Butler, 2013). At the time, no Ka or S band flux density standard models were available so instead for these we used the K and L band models, respectively, which were scaled according to their spectral indices. The absolute flux scale for CARMA observations is often determined by observing a planet and using a model of its flux as a function of baseline length. However, no such models were available in the earlier versions

of CASA which we used at the time and so the flux calibration was carried out with the quasars, 0530+135 and 3C120. The continuously updated CARMA flux catalog was accessed via the *xplore* GUI to obtain their flux values at each observation. The flux of these objects are more unpredictable and the systematic uncertainties are about 20%.

4.2.2 Bandpass Calibration

The bandpass is the relative gain as a function of frequency and solving for it is the first part of the calibration process. Variation in frequency arises from frequency dependent effects in signal transmission. Such variation is shown in Figure 4.6 for both phase and amplitude for a single antenna. For the VLA data, the flux calibrators were also used as the bandpass calibrators. Their phases were found to vary significantly over the 5 – 10 minutes of observation especially at high frequencies; in most cases by a few 10s of degrees. Before a solution to the bandpass could be found, these phase variations needed to be corrected, to prevent decorrelation of the vector averaged bandpass solution. The complex bandpass, B_i , could then be solved using the *bandpass* task and applying the antenna positions and phase solutions. The bandpass solutions were then applied to the bandpass calibrator to check that both the amplitude and phase were then almost constant across channels/frequency.

The CARMA data contained three spectral windows (i.e., 468, 62, and 31 MHz in width), each having independent bandpass shapes in both amplitude and phase. In theory, one could calculate the bandpass of each spectral window individually by observing a bright astronomical source. However, for narrow spectral windows this would be too costly in observing time in order to reach a sufficient S/N. Thankfully, for each of these spectral windows, the gain calibrations are typically the same after the full bandpass dependence has been removed. The strategy to calibrate the CARMA data was to initially carry out the bandpass calibration on the wideband data (i.e., 468 MHz) using the same strategy outlined in the previous paragraph, and then carry out the gain calibration on this wideband data. Once this had been done, these bandpass independent gain solutions were applied to the narrow band data (i.e., 62, and 31 MHz) while solving for their

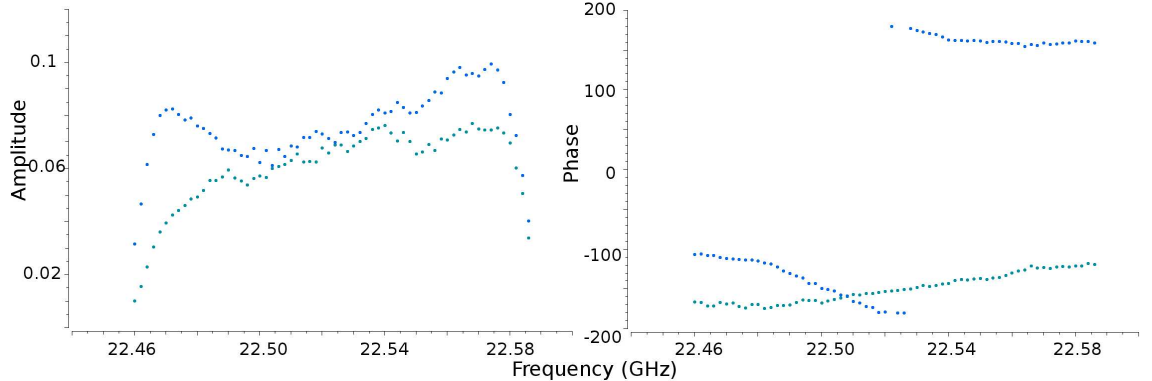


Figure 4.6: One antenna’s gain variation as a function of frequency for the flux calibrator 3C138 at 1.3 cm. Bandpass calibration corrects for this variation.

bandpass. This narrow band bandpass solution could then be applied to the target and phase calibrator.

4.2.3 Gain Calibration

Once a bandpass solution has been applied, the next step is to derive corrections for the antenna amplitude and phase gains, g_i and θ_i , as a function of time. The amplitude changes on a much longer timescale than the phase and so they are solved separately. The general procedure then is to solve for these antenna-based gain factors for each scan on all calibrators. In order to determine the appropriate antenna-based complex gains for the science target, a phase calibrator which is always a point source and located much closer to the target than the flux calibrator, is regularly observed to minimize differences through the atmosphere. If there is a substantial change in phase over a scan, and the uncorrected phases were averaged over this timescale, then the amplitude would be decorrelated. It is therefore important to correctly determine appropriate scan lengths when preparing the observations, especially at high frequencies, where time-dependent gain errors are introduced by the troposphere.

During gain calibration, the relative gain amplitudes and phases for different antennas are determined using the phase calibrator. The *gaincal* task is used to do this. The absolute flux density scale of the phase calibrator is later determined by

comparison against the gain amplitudes g_i derived for the flux calibrator. To find the relative phases, a zero phase is determined by selecting a reference antenna for which the phase is defined to be zero. In the first step new solutions of complex gains g_i and θ_i are derived for the flux density calibrator which are corrected for the bandpass shape (here we assume the flux density calibrator has been used as the bandpass calibrator as was the case for our observations). The second and final step requires the determination of the appropriate complex gains from the phase calibrator.

4.2.4 Flux Scale Calibration and Application of Solutions

The penultimate stage of the calibration process is to use the known flux density of our flux calibrator (whose flux density was set using *setjy*) to derive the flux density of the phase calibrator, which was previously assumed to be a point source of 1 Jy located at the phase center. This is achieved using the *fluxscale* task. The final step of the calibration process is to apply the calibration solutions to all the targets, using the task *applycal*. During this process, the calibration solutions are applied to the DATA column in the measurement set, and the results are written in the CORRECTED_DATA column of the measurement set. For the calibrators, the phase and amplitude calibration solutions come from their own solutions and the bandpass solutions come from the bandpass calibrator. For the science target we again apply the bandpass solution of the bandpass calibrator but the gain solutions come from the nearby phase calibrator.

Once calibration of the data is complete, it is worth spending time inspecting the corrected data to make sure there are no obvious errors in the data. If such errors are indeed found at this stage, then their cause will need to be flagged and the data must be re-calibrated. Some insightful plots to investigate how successful the calibration was, are: amplitude vs. time, amplitude vs. $u - v$ distance, and amplitude vs. phase. If a point source has being successfully calibrated then it will have an appearance similar to that in Figure 4.7, i.e., a compact ball of visibilities centered at zero phase and at the amplitude found for that source. Once the data has been successfully calibrated, the science data is split off into a separate measurement set using the *split* task. The calibrated visibilities can

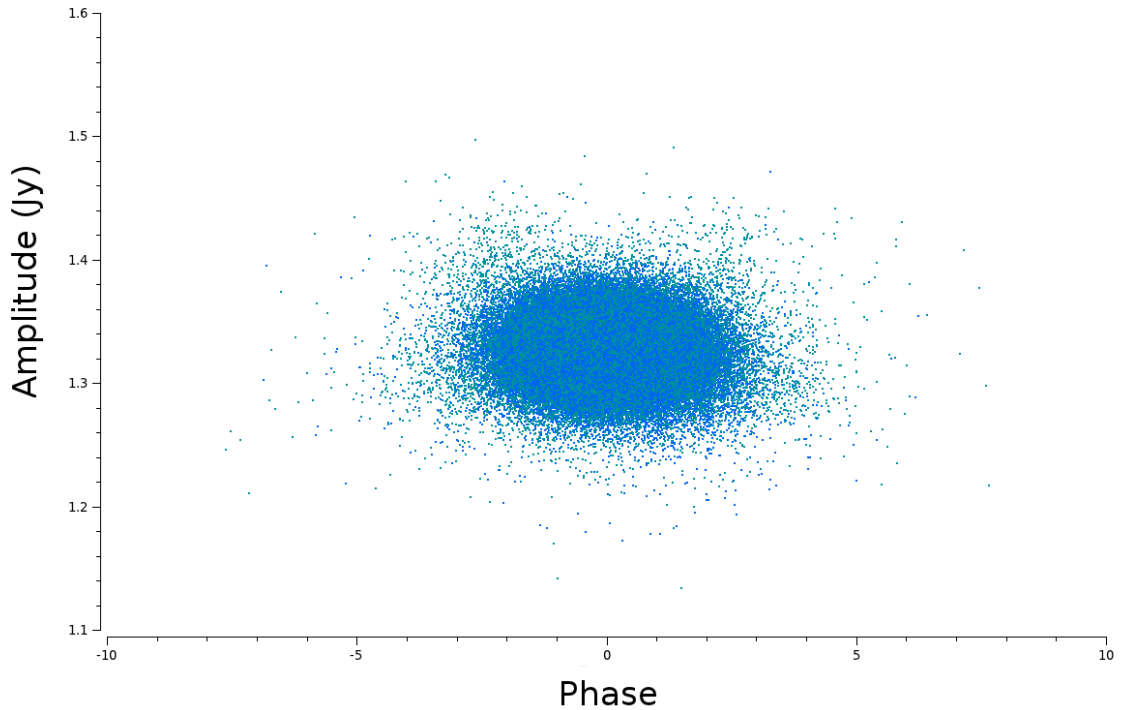


Figure 4.7: A well calibrated source will produce a compact ball of visibilities centered at zero phase and at the amplitude found for that source. Here we plot the calibrated visibilities at 3 cm for J0449+1121; the phase calibrator in the 3 cm data set for Aldebaran.

then be either directly analyzed by fitting simple models (e.g., point sources, disks, etc.,) to them or, as is more common, Fourier transformed and CLEANed to create an image of the source.

4.3 Imaging

We have shown in Chapter 2 that the visibility as a function of baseline coordinates (u, v) is the Fourier transform of the sky brightness distribution as a function of the sky coordinates (l, m) , i.e.,

$$I(l, m) = \int \int V(u, v) e^{2\pi i(ul+vm)} du dv. \quad (4.4)$$

Taking the inverse Fourier transform of the calibrated visibilities results in a dirty image which can then be deconvolved to produce a good estimate of the true sky brightness distribution. CASA has a single task called *clean* which carries out both of these operations on the data. In the following two sections we describe how both the VLA and the CARMA visibility data sets were imaged using this task.

4.3.1 Imaging the VLA Data

The calibrated visibilities were both inverse Fourier transformed and deconvolved using the CASA *clean* task in multi-frequency synthesis imaging mode. This imaging mode separately grids the multiple spectral channels onto the $u-v$ plane and therefore improves the overall $u-v$ coverage. As all science targets were expected to be point sources at all wavelengths, resolution was not paramount and so we used natural weighting for maximum sensitivity. The cell size was chosen so that the synthesized beam was about five pixels across. The FOV of the VLA at short wavelengths is small (see Table 3.6) and at these wavelengths there are less serendipitous background objects. This meant that the science targets were the only objects within a few primary beams of the phase center and so it was sufficient to place just one CLEAN circle around the target source. The general procedure was to first use *clean* to create a dirty image (i.e., by setting $niter = 0$) allowing the root mean square noise of this dirty image, σ_{rms} , to be determined. The final CLEAN image was then created by setting $niter$ to a very large number and setting the CLEANing threshold to be $\sim 3\sigma_{rms}$. Setting $niter$ to a very large number ensures that this CLEANing threshold is reached.

At long VLA wavelengths the primary beam becomes larger and the background sky sources become brighter. The new wide bandwidth capabilities of the VLA means that it is quite sensitive to emission far from phase center. For example, at ~ 20 cm (L band), the HPBW of the primary beam is $\sim 30'$ and yet the primary beam gain is as much as 10% around 1° away. In Figure 4.8 we show a wide field view of our VLA 20 cm image clearly showing many serendipitous sources out to and beyond the HPBW of the primary beam, all of which needed to

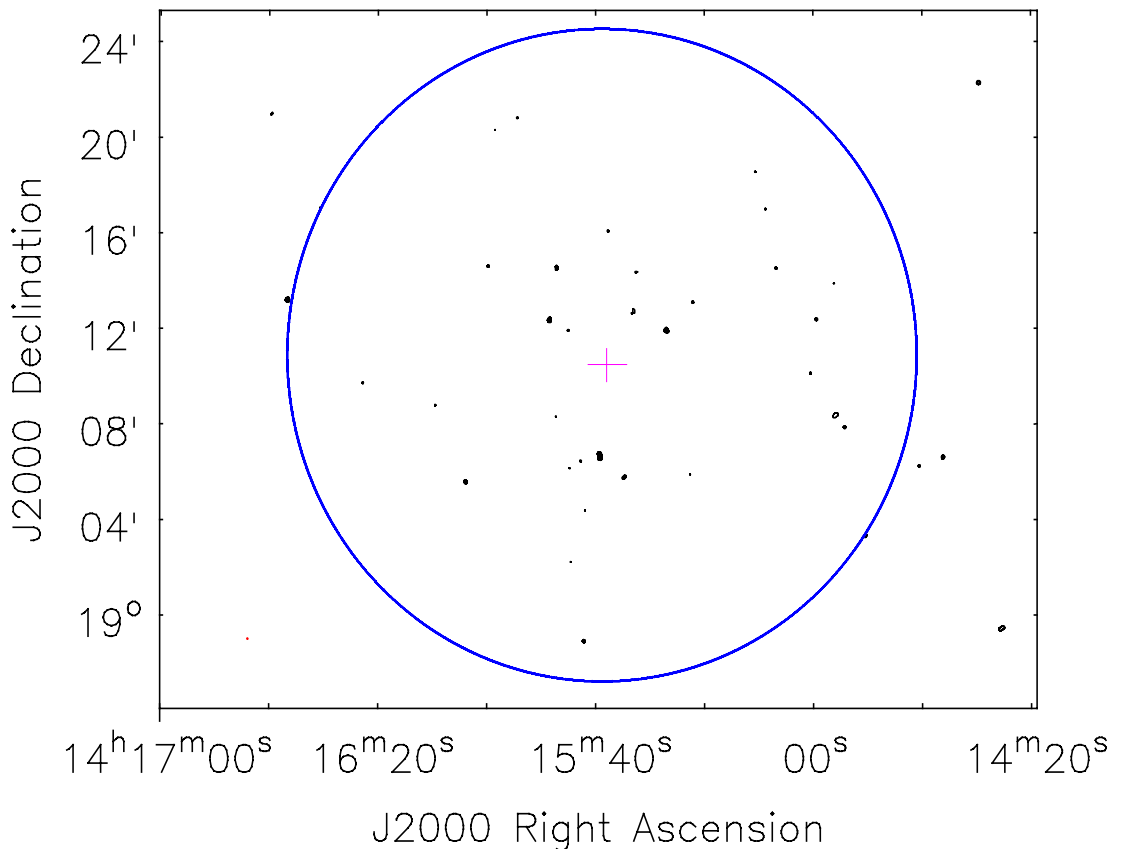


Figure 4.8: Wide field view of the VLA 20 cm CLEANed image showing the many serendipitous background sources close to Arcturus (pink cross). Many of these sources were a few orders of magnitude brighter than Arcturus at 20 cm. CLEAN circles were placed around all these sources during interactive CLEANing. The blue circle marks the FOV (i.e., the HPBW of the primary beam) of the VLA at 20 cm while the pink cross in the center marks the position of Arcturus. The contour levels are set at $(0.005, 0.01, 0.05, 0.1, 0.2, 0.4, 0.6, 0.8) \times 80.3 \text{ mJy}$, where 80.3 mJy is the flux of the brightest source in the image.

be individually CLEANed to reduce their sidelobe contamination of the final image. For this reason the image sizes were usually set to a few times the size of the primary beam (if not too computationally expensive) so that any nearby strong serendipitous sources could be CLEANed. These images were again CLEANed interactively while taking sky curvature into account. CLEANing was carried out interactively with CLEAN circles first placed around the strongest sources in the image and then placing them around weaker sources as they appeared in the residual image.

4.3.2 Imaging the CARMA Data

The CO emission around Betelgeuse is extended and has many different spatial scales. Traditional deconvolution techniques such as the CLEAN and MEM algorithms are scale-free and have no concept of source size. Both algorithms treat each pixel as an independent degree of freedom. However, adjacent pixels in an image are not independent due to the limiting resolution set by the dirty beam and the intrinsic source size. For example a Gaussian source covering 50 pixels can be characterized by only 5 parameters, not 50. The CASA multi-scale algorithm uses “Multi-scale CLEAN” (Cornwell, 2008) which is a scale sensitive algorithm that employs fewer degrees of freedom to model plausible sky brightness distributions. Instead of deconvolving using just delta-functions (or pixels) as in other clean algorithms, Multi-scale CLEAN carries out the deconvolution using delta-functions and circular Gaussians of various scales. It has been shown to produce more realistic representations of the sky brightness distribution for extended complex emission than the traditional CLEAN algorithm does (Rich *et al.*, 2008).

Multi-Scale CLEAN is really just a modification of the classical CLEAN algorithm. It assumes that sources in the sky are actually extended structures of different scales (which can include point sources), unlike the traditional CLEAN algorithm which assumes the sky is empty apart from a limited number of point sources. The function used to define the shape of the different spatial scales (usually a truncated circular Gaussian) has a finite extent and becomes a delta-function in the limit of zero scale-size. The Multi-scale CLEANing process is then

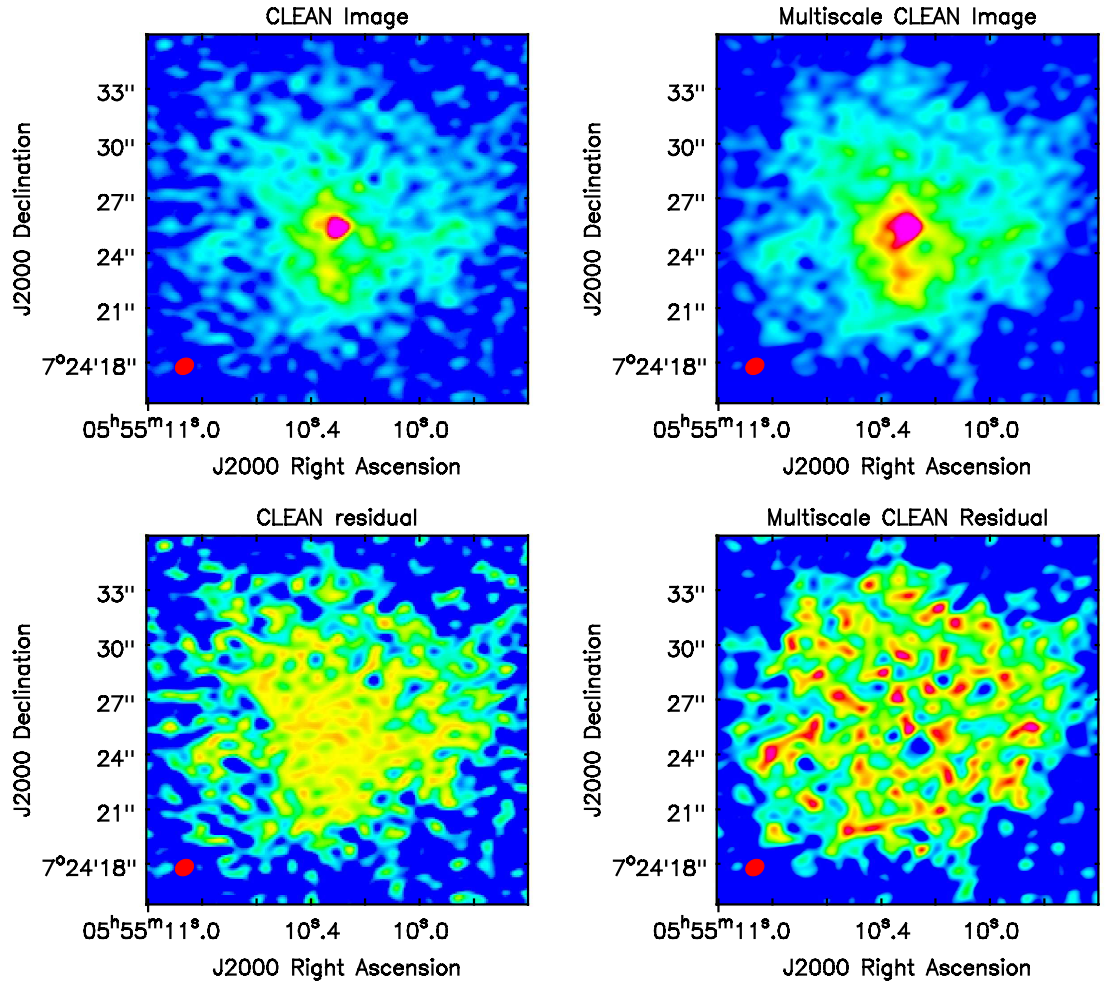


Figure 4.9: Comparing CLEAN to Multi-scale CLEAN using one of the combined configuration CARMA channel maps at -14.1 km s^{-1} . The top panel shows the final deconvolved images using CLEAN (left) and Multi-scale CLEAN (right) with the emission in both maps truncated between 0 and 0.2 Jy beam^{-1} to enhance weak emission. Multi-scale CLEAN is more successful at recovering large-scale structure. The bottom panel shows the residual images after using CLEAN (left) and Multi-scale CLEAN (right) where the emission in both images have been truncated between 0 and $0.06 \text{ Jy beam}^{-1}$. The emission appears more noise-like in the Multi-scale residual image while the CLEAN residual image contains some uncleaned flux.

as follows:

1. The dirty map is convolved with each scale size to create n convolved images, where n is the number of defined scale sizes.
2. The global scale among these images that contains the maximum total flux has its position, flux, and scale size recorded.
3. The pre-computed scale in which the peak was found, is convolved by the dirty beam, multiplied by some gain factor, and the subtracted from all the images made in the first step.
4. The subtracted component and its scale size is stored in a table.
5. Steps 1 – 4 are repeated until a flux threshold is reached in one of the residual images.

The new model is then convolved with a CLEAN beam and the residuals are added to it to get the restored image.

The combined CARMA configuration image cubes were Multi-scale CLEANed down to the $3\sigma_{\text{rms}}$ threshold. Natural weighting was applied to the $u - v$ data to optimize the sensitivity for the weak CO emission and the CLEAN region was set to be about the size of the HPBW of the primary beam. The Multi-scale algorithm within CASA was set to four unique scales; the largest corresponding to the largest structures visible in individual channel maps. Each scale was approximately set to three times smaller than the preceding scale and a zero-scale was included to account for point sources. In Figure 4.9 we plot one channel from the final restored image cube and compare this to the same channel from an image cube that was deconvolved using the traditional CLEAN algorithm. It can clearly be seen that Multi-scale CLEAN produces more extended emission around the star. This is because Multi-scale CLEAN removes large-scale structure before finer details while the CLEAN algorithm cannot distinguish noise peaks from faint real signals (Rich *et al.*, 2008). We also include the resultant residual images from both algorithms in the bottom panel of Figure 4.9. The CLEAN residual image still contains some uncleaned flux while the emission appears more noise-like in the Multi-scale residual image.

5

Multi-wavelength Radio Emission Study of Betelgeuse’s Extended Atmosphere

The results from our multi-wavelength high spatial resolution study of Betelgeuse’s extended atmosphere are presented in this chapter. The majority of the chapter is based on the work of O’Gorman *et al.* (2012) and presents the results of our sub-arcsecond resolution study into the distribution and kinematics of $^{12}\text{C}^{16}\text{O}$ around Betelgeuse using the $^{12}\text{C}^{16}\text{O}(J = 2 - 1)$ rotational line as the main probe. The variation of the emission line profile with different CARMA array configurations provides us with a unique insight into the distribution and kinematics of the two previously known flows, S1 and S2, around Betelgeuse. We successfully image the star on spatial scales as small as $0''.9$ ($\sim 40 R_\star$) over a $32''$ ($\sim 1500 R_\star$) field of view and we discuss these radio maps in detail. We then compare these results to higher CO¹ rotational lines obtained with other instruments. We also present the recent findings of Richards *et al.* (2013) who image two distinct chromospheric features at centimeter wavelengths. These surprising findings motivated us to re-analyze archival VLA-Pie Town data to search for

¹Throughout this thesis, the term CO refers to the molecular isotopologue $^{12}\text{C}^{16}\text{O}$.

5.1 CO molecules in the CSE of Betelgeuse

these features at shorter wavelengths with comparable resolution, the results of which are presented at the end of the chapter.

5.1 CO molecules in the CSE of Betelgeuse

The CSE of Betelgeuse (α Ori) is a proving ground for ideas and theories of mass-loss from oxygen-rich M-type supergiants. Currently it is losing mass at a respectable rate $\sim 2 \times 10^{-6} M_{\odot} \text{ yr}^{-1}$ (Harper *et al.*, 2001), as it has been over the past ~ 1000 years. Most of the optically thin silicate dust lies beyond $\sim 46 R_{\star}$ (Danchi *et al.*, 1994) and therefore dust is unlikely to be responsible for the bulk mass-loss. This raises the important point that if the mass-loss from Betelgeuse is not a result of dust then perhaps the same mechanisms that are responsible might also be active in the more dusty later M-type supergiants. Radiation pressure on atoms and molecules is another potential contributing candidate as a mass-loss mechanism and so spatial and dynamical studies of molecules are a fruitful line of investigation, especially in relation to eventual formation of dust. Such studies also allow us to calculate the time scales on which certain mass-loss episodes have occurred, and these can then be compared to the time scales of potential mass-loss initiators such as convection or magnetic dynamo cycles.

Despite the initial reports of an enhancement of C abundance in its atmosphere (Spinrad & Vardya, 1966), Betelgeuse is now known to be an oxygen-rich star. The comprehensive study of CO and OH ro-vibrational bands by Lambert *et al.* (1984) found $\log_{10} \epsilon(\text{C}) = 8.4$ and $\log_{10} \epsilon(\text{O}) = 8.8$. For any species X

$$\log_{10} \epsilon(\text{X}) = \log_{10} (\text{X}/\text{H}) + 12 \quad (5.1)$$

which can be used to show O/C = 2.5. Lambert *et al.* (1984) also found $\log_{10} \epsilon(\text{N}) = 8.6$ which indicates a contamination of the atmosphere with C-N processed material. This is in agreement with the theoretical work of Lamb *et al.* (1976) who predict the dredging up of processed material by the deep convective envelope which a supergiant like Betelgeuse is expected to possess. Betelgeuse is unlikely to have undergone a second dredge-up of material that would cause small changes in the CNO abundances due to its mass being greater than the upper mass limit for a second dredge-up to occur (see Chapter 1). This second dredge-up is predicted

5.1 CO molecules in the CSE of Betelgeuse

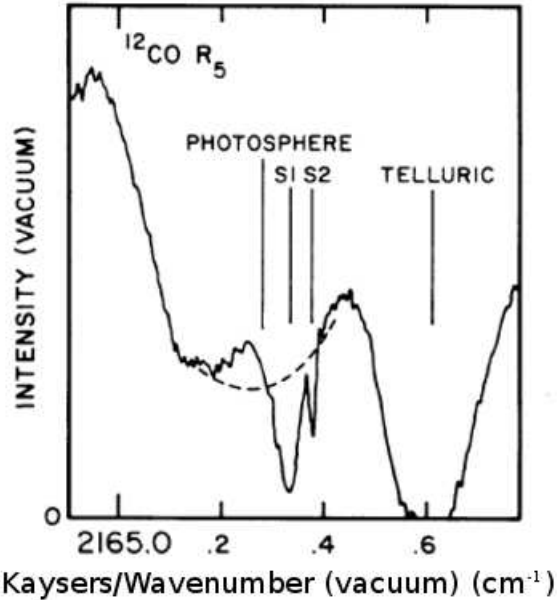


Figure 5.1: CO ro-vibrational fundamental line showing two sharp blueshifted absorption features originating from the expanding envelope (Bernat *et al.*, 1979). These two features became known as the S1 and S2 components of Betelgeuse’s outflow having outflow velocities of ~ 9 and $\sim 16 \text{ km s}^{-1}$, respectively. The units of the x-axis are in Kaysers, where $1 \text{ Kayser} = 1 \text{ cm}^{-1}$.

to occur after He core exhaustion for stars below $8 - 10 M_{\odot}$ (Kaler *et al.*, 1978). The observed $^{12}\text{C}/^{13}\text{C}$ ratio, which is an indication of the history of nuclear processing and mixing in the interior of stars (Eggleton *et al.*, 2007; Pavlenko *et al.*, 2003), has consistently found to be between 6 and 7 in both the photosphere and CSE (Bernat *et al.*, 1979; Harris & Lambert, 1984; Hinkle *et al.*, 1976; Lambert *et al.*, 1974). These values are well below the predicted value of 20 (Charbonnel, 1995; Pavlenko *et al.*, 2003), which is expected for most lower mass red giant stars (e.g., Boothroyd & Sackmann, 1999).

The study of CO molecules in the CSE of Betelgeuse began with the detection of $4.6 \mu\text{m}$ ro-vibrational absorption lines of $^{12}\text{C}^{16}\text{O}$ and $^{13}\text{C}^{16}\text{O}$ by Bernat *et al.* (1979) who identified two absorption features shown in Figure 5.1, implying two distinct components within the overall outflow. One component, known as S1, has a Doppler shift of 9 km s^{-1} towards us with $T_{\text{exc}} \simeq 200_{-10}^{+50} \text{ K}$, $v_{\text{turb}} \simeq 4 \text{ km s}^{-1}$,

5.2 Adopted Radial Velocity

and $N_{CO} = 4.7 \times 10^{17} \text{ cm}^{-2}$. The second faster component, known as S2, has a Doppler shift of 16 km s^{-1} towards us with $T_{\text{exc}} \simeq 70 \pm 10 \text{ K}$, $v_{\text{turb}} \simeq 1 \text{ km s}^{-1}$, and $N_{CO} = 1.2 \times 10^{16} \text{ cm}^{-2}$. Bernat *et al.* (1979) noted that a simple assumption of the dust and gas being in thermal equilibrium would infer that the S1 and S2 components have a spatial extent of 4 and $55''$ respectively, using the dust model of Tsuji (1979). The S1 feature with its higher column density was well known from atomic absorption line studies (e.g., Weymann, 1962) and both features had been detected in high spectral resolution atomic Na and K absorption profiles (Goldberg *et al.*, 1975).

CO was first detected at radio wavelengths by Knapp *et al.* (1980) who presented a low S/N spectrum of the $J = 2 - 1$ rotational emission line at 230 GHz. They used a single dish antenna with a HPBW of $\sim 30''$ and detected one component expanding at 15 km s^{-1} . They assumed this component to be the S2 component detected by Bernat *et al.* (1979) and by assuming that they had resolved a flat top profile, predicted that its spatial extent did not exceed $10''$. The weaker CO($J = 1 - 0$) line was tentatively detected by Knapp & Morris (1985) with a 7 m dish which had a HPBW of $100''$. Huggins (1987) presented a higher S/N CO($J = 2 - 1$) profile that was obtained with a HPBW of $32''$ and is shown in Figure 5.2. By comparing the $(2 - 1)/(1 - 0)$ line intensities they found some evidence for an S2 radius of $\sim 16''$. However, a 30 m IRAM $J = 2 - 1$ line profile was later presented by Huggins *et al.* (1994) and as can be seen in Figure 5.2 looks remarkably similar, even though it was observed with a smaller $12''$ HPBW. The profile did not show the horned wing signature expected if it had been resolved as discussed in Chapter 1, apparently in conflict with the previous S2 radius estimate. These single dish line profiles also showed no obvious signature of the slower S1 shell and so questions remained about the spatial extent of these two distinct outflow components in the CSE of Betelgeuse. A sensitive high spatial resolution study of its atmosphere was needed to untangle this puzzling evidence.

5.2 Adopted Radial Velocity

Before we discuss the CO($J = 2 - 1$) spectra obtained from our multi-configuration CARMA observations, which are summarized in Chapter 3, we begin by explain-

5.2 Adopted Radial Velocity

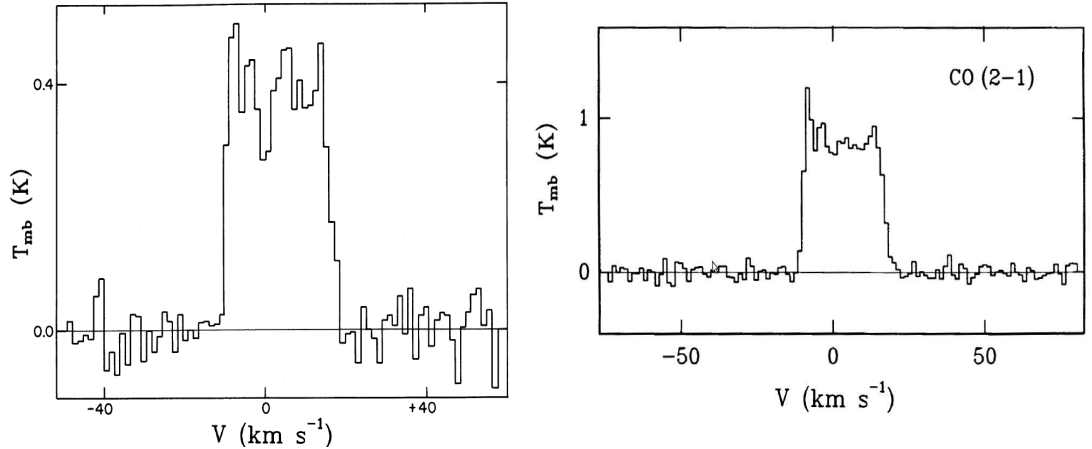


Figure 5.2: Previous single dish CO($J = 2 - 1$) rotational emission line profiles of Betelgeuse. *Left:* Huggins (1987) line profile using a HPBW of $32''$. *Right:* The line of Huggins *et al.* (1994) looks very similar even using a smaller HPBW in conflict with the findings of Huggins (1987). Velocities are plotted in the local standard of rest (LSR) frame.

ing which radial velocity value v_{rad} , for Betelgeuse was adopted. An accurate value of v_{rad} is necessary when plotting the spectra of any star with respect to its center of mass rest frame, as we do for all spectra in this chapter. Plotting spectra in this frame of reference is intuitive as it allows the reader to immediately see the gas expansion velocity relative to the photosphere. A positive v_{rad} denotes recession (i.e., redshifted lines) while a negative v_{rad} denotes advancement (i.e., blueshifted lines).

Betelgeuse is a semi-regular variable and its radial velocity exhibits variability on time scales ranging from short 1.5 year periods as suggested by Stebbins & Huffer (1931) to longer 5.8 year periods (Smith *et al.*, 1989; Spencer Jones, 1928). Stothers & Leung (1971) interpreted the long period as being the convective turnover time of giant convection cells on the stellar surface while Dupree *et al.* (1990) attribute the shorter period with pulsation. Betelgeuse's radial velocity amplitudes are also known to vary by at least $\pm 3 \text{ km s}^{-1}$ (Smith *et al.*, 1989) making it difficult to determine a precise value for the stellar center of mass radial velocity. In Figure 5.3 we plot the radial velocity data and the corresponding model derived by Sanford (1933) which is based on observations spanning 1923

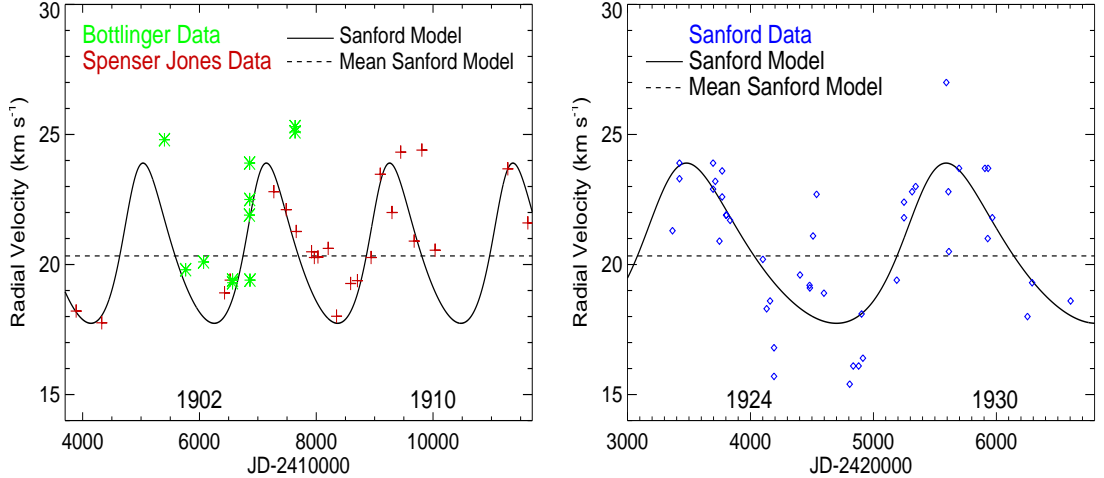


Figure 5.3: The radial velocity model of Sanford (1933) along with measurements from Bottlinger (1911), Spencer Jones (1928), and Sanford (1933) spanning the period 1897 – 1931. In this study we use $+20.7 \text{ km s}^{-1}$ which is the mean value from the models of Spencer Jones (1928) and Sanford (1933). The radial velocity amplitude variations of $\sim \pm 3 \text{ km s}^{-1}$ is clearly evident in these data.

to 1931. We have also extrapolated the model back to show that it matches the earlier data of Bottlinger (1911) and Spencer Jones (1928) quite well, as shown in Figure 5.3. Goldberg (1984) has also shown that the model of Sanford (1933) can be extrapolated forward to give a reasonable fit to his measurements. In this study we adopt a heliocentric radial velocity of $+20.7 \text{ km s}^{-1}$; a value used by Weymann (1962) and Harper *et al.* (2008) and is based on the mean values of Spencer Jones (1928) and Sanford (1933) radial velocity models.

5.3 CARMA CO($J = 2 - 1$) Spectra

The spectrum for each individual CARMA configuration image cube (which are composed of all the appropriate configuration tracks listed in Table 3.3) along with the multi-configuration image cube (which is composed of the entire data set spanning $\sim 2.5 \text{ yr}$) can be used to obtain information on the kinematics of the S1 and S2 flows. In particular, it is of interest to see how the CO($J = 2 - 1$) line profile changes, when observed with different array configurations, as each of these

5.3 CARMA CO($J = 2 - 1$) Spectra

will be sensitive to emission on different spatial scales. The spectra corresponding to the C, D, and E configuration image cubes are plotted in Figure 5.4 for both the high ($0.65 \text{ km s}^{-1} \text{ bin}^{-1}$) and low ($1.3 \text{ km s}^{-1} \text{ bin}^{-1}$) spectral resolution data and were obtained by integrating all emission within a circular area of radius $5''$ centered on the source. The high and low spectral resolution modes allow two independent sets of spectra to be measured for each observation and thus provide a good check on the data quality. The high resolution spectra (channel width = 0.65 km s^{-1}) give the best measure of the S1 and S2 flow kinematics and therefore all outflow velocities are derived from these spectra.

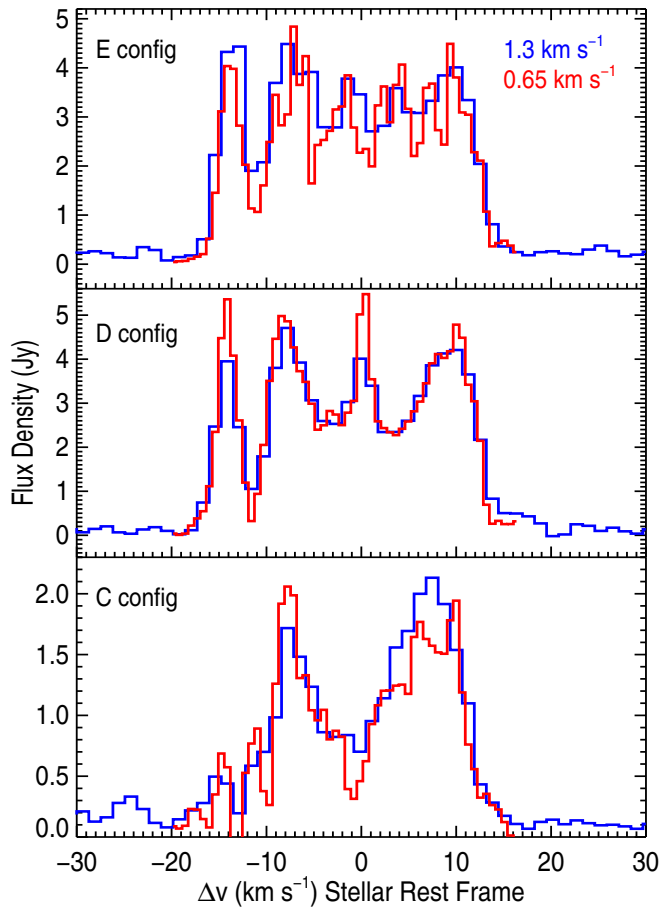


Figure 5.4: Spectra integrated over a radius of $5''$ for each array configuration image cube. The red and blue lines correspond to the high and low spectral resolution data respectively. The blueshifted emission component between -16.0 km s^{-1} and -10.0 km s^{-1} is almost resolved out in the C configuration image cube spectrum along with material with low absolute velocities.

5.3 CARMA CO($J = 2 - 1$) Spectra

The E configuration image cube spectrum has a total line width of 29.2 km s^{-1} and the low spectral resolution profile contains a steep blue wing emission feature between -16.0 km s^{-1} and -11 km s^{-1} and a more flat-topped feature between -10.3 km s^{-1} and $+13.2 \text{ km s}^{-1}$. This steep emission wing shows that the turbulence in the flow is less than or equal to the velocity bin size. The blue wing in the high resolution profile matches the lower resolution profile well but the remainder of the profile looks more complex than the flat-topped feature seen in the lower resolution profile. The line profile shape has been well documented by previous single dish observations (e.g., Figure 5.2) and, out of our three individual configuration spectra, we expect the most compact E configuration spectra to resemble these single dish measurements the closest due to its better sampling of the inner $u - v$ plane and consequent sensitivity to extended structures. This indeed turns out to be the case when we compare our three individual configuration spectra to those previous single dish profiles. The blue wing emission feature appears again in the D configuration spectrum at the same velocities as those in the E configuration spectrum but the remainder of the profile appears quite different. Between -10.3 km s^{-1} and $+13.2 \text{ km s}^{-1}$ the D configuration spectrum is dominated by a blue wing at $\sim -10.0 \text{ km s}^{-1}$, a red wing at $\sim +13.0 \text{ km s}^{-1}$ and an emission feature at $\sim 0 \text{ km s}^{-1}$. The large drop in emission at certain velocities in the D configuration spectrum is probably a result of the lower sensitivity to large scale structure in comparison to the E configuration as described in Table 3.2.

The line profile has a lower flux ($\sim 50\%$) in the high spatial resolution C configuration spectrum due to its lack of sensitivity to extended structure. Notably, the blueshifted emission feature located between -16.0 km s^{-1} and -11.0 km s^{-1} in the E and D configuration spectra is almost completely spatially filtered by the extended C configuration. This component of the line has previously been associated with the outer S2 flow (Huggins, 1987) and as the majority of it has been spatially filtered by our C configuration we expect even less contribution from the S2 flow at even lower absolute velocities. For the redshifted line emission we again expect the majority of the S2 contribution to be spatially filtered, so we conclude that most, if not all of the emission in the C configuration spectrum emanates from the inner S1 flow. The spectrum is double peaked with the blue and redshifted wings extending to $-9.0 \pm 0.7 \text{ km s}^{-1}$ and $+10.6 \pm 0.7 \text{ km s}^{-1}$.

5.3 CARMA CO($J = 2 - 1$) Spectra

respectively, and we define these as the outflow velocities of S1. As discussed in Chapter 3 the C configuration has a resolving out scale of $\sim 6''$ at 1.3 mm and so is not sensitive to angular scales larger than this. If the emission between -9.0 km s^{-1} and $+10.6 \text{ km s}^{-1}$ in the C configuration spectrum appeared as a flat topped profile then we could conclude that the S1 flow lies within a radius of $3''$ from the star. Clearly however, the profile has a more *horned* shaped appearance and so the lower absolute velocity components of this profile have been spatially filtered. We can therefore conclude that the radial extent of the S1 from the star is greater than $3''$. If we assume that the S1 flow would produce a 19.6 km s^{-1} wide top-hat line profile of 2 mJy were it not for the resolving out effects of the interferometer, its minimum integrated line flux is then

$$F_{\text{tot S1}} = F_\nu \times \left(\frac{\Delta v}{\lambda} \right) = 3.1 \times 10^{-19} \text{ W m}^{-2}. \quad (5.2)$$

To obtain the most robust value for the S2 outflow velocities we examine the high spectral resolution multi-configuration image cube spectrum which is composed of all tracks from all three configurations. It is worth stressing that by analyzing the multi-configuration image cube we make the assumption that the physical properties of all three components (i.e., α Ori, S1 and S2) have not changed over the total observation period (i.e., ~ 2.5 yr). The profile is found to have a total linewidth of $28.6 \pm 0.7 \text{ km s}^{-1}$, which is in good agreement with previous single dish observations of the line where values of $30.6 \pm 2.5 \text{ km s}^{-1}$ and 28.6 km s^{-1} were reported by Knapp *et al.* (1980) and Huggins (1987), respectively. The centroid velocity of the spectrum is $-1.1 \pm 0.7 \text{ km s}^{-1}$ ($v_{\text{lsr}} = 3.7 \pm 0.7 \text{ km s}^{-1}$) which again is in good agreement with Knapp *et al.* (1980) and Huggins (1987) values of $v_{\text{lsr}} = 3.0 \pm 2.5 \text{ km s}^{-1}$ and $v_{\text{lsr}} = 3.7 \pm 0.4 \text{ km s}^{-1}$, respectively. We use Equation 5.2 to find the integrated total line flux to be $1.5 \times 10^{-18} \text{ W m}^{-2}$, of which at least 20% emanates from the S1 flow.

The outflow velocities of S2 are $-15.4 \pm 0.7 \text{ km s}^{-1}$ and $+13.2 \pm 0.7 \text{ km s}^{-1}$ which, like the S1 flow, are slightly asymmetric but in the opposite sense. Note that the S1 and S2 outflow velocities are dependent on the adopted radial velocity of Betelgeuse. If for instance, we instead adopt a radial velocity of 21.9 km s^{-1} (Famaey *et al.*, 2005) then the S2 outflow velocities become even more

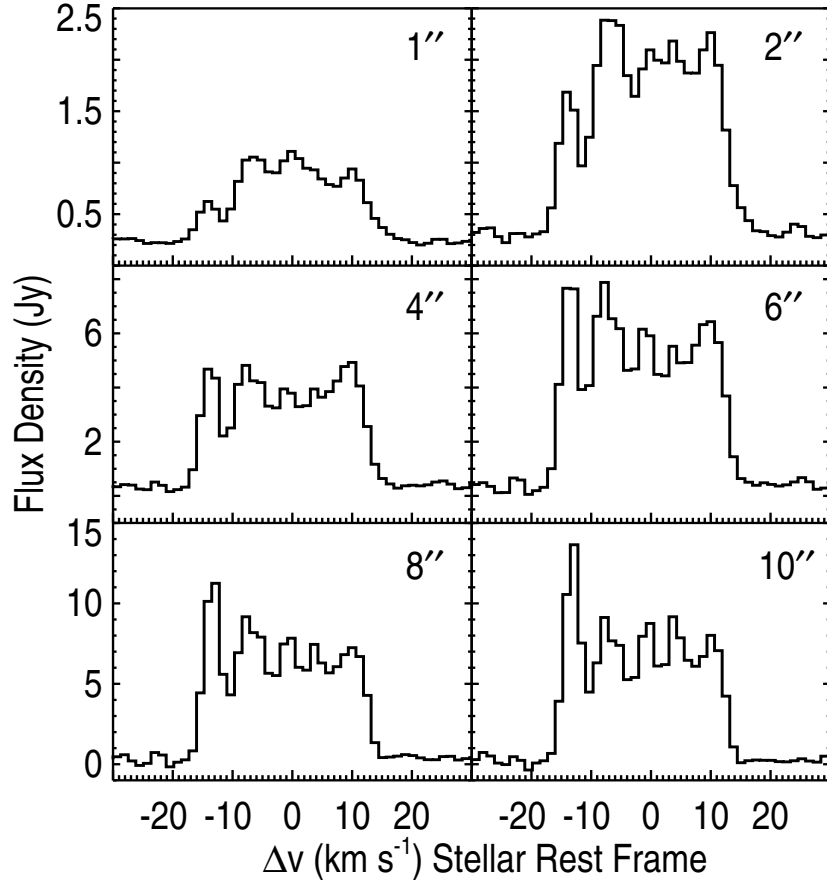


Figure 5.5: Spectral profiles of the low spectral resolution multi-configuration image cube for circular extraction areas of radius 1'', 2'', 4'', 6'', 8'', and 10''. The S/N of the line profile reduces at larger extraction areas as more noise is included from the outer more noisy regions of the channel maps.

asymmetric (-16.6 and +12.0 km s⁻¹) while the S1 outflow becomes less so (-10.2 and +9.4 km s⁻¹). Both S1 and S2 therefore cannot have spherically symmetric outflow velocities regardless of the adopted stellar radial velocity. Adopting a mass of $18 M_{\odot}$ (Meynet & Maeder, 2003) and a radius of $950 R_{\odot}$ (Harper *et al.*, 2008) then the escape velocity for Betelgeuse is 85 km s⁻¹ which is much greater than the S1 and S2 outflow velocities. This indicates that the majority of the stellar mass-loss mechanism's energy goes into lifting the CO molecules out of the gravitational potential and not into their outflow velocities. These outflow velocities are greater than the adiabatic hydrogen sound speed (i.e., $11.7\sqrt{10^{-4}T_e}$

5.4 Individual Configuration Image Cubes

km s^{-1}), which, if we assume that the gas temperature is the same as the excitation temperature, are 1.7 km s^{-1} and 1 km s^{-1} for S1 and S2 respectively.

The spectra in Figure 5.5 are taken from the low resolution multi-configuration image cube using circular extraction areas ranging in radius from $1''$ to $10''$ and demonstrates how the line profile changes over these different extraction areas. The most striking change in the line profile is the change in appearance of the extreme blue wing. At small extraction radii where we sample the most compact emission, the feature is weak in comparison to the rest of the line but becomes more dominant as we begin to sample more of the extended emission. This indicates that even the high absolute velocity components of the S2 flow have extended emission and this is why they are almost completely spatially filtered by CARMA’s C configuration. The large reduction of flux at -11 km s^{-1} suggests that there is more material moving towards the observer than at other lower absolute velocities, indicating a non-isotropic (or non-spherical) S2 flow. This suggests a more sheet like (flatter) structure rather than a spherical cap.

5.4 Individual Configuration Image Cubes

We created three image cubes for each configuration by concatenating all good tracks together per configuration. The gradual formation of a ring type structure as one goes from high absolute velocities to lower absolute velocities indicative of a shell was not seen in any of these three image cubes. An additional spatially unresolved source was clearly detected in a number of the D configuration image cube maps (both high and low spectral resolution). The component is present in five continuous channel maps between $\sim -4.0 \text{ km s}^{-1}$ and $+2.4 \text{ km s}^{-1}$ and is located $\sim 5''$ S-W of α Ori. Its peak emission lies at $\sim 0 \text{ km s}^{-1}$ and has a flux density of 1.8 mJy which is approximately 60% of the total source flux density at this velocity. The middle row in Figure 5.6 are two of these D configuration channel maps which clearly show this discrete source. The contour levels are set at the $4\sigma_{\text{rms}}$ level so the detection of the second source in the D configuration is significant. The corresponding channel maps in the E configuration image cube show extended emission out to $8''$ in the same S-W direction as can be seen in the lower panel of Figure 5.6. There is only weak emission detected in

5.4 Individual Configuration Image Cubes

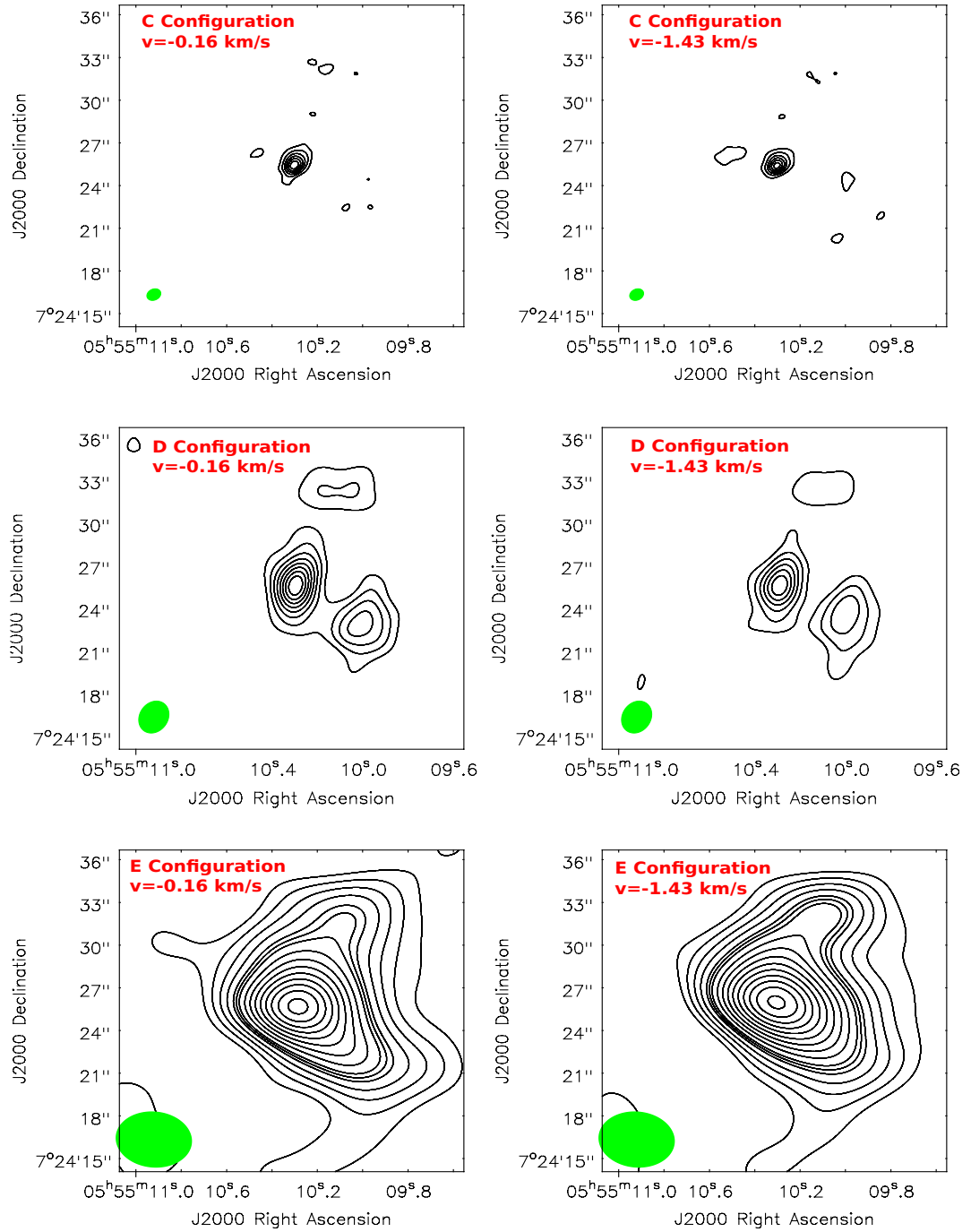


Figure 5.6: Two channel maps from each of the three individual configuration image cubes. A spatially unresolved source is present in five continuous channel maps between $\sim -4.0 \text{ km s}^{-1}$ and $+2.4 \text{ km s}^{-1}$ and is located $\sim 5''$ S-W of α Ori. Contour levels begin at $4\sigma_{\text{rms}}$ where $1\sigma_{\text{rms}}$ is the rms channel noise. The restoring beam is shown in green in the lower left corner of each map.

5.5 Multi-configuration Image Cube Inspection

the same position in the corresponding C configuration channel maps, probably due to the lower sensitivity resulting from the smaller HPBW (i.e., the flux is diluted). This discrete second source thus has the effect of adding extra emission to the corresponding multi-configuration image cube spectrum at the low absolute velocities where it is present. The presence of this addition source at these low absolute velocities is probably one of the reasons why Huggins *et al.* (1994) did not detect a horned shaped spectrum with his 12'' HPBW. We also note that that there is a weaker emission feature 7'' north north-west of α Ori in these maps also which too can be seen in Figure 5.6. Finally, the Submillimeter Array CO($J = 3 - 2$) line profile will be discussed in Section 5.10 but here we confirm that its image cube also contains this spatially unresolved source $\sim 5''$ S-W of α Ori at the same velocities.

5.5 Multi-configuration Image Cube Inspection

A subset of the blueshifted velocity channel maps of the low spectral resolution multi-configuration image cube is presented in Figure 5.7. The first channel map at -17.9 km s^{-1} shows just the compact unresolved continuum emission with no extended emission present. Between -16.7 km s^{-1} and -9.0 km s^{-1} we see evidence for the development of a classical shell signature for the S2 flow. We first sample the highest velocity components where the emission is relatively compact (i.e., between -16.7 km s^{-1} and -12.9 km s^{-1}) and then sample lower absolute velocity components where S2 becomes a faint ring (i.e., between -11.6 km s^{-1} and -9.0 km s^{-1}). At lower velocities again, these rings disappear into the noise of the maps and possibly extend out beyond the primary beam at zero velocity where S2 should have maximum radial extent. The emission from the channel maps between -15.3 km s^{-1} and -11.6 km s^{-1} correspond to all the emission in the extreme blue wing component of the multi-configuration image cube line profile discussed in Section 5.3. We can see in Figure 5.7 that all of this emission is greater than the C configuration resolving out scale of $\sim 6''$, therefore confirming that our C configuration line profile is mainly composed of S1 emission. The shell formation signature of S2 is also apparent in the redshifted velocity channel maps between $+7.5 \text{ km s}^{-1}$ and $+13.8 \text{ km s}^{-1}$ but the emission appears weaker and the

5.5 Multi-configuration Image Cube Inspection

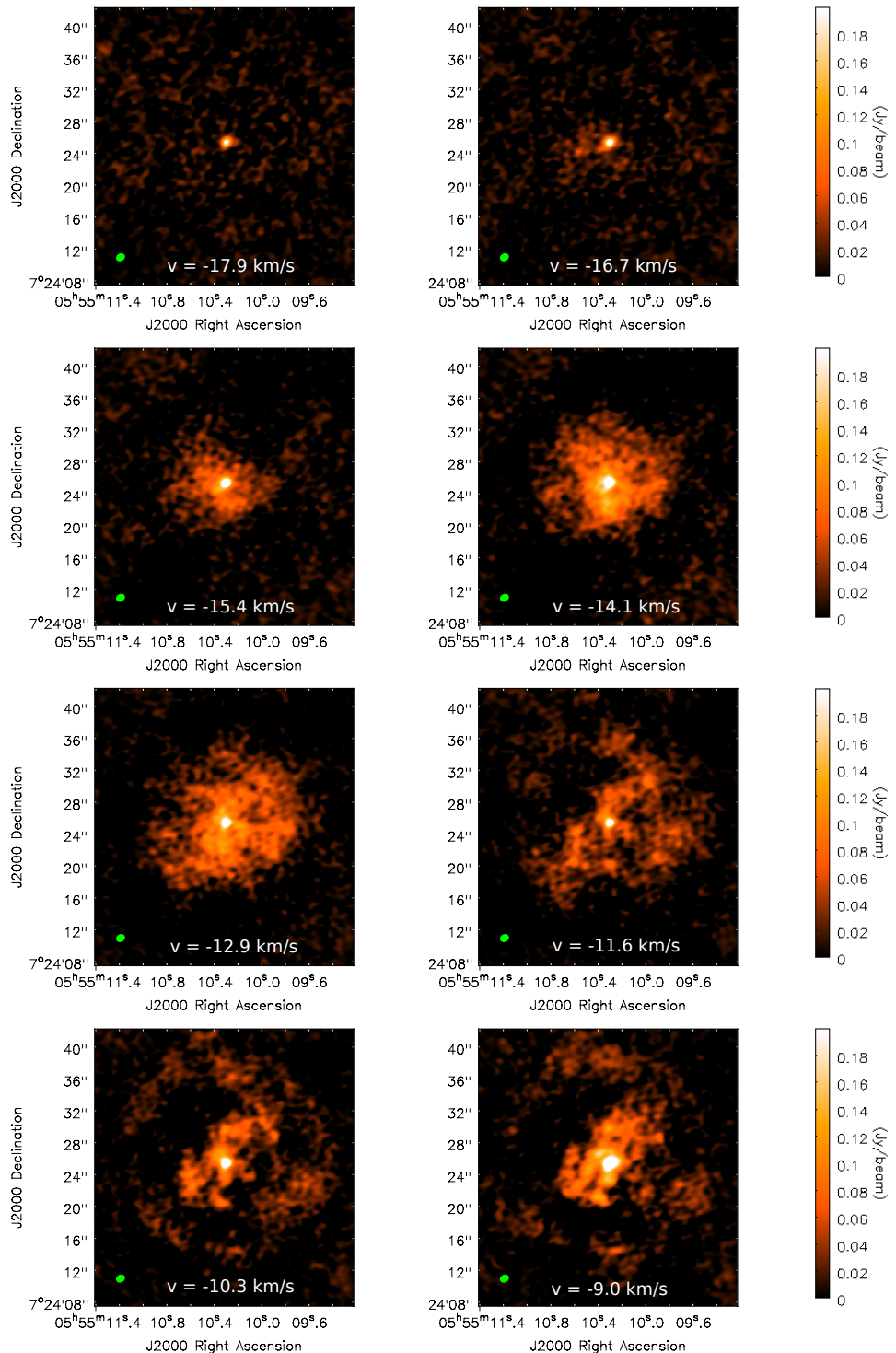


Figure 5.7: 8 channel maps from the multi-configuration image cube ($\Delta v = 1.3 \text{ km s}^{-1}$). The peak emission has been cut at 0.2 Jy beam^{-1} to emphasize the fainter emission. The map at -17.9 km s^{-1} is the star in the continuum while the blue wing of the line starts at -16.7 km s^{-1} . The formation of a weak ring-like structure is seen as one goes from high absolute velocities to lower ones.

rings fainter confirming that S2 is inhomogeneous. The multi-configuration maps also show the central compact emission from the S1 flow at velocities between -10.3 km s^{-1} and $+11.3 \text{ km s}^{-1}$. This S1 emission can be seen in the final two maps of Figure 5.7 as a central slightly elongated emission feature surrounded by the fainter rings of the S2 flow.

5.6 Spatial Extent of S2

The spatial extent of the S2 flow around Betelgeuse was not directly determined from either the CO infrared absorption spectra of Bernat *et al.* (1979) or previous CO single dish radio observations (Huggins, 1987; Huggins *et al.*, 1994; Knapp *et al.*, 1980). Our low spectral resolution multi-configuration image cube has sufficient spatial resolution and S/N to make direct estimates of its maximum radius. We find that little or no signature of the S2 flow is present in the low absolute velocity channel maps where its spatial extent is maximum and either lies outside of the primary beam or is lost into the noise near the edge of the maps. Therefore we cannot make a simple direct measurement of its maximum size. However, by measuring how its size varies in the higher absolute velocity maps where it is clearly present allows us to derive its maximum radial extent.

If we assume that S2 is spherically symmetric with an outer radius R_{S2} , and is undergoing steady expansion with velocity V_{S2} , then its geometry is described by Figure 5.8. As we sample the line at different velocities, the spatial extent of S2 changes and gets progressively larger at lower absolute velocities as can be seen in Figure 5.7. The projected radius of S2 in each map is

$$r_{\text{chan}} = R_{S2} \times \sin\theta \quad (5.3)$$

which can be directly measured in many of the channel maps. Each of these channel maps have an associated velocity V_{chan} , which we know, and is related to the actual velocity of the S2 flow by

$$V_{\text{chan}} = V_{S2} \times \cos\theta. \quad (5.4)$$

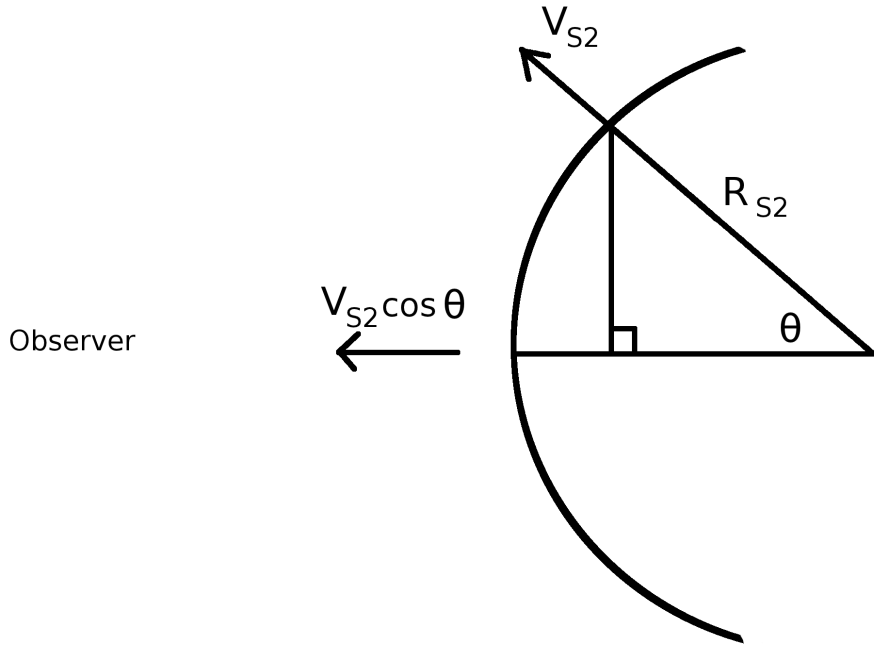


Figure 5.8: Geometry of a spherical symmetric flow used to derive the spatial extent of the S2 flow. By measuring the spatial extent of S2 (i.e., $R_{S2}\sin\theta$) as a function of channel/velocity (i.e., $V_{S2}\cos\theta$) the maximum radial extent of the S2 flow can be derived.

Combining Equations 5.3 and 5.4 via the angle dependence, gives the following equation which contains R_{S2} as the only unknown parameter,

$$r_{\text{chan}} = R_{S2} \times \sin \left[\cos^{-1} \left(\frac{V_{\text{chan}}}{V_{S2}} \right) \right]. \quad (5.5)$$

An estimate of the S2 radius per channel (r_{chan}) was found by creating annuli of increasing radius around the central emission in each relevant line channel map of the multi-configuration image cube, extracting all flux within each annulus and then plotting the integrated flux against distance from the star for each channel map. The maximum of these resultant curves were then deemed to be the maximum radius of S2 per channel map. Figure 5.9 shows these data overplotted with two model outflows which were created using Equation 5.5. The blueshifted data points were best fitted by a model outflow having a maximum radius $17''$ and outflow velocity 16.7 km s^{-1} , while the redshifted data points were

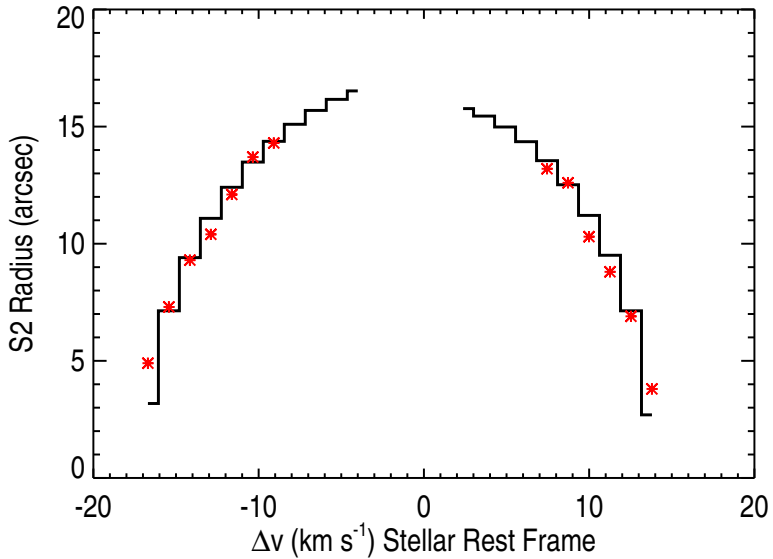


Figure 5.9: The derived S2 radius as a function of velocity (red points) overplotted with two model outflows. The blueshifted model (left) corresponds to an outflow with a maximum radius of $17''$ and a velocity of 16.7 km s^{-1} while the redshifted model (right) corresponds to an outflow with a maximum radius of $16''$ and a velocity of 13.8 km s^{-1} .

best fitted by a model outflow with a maximum radius $16''$ and outflow velocity 13.8 km s^{-1} . It is worth mentioning that this estimate for the spatial extent of S2 is only weakly dependent on our adopted radial velocity value for Betelgeuse and adopting a slightly different value would simply alter the outflow velocities.

5.7 Intensity distribution of CO

We first investigate how one would expect the intensity of CO to vary as a function of distance from the star for a spherically symmetric optically thin outflow. The CO($J = 2 - 1$) emission line is formed over an extended region around Betelgeuse so a constant outflow velocity can be assumed when investigating the intensity distribution of the S1 and S2 outflow. This allows us to use the equation of mass continuity to find the number density of the molecules in the lower level of the transition, n_l , i.e., $n_l \propto r^{-2}$. The Boltzmann formula can then be used to find

5.7 Intensity distribution of CO

the number density of CO molecules in the upper level, n_u ,

$$n_u(r) = n_l(r) \frac{g_u}{g_l} e^{-(E_u - E_l)/kT_{\text{exc}}(r)} \quad (5.6)$$

where g_u and g_l are the statistical weights of the two rotational levels, and E_u and E_l are their respective energies. Here, T_{exc} is the excitation temperature and equals to the gas temperature if collisions dominate the redistribution of the populations over the vibrational ladder. To find the intensity we first need to know the emissivity, j_l , of the line photons which is just $n_u(r)$ times the probability for spontaneous de-excitation per second, A_{ul} , times the energy of the emitted photons, $h\nu$, i.e.,

$$j_l(r) = n_u(r) A_{ul} h\nu \propto r^{-2} e^{-(E_u - E_l)/kT_{\text{exc}}(r)}. \quad (5.7)$$

If T_{exc} is constant, then the line intensity, I_{CO} , is the integral of the emissivity along the line of sight in direction z , at some impact parameter (or projected radius), R ,

$$I_{\text{CO}} = \int j_l(r) dz \propto R^{-1}. \quad (5.8)$$

Therefore, the intensity distribution for an optically thin spherically symmetric constant velocity outflow should vary as R^{-1} .

In the left column of Figure 5.10 we investigate the intensity distribution of CO emission as a function of projected radius, R , for both the S1 and S2 flows. From our discussions in Section 5.3 we can assume that all line emission between $-15.4 \rightarrow -10.3 \text{ km s}^{-1}$ and $+12.4 \rightarrow +13.8 \text{ km s}^{-1}$ emanates solely from the S2 flow. Using the low spectral resolution multi-configuration image cube we integrate the surface brightness over these channels and find that the intensity fall-off is close to being proportional to R^{-1} (Figure 5.10: *top left*). To investigate the S1 flow intensity distribution around α Ori we integrate the surface brightness over the channels between $-9 \rightarrow +10.6 \text{ km s}^{-1}$. Although these channels contain emission from both S1 and S2, most of the S2 emission here will have larger projected radii and thus the majority of the inner emission should emanate from the S1 flow. Between $0.5''$ and $4''$ from the star the intensity is again found to be close to proportional to R^{-1} (Figure 5.10: *bottom left*). We have just showed

5.7 Intensity distribution of CO

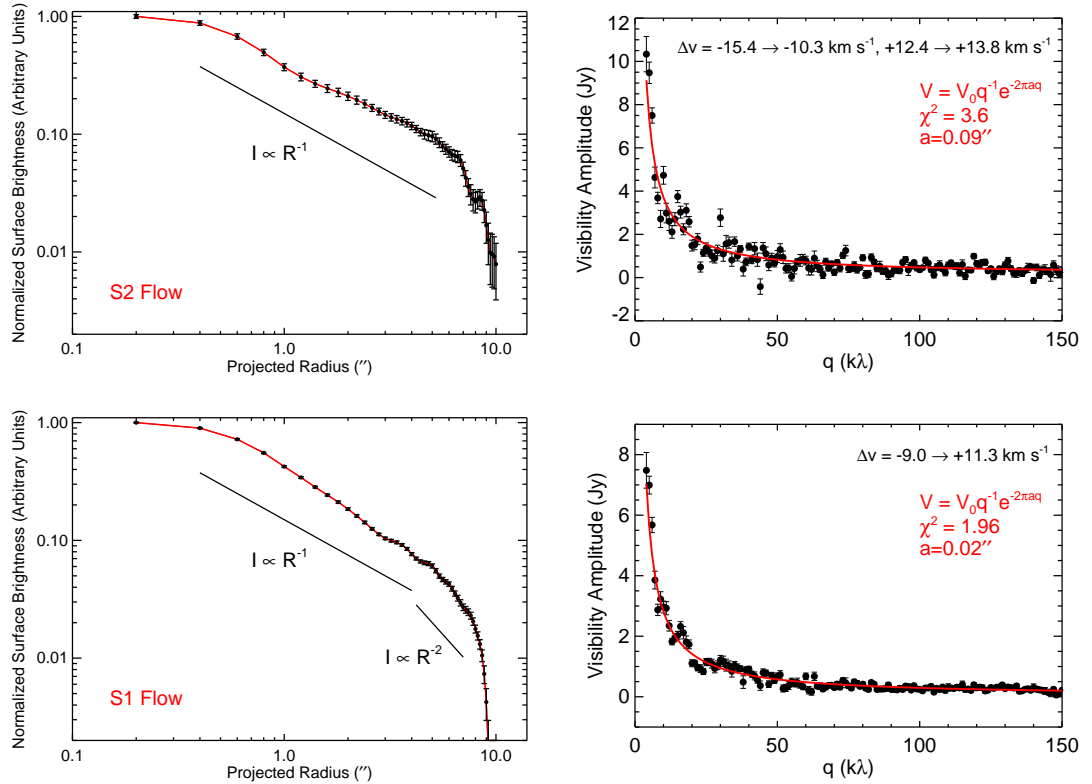


Figure 5.10: *Left Column:* Surface Brightness as a function of projected radius on sky, R (red line). The emission has been extracted from the low spectral resolution multi-configuration image cube and is integrated over the channels where S1 is present (bottom) and over the channels where only S2 is present (top). Intensity proportional to R^{-1} and R^{-2} is also shown for comparison. *Right Column:* The corresponding visibility amplitude as a function of $u-v$ distance (q) of both outflows can be modeled well by a R^{-1} fall off in intensity. The error bars in all plots represent the standard error of the mean.

that such an intensity distribution is expected for an optically thin spherically symmetric constant velocity outflow with $\rho \propto 1/R^2$. Beyond $\sim 6''$ the intensity fall off is more rapid and is steeper than a R^{-2} distribution and may be caused by factors such as a variation in the thermal or velocity profile, or even the absence of emitting material altogether. This region may mark the initiation of the current epoch of mass-loss.

Insight can also be gained into how the intensity varies on different size scales

by conducting analysis in the $u - v$ plane and plotting the visibility amplitude of our CO data against $u - v$ distance. The result of this is shown in the right column of Figure 5.10 where the same channels corresponding to the S1 and S2 flows defined in the last paragraph have been used. The data are azimuthally averaged, and have been binned to produce one data point per $k\lambda$. The result for both the S1 and S2 data is a steep drop-off in visibility amplitude over a relatively short $u - v$ distance, signaling that the sources are well resolved, as expected. Both sets of visibility data are consistent with an intensity proportional to $(a^2 + R^2)^{-1/2}$, where a is an inner spatial limit. This is because the Hankel transform of this function is $q^{-1}e^{-2\pi aq}$ (Bracewell, 2000), where q is the $u - v$ distance, and a vertically scaled version of this function is shown to match the visibility data very well in Figure 5.10. As analysis in both the sky and $u - v$ plane indicate the intensity of both flows is proportional to R^{-1} we conclude that both outflows are consistent with an optically thin and quasi-steady flow which is in agreement with Smith *et al.* (2009) (i.e., S1) and Plez & Lambert (2002) (i.e., S2).

5.8 Spatial Extent of S1

It is difficult to exactly determine of the maximum radial extent of the S1 flow as we do not see the classical shell formation signature as we sample across velocities, like we do for the S2 flow. Its spatial extent varies in different channel maps and, as can be seen in Figure 5.11, the emission is very inhomogeneous/clumpy. This clumpy nature of the S1 flow has been previously reported in other studies (Kervella *et al.*, 2011; Smith *et al.*, 2009) and Smith *et al.* (2009), who studied photospheric scattered emission, estimated its spatial extent to lie within $3''$ from the star. At 20% of maximum emission in the integrated intensity S1 map (i.e., composed of all channels between $-9 \rightarrow +10.6 \text{ km s}^{-1}$) the S1 flow extends out to a mean distance of $\sim 4''$ and is even more extended in the S-W direction due to the presence of the second emission feature in the compact configuration data sets. Even though the emission is inhomogeneous, the intensity when averaged on the sky is consistent with a $\sim R^{-2}$ density distribution out to $\sim 6''$, as discussed in Section 5.7, and may mark the end of the S1 flow. The HPBW of $0.9''$ is

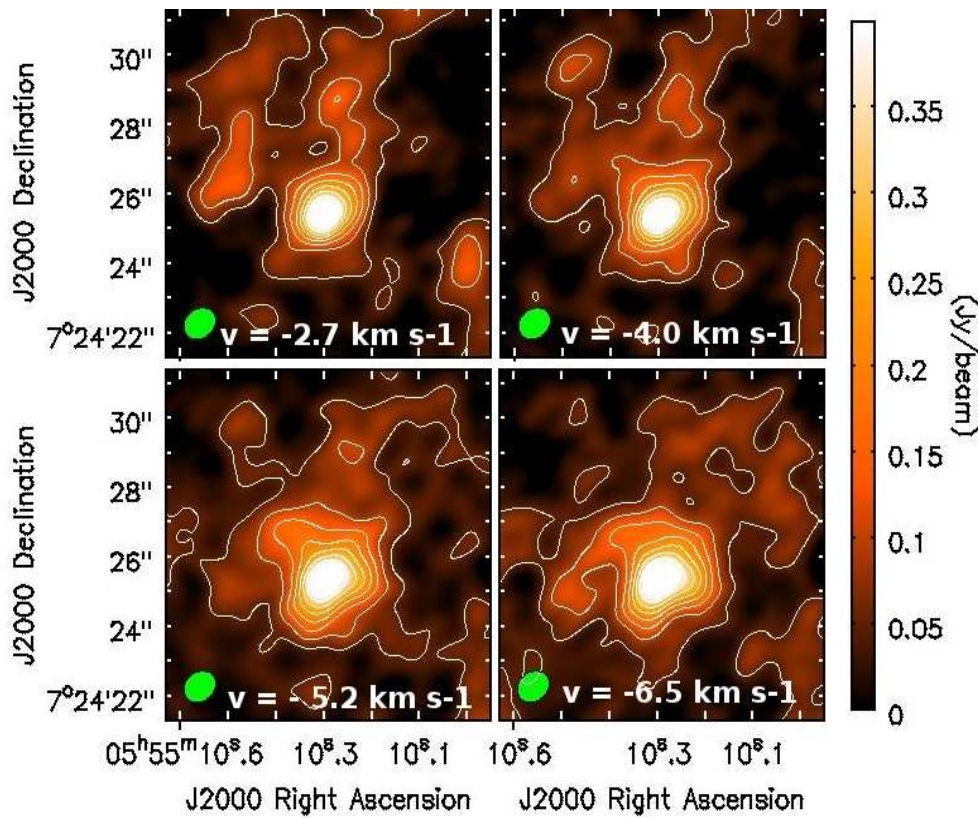


Figure 5.11: CARMA combined image cube low spectral resolution, 1.3 km s^{-1} , maps of the inner S1 flow. These maps are $10'' \times 10''$ in size and show the irregular nature of the S1 emission around the star. Going clockwise from the top left panel, the channel map velocities are -2.7 , -4.0 , -5.2 , and -6.5 km s^{-1} . The restoring beam is shown in green in the bottom left of each map. Contour levels are at $(3, 6, 9\dots) \times \sigma_{\text{rms}}$ where $\sigma_{\text{rms}} = 16 \text{ mJy beam}^{-1}$.

not sufficient to determine whether the S1 flow is discrete or an extension of the current wind phase seen in ultraviolet spectra (e.g., Carpenter & Robinson, 1997) and cm-radio continuum interferometry (Lim *et al.*, 1998).

5.9 Continuum Flux Densities

Betelgeuse is known to show brightness variations at many continuum wavelengths. Goldberg (1984) reports a decrease of half a magnitude in visual brightness over a period of six years. Bookbinder *et al.* (1987) found stochastic 30%-40%

5.9 Continuum Flux Densities

variations in flux density at 6 cm over timescales as short as 10 days to as long as 8 months (i.e., the observational period). A more comprehensive study was carried out by Drake *et al.* (1992) who observed Betelgeuse with the VLA at centimeter wavelengths from 1986 to 1990 and found stochastic variability of 22%, 15%, and 21% at 6 cm, 3.6 cm, and 2 cm respectively, at a variety of different timescales down to less than one month (a possible source for this variability will be described in Section 5.11). The mm-continuum emission that we measure arises mainly from electron-ion and electron-atom bremsstrahlung (also the source of the longer wavelength continuum emission) and possibly dust emission, so it is not unreasonable to also expect variability at mm-wavelengths too.

In Table 5.1 we list the derived continuum flux densities for each of the three configuration image cubes and also the multi-configuration image cube. The high spectral resolution ($\Delta v = 0.65 \text{ km s}^{-1}$) image cubes were just wide enough to image the CO line but were too narrow to make accurate estimates of the continuum flux density. Therefore, all continuum flux density estimates are derived from the lower spectral resolution ($\Delta v = 1.3 \text{ km s}^{-1}$) image cubes from which we were able to take accurate measurements at both sides of the line. We fitted elliptical Gaussians to ~ 20 continuum channels using CASA's *imfit* routine allowing the flux and corresponding uncertainties to be calculated. The source was unresolved in almost all of these continuum channels which means that the continuum emission is formed within $\sim 0.9''$. The D configuration data were acquired under adverse weather conditions and these data have the highest noise levels out of the three configurations. Its continuum emission measurement is approximately 50% greater than the C and E configuration continuum measurements which were also acquired approximately two years after the D configuration data. We believe the continuum emission value of $289 \pm 21 \text{ mJy}$ derived from the multi-configuration image cube is a reasonable estimation of the mean mm-continuum flux density over the 2.5 yr period, 2007 → 2009. It is in reasonably good agreement with the 250 GHz flux density of Altenhoff *et al.* (1994) who report a mean value of $351 \pm 25 \text{ mJy}$ for 1986 → 1989.

5.10 Higher CO rotational lines

Table 5.1: CARMA Continuum Fluxes at 230 GHz between 2007 → 2009.

Configuration	Date	Restoring Beam ("×")	Flux (mJy)	Uncertainty (mJy)
C	2007 Jun	0.96×0.76	234	18
D	2009 Jul	2.33×1.87	389	72
E	2009 Nov	4.93×3.84	278	40
Multi-configuration	2007 → 2009	1.05×0.84	289	21

5.10 Higher CO rotational lines

As part of our larger multi-wavelength study of the CO surrounding Betelgeuse, we were also able to obtain emission line profiles of higher rotational CO lines. We observed the star (PI Harper: ID 81-0005-1) with the German Receiver for Astronomy at Terahertz Frequencies (GREAT; Guesten *et al.*, 2000) instrument on NASA and DLR’s Stratospheric Observatory for Infrared Astronomy (SOFIA; Becklin & Gehrz, 2009) 2.5 m airborne observatory. Observations of the CO($J = 12 - 11$; 1.382 THz) line were made during Flight 86 on 2011 November 10 at 13,100 m ($\sim 43,000$ ft) when the star had an elevation of 45° . The HPBW was $\sim 19''$ and the effective on source exposure time was 12 minutes, which was considerably lower than the requested on source time of 70 minutes due to technical difficulties during the flight. We also obtained 4.1 hours on source at 345 GHz with the Submillimeter Array (SMA; Blundell, 2007) on 2012 January 12 (PI J. Brown: ID 2011B-S051). The SMA is a submillimeter interferometer located atop Mauna Kea in Hawaii and consists of eight antennas, each 6 m in diameter. Our data were acquired in the compact configuration ($B_{\max} = 70$ m) which at the observing frequency of ~ 345 GHz, gave a synthesized beam of 5×4.5 arcsec 2 (similar to the CARMA E configuration at 230 GHz). We obtained very high spectral resolution ($\Delta v = 0.088$ km s $^{-1}$) of the CO($J = 3 - 2$; 345.796 GHz) line which is more than a factor of 7 better than the highest spectral resolution CARMA data. Finally we obtained archival data of the CO($J = 6 - 5$; 691.473 GHz), CO($J = 10 - 9$; 1.15198 THz), and CO($J = 16 - 15$; 1.84135 THz) rotational lines which were obtained with the Heterodyne Instrument for the Far Infrared (HIFI; de Graauw *et al.*, 2010), on board the Herschel Space Observatory

5.10 Higher CO rotational lines

(Pilbratt *et al.*, 2010). The HPBW for these lines were $31''$, $18''$, and $11.5''$, for the $J = 6 - 5$, $J = 10 - 9$, and $J = 16 - 15$ transitions, respectively.

We plot all these line profiles in order of excitation energy in the stellar rest frame in Figure 5.12, to allow easy comparison. The profiles have been binned to 1.3 km s^{-1} spectral resolution to match the CARMA low resolution profiles described in Section 5.3, except for the SMA profile which has excellent spectral resolution. In this figure the dashed vertical red lines mark the derived outflow velocities of the S1 flow from Section 5.3. This figure clearly demonstrates that the CO rotational lines get narrower as one goes from lower rotational levels to higher ones, i.e., as the excitation temperature increases. A noticeable consequence of this is the evolution of the contribution of the S2 blueshifted component which is the dominant feature in the $\text{CO}(J = 2 - 1)$ combined configuration CARMA profile; its relative strength in relation to the rest of the line dramatically reduces at higher excitation temperatures. This indicates that the higher lines are predominately formed in the S1 flow region. The SOFIA $\text{CO}(J = 12 - 11)$ profile is found to have a line width of $\sim \pm 7.5 \text{ km s}^{-1}$ when centered on the stellar rest frame but because the higher S/N $\text{CO}(J = 16 - 15)$ HIFI profile is slightly wider, the narrowness of the SOFIA line is probably due to its low S/N.

For the lower rotational line profiles, it is difficult to infer the level of flux contribution from each of the S1 and S2 components making the analysis of integrated line flux ratios difficult. Also, some of these profiles shown in Figure 5.12 were obtained over many years with different instruments and techniques. It appears likely however, that the majority of the emission in the higher rotational profiles [i.e., the $\text{CO}(J = 16 - 15)$, $\text{CO}(J = 12 - 11)$, and $\text{CO}(J = 10 - 9)$ line profiles] emanates from the S1 flow, while the other lower level lines contain various amounts of emission from both flows. However, the $\text{CO}(J = 12 - 11)$ line profile has a low S/N and its flux scale is rather uncertain due to the poor pointing accuracy during our SOFIA-GREAT observation. For this reason only the Herschel/HIFI $\text{CO}(J = 16 - 15)$ and the $\text{CO}(J = 10 - 9)$ line profiles are suited for probing the thermodynamics of one of the flows, i.e., the S1 flow.

The ratio of the integrated flux from these two rotational emission lines in a

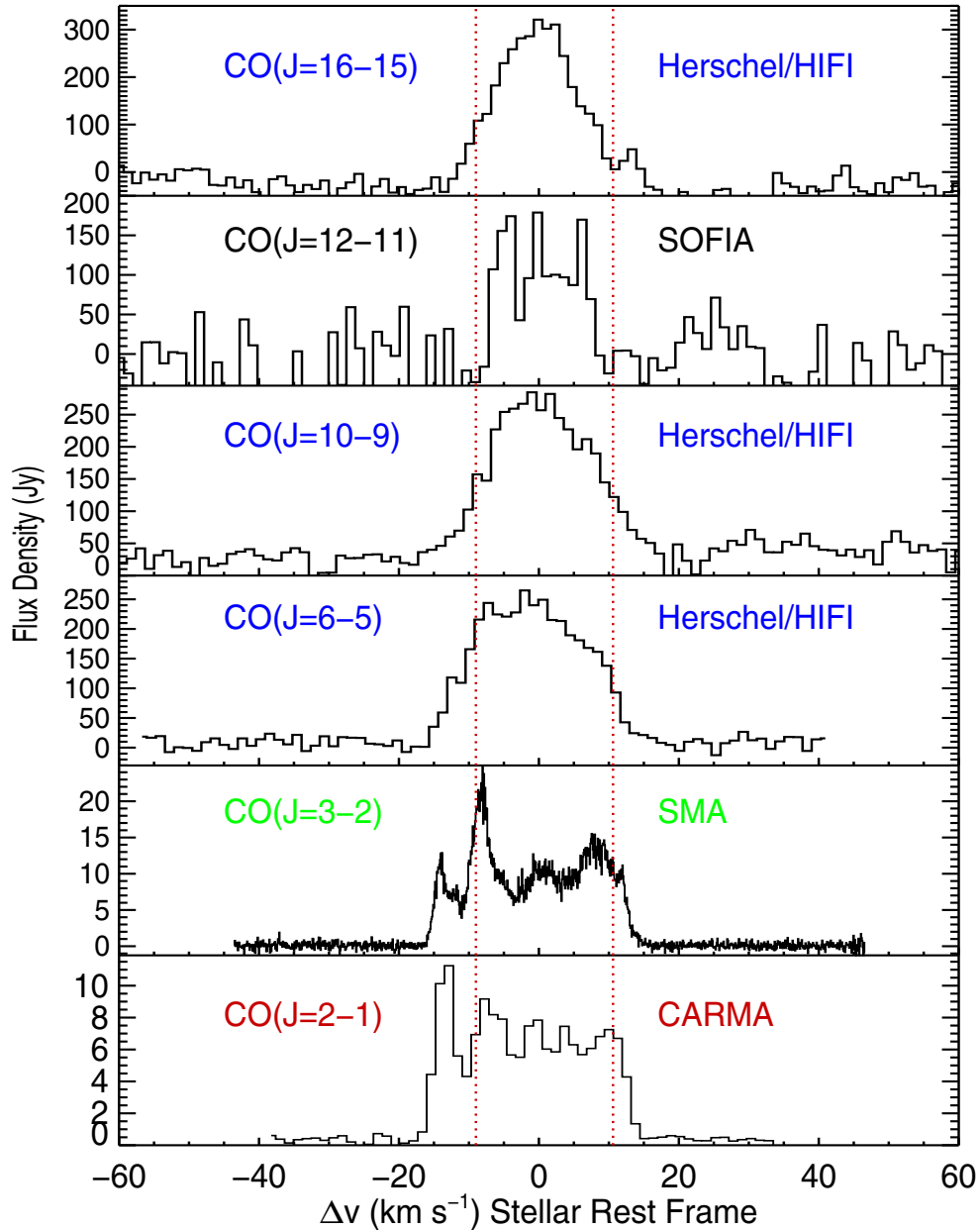


Figure 5.12: CO rotational emission lines from the CSE of Betelgeuse. The lines are listed in order of decreasing excitation energy from top to bottom, and are plotted in the stellar rest frame. The vertical dashed red lines mark the outflow velocities of the S1 flow. At higher excitation energies the relative strength of the blueshifted S2 feature in relation to the rest of the line decreases dramatically and the lines get narrower. This indicates that the higher excitation lines are formed mainly in the S1 flow.

5.10 Higher CO rotational lines

linear molecule like CO can be written as

$$\frac{F_{10-9}}{F_{16-15}} = \left(\frac{J_{10}}{J_{16}} \right)^5 \exp \left(\frac{B_v [J_{16}(J_{16}+1) - J_{10}(J_{10}+1)]}{T_{\text{exc}}} \right) \quad (5.9)$$

where F , J , and B_v are the integrated line flux, the rotational quantum number, and the rotational constant, respectively. For the CO molecule, $B_v = 2.77 \text{ K}$. Equation 5.9 is derived from the relation, $F_{j,j-1} \propto n_j A_{j,j-1} h \nu_{j,j-1}$, where n_j and $A_{j,j-1}$ are found from Equations 1.20 and 1.27, respectively. The integrated line fluxes for the CO($J = 16 - 15$) and the CO($J = 10 - 9$) profiles are 2.4×10^{-16} and $1.8 \times 10^{-16} \text{ W m}^2$, respectively. Equation 5.9 can then be used to show $T_{\text{exc}} = 220 \text{ K}$. This is in excellent agreement with Bernat *et al.*'s 1979 value of $200^{+50}_{-10} \text{ K}$ for the S1 flow who analyzed ro-vibrational fundamental lines near $4.6 \mu\text{m}$.

Through a judicious choice of the SMA correlator setup, we simultaneously observed the SiO($J = 8 - 7$; 347.331 GHz) line while observing the CO($J = 3 - 2$) line. We report a weak detection of SiO($J = 8 - 7$) at a spectral resolution of 0.55 km s^{-1} , as shown in Figure 5.13. Previous searches for SiO in the CSE of Betelgeuse have been unsuccessful (e.g., Lambert & Vanden Bout, 1978) and this may be the first, albeit weak, detection of the molecule. The weak SiO($J = 8 - 7$) line profile is unfortunately contaminated with an atmospheric absorption feature but its linewidth is comparable to the CO($J = 2 - 1$) line profile, which means that SiO is also present in the S2 flow. A crude estimate of the CO($J = 8 - 7$) flux density from the S2 flow can be found by taking the mean value of the blueshifted emission feature in the Herschel $J = 10 - 9$ and $J = 6 - 5$ lines. From this we see that CO is ~ 100 times more abundant in the S2 flow than SiO. For an O-rich star like Betelgeuse we can expect that all C and Si will be in the form of CO and SiO, respectively. The CO/SiO ratio should then represent the C/Si ratio. Assuming solar abundances¹ this ratio should be only ~ 8 . The much larger ratio observed is probably a consequence of the role played by SiO molecules in the formation of silicate dust.

¹As Betelgeuse is a Population I star

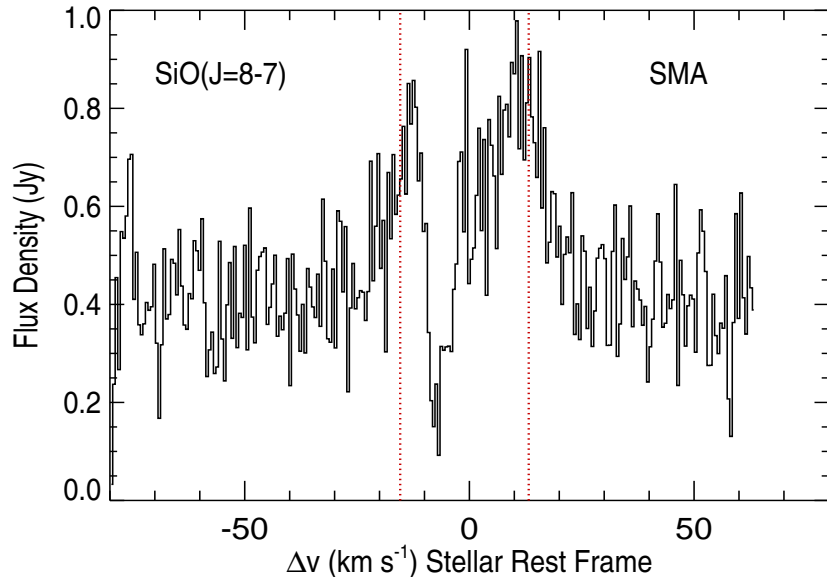


Figure 5.13: SiO($J = 8 - 7$) rotational emission line from the CSE of Betelgeuse obtained using the SMA. The linewidth is similar to the CARMA combined configuration CO($J = 2 - 1$) line profile, signaling that the S2 flow contains SiO. The dotted red lines are the previously derived S2 outflow velocities.

5.11 CARMA CO observations in Context

We have found the spatial extent of the S2 flow to be greater than the HPBWs of some of the previous single dish antenna observations of the CO($J = 2 - 1$) line. So why did these single dish line profiles not show the classical resolved signature of high emission at large absolute velocities and low emission at low absolute velocities? First, the S1 flow was still unresolved in these single dish observations and thus contributes emission at the lower absolute velocities. As well as this, the multi-configuration CARMA maps show that the S2 emission is brighter at higher absolute velocities than at lower absolute velocities and so when the emission from the fainter rings is neglected (i.e., when observed with a small HPBW), the overall line profile does not change significantly. Finally, our maps have revealed that some discrete strong emission features are present at low absolute velocities, which would also have been present in the HPBW of previous single dish observations, thus contributing to the line profile flux at these velocities.

5.11 CARMA CO observations in Context

Table 5.2: Summary of the S1 and S2 Flow Properties.

	S1	S2
Outflow Velocities (km s^{-1})	−9.0 & +10.6	−15.4 & +13.2
Maximum Radial Extent ('')	$\sim 4 - 6$	~ 17
Age (yr)	$\sim 400 - 600$	1100

The main properties of the S1 and S2 flows, which have been derived in the previous sections of this chapter, are summarized in Table 5.2. Assuming a mean outflow velocity of 14.3 km s^{-1} and 9.8 km s^{-1} for the S2 and S1 flows respectively, then their ages are ~ 1100 yr and $\sim 400 - 600$ yr. Since Plez & Lambert (2002) have detected K I out to $55''$ at a similar velocity (i.e., $18 \pm 2 \text{ km s}^{-1}$) to the CO S2 flow, then, assuming the CO and K I are coupled, there appears to be little further acceleration in Betelgeuse's outflow once the S2 flow begins (which is somewhere greater than $6''$).

Despite decades of research, it is unknown if Betelgeuse loses mass through episodic ejections or through more of a constant and global process. We have shown that when averaged across the sky, the variation in mean density is consistent with a spherically symmetric and constant velocity outflow. However, the presence of clumping is also evident in our radio maps and emission from the S2 flow appears weaker at redshifted stellar rest frame velocities indicating an inhomogeneous flow. Higher spatial resolution studies like those described in the following sections, are needed to determine if clumping is a result of growing instabilities in a global outflow or as a product of the mass-loss mechanism. The reason for two unique velocities in the outflow are also a puzzle. One possibility is that the dust properties change at $\sim 6''$ leading to a sudden acceleration of the flow. However, the S2 component has a small velocity dispersion along the line of sight (Bernat *et al.*, 1979) and appears as a shell like structure in our CARMA data so this scenario is unlikely. Another possibility is that the mass-loss mechanism is magnetic in origin and that these components represent phases in the order of ~ 600 yr of a stellar dynamo cycle (Harper, 2013).

5.12 e-Merlin 5 cm Results

The first detailed study of Betelgeuse at centimeter wavelengths was carried out by Newell & Hjellming (1982) who observed the star at multiple wavelengths (20, 6, 2, and 1.3 cm) in the compact VLA C configuration. The star was unresolved but a radio spectral index of 1.32 was derived and the radio emission was interpreted as emanating from a spherically symmetric, partially ionized chromosphere with an temperature of $\sim 10,000$ K extending from 1 to $4 R_\star$, in agreement with the Alfvén wave models to follow (Hartmann & Avrett, 1984). The star was first spatially resolved at radio wavelengths by Skinner *et al.* (1997) with both the “old” VLA in its most extended configuration, and MERLIN (the predecessor to e-MERLIN). The data were taken ~ 2.5 yr apart and it was found that the 6 cm radio emitting region was up to three times larger than the optical photosphere. Combined VLA and MERLIN 6 cm observations throughout the 1990s confirmed this large radio emitting size (Morris, 2001). The spatially resolved multi-wavelength study of Lim *et al.* (1998) revealed a cool, low hydrogen ionization inner atmosphere. To reconcile these radio observations with spatially resolved UV observations Gilliland & Dupree (1996), which showed a much warmer inner atmosphere, Lim *et al.* (1998) concluded that there must be at least 3 orders of magnitude more cooler plasma than hot chromospheric plasma. This is because the radio opacity of the warm more ionized gas is much greater than that of the cooler less ionized gas, and yet the radio observations of Lim *et al.* (1998) preferentially detect the cooler gas. We now discuss the recent findings of Richards *et al.* (2013) who observed Betelgeuse at 5 cm with the very long baseline interferometer, e-MERLIN.

e-MERLIN (Muxlow, 2003) consists of seven radio antennas spread out across the United Kingdom that are connected via a fiber optic network to a central correlator at Jodrell Bank Observatory. It will eventually be able to observe in three frequency bands at 1.3 – 1.8 GHz, 4 – 8 GHz, 22 – 24 GHz, and its maximum baseline of 220 km will provide resolution up to 10 mas at the μ Jy sensitivity level. Betelgeuse was observed at 5.76 GHz (5.2 cm) in 2012 July with e-MERLIN as part of Cycle-0 observations, with a total bandwidth of 0.512 GHz. The final high resolution image which is shown in Figure 5.14 had a $\sigma_{\text{rms}} = 9 \mu$ Jy and was

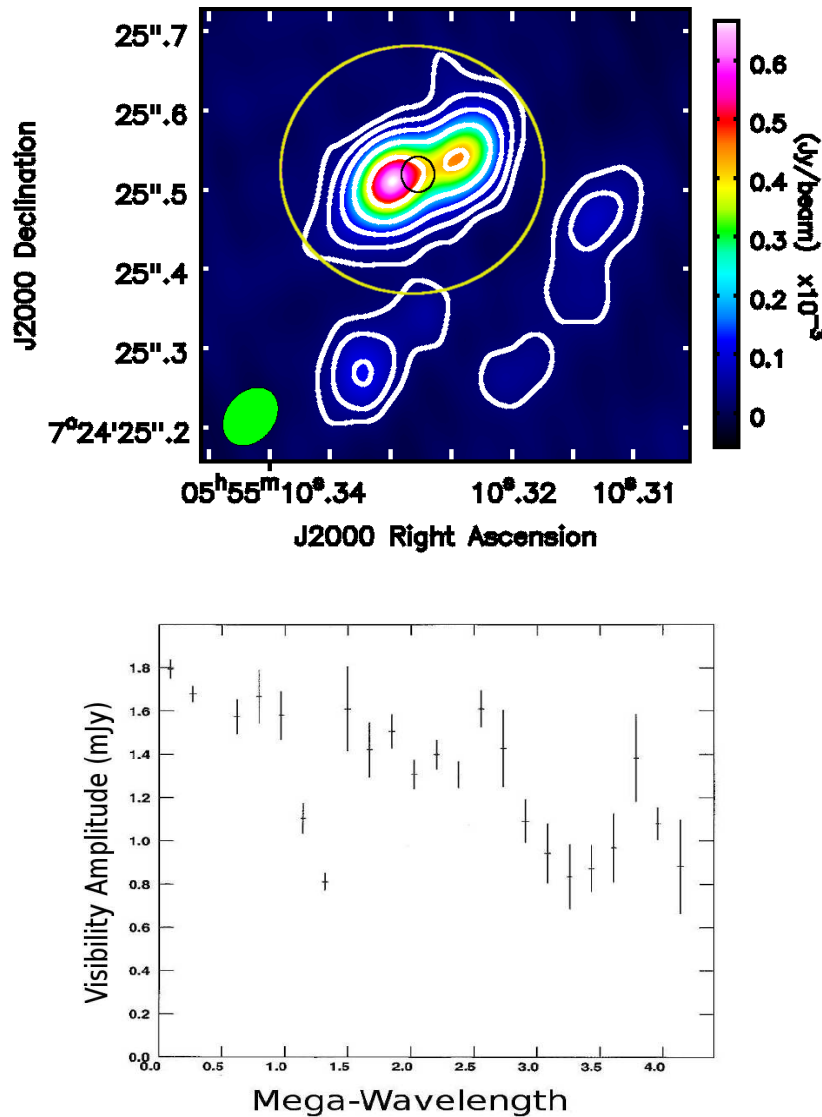


Figure 5.14: First e-MERLIN results for Betelgeuse. *Top:* 5.2 cm e-MERLIN image of Betelgeuse taken in July 2012 showing two unresolved emission features separated by 90 ± 10 mas. The image was restored with a 80×60 mas 2 beam marked in green in the lower left corner and using uniform weighting. Contour levels are at $(-3, 3, 6, 12, 24, 48) \times \sigma_{\text{rms}}$ where $\sigma_{\text{rms}} = 9 \mu\text{Jy}$. The photospheric radius is the small black circle while the large yellow circle defines the 6 cm radio disk of Lim *et al.* (1998). *Bottom:* The calibrated visibility amplitudes (in mJy) versus $u - v$ distance measured in mega-wavelengths with the possible signature of two unresolved components with a brightness ratio differing from unity.

5.12 e-Merlin 5 cm Results

produced using uniform weighting with a restoring beam of 80×60 mas 2 . The first thing to notice about the radio map is the presence of three clumps of radio emission in the south-west quadrant approximately 250 mas ($11.5 R_\star$) from the star, with detections ranging from 4 to $12\sigma_{\text{rms}}$. These clumps of radio emitting plasma may be the remnants of past localized episodic mass-loss events from the star, which as they escaped the gravitational potential of the star, expanded and cooled, allowing hydrogen to recombine. These features would then become fainter radio continuum emitters than they initially were. Assuming a mean constant flow velocity of 10 km s^{-1} (the velocity of the S1 flow), then this plasma was ejected from the star ~ 22 yr prior to these observations. The time since ejection could in fact be much longer than this (~ 90 yr) if the slow wind acceleration profile given in Harper *et al.* (2001) is assumed.

The second and more remarkable feature of the image is that the star at 6 cm appears as two unresolved peaks separated by ~ 90 mas. To make sure this unexpected result was not an artifact of the imaging process we plotted the visibility amplitude as a function of projected baseline (i.e., $\sqrt{u^2 + v^2}$) as shown also in Figure 5.14. If we had fully resolved a standard uniform disk, which should be a good first order approximation for any *standard* star, then we would expect the visibility amplitude to drop to zero at some baseline, which clearly does not happen. On the other hand, the visibility amplitude for a double source would depict two peaks with the minimum visibility amplitude being a function of the component brightness ratio. For equal brightness (i.e., the ratio is 1) the first visibility amplitude minimum drops to zero but does not for sources of different brightness (Saha, 2011). Therefore, the visibility amplitudes of our calibrated data appear to be in agreement with what is seen in the final image, i.e., two sources of different brightness producing a sinusoidal visibility pattern which does not drop to zero.

The brighter feature was found to have a brightness temperature of $T_b = 5400 \pm 600$ K while the weaker feature had $T_b = 3800 \pm 500$ K. To estimate the position of the optical photosphere, Richards *et al.* (2013) took the peak flux position from a low resolution radio map which was optimized for sensitivity to extended structure. In this scenario the two features, referred to as *hotspots* by Richards *et al.* (2013) are located $\sim 1.0 R_\star$ ($T_b = 5,400$ K) and $\sim 1.5 R_\star$

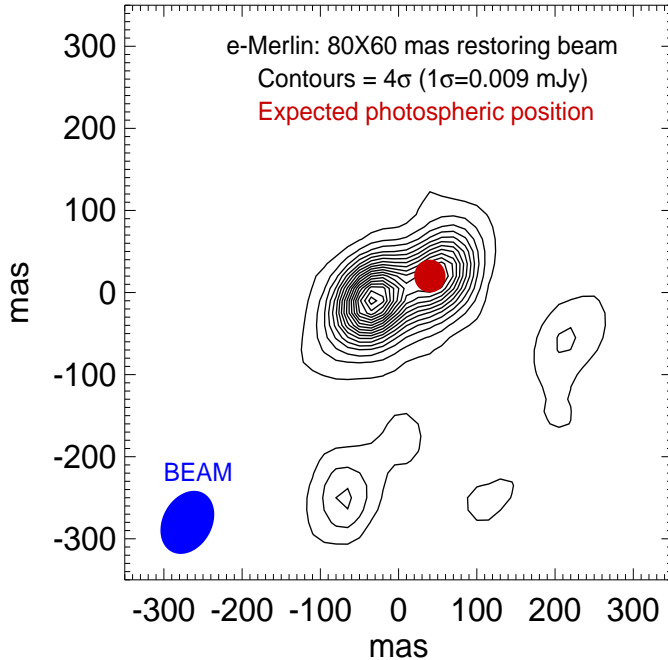


Figure 5.15: The red filled circle marks the predicted position of the optical photosphere of Betelgeuse on 2012 July using the astrometric solutions of Harper *et al.* (2001). The black contours represent the high spatial resolution 6 cm image of the star from Richards *et al.* (2013) and are at the $4\sigma_{\text{rms}}$ level. This solution puts the optical photospheric position almost at the position of the weaker unresolved peak.

($T_b = 3,800 \text{ K}$) from the optical photosphere. A more rigorous approach to finding the position of the optical photosphere is to use the astrometric solutions derived in a study to find the distance to Betelgeuse (Solution 5 in Harper *et al.*, 2008) and propagate these forward to find its expected position in 2012 July. Doing this we get RA = 05:55:10.3250 and Dec = +07:24:25.536 which includes the correction for parallax. We plot this expected position on top of the e-MERLIN map in Figure 5.15 but note that there may be systematic errors in this parallax solution. Interestingly, this puts the expected optical photospheric position almost directly on top of the weaker emission feature. The effective temperature of Betelgeuse is 3,650 K (Levesque *et al.*, 2005) which is slightly below the brightness temperature derived for this feature but well within its

5.13 VLA-Pie Town Maps Versus e-MERLIN

errors (i.e., $T_b = 3,800 \pm 500$ K). If this weaker source is indeed the optical photosphere, then the brighter source with $T_b = 5,400 \pm 600$ K is located at least $3.5 R_\star$ from the surface of the optical photosphere. Its value is significantly higher than that predicted in the spherically symmetric semi-empirical model of Harper *et al.* (2001) who predict a value of 2,300 K at a projected radius of 95 mas (i.e., $3.5 R_\star$ from the photosphere).

The semi-empirical model of Harper *et al.* (2001) is the current *state of the art* inner (i.e., $1 - 10 R_\star$) atmospheric model for Betelgeuse. It consists of a detailed mean density and temperature 1-D model and is based on the spatially resolved VLA data of Lim *et al.* (1998). In this model the temperature distribution peaks at $1.45 R_\star$ where it reaches ~ 3800 K and decreases to ~ 1200 K at $10 R_\star$. The dominant source of electrons is from photoionized metals while hydrogen has a low level of ionization. We use this model to create a two-dimensional axisymmetric specific intensity map to examine how it compares with the new e-MERLIN high resolution data at 5.2 cm (5.75 GHz). As shown in Figure 5.16, we convolved this map with a restoring beam, first with dimensions 180×180 mas 2 to match the low resolution e-MERLIN image and then with dimensions 80×60 mas 2 to match the high resolution e-MERLIN image. As can be seen from Figure 5.16, the atmospheric model of Harper *et al.* (2001) does a good job in reproducing the low resolution e-MERLIN image but, as would be expected from a spherically symmetric 1-D model, fails to reproduce the more complex structure which is seen in the higher resolution e-MERLIN image. The advent of the new e-MERLIN interferometer with its superior spatial resolution to that of the VLA has revealed that 1-D spherically symmetric atmospheric models are probably inadequate to describe the inner wind conditions of Betelgeuse. Time dependent models which radically diverge from spherical symmetry will ultimately be needed to accurately describe the inner atmospheric conditions of Betelgeuse.

5.13 VLA-Pie Town Maps Versus e-MERLIN

At the end of Chapter 3 the VLA-Pie Town observations of Betelgeuse from the early 2000s were described, along with the motivation for analyzing it. In

5.13 VLA-Pie Town Maps Versus e-MERLIN

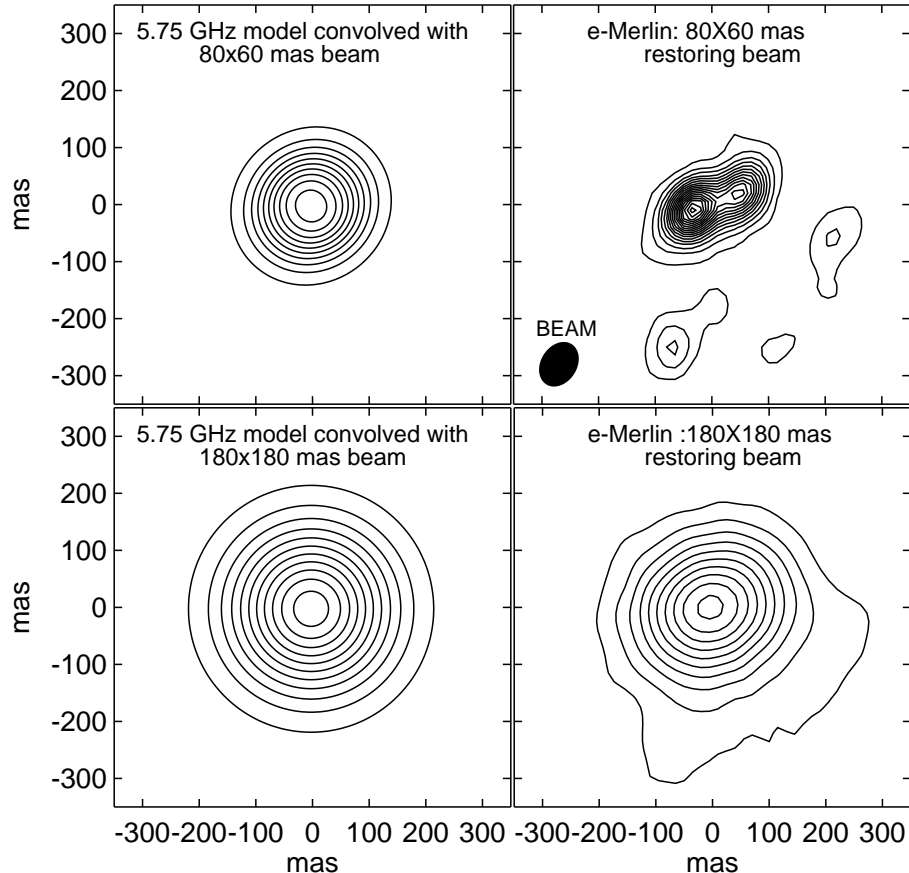


Figure 5.16: *Left column:* Two-dimensional specific intensity contour maps at 5.2 cm (5.75 GHz) created using the 1-D inner atmospheric model of Betelgeuse by Harper *et al.* (2001). The maps have been convolved with a beam having dimensions $80 \times 60 \text{ mas}^2$ (top) and $180 \times 180 \text{ mas}^2$ (bottom). *Right column:* The observed high (top) and low (bottom) resolution e-MERLIN images. The high resolution image is poorly described by the model of Harper *et al.* (2001) highlighting the inadequacies of 1-D spherically symmetric models in describing the inner atmosphere of Betelgeuse. Contour levels are $(4, 8, 12, \dots) \times \sigma_{\text{rms}}$ where $\sigma_{\text{rms}} = 6 \mu \text{Jy}$ in the top row and $\sigma_{\text{rms}} = 27 \mu \text{Jy}$ in the bottom row.

summary, we wanted to see if there were some signatures of the e-MERLIN asymmetries in the data set. This is because the Pie-Town link, when connected to the VLA, provides spatial resolution comparable to or exceeding that of the high resolution e-MERLIN image at the shortest wavelengths. The two main features present in the e-MERLIN map were separated by $\sim 90 \text{ mas}$ and so the most in-

5.13 VLA-Pie Town Maps Versus e-MERLIN

teresting VLA-Pie Town data sets were the 0.7, 1.3, and 2.0 cm maps which had restoring beams of $\sim 40 \times 25$, $\sim 80 \times 40$, and $\sim 120 \times 90$ mas² when imaged with uniform weighting.

All the data sets listed in Table 3.8 were CLEANed using uniform weighting and using a conservative, slow CLEAN to accommodate the frequent elliptical shape of the beam caused by the Pie Town link. The images were subsequently investigated for signs of asymmetries. The 6 cm VLA-Pie Town data sets had synthesized beams typically of size $\sim 380 \times 270$ mas² which were too large to be capable of resolving the structures seen with e-MERLIN at similar wavelengths. As expected, the VLA-Pie Town 6 cm images show no signs of asymmetries. In fact, all data sets at wavelengths at or longer than 1.3 cm show no obvious asymmetries apart from that caused by the asymmetric nature of the restoring beam. This is surprising because the north-west location of the Pie Town antenna relative to the VLA array results in an elliptical beam with a semi-minor axis lying in the same direction as that of the two peaks seen with e-MERLIN, i.e., the beam shape should be well suited to resolving these peaks. There are two possible reasons why the shorter wavelength VLA-Pie Town maps do not contain the asymmetries which are present in the longer wavelength e-MERLIN map:

1. In an ionized or partially ionized outflow, the radio opacity, $\kappa_\lambda \propto \lambda^{2.1}$. This means that the longer wavelengths probe farther out in the atmosphere than the shorter wavelengths. It is possible that at the short wavelengths (where the VLA-Pie Town data have the capability to resolve these features) the outer atmosphere where the features are located is optically thin (i.e., $\tau_\lambda \ll 1$), and therefore the features are not present in the short wavelength VLA-Pie Town maps. However, the e-MERLIN data have shown that the outflow is clearly not spherically symmetric. In fact, the radio opacity also varies as, $\kappa_\lambda \propto n_e n_{\text{ion}}$, and because the e-MERLIN features should be more ionized than the surround plasma, they could expect to be present even at the shortest wavelengths.
2. The VLA-Pie Town data were taken ~ 10 yr prior to the e-MERLIN data when the separation of the two peaks may have been less. This reduction in separation could be so significant that they could be unresolvable even at the

5.14 Long Term Radio Variability and Thermal Structure

shortest wavelengths. Let us now consider this possibility and estimate their separation 10 yr prior to the e-MERLIN observations. First, as highlighted in the Section 5.12, the astrometric solutions of Harper *et al.* (2008) indicate that the star is located on the weaker emission peak. If we then assume that the stronger emission peak has been moving away from the star at the velocity of the S1 flow (i.e., 10 km s^{-1}) then the distance traversed in 10 yr would be $\sim 4.8 R_\star$ which means that these features would not have been present. However, the outflow is still expected to be accelerating with velocities only between $1 - 7 \text{ km s}^{-1}$ within these spatial scales (Carpenter & Robinson, 1997) and so the actual distance traversed is probably much less than $4.8 R_\star$.

At these spatial scales the structural changes over a few years will probably be important and may be the reason for not seeing the expected asymmetries in the VLA-Pie Town data. In fact, if the star is close to the center of these two peaks as was assumed by Richards *et al.* (2013), then the two features are presumably moving away from each other which would strengthen the idea that time variability is the reason why they are not seen in the VLA-Pie Town data. The discovery of these bright radio peaks by Richards *et al.* (2013) along with their notable absence in data with superior resolution less than 10 yrs before (albeit at higher frequencies) is a compelling case for consistent monitoring with e-MERLIN over a number of years at multiple wavelengths.

5.14 Long Term Radio Variability and Thermal Structure

Betelgeuse's atmosphere is optically thick at radio wavelengths allowing its radio flux to be characterized as resulting from an opaque disk with $F_\nu \propto T_e \phi_\nu^2$. This relationship tells us that variations in radio flux are caused by either changes in size or changes in the gas temperature distribution. The size of the radio emitting region is controlled mainly by the distribution in ionized material. Betelgeuse has been observed at radio wavelengths since the mid 1970's (e.g. Newell & Hjellming, 1982). Bookbinder *et al.* (1987) found that the 6 cm flux can vary by as much

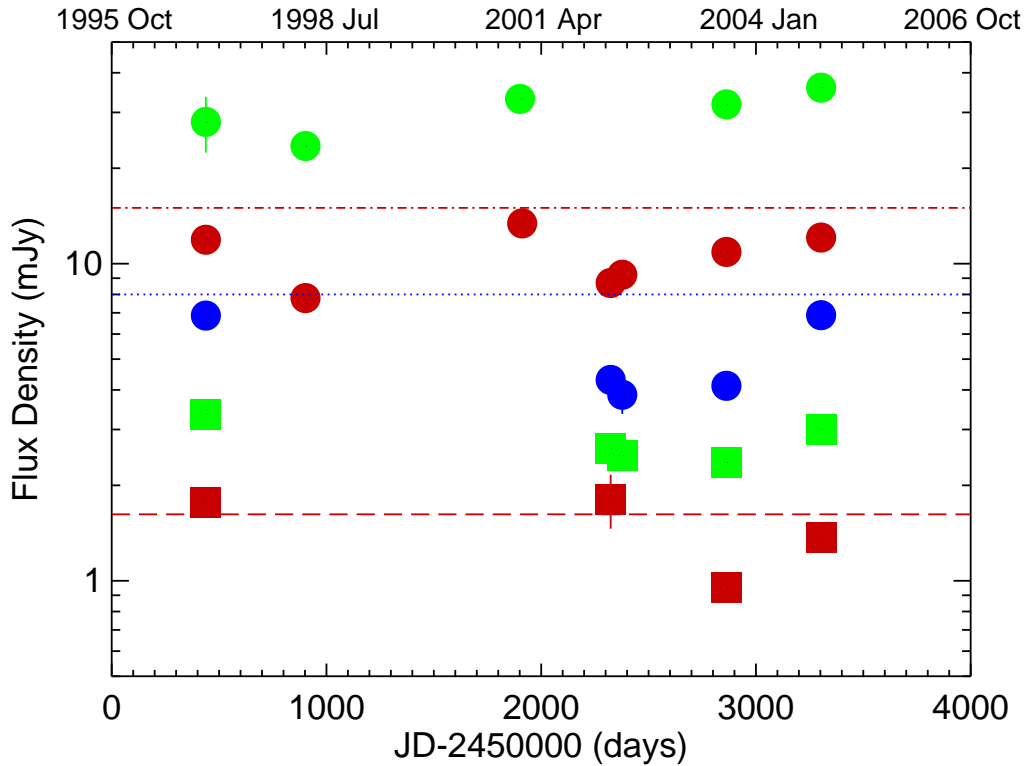


Figure 5.17: Radio flux density variation of Betelgeuse between 1996 and 2004. The green, red, and blue filled circles are the 0.7, 1.3, and 2.0 cm measurements respectively, while the green and red filled squares are the 3.5 and 6.2 measurements, respectively. The red dot-dash line and the blue dotted line represent the mean of two 1.3 and 2.0 cm flux density values taken between 1978-1981 and when their error values are included, are not significantly different from our data. The dashed red line represents the e-MERLIN 6 cm flux from 2012 and lies within the range of 6 cm values observed between 1996 and 2004. Note: Most error bars are located inside their data points.

as $\sim 40\%$ over a 20 day timescale, while Drake *et al.* (1992) monitored the star over a four year period and reported stochastic flux variability at 2.0 and 3.6 cm of $\lesssim 25\%$ and possibly at 6 cm on a timescale $\lesssim 1$ month. Here we report on how the radio flux has varied during the period 1996 – 2004 using the measurements of Lim *et al.* (1998) and the VLA-Pie Town data.

To obtain a value for the total flux density at each wavelength and epoch, we fitted 2-D Gaussians to the source to obtain the integrated flux. To get a better

5.14 Long Term Radio Variability and Thermal Structure

fit to the 0.7cm data, (where the source size was found to be asymmetric as outlined in the next section) we re-imaged the visibilities using natural weighting and then carried out the fit. We plot the resulting flux densities against time in Figure 5.17 and also include the measurements of Lim *et al.* (1998). We find significant variability at all wavelengths and at all epochs apart from the 2002 data sets which were only obtained two months apart from each other. Over the 10yr period, the maximum variability is found to be 23, 27, 32, 21, and 35% at 0.7, 1.3, 2.0, 3.5, and 6.2cm respectively, which are similar to those reported by Drake *et al.* (1992) and Bookbinder *et al.* (1987). The shortest wavelengths (i.e., 0.7 and 1.3cm) are the most sampled and although there are only five data points at these wavelengths to compare, there does appear to be a correlation in their flux variability. The contribution functions given in Harper *et al.* (2001) show that the peak flux contribution at both 0.7 and 1.3cm come from a similar region of the atmosphere (i.e., $\sim 1.2 R_\star$) and so at these wavelengths a correlation is not surprising.

The red dot-dash line and the blue dotted line in Figure 5.17 represent the mean of the two 1.3 and 2.0cm flux density values between 1978 – 1981 (Newell & Hjellming, 1982) which are not significantly different from our maximum measurements at the same wavelengths. This would indicate that there has been no significant long term change in atmospheric or thermal structure over ~ 3 decades. However, the flux variability may be a manifestation of significant structural changes or thermal changes over the order of only a few years. The dashed red line represents the 6cm flux of Richards *et al.* (2013) which lies within the range of 6cm values observed between 1996 and 2004. This is surprising because most of the 6cm flux in the e-MERLIN map is contained in the two bright features and, as we see no evidence for these features in our VLA-Pie Town data, we would expect the 6cm flux in the e-MERLIN map to be larger. This adds weight to the idea discussed in Section 5.13 that the e-MERLIN feature(s) are optically thin at the shorter VLA wavelengths and therefore are not detectable in our highest resolution data sets. Nevertheless, the large variations at 6cm could still indicate that these features undergo large structural changes on timescales of only a few years or perhaps even shorter.

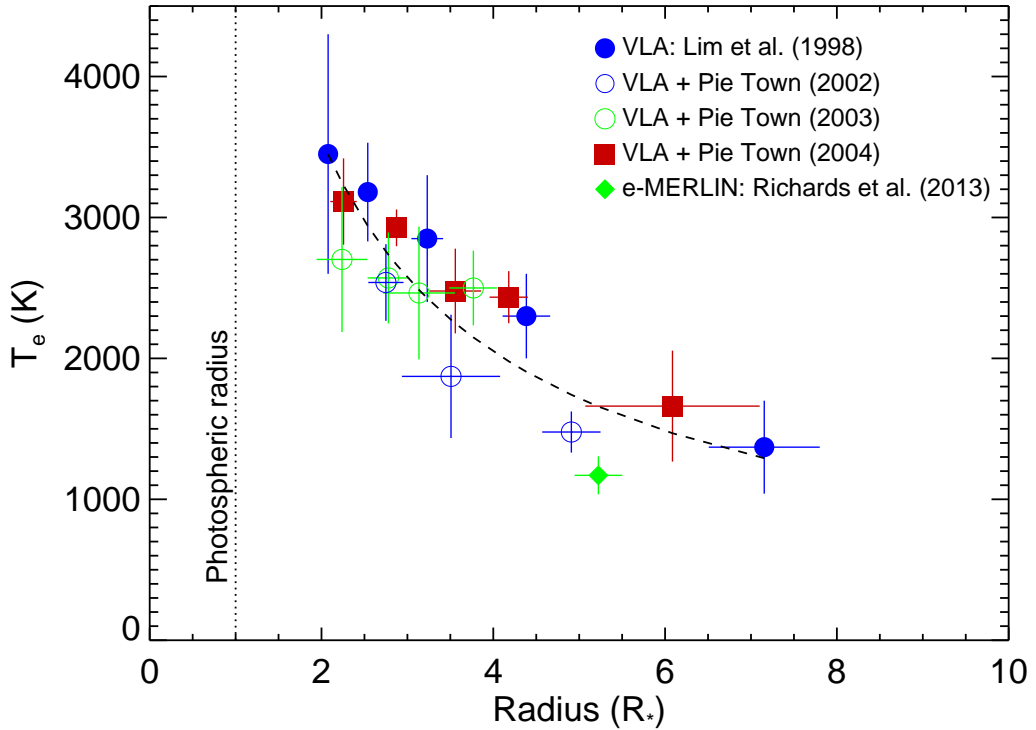


Figure 5.18: Mean thermal profile of Betelgeuse’s inner atmosphere using spatially resolved radio data spanning 1998–2013. Our VLA + Pie Town data confirm the relatively low temperature (< 4000 K) of Betelgeuse’s expended atmosphere. Uniform bright disks were fitted to the calibrated visibilities at each wavelength allowing the temperature to be derived as a function of distance from the star. The dashed line represents the power-law fit, $T_e \propto r^{-0.79}$, to the electron temperature.

To verify that our 2-D Gaussian fits to the radio images produced accurate total flux density values, we fitted uniform disks to the calibrated visibilities. We found that all flux density values produced using this method were in good agreement with the values plotted in Figure 5.17. Fitting circular disks to the measured visibilities was a method used by Lim *et al.* (1998) to quantify not only the total flux, but also the area of the region where the radio emission is emanating from. Knowing this area, the brightness temperature (and thus the electron temperature) can be calculated using Equation 1.45. We followed the same method and applied this equation to our VLA-Pie Town data. The derived electron temperature as a function of distance from the star is plotted

in Figure 5.18 along with the values from Lim *et al.* (1998) and the single value from Richards *et al.* (2013) (which was derived by fitting a 2-D ellipse to the low resolution e-MERLIN data set and finding the area of the Gaussian). Although there appears to be some variability in the mean electron temperature at various epochs, our values are consistent with a relatively low temperature wind, which was one of the main findings of Lim *et al.* (1998).

A detailed discussion on how spectral indices can be used to infer properties of stellar winds is presented in Chapter 6. For now, we note that if the electron temperature and density are represented as different power laws in radius, then a simple relationship exists between the power-law coefficients and the spectral index (see section 6.5). The mean spectral index between 4.5 and 43 GHz over all epochs is found to be $\alpha = 1.31$, while the dashed line in Figure 5.18 represents the derived power-law fit, $T_e \propto r^{-0.79}$, to the electron temperature. These two values can then be used to derive a power law for the density of $n_e \propto r^{-2.93}$, which is in excellent agreement with the semi-empirically derived value of $n_e \propto r^{-2.85}$ from Harper *et al.* (2001).

5.15 0.7 cm VLA-Pie Town Maps

All the VLA-Pie Town data were imaged using uniform weighting where each unit of area in the $u - v$ plane is given the same weight irrespective of the number of visibility measurements it contains. The 0.7 cm (i.e., Q band) maps are presented in Figure 5.19 and were the only maps to show significant asymmetric structure in them. The 2004 and 2003 data contain two and three distinct unresolved features respectively, all separated from each other by only ~ 40 mas. The elongated restoring beam in the 2000 data set makes it difficult to detect any distinct features in the north south direction although asymmetries are clearly present at a high level of significance. Finally the 1998 data set which does not contain the Pie Town link but has a very circular restoring beam once again looks highly asymmetric but in a different direction to the other epochs.

These high spatial resolution data sets indicate dramatic changes in the radio emitting morphology over a time period of only one to two years. However, before drawing conclusions on the variation of the morphology, it is important to

5.15 0.7 cm VLA-Pie Town Maps

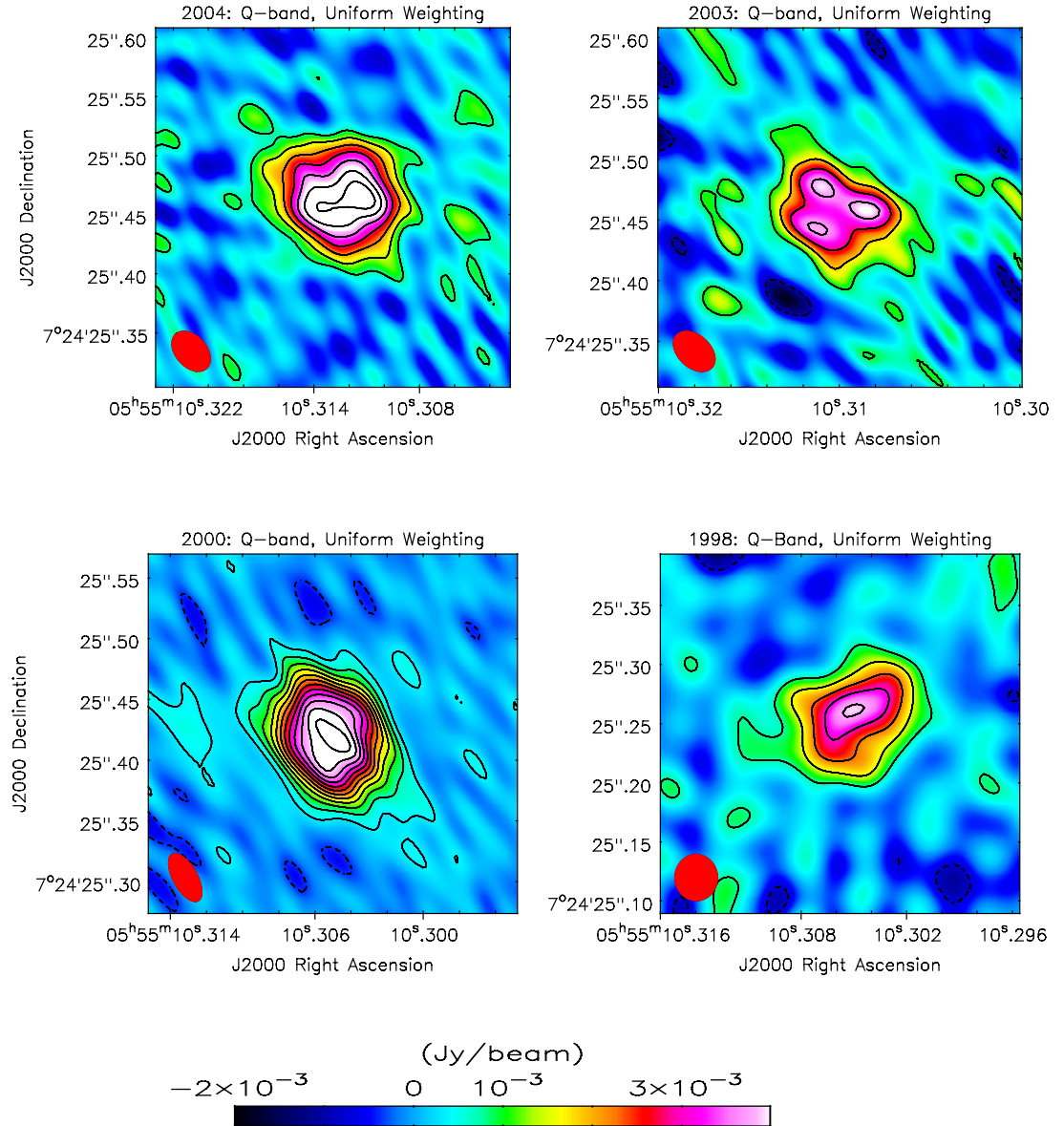


Figure 5.19: High resolution Q band images of Betelgeuse spanning six years. Asymmetries in the inner atmosphere are clearly present in all images. Image contours are set at $(2, 4, 6, \dots, 24) \times \sigma_{rms}$ where $\sigma_{rms} = 0.35, 0.46, 0.18$, and 0.38 mJy for the 2004, 2003, 2000, and 1998 data respectively. The restoring beam is shown in red at the bottom left corner of each image. The 1998 data does not contain the Pie Town link and thus has a more circular restoring beam. The color scheme in all images have the same scaling, i.e., between -2 and $+4 \text{ mJy}$. Each image represents $300 \times 300 \text{ mas}^2$ in area.

5.15 0.7 cm VLA-Pie Town Maps

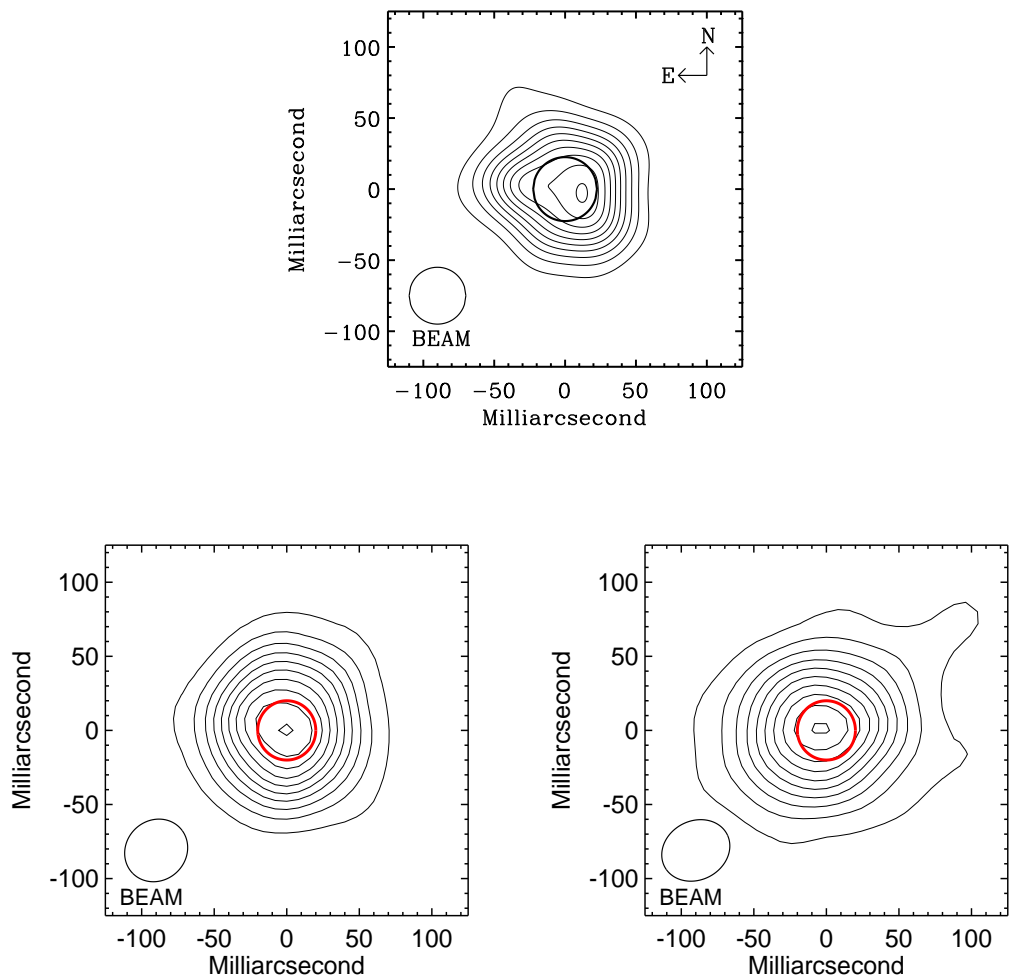


Figure 5.20: VLA A-configuration (no Pie Town link) Q band maps of Betelgeuse. These images were constructed using natural weighting and using a restoring beam with size corresponding to that produced by uniform weighting. Contours are 10%, 20%, ..., 90%, and 99% of peak intensity. The black and red circles at the center of all images represent the optical photosphere. *Top panel:* Betelgeuse observed by Lim *et al.* (1998) in 1996 with clear asymmetries present. *Bottom panel:* Betelgeuse observed in 2000 (left) and 2004 (right) with no clear asymmetries present.

point out that different imaging techniques on these data sets can produce inconsistencies in the morphology. For example, uniform weighting does not produce the same morphology as does using natural weighting with a restoring beam of size corresponding to that produced with uniform weighting. Such inconsisten-

cies in structure are probably due to poor phase stability resulting from rapid tropospheric phase fluctuations. To investigate this further, we removed the Pie Town antenna baselines and again imaged the data using the two aforementioned imaging techniques. We found that two data sets (i.e., from 2000 and 2004) produced images that had consistent morphology when either of the two imaging techniques were applied. The observing logs of the other data sets report poorer weather conditions in agreement with our imaging analysis. The resulting images are plotted in Figure 5.20 along with the Q band image from Lim *et al.* (1998) for comparison. In these data sets, the cycle time was adequate to obtain reasonable phase transfer from the calibrator to the source but shorter cycle times were probably required for the other data sets due to poorer weather. Unlike the Lim *et al.* (1998) map, no asymmetries are present in either of our two maps as is clearly evident in Figure 5.20. As these Q band maps probe Betelgeuse's chromosphere, our maps indicate that large scale asymmetries are not always present in this region of the atmosphere. Monitoring of Betelgeuse with the new Karl G. Jansky VLA at Q band should tell us on what time scale these asymmetries vary on and also if they are related to the asymmetries detected at shorter wavelengths (e.g., Buscher *et al.*, 1990; Chiavassa *et al.*, 2010; Tuthill *et al.*, 1997; Wilson *et al.*, 1992).

5.16 VLA, VLA-Pie Town, e-MERLIN: Putting it all together

Our VLA-Pie Town data are in good agreement with the findings of Lim *et al.* (1998). We find that the mean electron temperature falls from a value of ~ 3000 K at $\sim 2 R_\star$ to 1500 K at $\sim 6 R_\star$. Our 0.7 cm radio maps show even more dramatic asymmetries than those seen by Lim *et al.* (1998) when the Pie Town baselines are included; but inconsistencies in the morphology during the imaging process indicate that phase stability may be a problem. Our VLA A-configuration Q band maps contain no asymmetries and we conclude that the inner atmosphere contains no long term large scale asymmetries. The recent e-MERLIN findings of two unresolved *hotspots* separated by 90 mas (i.e., $4 R_\star$) are difficult to explain by referring to our VLA-Pie Town data. Surprisingly, we find no evidence for these

5.16 VLA, VLA-Pie Town, e-MERLIN: Putting it all together

features at any wavelengths in our data sets. There are two ways to account for this. The first is that these features are highly time variable and were not as extended, or maybe not even present, when our VLA-Pie Town measurements were taken. The other alternative is that these features are optically thin at the high frequencies where we should have sufficient spatial resolution to resolve them from each other.

Since the majority of the radio flux at 6 cm, is contained within two compact features, it is worth asking the question: “what does the electron temperature profile plotted in Figure 5.18 represent?”. e-MERLIN has shown that at 6 cm at least, the values representing the wind temperature found by Lim *et al.* (1998) are not a true representation of the actual values. If such hotspots were present at higher frequencies again, then we could make the same conclusion about the inaccuracy of the temperature profile throughout the inner atmosphere. This would have major consequences for the theory of mass-loss in Betelgeuse (and M supergiants in general) as the conclusion of Lim *et al.* (1998) was that magnetic waves, acoustic waves, and pulsations all required higher atmospheric temperatures than those found, and were thus not the source of Betelgeuse’s mass-loss. High resolution, multi-wavelength, multi-epoch observations will finally help solve the puzzle as to what is driving Betelgeuse’s mass-loss.

6

Multi-wavelength Radio Continuum Emission Studies of Dust-free Red Giants

The vast increase in bandwidth coverage of the new VLA now allows possible detections of historically weak or undetectable red giants at multiple radio wavelengths. In this chapter, we present and analyze the most comprehensive set of multi-wavelength thermal radio continuum observations of two standard luminosity class III red giants, Arcturus (α Boo: K2 III) and Aldebaran (α Tau: K5 III), to date. We report the first detections at several wavelengths for each star including a detection at 10 cm (3.0 GHz: S band) for both stars and a 20 cm (1.5 GHz: L band) detection for α Boo. This is the first time single luminosity class III red giants have been detected at these continuum wavelengths. We compare our data with published semi-empirical atmospheric models based on UV data, and spectral indices are used to discuss the possible properties of the stellar atmospheres. Finally, we develop a simple analytical wind model for α Boo based on our new long wavelength flux measurements. This chapter is based on the main results of O’Gorman *et al.* (2013).

6.1 Why Study Red Giants with the VLA?

Although studies of wind-scattered UV and optical line profiles have provided clues to the mass-loss rates and radial distribution of the mean and turbulent velocity fields, the thermal structure remains poorly constrained. In the UV, the source function S_ν , of electron collisionally excited emission lines is sensitive to electron temperature T_e , (i.e., $S_\nu \propto e^{-h\nu/kT_e}/\sqrt{T_e}$). Therefore, a localized hot plasma component in a dynamic atmosphere can completely dominate the temporally and spatially averaged emission and hence not reflect the mean radial electron temperature distribution. At radio wavelengths however, the source function is thermal and is just the Rayleigh-Jeans tail of the Planck function, which is linear in electron temperature (i.e., $S_\nu = 2kT_e\nu^2/c^2$). This should give a more appropriate estimate of the mean radial electron temperature. It is this value that controls the atomic level populations and ionization of the mean plasma which is needed to quantify the implied thermal heating supplied to the wind by the unknown driving source/sources, allowing constraints on potential mass-loss mechanisms to be derived.

In the cm-radio regime the radio opacity κ_λ , strongly increases with wavelength (i.e., $\kappa_\lambda \propto \lambda^{2.1}$) and so the longer wavelengths sample the extended layers of a stars atmosphere, thus providing us with spatial information about the star's mass outflow region. The VLA is sensitive to over three orders of magnitude in continuum optical depth τ_λ , ($\tau_{20 \text{ cm}}/\tau_{0.7 \text{ cm}} \approx 10^3$) and provides an area-averaged sweep through the wind acceleration zone of evolved late-type stars. The thermodynamic properties in this spatial region control the ionization in the far wind because the ionization balance, which also controls the cooling rates, becomes *frozen-in* at large radii due to advection. Furthermore, it is these outer extended regions of the star's atmosphere that contribute to the commonly seen P Cygni line profiles in the UV. In these profiles the line-of-sight absorption caused by the star's wind is superimposed on the blueshifted scattered emission. Thus, centimeter radio continuum observations can provide a test of models based on these UV profiles.

Despite the importance of radio continuum emission as a tool for studying cool evolved stellar outflows, red giants are feeble emitters at these wavelengths

however, and previous observations have provided only a small number of modest signal-to-noise measurements slowly accumulated over three decades. As most of our VLA observations were carried out over just a few days, we have obtained a unique snapshot of the different stellar atmospheric layers sampled at different wavelengths, independent of any long-term variability.

6.2 Radio Maps

Apart from α Boo at C band and α Tau at S band, detections were made in every sub-band for the 2011 data. For all other bands, the flux densities of the targets in both sub-bands were found to be the same within their uncertainties so we do not present separate values here. Instead we give the values from the radio maps produced by concatenating the two sub-bands. We present in Table 6.1 the target flux densities extracted from these concatenated radio maps. In each of these maps the flux density from the unresolved target source was calculated by, 1) taking the peak pixel value from the source, 2) manually integrating the flux density around the source, and 3) fitting an elliptical Gaussian model to the source and deriving the integrated flux density using the CASA *imfit* task. Each of these values along with the image rms noise measured from adjacent background regions and fitting error produced by *imfit* are given in Table 6.1 to indicate the quality of each radio map. Both sources are point sources at all frequencies so the peak flux value given in Table 6.1 will also be its total flux density value. For weak detections (i.e., $F_\nu \lesssim 5\sigma$) we avoid using the *imfit* task to obtain a flux density estimate, as this may produce biased parameter estimates (Taylor *et al.*, 1999). The flux density values used in the following Sections are the peak values listed in Table 6.1. We assume absolute flux density scale systematic uncertainties of 3% at all frequencies (Perley & Butler, 2013). In the following two sections we briefly discuss the properties of these maps for both targets which are shown in Figure 6.1.

6.2.1 α Boo Maps

High S/N detections ($>19\sigma$) of α Boo were made at 22.5, 33.6, and 43.3 GHz. Some residuals of the dirty beam remained in the CLEANed maps due to the

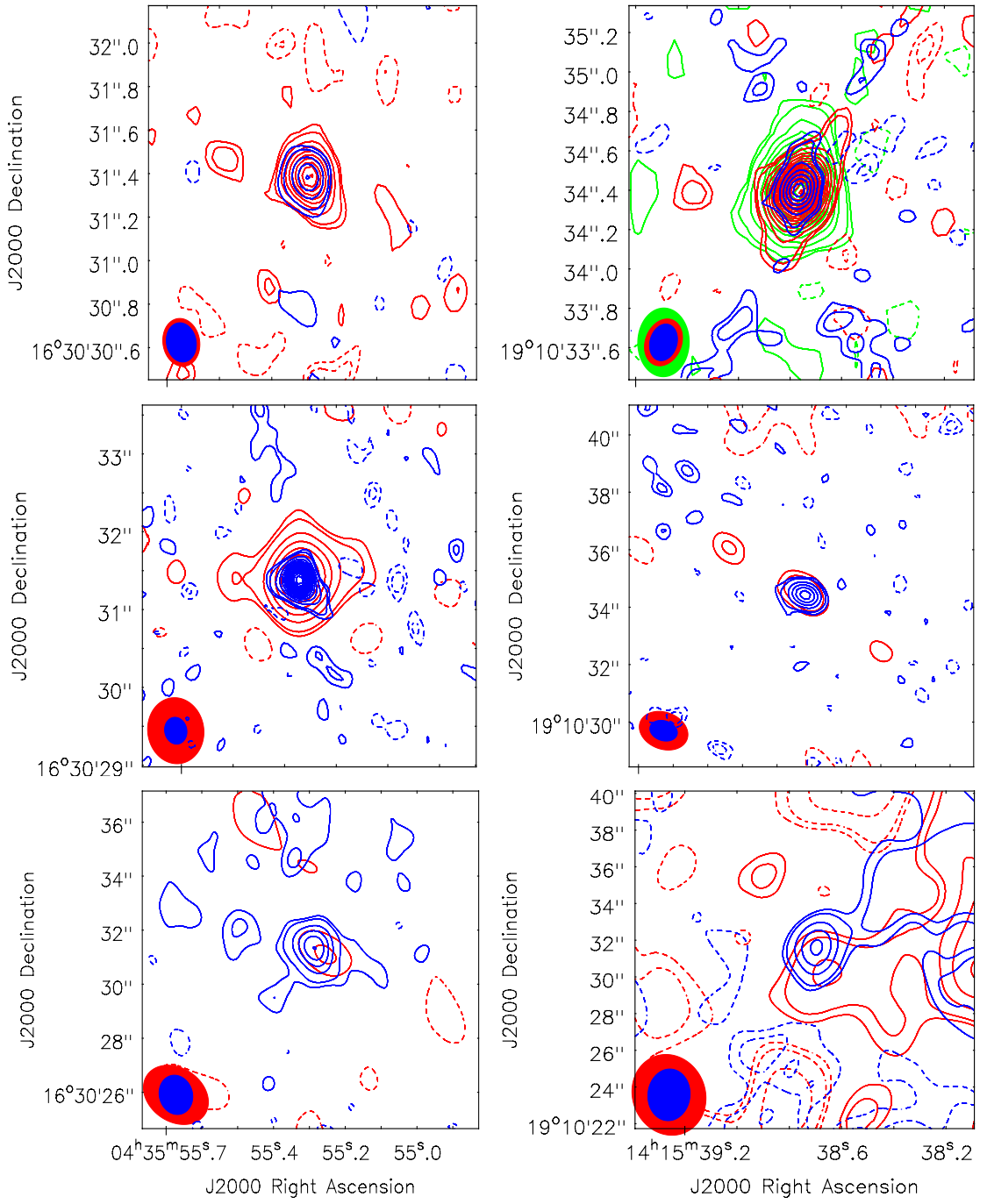


Figure 6.1: Final VLA multi-wavelength radio maps of α Tau and α Boo. *Left column:* Q and Ka band (top), K and X band (middle), C and S band (bottom) maps of α Tau. *Right column:* Q, Ka, and K band (top), X and C band (middle), S and L band (bottom) maps of α Boo. Contour levels are set at $(-6, -3, -2, +2, +3, +6, +9, \dots) \times \sigma$ where σ is the rms noise of each radio map. For α Boo, artifacts from the dirty beam can be seen in the Q band map, while artifacts caused by the serendipitous strong source in the S and L band maps are also present.

Table 6.1: VLA Flux Densities of α Boo and α Tau.

Star	Band	ν^a (GHz)	λ (cm)	Peak F_ν (mJy beam $^{-1}$)	Integrated F_ν (mJy)	<i>Imfit</i> Integrated F_ν (mJy)	Image rms (mJy beam $^{-1}$)	<i>Imfit</i> Fitting Error (mJy)
α Boo	Q	43.28	0.7	5.94	6.09	6.42	0.30	0.26
	Ka	33.56	0.9	4.16	4.32	4.49	0.08	0.09
	K	22.46	1.3	1.83	1.78	1.81	0.04	0.05
	X	8.46	3.5	0.51	0.51	0.53	0.03	0.02
	C	4.90	6.1	0.21	0.14	0.16	0.04	0.01
	S	3.15	9.5	0.15	0.14	-	0.03	-
	S	2.87	10.4	0.13	0.12	0.12	0.01	0.02
	L	1.63	18.4	0.07	0.07	-	0.01	-
α Tau	Q	43.28	0.7	3.67	3.73	4.08	0.26	0.18
	Ka	33.56	0.9	2.19	1.96	2.13	0.09	0.07
	K	22.46	1.3	1.86	1.88	2.07	0.04	0.08
	X	8.46	3.5	0.30	0.29	0.28	0.01	0.02
	C	4.96	6.0	0.15	0.17	0.18	0.01	0.01
	S	3.15	9.5	0.06	0.04	-	0.02	-

^aFrequency of the final image produced using the multi-frequency synthesis imaging mode within CASA's *clean* task.

paucity of uv-coverage in these short high frequency observations (see Figure 6.1, top right panel). At the lower frequencies, it was necessary to image confusing sources, notably a strong radio source located 186'' north-west of α Boo. This non-thermal source was reported by Drake & Linsky (1983a) and their flux density of 25 mJy at 4.9 GHz is in close agreement with our measurement of 23.2 mJy at the same frequency. We find the source to have a spectral index α ($F_\nu \propto \nu^\alpha$) of -1.4 between 8.5 and 1.6 GHz; its flux density reaches 80.3 mJy at 1.6 GHz.

We detected α Boo at 6σ in the lower frequency sub-band of C band, at 4.9 GHz. The noise was slightly higher and the images were poorer quality in the C band higher frequency sub-band, with artifacts exceeding $\pm 200 \mu\text{Jy}$, and we cannot report a detection in this sub-band, so values given in Table 6.1 are taken from the lower frequency sub-band only. We obtain good detections ($>5\sigma$) of the star for both epochs at ~ 3 GHz (S band) and the peak flux densities agree within their uncertainties. We can therefore safely assume that the 1.5 GHz (L band) flux density has not changed significantly over that period either, and so can safely be included in any analysis. The map at L band was highly contaminated by the sidelobes of the strong source north-west of α Boo but the star is still detected at the 5σ level. There is a slight positional offset of 1'' between the position of the peak flux density at 1.5 and at 3.0 GHz for the 2012 data, which were taken within 1 day of each other. However, the position uncertainties due to noise and phase uncertainties between the directions of the phase reference source and the target are at least 1'', and so we feel that it is highly likely that both detections are of α Boo.

6.2.2 α Tau Maps

The final deconvolved radio maps of α Tau were of excellent quality with the rms noise reaching the predicted noise levels in many cases. The target field at all frequencies was free from strong serendipitous radio sources and thus the final images were free of the sidelobe contamination that were present in the low frequency α Boo images. α Tau was the only source in the high frequency maps while the brightest source in the low frequency maps was located 106'' north north-east of α Tau and had flux densities of 0.85, 1.35, and 1.7 mJy at 8.5, 5.0,

6.3 Results Versus Previous Observations

and 3.5 GHz, respectively. Detections of high significance ($>14\sigma$) were made at all frequencies between 5.0 and 43.3 GHz for α Tau. Due to the limited number of S band receivers available at the time, a full 2.5 hr track was dedicated to α Tau at 3.1 GHz in order to achieve the required sensitivity to give a possible detection. We report a tentative 3σ detection of α Tau at 3.1 GHz when we take its peak pixel value as its total flux density.

6.3 Results Versus Previous Observations

Prior to and during the early operation of the “old” VLA, a small number of single dish radio observations, such as those from the Arecibo (Boice *et al.*, 1981) and Parkes (Slee *et al.*, 1989) radio telescopes, reported the detection of flares from single red giants. These transient radio events have never been re-observed however, even with more sensitive interferometers, suggesting that such detections were spurious (e.g., Beasley *et al.* 1992). The first definitive detection of thermal free-free emission from a luminosity class III single red giant at centimeter wavelengths was of α Boo at 6 cm (Drake & Linsky, 1986, 1983a). Since then there has been a modest number of centimeter and millimeter observations of this star. In Table 6.2 we list the majority of these observations and plot their flux densities as a function of frequency in Figure 6.2 (red diamonds). In comparison to other single red giants, α Boo had been relatively well observed at radio continuum wavelengths before this study, including detections in four VLA bands (i.e., Q, K, Ku, and C). No Ku band receivers were available during the commissioning phase of the VLA in early 2011 so we can compare three of our detections with previous ones.

Previous detections of α Boo at 6 cm ranged from a 3σ upper limit of 0.18 mJy to a 3σ detection at 0.39 mJy. Our 6 cm value agrees to within $\sim 10\%$ of the highest S/N (5σ) value of Drake & Linsky (1986). There is no significant difference between our 1.3 cm value and that of Dehaes *et al.* (2011). There is however a notable difference in flux density values at 0.7 cm where Dehaes *et al.* (2011) report values that are lower than ours by over 40%. Although we do not rule out such a level of chromospheric radio variability, it is not expected based on the small level of UV variability observed from such supposedly inactive stars

6.3 Results Versus Previous Observations

Table 6.2: Compilation of Previous Radio Observations ($\nu \leq 250$ GHz).

Source	ν (GHz)	Date	F_ν (mJy)	S/N	Reference
α Boo	4.9	1983 Jan 21	0.39	3.0	1
	4.9	1983 May 20	0.26	3.3	1
	4.9	1983 Dec 26	$\leq 0.18(3\sigma)$	-	1
	4.9	1984 Mar 17	0.24	4.8	1
	15.0	1984 Nov 6	0.68	7.6	1
	22.5	1999 Jan 06	1.7	8.5	2
	43.3	1999 Jan 06	3.3	8.3	2
	43.3	2004 Jan 25	3.34	41.8	2
	86.0	1985 Nov	21.4	3.0	3
	108.4	1997 Nov - 2000 Jun	20.1	29.1	4
α Tau	217.8	1997 Nov - 2000 Jun	83.5	48.8	4
	250.0	1986 Dec - 1989 Mar	78.0	9.8	5
	4.9	1983 Jan 21	$\leq 0.27(3\sigma)$	-	1
α Tau	4.9	1984 Nov 6	$\leq 0.22(3\sigma)$	-	1
	5.0	1997 Sep 27	$\leq 0.07(3\sigma)$	-	6
	8.5	1997 Sep 27	0.28	9.3	6
	14.9	1997 Sep 27	0.95	11.9	6
	15.0	1984 Nov 6	0.60	6.0	1
	108.4	1997 Nov - 2000 Dec	14.0	9.6	4
	217.8	1999 Sep - 2000 Dec	25.8	4.6	4
	250.0	1986 Dec - 1987 Jan	51.0	8.5	5

References.-(1) Drake & Linsky (1986); (2) Dehaes *et al.* (2011); (3) Altenhoff *et al.* (1986); (4) Cohen *et al.* (2005); (5) Altenhoff *et al.* (1994); (6) Wood *et al.* (2007).

(Harper *et al.*, 2013). Another possibility for the difference in values is that the longer cycle time used by Dehaes *et al.* (2011), which was over double our value, may lead to larger phase errors and thus lower final flux density values. Future high frequency VLA observations of α Boo will clarify this discrepancy at 0.7 cm but past detections at longer wavelengths appear to be in good agreement with our data.

In Figure 6.3 we plot the previous radio measurements of α Tau at all frequencies below 250 GHz (i.e., > 0.12 cm). Prior to this study, α Tau had only been detected at two VLA bands (i.e., X and Ku) and had never been detected

6.3 Results Versus Previous Observations

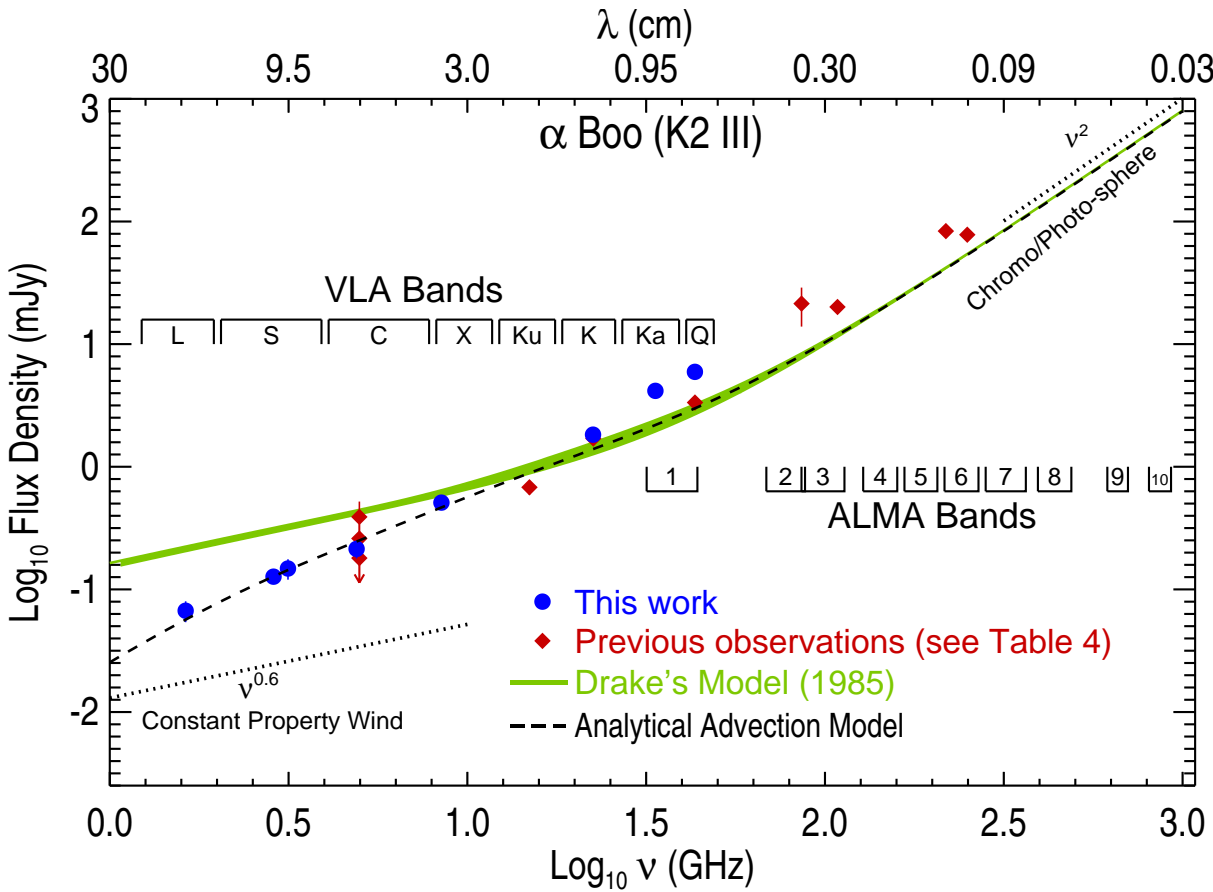


Figure 6.2: Spectral energy distribution of α Boo for $1 \text{ GHz} \leq \nu \leq 1 \text{ THz}$. Our new multi-frequency VLA observations which were mainly acquired over a few days in February 2011 are the blue circles and disagree with the existing chromospheric and wind models of Drake (1985). The overlap between the two models is represented by the green shaded area. The red diamonds are previous observations which were acquired sporadically over the last three decades with the ‘old’ VLA, IRAM and BIMA. The black dashed line is the expected radio emission from the Drake model which undergoes rapid wind cooling beyond $\sim 2.3 R_\star$ (see Section 6.5 and 6.6).

6.3 Results Versus Previous Observations

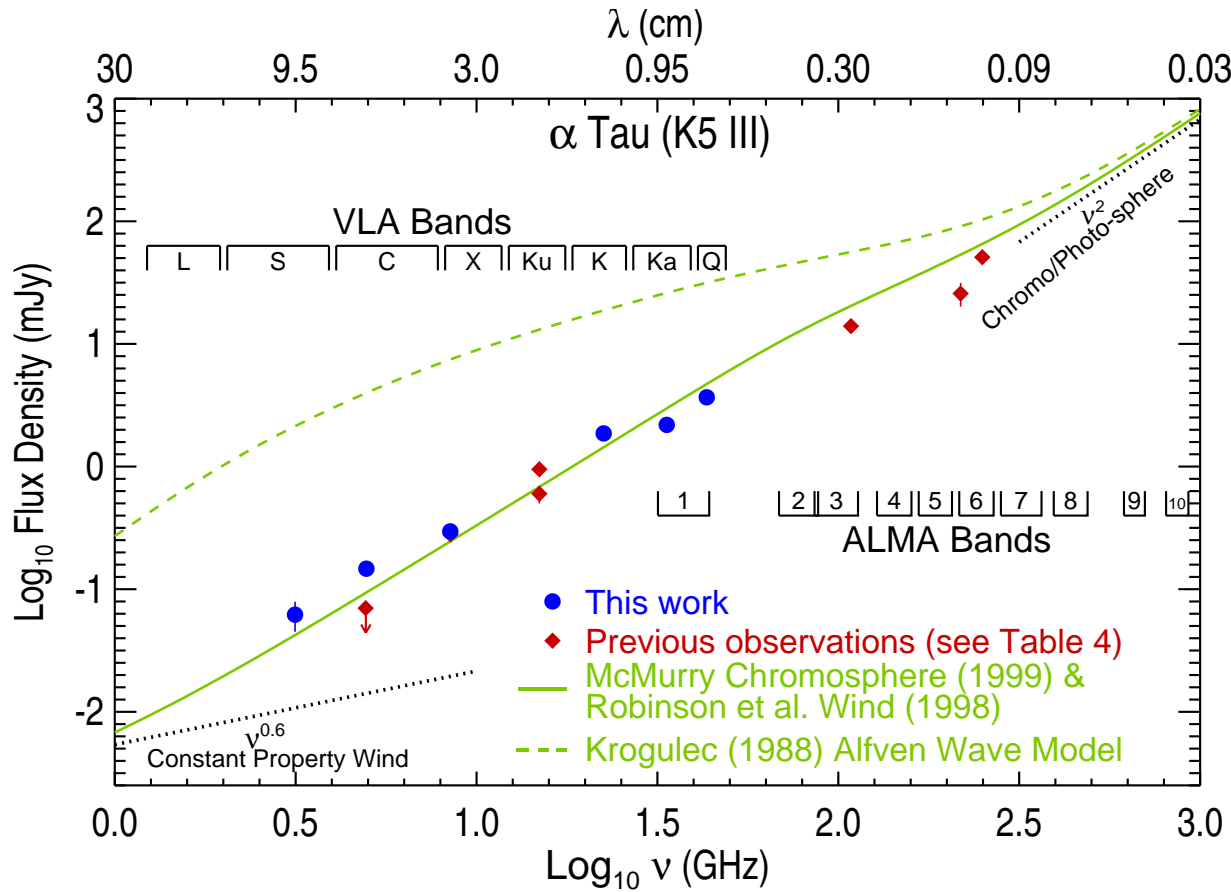


Figure 6.3: Spectral energy distribution of α Tau for $1 \text{ GHz} \leq \nu \leq 1 \text{ THz}$. Our new multi-frequency VLA observations of α Tau (blue circles) were acquired in just two days in February 2011. The red diamonds are the previous radio observations of the star which were acquired over many years (see Table 6.1). The green line is the expected radio emission from the existing hybrid chromosphere and wind model, while the dashed green line is the expected radio emission from a theoretical Alfvén wave driven model atmosphere.

6.4 Results Versus Existing Models

at wavelengths longer than 3 cm due to its relatively low mass-loss rate. Our lack of a Ku band measurement means that we can only compare the previous 3 cm detection reported in Wood *et al.* (2007) to ours. We find that there is no significant difference between the two. Interestingly, Wood *et al.* (2007) report a non-detection of α Tau at 6 cm and placed a 3σ upper limit of 0.07 mJy on its emission. In stark contrast to this, we were able to detect the star at 6 cm with a flux density over two times greater than this value. This hint of variability at long wavelengths would be consistent with the predictions of the broadband nonlinear Alfvén wave model of Airapetian *et al.* (2010) but can again only be confirmed with future high S/N observations.

6.4 Results Versus Existing Models

One of the most important diagnostic features indicating mass outflows in late-type evolved stars are the blue shifted absorption components present in the Ca II H and K and Mg II h and k resonance lines¹. Figure 6.4 shows one of the two chromosphere and wind models of α Boo (Drake, 1985, ‘model A’) which is based on the Mg II k 2796 Å emission line observed with the International Ultraviolet Explorer. The line was modeled by solving the radiative transfer equation in a spherical co-moving frame and the effects of partial redistribution (e.g., Drake & Linsky, 1983b) were taken into account. Both of Drakes atmospheric models are semi-empirical and contain no assumptions about the wind driving mechanism. They contain the photospheric model of Ayres & Linsky (1975), predict the wind to reach a terminal velocity of 35 - 40 km s⁻¹ by $2 R_*$, and reach a maximum microturbulence of 5 km s⁻¹. They contain a broad temperature plateau with $T_e \approx 8,000$ K between 1.2 and $\sim 20 R_*$ with a cooler region farther out, and hydrogen is 50% ionized throughout. We compute the radio spectrum from these models assuming spherical 1-D geometry (Harper, 1994) with the free-free Gaunt factors from Hummer (1988). The radiative transfer equation is solved using the Feautrier technique (Mihalas, 1978) and the boundary condition is determined by ensuring the atmosphere is optically thick at the deepest layers. Drake (1985) predicts that their atmospheric model would produce a flux density value of 0.4 mJy

¹Examples of these features are shown in Figures 1.2 and 3.5.

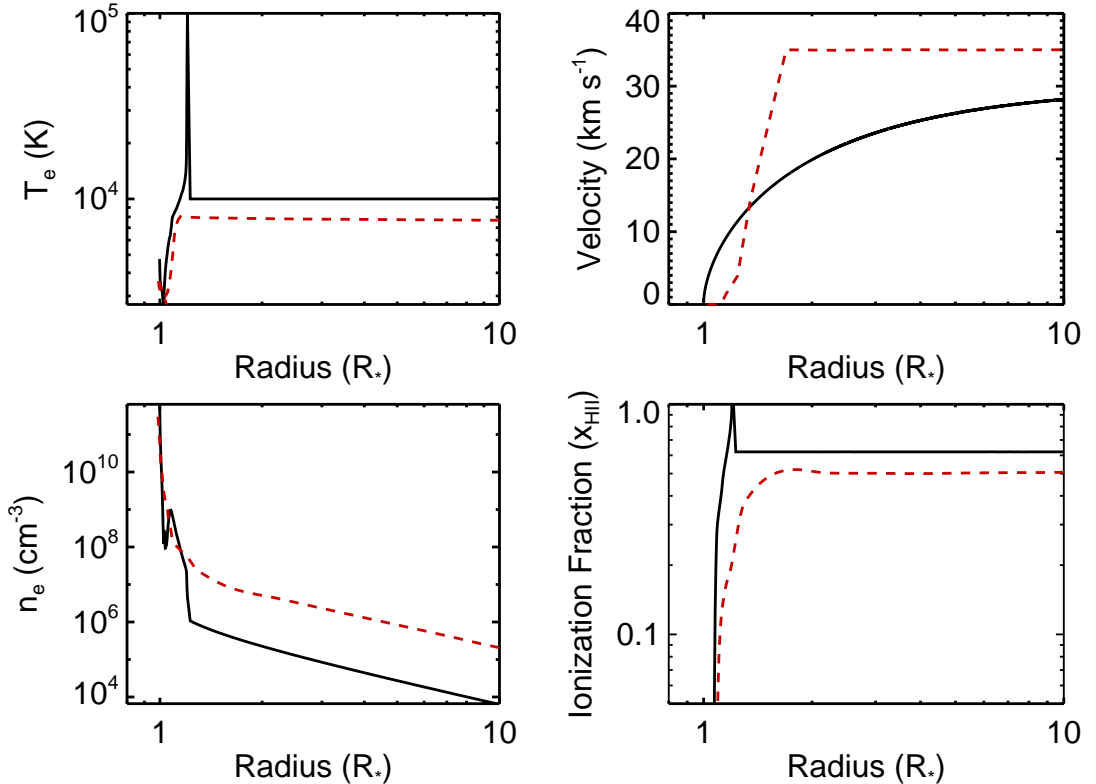


Figure 6.4: 1-D semi-empirical model atmospheres for α Boo and α Tau. The dashed red line is the model atmosphere for α Boo (Drake, 1985) while the solid black line is the model atmosphere of α Tau which consists of the chromosphere and transition region model of McMurry (1999) and the wind model of Robinson *et al.* (1998).

at 6 cm and encouragingly, our radio spectrum reproduces this value. Departures from spherical symmetry are to be expected in magnetic stellar atmospheres. For example, α Boo has an inclination axis of $58^\circ \pm 25^\circ$ (Gray *et al.*, 2006) and a global magnetic dipole could cause density variations between the equator and the polar regions. Despite this fact, the study of a spherically symmetric atmosphere forms the basis of understanding the more complex environments in real stellar atmospheres.

Figure 6.2 shows the resulting predicted radio spectrum between 1 GHz and 1 THz for α Boo from these chromosphere and wind models (green line). At high frequencies the radio spectra produced by these models have a blackbody-

6.4 Results Versus Existing Models

like slope (i.e., $\sim \nu^2$) as a result of the small ion density scale heights close to the star where the temperature is changing slowly. At low frequencies however, where the Drake models predict the wind to have constant velocity, ionization fraction, and temperature, the slopes approaches the well known $\sim \nu^{0.6}$ limit (Olnon, 1975; Panagia & Felli, 1975; Wright & Barlow, 1975). The paucity and, in some cases low S/N, of previous observations made it difficult to discern the validity of this model prior to our multi-frequency study of α Boo. Our new data reveal significant deviations from the semi-empirical model at both low and high frequencies (in this case below ~ 8 GHz and above ~ 25 GHz). At high frequencies our VLA data indicates a flux excess which is in agreement with previous mm-observations. This may be due to larger chromospheric ion densities or to the possible presence of transition region plasma not accounted for in the Drake model. The discrepancy at low frequencies may be due to a lower ionization fraction in the wind, or a lower mass-loss rate than that used in the Drake model and this will be discussed further in Section 6.6.

In Figure 6.3 we plot the expected radio spectrum of α Tau based on the semi-empirical 1-D chromosphere and transition region model of McMurry (1999) embedded in the 1-D wind model of Robinson *et al.* (1998). The semi-empirical McMurry model was created by using the radiative transfer code MULTI (Carlsson, 1986) to reproduce the fluxes of collisionally excited C I, C II, Si III, Mg II, and C IV lines in a plane-parallel, hydrostatic, one-component atmosphere. It contains the photospheric model of Johnson (1973) and reaches a maximum temperature of 10^5 K at $1.2 R_\star$. As it does not contain a wind outflow, we use Robinson *et al.*'s wind characteristics beyond $1.2 R_\star$ to describe the outflow velocity. In this wind model, the wind reaches $\sim 80\%$ of its terminal value of 30 km s^{-1} by $3 R_\star$. The Robinson *et al.* wind characteristics are based on matching the Fe II 2755 Å line and the O I triplet near 1304 Å with a simplified wind model using the SEI computer code (Lamers *et al.*, 1987). We assume the wind to have a constant temperature of 10,000 K and have a constant ionization fraction of $x_e = 0.6$ throughout, based on the ionization fraction at the corresponding temperature in the McMurry model. This idealized *hybrid* model atmosphere for α Tau is plotted in Figure 6.4.

6.4 Results Versus Existing Models

The radio flux densities at high frequencies (i.e., $\nu > 30$ GHz) are overestimated by the combination of both atmospheric models, although this approach does well in reproducing the VLA flux densities below 30 GHz. The VLA, Institut de Radioastronomie Millimétrique (IRAM) 30 m-telescope and Berkeley Illinois Maryland Association (BIMA) continuum flux densities confirm that this model predicts a flux excess at even higher frequencies. One possible explanation for this is that the inner atmosphere contains extensive amounts of cooler gas than that predicted by the 1-D static chromospheric model of McMurry. This scenario agrees with the findings of Wiedemann *et al.* (1994) who conclude that cool regions exist close to the stellar surface with large ($> 99\%$) filling factors i.e., a thermally bifurcated CO-mosphere (Ayres, 1996). The wind, which we have overlain on top of the McMurry chromosphere and transition region, is found to be optically thin at nearly all VLA wavelengths, and only contributes a very small flux density at the longest wavelengths. As our model matches the data reasonably well below 30 GHz we conclude that α Tau's wind is optically thin and the VLA radio emission at all wavelengths emanates from the inner atmosphere.

We also include the predicted radio spectrum from the theoretical Alfvén wave-driven outflow model for α Tau (Krogulec, 1989) in Figure 6.3 to demonstrate how radio observations can empirically challenge theoretical models. This model has a fully-ionized outflow inside $10 R_\star$, and has a mass-loss rate of $6.3 \times 10^{-9} M_\odot \text{ yr}^{-1}$, more than two orders of magnitude higher than the more recent estimate given in Table 6.1. As the radio opacity is proportional to $n_e n_{\text{ion}}$, where n_e and n_{ion} are the electron and ion number densities respectively, this model greatly overestimates the actual radio flux density at all VLA wavelengths. The linear Alfvén wave models for α Boo (Krogulec, 1988) also assume full ionization and have higher mass-loss rates than the value given in Table 6.1, predicting higher flux densities than observed. The lack of agreement between the Alfvén wave-driven wind models of Krogulec (1988, 1989) and our observed radio fluxes may not necessarily be due to an incorrect wind driving mechanism and instead may be due to the simplifications and uncertainties in these models, such as wind densities, magnetic field strengths, damping lengths, and flow geometries close to the star. For example, the mass-loss rate is very sensitive to the radial surface magnetic field strength (i.e., $\dot{M} \propto B^4$) in these Alfvén wave models (Holzer *et al.*,

1983) so a small uncertainty in the magnetic field strength can lead to a large uncertainty in the mass-loss rate. Relaxing some of these simplifications such as purely radial flows or non-assumption of the WKB approximation (Charbonneau & MacGregor, 1995) may also also lead to better agreement with our radio data.

6.5 Spectral Indices

Long wavelength radio emission from non-dusty K spectral-type red giants is due to thermal free-free emission in their partially ionized winds while shorter wavelength radio emission emanates from the near static and more ionized lower atmospheric layers. The radio flux density-frequency relationship for these stars is usually found to be intermediate between that expected from the isothermal stellar disk emission, where α follows the Rayleigh-Jeans tail of the Planck function (i.e., $\alpha = +2$), and that from an optically thin plasma (i.e., $\alpha = -0.1$). We have shown in Chapter 1 that the expected radio spectrum from a spherically symmetric isothermal outflow with a constant velocity and ionization fraction varies as $\nu^{0.6}$ (Olonon, 1975; Panagia & Felli, 1975; Wright & Barlow, 1975). In reality however, thermal gradients will exist in the wind when the heating mechanisms become insufficient to counteract adiabatic and line cooling, so one would expect a temperature decrease in the wind at some point. Also, if the radio emission emanates from the wind acceleration zone then the electron density will not follow $n_e \propto r^{-2}$.

We therefore relax some of the constant property wind model assumptions and assume that the electron density and temperature vary as a function of distance from the star r , and have the power-law form $n_e \propto r^{-p}$ and $T_e \propto r^{-n}$, respectively (e.g., Seaquist & Taylor, 1987). Finding the spectral index for an outflow with these conditions is non-trivial, so we highlight the main steps required to do so here. We assume the same geometry and notation used for the constant property wind model in section 1.8.4 of Chapter 1, and start by calculating the optical depth along a ray at position z with an impact parameter b through the atmosphere

$$\tau_\nu(z, b) = \frac{0.212 Z^2 n_0^2 r_0^\Pi}{\nu^{2.1} T_0^{1.35}} \int_{-\infty}^z \frac{dz}{(z^2 + b^2)^{\Pi/2}} \quad (6.1)$$

6.5 Spectral Indices

where T_0 and n_0 are the gas temperature and density, respectively, at the base of the wind, r_0 , and $\Pi = 2p - 1.35n$. We have also assumed that the electron density is the same as the ion density throughout. Following the method of Seaquist & Taylor (1987) we introduce the new spatial variables $l = z/\sigma_\nu$ and $q = b/\sigma_\nu$, where σ_ν is a frequency dependent function. Doing so removes the spatial-frequency coupling to give

$$\tau_\nu(l, q) = \frac{0.212Z^2 n_0^2 r_0^\Pi \sigma_\nu^{1-\Pi}}{\nu^{2.1} T_0^{1.35}} \int_{-\infty}^l \frac{dl}{(l^2 + q^2)^{\Pi/2}}. \quad (6.2)$$

Defining σ_ν as

$$\sigma_\nu = \left(\frac{0.212Z^2 n_0^2 r_0^\Pi}{\nu^{2.1} T_0^{1.35}} \right)^{\frac{1}{\Pi-1}} \quad (6.3)$$

then gives the following simplified expressions for the optical depth

$$\tau_\nu = \int_{-\infty}^l \frac{dl}{(l^2 + q^2)^{\Pi/2}} \quad (6.4)$$

and

$$d\tau_\nu = \frac{dl}{(l^2 + q^2)^{\Pi/2}}. \quad (6.5)$$

The total flux can be written as

$$F_\nu = 2\pi \left(\frac{\phi}{2} \right)^2 \int_{b=0}^{\infty} \int_{\tau=0}^{\tau_{\max}} B_\nu \exp(-\tau) d\tau b db \quad (6.6)$$

where ϕ is the angular diameter of the radio emitting region, τ_{\max} is the total optical depth, and B_ν is the Rayleigh-Jeans expression of the Planck function. This then becomes

$$F_\nu = 2\pi \left(\frac{\phi}{2} \right)^2 \frac{2\nu^2 k T_0}{c^2} r_0^d \sigma_\nu^{2-d} \int_{q=0}^{\infty} \int_{l=-\infty}^{\infty} \frac{q}{(l^2 + q^2)^{d/2}} \exp \left(- \int_{-\infty}^l \frac{dl}{(l^2 + q^2)^{\Pi/2}} \right) dq dl \quad (6.7)$$

where the double integral is a geometric term independent of frequency. The spectral index, α , is defined as

$$F_\nu \propto \nu^\alpha \quad (6.8)$$

and so in this model

$$F_\nu \propto \nu^2 \nu^{\frac{-2.1(2-d)}{\Pi-1}} \quad (6.9)$$

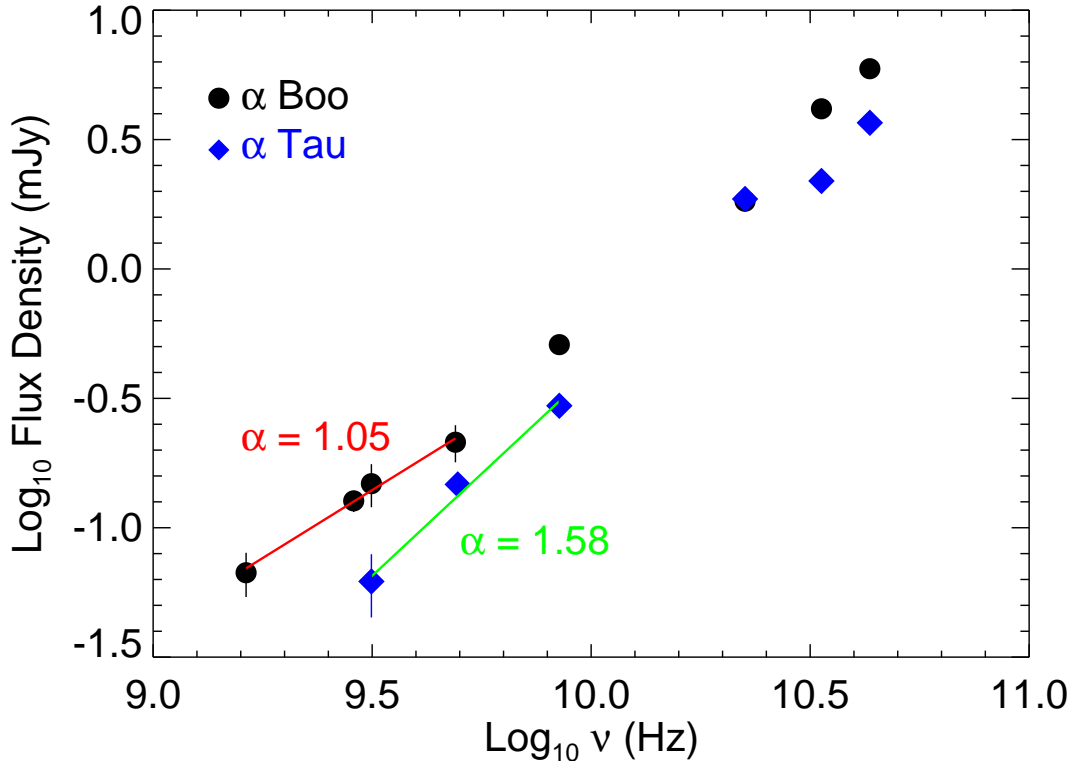


Figure 6.5: Radio spectra for α Boo and α Tau, together with the best fit power law to their long wavelength flux densities and the resulting spectral indices. The spectral indices for α Boo and α Tau are found to be 1.05 and 1.58, respectively, which are both larger than the 0.6 value expected for a constant property wind model.

i.e.,

$$\alpha = \frac{4p - 6.2 - 0.6n}{2p - 1 - 1.35n}. \quad (6.10)$$

Therefore, if the spectral index of a stellar outflow can be measured, and if we make an assumption about the property of either the thermal or electron density profile of the wind, then Equation 6.10 provides us with information on how the other value varies.

The radio spectra for both stars are shown in Figure 6.5, together with the power laws that were fitted to the long wavelength flux densities by minimizing the chi-square error statistic. For α Boo, a power law with $F_\nu \propto \nu^{1.05 \pm 0.05}$ fits

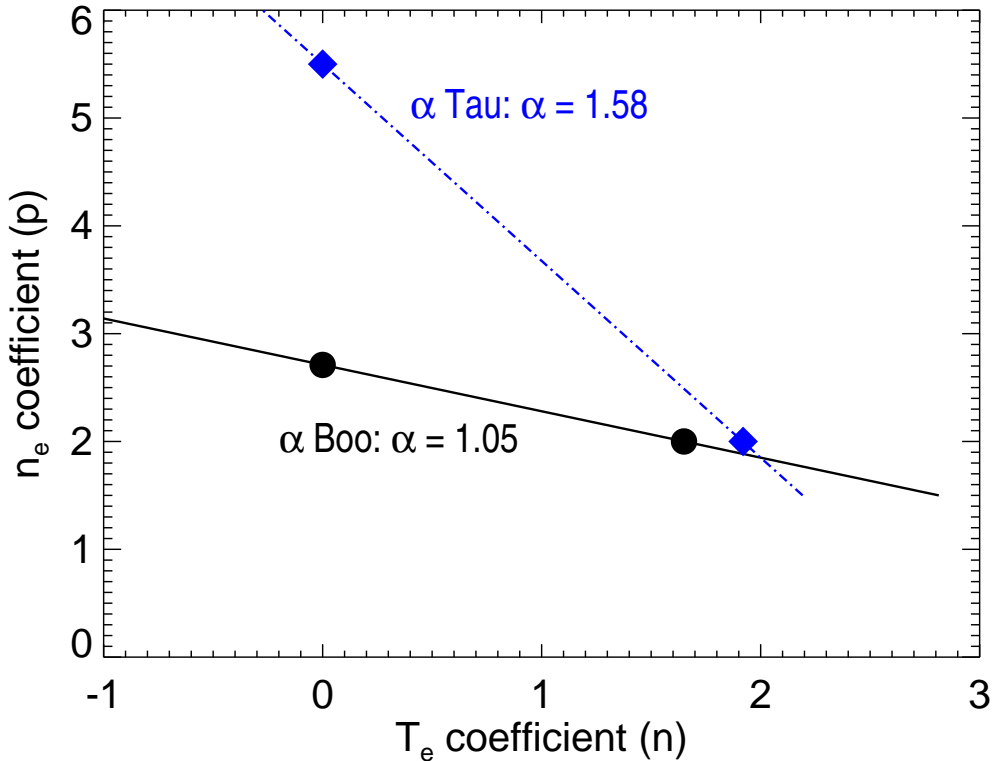


Figure 6.6: The variation of density and temperature coefficients for the empirically derived spectral indices. The density coefficients for an isothermal flow ($n=0$) along with the temperature coefficients for a constant outflow velocity ($p=2$) are also shown for both stars.

the four longest wavelength data points well. This spectral index is larger than the 0.8 value obtained by Drake & Linsky (1986) whose value was based on a shorter wavelength (2 cm) value and a mean value of four low S/N measurements at 6 cm. α Tau was found to have a larger spectral index and a power law with $S_\nu \propto \nu^{1.58 \pm 0.25}$ best fitted the three longest wavelength data points. This value is in agreement with Drake & Linsky (1986) who report a value ≥ 0.84 and is lower than the value of 2.18 that can be derived from the shorter wavelength data given in Wood *et al.* (2007). It should be emphasized that the spectral index for both stars is a lot steeper than that expected from the idealized constant property wind model.

Equation 6.10 can be used in conjunction with our new spectral index for each

6.5 Spectral Indices

star to calculate the density and temperature coefficients that may describe their outflows. The combinations of the electron temperature and density coefficients are shown for each star in Figure 6.6 (α Boo is represented by the solid line and α Tau by the dash-dotted line) along with the coefficients obtained by assuming either an isothermal flow ($n = 0$) or a constant velocity flow ($p = 2$). One potential explanation for spectral indices of stellar outflows being larger than 0.6 is that the wind is still accelerating in the radio emitting region, if the thermal gradients are assumed to be small. For an isothermal flow, the density coefficients are $p = 2.7$ and 5.5 for α Boo and α Tau, respectively. From mass conservation and assuming a steady flow, the power law coefficients for the velocity profiles of each star can be found, ie., $v(r) \propto r^{p-2}$. For α Boo we find $v(r) \propto r^{0.7}$ while for α Tau we find $v(r) \propto r^{3.5}$. This suggests that our long VLA wavelengths may probe a steep acceleration region for α Tau's outflow but for α Boo, may probe a region where the wind is close to its terminal velocity.

The assumption of shallow thermal gradients in a stellar outflow is probably unreliable however. It is likely that some form of Alfvèn waves are required to lift the material out of the gravitational potential as suggested by Hartmann & MacGregor (1980). These waves need damping lengths which are much larger than the chromospheric density scale height H (where $H \sim 0.01 R_\star$ for our targets), in order to lift the material out of the gravitational potential but $\lesssim 1 R_\star$ in order to avoid wind terminal velocities greater than those observed (e.g., Holzer *et al.*, 1983). It has also been shown that these waves are expected to produce substantial heating near the base of the wind (e.g., Hartmann *et al.*, 1982). If the long wavelength radio emission from α Tau is indeed emanating from the wind acceleration region, then the dissipation of these Alfvèn waves may introduce thermal gradients in this region and its velocity profile will not be described by $v(r) \propto r^{3.5}$. Furthermore, diverging flow geometries have been invoked as a more realistic representation of stellar atmospheres (Hartmann *et al.*, 1982; Jatenco-Pereira & Opher, 1989; Vidotto *et al.*, 2006) and so one could write the area of a flux tube (normalized to its value at r_1) as $(r/r_1)^2 f(r)$ where $f(r)$ is a function describing the divergence from a purely radial flow [i.e., when $f(r) = 1$]. If the non-radial expansion term can be described by a power law $f(r) \propto r^s$, where $s > 1$ indicates super-radial expansion, then $v(r) \propto r^{3.5-s}$ would describe the

velocity profile of α Tau (assuming an isothermal flow with a constant ionization fraction). Therefore, including diverging geometries reduces the magnitude of the acceleration. Farther out in the wind, where it has reached its terminal velocity, one would also expect a thermal gradient (but now of opposite sign) due to adiabatic expansion and line cooling. If the long wavelength radio emission emanates from this region of the wind, then Equation 6.10 provides us with a direct estimate of the temperature coefficient as we can assume the density coefficient is $p = 2$. This may be the case for our long VLA wavelength measurements of α Boo in which case $T_e(r) \propto r^{-1.65}$.

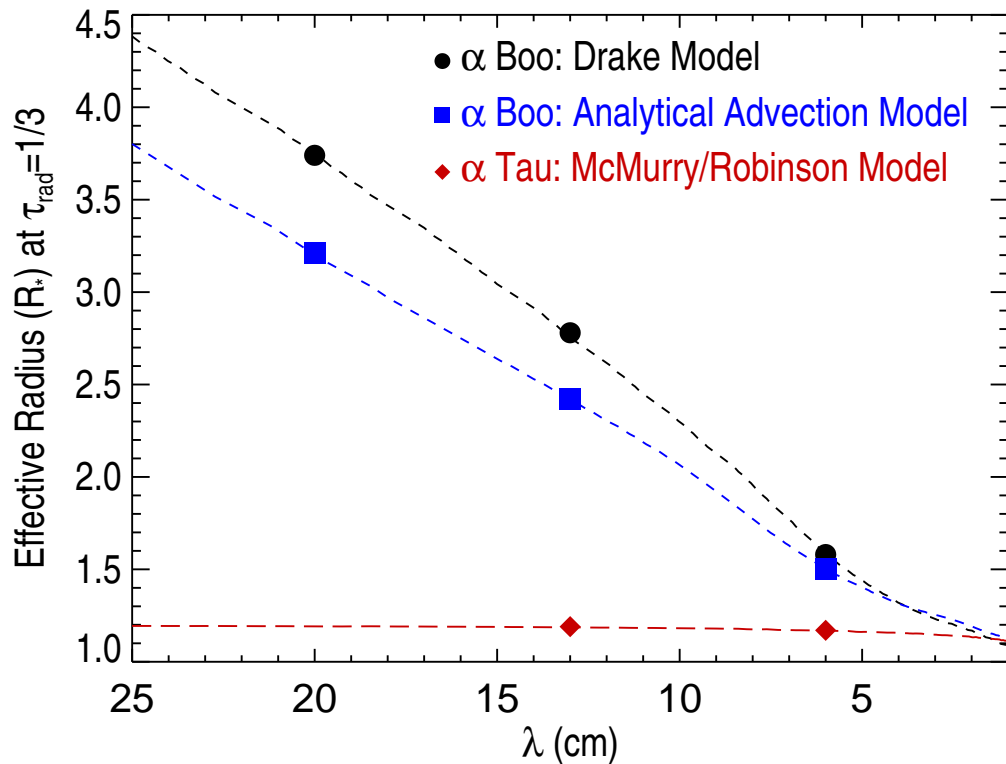


Figure 6.7: Predicted effective radius (dashed lines) as a function of wavelength derived from the existing atmospheric models of α Boo and α Tau. Also plotted is the predicted effective radius derived from our analytical advection model for α Boo (discussed in Section 6.6). Points corresponding to our long wavelength VLA measurements are also shown. At the same radio wavelengths the lower mass-loss rate of α Tau's outflow results in a smaller effective radius than that for α Boo.

6.5 Spectral Indices

To investigate this matter further, we estimate the effective radius of the radio emitting region as a function of wavelength based on the Drake model for α Boo and the hybrid McMurry and Robinson et al. model for α Tau. We follow the approach used by Cassinelli & Hartmann (1977) and assume that the radio emission at each wavelength is characterized by emission from a radial optical depth $\tau_{\text{rad}} \sim 1/3$. This is a modification of the Eddington-Barbier relation for an extended atmosphere where emission from smaller optical depths has added weight. Since the radio free-free opacity increases at longer wavelengths the optical depth along a line of sight into the stellar outflow also increases at longer wavelengths. This implies that the effective radius (i.e., the radius where $\tau_\lambda = \tau_{\text{rad}}$) will increase with longer wavelengths and will be greater for outflows with higher densities of ionized material as $\tau_\lambda(r) \propto \lambda^{2.1} \int n_{\text{ion}}(r)n_e(r)dr$.

The larger mass-loss rate of α Boo in comparison to α Tau means that the latter has a substantially smaller effective radius at longer wavelengths, as seen in Figure 6.7. At 6, 13, and 20 cm the effective radius of α Boo at $\tau_{\text{rad}} = 1/3$ is predicted to be 1.6, 2.8, and $3.7 R_\star$ but is only $\sim 1.2 R_\star$ at 6 and 13 cm for α Tau. Robinson et al. (1998) predict that α Tau's wind reaches $\sim 80\%$ of its terminal velocity by $3 R_\star$, but even our longest-wavelength observations are highly unlikely to sample the wind outside the lower velocity layers closer to the star. For α Boo however, Drake (1985) predicts that the wind has reached its terminal velocity by $\sim 2 R_\star$ so based on this model our longest-wavelength measurements are of the region where the wind has reached a steady terminal velocity. From Figure 6.6, this implies that the n_e coefficient is $p = 2$ and thus the T_e coefficient is $n = 1.65$. Pure adiabatic spherical expansion cooling with no heat source has $n = 1.33$ so additional cooling routes must be operating, possibly due to line cooling. Finally, the wind ionization balance may not have become *frozen-in* in the region of α Boo's wind where the radio emission emanates from. If this is true, then the excess slope of the spectral index could be due to a combination of both cooling and changing ionization fraction. In this scenario the temperature coefficient n , would be smaller than our derived value because Equation 6.10 assumes a constant ionization fraction.

6.6 Analytical Advection Model for α Boo's Wind

A failure of the Drake model for α Boo is that it overestimates the long wavelength VLA radio flux densities which sample the outer atmosphere, as clearly shown in Figure 6.2. If these wavelengths are indeed sampling the wind at its terminal velocity then one reason for this overestimation is that the wind is cooling closer in than predicted by the existing model, which assumes a constant temperature of 8,000 K out to $\sim 20 R_\star$. The main mechanism for such cooling would be adiabatic expansion (O'Gorman & Harper, 2011) and would cause lower electron densities than those predicted by the existing model due to larger recombination rates. In the next two sections we derive the fraction of ionized hydrogen in a stellar outflow with a temperature gradient based on the work of Glassgold & Huggins (1986), and use this method to insert a temperature gradient into the outer atmosphere of the Drake model to see if such an atmosphere could better reproduce the new long wavelength VLA flux densities.

6.6.1 H II recombination in a stellar outflow

The time dependent non-static rate/statistical equations can be written as

$$\frac{\partial n_i}{\partial t} + \nabla \cdot (n_i v) = \sum_{i \neq j}^n n_j P_{ji} - n_i \sum_{i \neq j}^n P_{ij} \quad (6.11)$$

where v is the flow velocity, $n_{i,j}$ are the population densities of the energy levels i, j which are functions of radial distance r , and $P_{ij} = C_{ij} + R_{ij}$ are the total transition probabilities (s^{-1}) from energy levels $i \rightarrow j$. C_{ij} are the total collision rates (electrons, protons, and ions), and R_{ij} are the problematic radiative rates, which account for spontaneous decay, stimulated emission, and absorption. The stimulated emission and absorption terms couple the particle densities, n_i , to the radiation field, making the problem *nonlocal* and *nonlinear* (Scharmer & Carlsson, 1985). In 1-D spherical geometry

$$\nabla \cdot (n_i v) = \frac{1}{r^2} \frac{d}{dr} (r^2 n_i v) \quad (6.12)$$

6.6 Analytical Advection Model for α Boo's Wind

and so for a steady flow the rate equations become

$$\frac{1}{r^2} \frac{d}{dr} (r^2 v n_{\text{tot}} \frac{n_i}{n_{\text{tot}}}) = \sum_{i \neq j}^n n_j P_{ji} - n_i \sum_{i \neq j}^n P_{ij} \quad (6.13)$$

where n_{tot} is the total hydrogen number density (i.e., $n_{\text{tot}} = n_{\text{HI}} + n_{\text{HII}}$). We note that $r^2 v n_{\text{tot}}$ is some constant of the flow defined by the mass continuity equation, and if we define the relative populations as $x_i = n_i / n_{\text{tot}}$ we get

$$v \frac{d}{dr} (x_i) = \sum_{i \neq j}^n x_j P_{ji} - x_i \sum_{i \neq j}^n P_{ij}. \quad (6.14)$$

To simplify Equation 6.14 further, we follow the approach of Glassgold & Huggins (1986) and assume:

1. A constant velocity mass outflow, i.e., $n_{\text{tot}} = C/r^2$ where C is a constant proportional to the ratio of the mass-loss rate divided by the terminal velocity.
2. All hydrogen ionization processes cease beyond some distance r_1 (i.e., $P_{ij} = 0$). The ionization of hydrogen in the chromosphere and wind is a two stage process: the $n = 2$ level is excited by electron collisions and Lyman-alpha scattering, followed by photoionization by the optically thin Balmer continuum. When the temperature begins to decrease in the wind the collisional excitation rate and thus ionization rate decrease rapidly.
3. Only radiative recombination of hydrogen is considered [i.e. $R_{ji} = \alpha_{\text{rr}}(T_e) n_e$ where α_{rr} is the total radiative recombination coefficient].
4. A fixed ion contribution from metals with a low first ionization potential, $x_{\text{ion}} = n_{\text{ion}} / n_{\text{tot}}$, as these are easily ionized in the outflow. The total electron density is then $n_e = n_{\text{tot}} x_{\text{HII}} + n_{\text{tot}} x_{\text{ion}}$ where $x_{\text{HII}} = n_{\text{HII}} / (n_{\text{HI}} + n_{\text{HII}})$.

Using these assumptions Equation 6.14 becomes

$$\frac{dx_{\text{HII}}}{dr} = \frac{\alpha_{\text{rr}} C}{vr^2} (x_{\text{HII}}^2 + x_{\text{ion}} x_{\text{HII}}) \quad (6.15)$$

which can be rearranged and integrated between r_1 and r to give

$$\int_{x_{\text{HII}(r_1)}}^{x_{\text{HII}(r)}} \frac{dx_{\text{HII}}}{x_{\text{HII}}(x_{\text{HII}} + x_{\text{ion}})} = \int_{r_1}^r \frac{\alpha_{\text{rr}} C}{vr^2} dr \quad (6.16)$$

6.6 Analytical Advection Model for α Boo's Wind

The ionization fraction beyond r_1 is then given by

$$x_{\text{HII}}(r) = \frac{x_{\text{HII}}(r_1)x_{\text{ion}}e^{-I(r)}}{x_{\text{ion}} + x_{\text{HII}}(r_1)[1 - e^{-I(r)}]} \quad (6.17)$$

where

$$I(r) = \int_{r_1}^r \frac{x_{\text{ion}}\alpha_{\text{rr}}C}{vr^2} dr \quad (6.18)$$

If we further assume a constant velocity, $T_e \propto r^{-n}$, and $\alpha_{\text{rr}} \propto T_e^{-\beta}$ giving $\alpha_{\text{rr}} \propto$

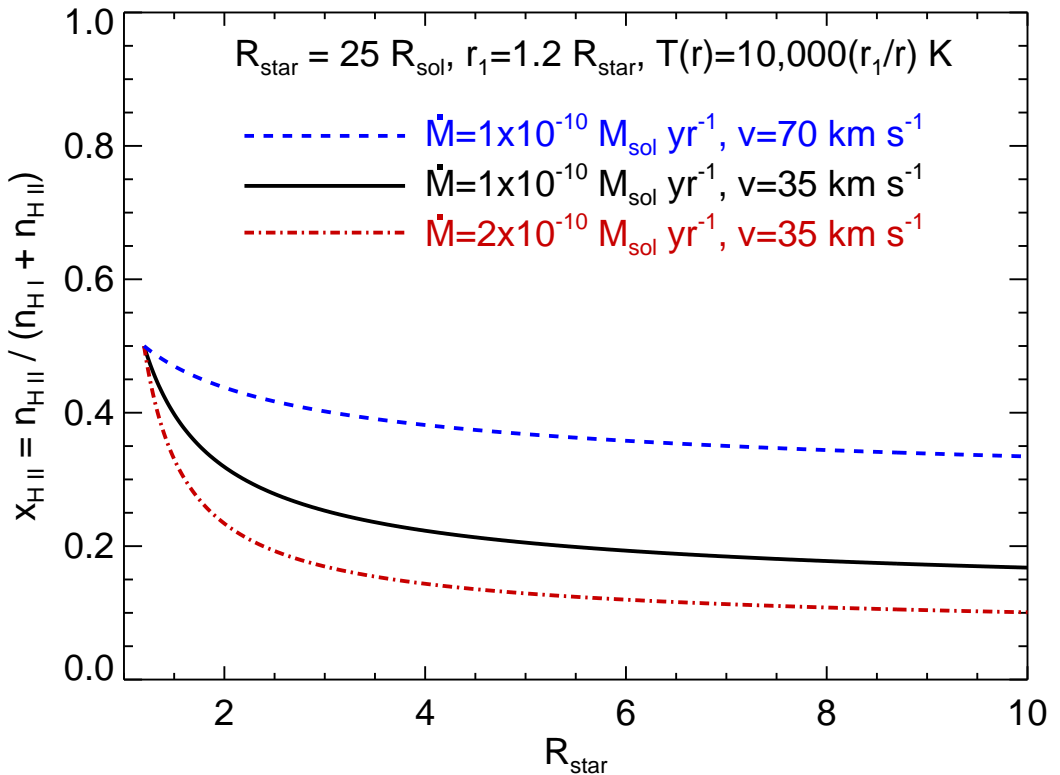


Figure 6.8: Illustration of how the ionization fraction *freezes-in* in a stellar wind for a hypothetical $25 R_{\star}$ star. The stars outflow has a maximum temperature of 10,000 K at $1.2 R_{\star}$ which then falls off linearly with distance. Blue dashed line: $\dot{M} = 1 \times 10^{-10} M_{\odot} \text{ yr}^{-1}$ and $v = 70 \text{ km s}^{-1}$. Black smooth line: $\dot{M} = 1 \times 10^{-10} M_{\odot} \text{ yr}^{-1}$ and $v = 35 \text{ km s}^{-1}$. Red dot-dashed line: $\dot{M} = 2 \times 10^{-10} M_{\odot} \text{ yr}^{-1}$ and $v = 35 \text{ km s}^{-1}$.

6.6 Analytical Advection Model for α Boo's Wind

$r^{-n\beta}$, then

$$x_{\text{HII}}(r) = \frac{x_{\text{HII}}(r_1)x_{\text{ion}}e^{-I(r)}}{x_{\text{ion}} + x_{\text{HII}}(r_1)(1 - e^{-I(r)})} \quad (6.19)$$

where

$$I(r) = w \left[1 - \left(\frac{r_1}{r} \right)^{1-n\beta} \right] \quad (6.20)$$

and

$$w = \frac{x_{\text{ion}}\alpha_{\text{rr}}(r_1)C}{vr_1(1 - n\beta)}. \quad (6.21)$$

As w is just a constant, $I(r)$ approaches a constant value for large r . This means that $x_{\text{HII}}(r)$ also approaches a constant value for large r , and the ionization fraction gets *frozen-in*. It occurs when the recombination timescale of the ions in the wind $\tau_{\text{rec}} = (\alpha_{\text{rec}}n_e)^{-1}$, becomes comparable to the wind expansion timescale, $\tau_{\text{exp}} = |\rho(d\rho/dt)|^{-1} \simeq 0.5r/v$ (Lamers & Cassinelli, 1999). Figure 6.5 shows that the ionization fraction in the outflow of a *typical* red giant *freezes-in* to higher values for winds with higher velocities and lower mass-loss rates.

6.6.2 Application to α Boo's Wind

To investigate the possibility that α Boo's wind may be undergoing more rapid cooling closer in to the star than originally predicted by the Drake Model, we adjust one of the existing models [referred to as 'Model A' in Drake (1985)] to include a temperature power-law falloff of the form

$$T_e(r) = T_e(r_1) \left(\frac{r_1}{r} \right)^n \quad (6.22)$$

at some distance r_1 from the star. We set the temperature coefficient to the value obtained from our new VLA data which was derived assuming a constant velocity flow, i.e., $n = 1.65$ (see Figure 6.6). We introduce the distance r_1 as the outer limit to ionization processes; at $r > r_1$, the ionization fraction is only determined by recombination. To calculate the new electron densities in the wind regime where this temperature falloff occurs, we use Equations 6.19, 6.20, and 6.21 to calculate the hydrogen ionization fraction, $x_{\text{HII}} = n_{\text{HII}}/n_{\text{H}}$. We assume a fixed ion contribution from metals with a low first ionization potential of $x_{\text{ion}} = 1 \times 10^{-4}$. So, knowing that the total hydrogen density does not change, the electron density

6.6 Analytical Advection Model for α Boo's Wind

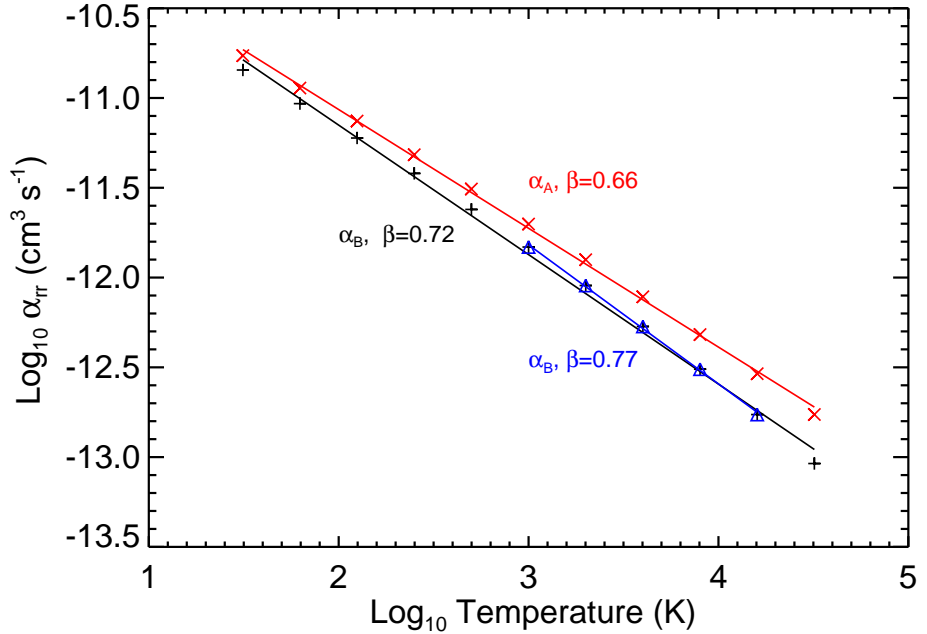


Figure 6.9: The temperature dependent recombination rates for hydrogen. The variation of the recombination rate (excluding captures to the $n=1$ level), α_B , with temperature is derived for the tabulated temperatures in Spitzer (1978) (black crosses), and for the more realistic temperatures existing in α Boo's outflow (blue triangles). We also show the how the recombination coefficient varies with temperature if captures to the $n=1$ level are included (red x's). This coefficient is often referred to as α_A .

at any point in the wind post r_1 can be found by the following formula

$$n_e(r) = n_{\text{tot}}(r)[x_{\text{HII}}(r) + x_{\text{ion}}]. \quad (6.23)$$

Using the same wind terminal velocity as that used in ‘Model A’ (i.e., 35 km s⁻¹) and the mass-loss rate defined in Table 3.4, we find the constant proportional to the ratio of the mass-loss rate divided by the terminal velocity to be $C = 1.7 \times 10^{32}$ cm⁻¹ for α Boo. To calculate the temperature dependent radiative recombination coefficient α_{rr} and its power law coefficient β used in Equation 6.21, we consider only radiative recombination of hydrogen and exclude captures to the $n=1$ level. Spitzer (1978) has tabulated values for the variation of this recombination coefficient with temperature and it is often referred to as α_B in

6.6 Analytical Advection Model for α Boo's Wind

the literature when captures to the $n=1$ level are excluded. To find the power law form of α_B we found the best fit to the tabulated data between the expected range of temperatures in the outflow of α Boo. This approach is shown in Figure 6.9, where β was found to be 0.77 by fitting a power law to values of α_B between 1,000 and 16,000 K. For completeness, we also show in Figure 6.9 the slight variation in β if a wider range of temperatures is used and also if captures to the $n=1$ level are included.

It can then be shown that the ionization fraction beyond r_1 is given by

$$x_{\text{HII}}(r) = \frac{x_{\text{HII}}(r_1)x_{\text{ion}}e^{-I(r)}}{x_{\text{ion}} + x_{\text{HII}}(r_1)[1 - e^{-I(r)}]} \quad (6.24)$$

where

$$I(r) = \frac{4.7 \times 10^9}{r_1} \left[\left(\frac{r_1}{r} \right)^{-0.27} - 1 \right] \text{ and } r \geq r_1. \quad (6.25)$$

We then adjusted the value of r_1 to obtain the best fit to our long wavelength observations and found this happened when $r_1 = 2.3 R_\star$. To get this best fit, the existing atmospheric model needed to be adjusted so that it now has a narrower and slightly larger temperature plateau of $T_e = 10,000$ K between 1.2 and 2.3 R_\star , and a temperature profile and a density profile governed by Equation 6.22 and Equation 6.24 beyond $r_1 = 2.3 R_\star$, respectively. This gives much better agreement with our new long wavelength VLA data as shown in Figure 6.2. This new *hybrid* atmospheric model which is plotted along with the original Drake model in Figure 6.10, still has the original ionization fraction of $x_{\text{HII}} \approx 0.5$ inside $2.3 R_\star$ but now contains an initial rapid decrease in x_{HII} beyond $2.3 R_\star$ which then *freezes-in* to a constant value of ~ 0.04 beyond $\sim 10 R_\star$.

Encouraging as it is that such a simple analytical model can reproduce values close to the observed radio fluxes at long wavelengths, it must be stressed that this *hybrid* model is just a first order approximation. It assumes that the excess slope from the radio spectrum is a result of rapid cooling only. It still does not reproduce the radio fluxes at wavelengths shorter than ~ 3 cm and therefore a new atmospheric model is still required that can reproduce all of the observed flux densities. To do so, the non-trivial task of simultaneously solving the radiative transfer equation and non-LTE atomic level populations which include advection will be required.

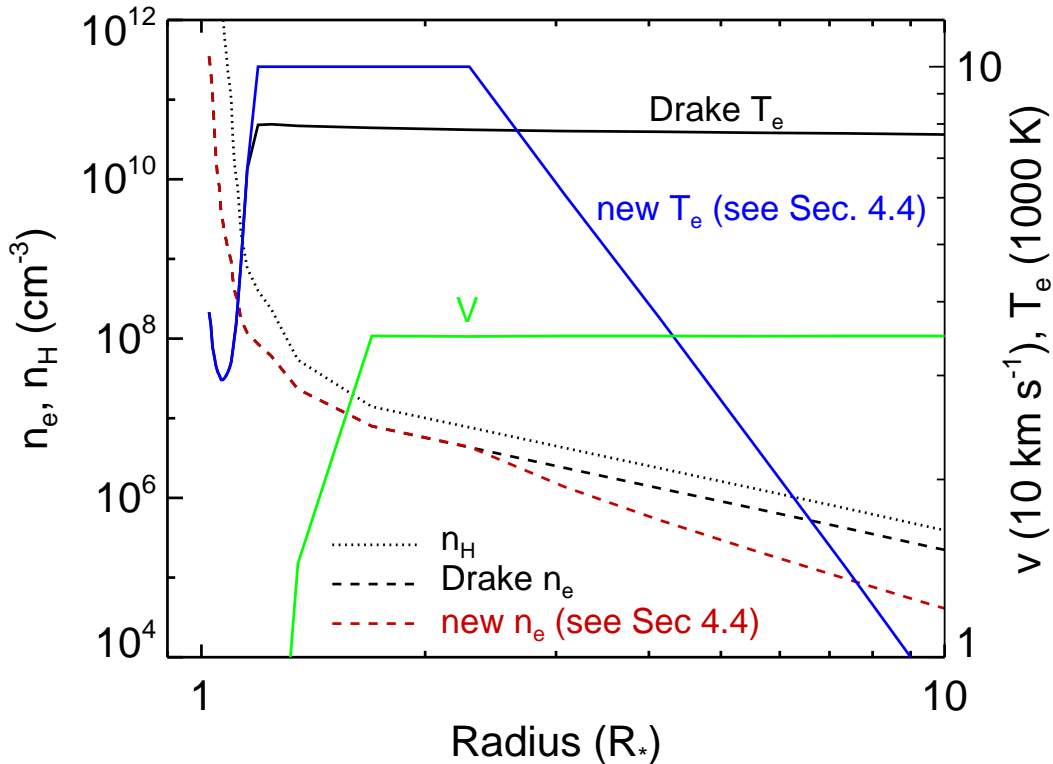


Figure 6.10: Existing atmospheric model for α Boo (Drake, 1985, ‘model A’) along with the same model which undergoes rapid wind cooling beyond $\sim 2.3 R_\star$. The original Drake Model’s have a temperature plateau of $\sim 8,000$ K between 1.2 and $\sim 20 R_\star$ (solid black line), reach a terminal velocity of $35 - 40$ km s^{-1} within $2 R_\star$ (solid green line), and have a wind which is 50% ionized (dashed and dotted black lines).

6.7 Constraining α Tau’s Molsphere

Recently, Ohnaka (2013) has detected a layer of CO in the outer atmosphere of α Tau (i.e., a so-called MOLsphere) which extends out to $\sim 2.5 R_\star$, has a temperature of 1500 ± 200 K, and a CO column density of $\sim 1 \times 10^{20} \text{ cm}^{-2}$. They were unable to constrain the geometrical thickness ΔL , of the MOLsphere from the data however, and arbitrarily set it to $0.1 R_\star$. We now try and constrain the thickness of this MOLsphere from our VLA data.

As shown in Chapter 1, the opacity corrected for stimulated emission at VLA

6.7 Constraining α Tau's MOLsphere

wavelengths is

$$\kappa_\nu = \frac{0.212 n_e n_{ion} Z_{ion}^2}{T_e^{1.35} \nu^{2.1}} \text{ cm}^{-1} \quad (6.26)$$

and the optical depth of a shell of width ΔL is

$$\tau_\nu = \kappa_\nu \Delta L. \quad (6.27)$$

To calculate the electron density within the MOLsphere we have conservatively assumed that the electrons only come from singly ionized metals and have an abundance of $n_{ion} = 1 \times 10^{-5} n_{tot}$, where n_{tot} is the total hydrogen number density whose value is constant throughout the MOLsphere. We estimate the CO number density by dividing the CO column density by the geometrical thickness of the shell and assume the CO filling factor to be unity. If the MOLsphere extends from the stars surface out to the derived distance of $2.5 R_\star$, then $\Delta L = 1.5$ and $n_{co} = 2.2 \times 10^7 \text{ cm}^{-3}$. This equates to a total hydrogen number density of $n_{tot} = 1.2 \times 10^{11} \text{ cm}^{-3}$ (Ohnaka, 2013) giving an abundance ratio of $n_{co}/n_{tot} = 3.3 \times 10^{-4}$. We can then use Equations 6.26 and 6.27 to show that such a MOLsphere would be optically thin at all VLA wavelengths that we observed the star with. If on the other hand, the MOLsphere has only a geometric width of $\Delta L = 0.1 R_\star$ then assuming the same abundances we get $n_H = 1.76 \times 10^{12} \text{ cm}^{-3}$, and the MOLsphere would be optically thick at 3.5, 6, and 9.5 cm (i.e., X, C, and S band).

Focusing on our high S/N C band measurement, it can be shown that such a MOLsphere would have an optical depth of $\tau_{6\text{cm}} = 4.6$ and would produce a corresponding flux density of 0.06 mJy (assuming an optically thick disk) which is considerably lower than our measurement of 0.15 mJy. The disagreement in values between our radio data and the predicted flux for an optically thick disk could mean that the MOLsphere is optically thin at long VLA wavelengths and that the radio emission emanates from the more ionized material closer to the star. It can also be shown that the MOLsphere becomes optically thin at C band (i.e., $\tau_{6\text{cm}} < 1$) for $\Delta L > 0.45 R_\star$. In the next section we argue that the radio emission from α Tau even at long VLA wavelengths comes from a region closer in to the star where the wind is undergoing rapid acceleration, which suggests that the MOLsphere either has a geometrical width $> 0.45 R_\star$ or has a filling factor less than unity.

6.8 Ionized Mass-Loss Rates

The free-free radio emission from the atmospheres of red giants is only sensitive to the ionized component of the outflow. Non-coronal and hybrid atmosphere red giants have only partially ionized atmospheres and so we are only ever capable of finding a lower limit on the mass-loss rate from their thermal continuum radio emission. Nevertheless, it is a sufficiently worthwhile goal and can test the validity of existing values obtained from optically thick emission lines in the UV or optical regime. For a partially ionized outflow such as that expected from α Boo and α Tau, the ionized mass-loss rate can be estimated from the radio emission assuming a constant velocity, constant temperature, and constant ionization fraction and can be written as

$$\dot{M}_{\text{ion}} \simeq 5.58 \times 10^{-14} \left(\frac{v_{\infty}}{\text{km s}^{-1}} \right) \left(\frac{d}{\text{pc}} \right)^{1.5} \left(\frac{F_{\nu}}{\text{mJy}} \right)^{0.75} \left(\frac{\lambda}{\text{cm}} \right)^{0.45} \left(\frac{T_{\text{e}}}{10^4 \text{K}} \right)^{0.1} \dot{M}_{\odot} \text{yr}^{-1} \quad (6.28)$$

(e.g., Drake & Linsky, 1986), where d is the distance, and v_{∞} is the wind terminal velocity defined previously in Table 3.1. Using this expression, the ionized mass-loss rates were derived for each of the long wavelength measurements for both stars and are listed in Table 6.3. These values are based on the assumption of a $T_{\text{e}} = 10^4$ K wind for both stars and the errors originate from the uncertainties in the distance and the flux density values.

Table 6.3: Ionized mass-loss rates for α Boo and α Tau.

Star	Wavelength (cm)	\dot{M}_{ion} (M_{\odot} yr $^{-1}$)
α Boo	6.0	$5.9 \pm 0.8 \times 10^{-11}$
	9.5	$5.5 \pm 0.9 \times 10^{-11}$
	10.0	$5.1 \pm 0.4 \times 10^{-11}$
	20.0	$4.3 \pm 0.7 \times 10^{-11}$
α Tau	6.0	$\leq 8.2 \pm 0.6 \times 10^{-11}$
	9.5	$\leq 5.3 \pm 1.2 \times 10^{-11}$

We have discussed in the previous sections that for α Boo, these long wavelengths sample the outer atmosphere of the star where the wind is close to, or

6.8 Ionized Mass-Loss Rates

has reached its terminal velocity, and is beginning to cool due to gas expansion. In this case, these \dot{M}_{ion} values would be lower than those given in Table 6.3 as the electron temperature is probably lower than 10,000 K. However, as \dot{M}_{ion} is only weakly dependent on T_e this makes only a small difference and amounts to about a 7% increase in the ionized mass-loss if the temperature is actually lower by 50%. If the ionization balance is frozen-in in the regions of the outflow where these long wavelengths sample, then the derived \dot{M}_{ion} should be the same for these wavelengths. The decrease in \dot{M}_{ion} with longer wavelengths is very small as seen in Table 6.3 and may be a hint that the ionization fraction may be close to frozen-in at these wavelengths. If we were to assume that the total stellar mass-loss rate derived by Drake (1985) is correct, then a comparison with our longest wavelength value for the ionized mass-loss rate suggests an ionization fraction of ~ 0.2 in the outer wind of α Boo. Deriving a reliable ionized mass-loss rate for α Tau is more difficult because as we have argued in the previous sections, the longest wavelengths are still sampling the acceleration zone, and thus the velocity in the region where the long wavelength radio emission emanates from will be less than 30 km s^{-1} . In Table 6.3 the values are derived assuming the radio emission emanates from the outer atmosphere where the wind has reached its terminal velocity (i.e., 30 km s^{-1}) and so are just upper limits.

7

Thermal Energy Balance of Arcturus' Outflow

The chapter investigates the various heating and cooling processes that control the thermal structure of Arcturus' mass outflow region. We use the hybrid chromosphere and wind model derived in Chapter 6 as the basis to derive the magnitude of these processes as function of distance from the star. The analysis focuses on distances relatively close to the star (i.e., between 1.2 and $10 R_\star$) and includes the wind acceleration zone (i.e., between ~ 1.2 and $1.7 R_\star$), a region where much of the energy that drives the wind is injected. The effect of adiabatic expansion cooling, line cooling from neutral and ionic species, and radiative recombination are investigated as wind coolants. The heating mechanisms investigated are the deposition of magnetic wave energy, ambipolar diffusion, and radiative heating. This work is a continuation of the initial findings of O'Gorman & Harper (2011).

7.1 Motivation for a Thermal Energy Balance

We have shown in Chapter 1 that for a monotonic ideal gas, the energy per unit mass, $e(r)$, is the sum of the kinetic and gravitational energies, and the enthalpy

$$e(r) = \frac{v^2(r)}{2} - \frac{GM_\star}{r} + \frac{5\mathcal{R}T}{2\mu}. \quad (7.1)$$

The lower boundary of a stellar outflow is the photosphere which is gravitationally bound to the star. This implies that the energy in Equation 7.1 must be negative at this point. If a star is to have an outflow, then the energy must become positive at large r to escape the gravitational well (i.e., $v^2(r) \geq v_{\text{esc}}^2(r)$). Therefore, energy must be added to the gas if the velocity is to reach (or exceed) the local escape velocity. The addition of this energy can be either in the form of heat input per unit mass, $q(r)$, or in the form of momentum input (i.e., an outward force per unit mass, $f(r)$; Lamers & Cassinelli (1999)). In other words, differentiating Equation 7.1 with respect to r gives the change in energy per unit distance from the star, and this becomes

$$\frac{d e(r)}{dr} = f(r) + \frac{dq(r)}{dr} \quad (7.2)$$

which is just a form of the *Bernoulli* equation. The unknown fundamental mechanisms responsible for driving the winds of cool evolved stars must therefore manifest themselves in either one or both of the quantities on the right hand side of Equation 7.2. Therefore, studying the heating deposition, $q(r)$, taking place in Arcturus's outflow, is a valuable exercise and should provide insight into its wind driving mechanism(s).

Our multi-wavelength radio study of Arcturus allowed us to refine its existing atmospheric model. We found that our long wavelength VLA flux density measurements could be reproduced by the existing model if the almost isothermal outflow was replaced with an outflow that contained a large thermal gradient. This new hybrid model is graphically summarized in Figure 6.10. The goal in this chapter is to use this new model as a foundation to study the thermal energy balance in Arcturus's atmosphere. The simple idea behind this is that all the heating and cooling processes taking place in the outflow should combine to

7.2 Thermal Model for a Spherically Symmetric Outflow

produce the derived thermal profile from Chapter 6. Knowing the main mechanisms through which the plasma can cool thus allows us to examine the possible mechanisms which heat the plasma to the known temperature. Investigating the magnitude of the heating deposition of various mechanisms then tells us if such a mechanism can play a part in the mass-loss process.

7.2 Thermal Model for a Spherically Symmetric Outflow

In this section we derive an expression to describe how the temperature in a stellar outflow changes as a function of distance from the star. In doing so, we also present the notation that is used in subsequent sections to describe the magnitude of the heating and cooling taking place at certain regions in a stellar outflow. We assume all quantities vary radially (i.e, spherical symmetry) and that the mass-loss rate is constant (i.e., time independent). The continuity equation can then be written as

$$v \frac{d\rho}{dr} = -\rho \left(\frac{dv}{dr} + \frac{2v}{r} \right) \quad (7.3)$$

where v and ρ are the flow velocity and mass density at a distance r from the star. The first law of thermodynamics tells us that the change in internal energy of a system is equal to the heat added to the system minus the work done by the system on its environment. For a reversible process in a closed system the work done is PdV , where P and V are the pressure and volume of the system. Writing the first law of thermodynamics in terms of rates per unit mass then gives

$$\frac{du}{dt} = \frac{dq}{dt} - \frac{P}{m} \frac{dV}{dt} \quad (7.4)$$

where u is the internal energy per unit mass and q is the net heat gained per unit mass. The time dependence in the first and last terms can be switched to a radial dependence via $v = dr/dt$, and m/ρ can be substituted for V to get

$$v \frac{du}{dr} = -\frac{P}{\rho} \left(v \frac{d\rho}{dr} \right) + \frac{dq}{dt}. \quad (7.5)$$

7.2 Thermal Model for a Spherically Symmetric Outflow

Substituting in Equation 7.3 and using $u = 3nkT/2\rho$ and $P = nkT$ gives

$$v \left(\frac{3nk}{2\rho} \frac{dT}{dr} \right) = -\frac{nkT}{\rho} \left(\frac{dv}{dr} + \frac{2v}{r} \right) + \frac{dq}{dt}. \quad (7.6)$$

If we define Γ and Λ as the heating and cooling rates per unit volume respectively, then we can rearrange this equation to get

$$\frac{dT}{dr} = -\frac{4T}{3r} - \frac{2T}{3v} \frac{dv}{dr} + \frac{2(\Gamma - \Lambda)}{3nkv}. \quad (7.7)$$

The first two terms on the right account for adiabatic expansion cooling. The second term is important in the wind acceleration region but is zero once the wind has reached its terminal velocity. The third term accounts for all other heating and cooling processes. This equation is equivalent to Equation 8 in Goldreich & Scoville (1976) and can also be written in dimensionless form (Rodgers & Glassgold, 1991) by multiplying across by r/T as follows:

$$\frac{d(\ln T)}{d(\ln r)} = -\frac{4}{3} - \frac{2}{3} \frac{d(\ln v)}{d(\ln r)} + \sum_{i=1} \mathcal{H}_i - \sum_{j=1} \mathcal{L}_j \quad (7.8)$$

where

$$\mathcal{H}_i = \frac{2r}{3nkvT} \Gamma_i \quad (7.9)$$

and

$$\mathcal{L}_j = \frac{2r}{3nkvT} \Lambda_j \quad (7.10)$$

are the various heating and cooling rates per unit volume respectively, normalized to constant velocity adiabatic expansion cooling. Finally, this equation can be expressed in terms of the gas kinetic temperature's local power law slope, λ ,

$$\frac{d(\ln T)}{d(\ln r)} = -\lambda \quad (7.11)$$

where

$$\lambda = \lambda_0 + \sum_{i=1} \lambda_i \quad (7.12)$$

which contains all of the wind heating and cooling processes, including that from adiabatic expansion cooling, λ_0 . We note that positive and negative λ values represent heating and cooling, respectively. This notation will be used through-

out this chapter and allows the various heating and cooling process to be easily compared to the $4/3$ exponent, characteristic of a constant velocity outflow undergoing adiabatic expansion cooling.

7.3 Cooling Processes

The three ways in which the gas in Arcturus' partially ionized outflow can cool are through adiabatic expansion, radiative recombination, and collisional excitation of neutral and ionized atoms. We now assess the importance of each of these cooling processes between $\sim 1 - 10 R_\star$.

7.3.1 Adiabatic Expansion Cooling

Adiabatic expansion cooling is the thermodynamic process in which a fixed quantity of gas cools as it expands into a larger volume of gas. It is composed of a geometric term and a velocity gradient term; these being the first two terms on the right of Equation 7.8. As shown in Figure 7.1, the dominant term close to the photosphere is the velocity gradient term due to the rapid wind acceleration, while farther out where the wind reaches its terminal velocity, the geometric term becomes dominant. Adiabatic expansion cooling is a very efficient cooling mechanism in stellar outflows. To demonstrate this we take the atmosphere of Arcturus as an example and assume the absence of all other heating and cooling mechanisms. Considering only the adiabatic geometric cooling factor, the gas temperature would decrease to 1K by $1500 R_\star$ which would lower the gas temperature to below the cosmic background temperature.

7.3.2 Radiative Recombination Cooling

Radiative recombination is the process by which an electron is captured by an ion into a bound state n with the emission of a photon. The overwhelming abundance of H along with it having a similar cross section for capture to heavier ions, means that it is by far the most important species to consider for this cooling process.

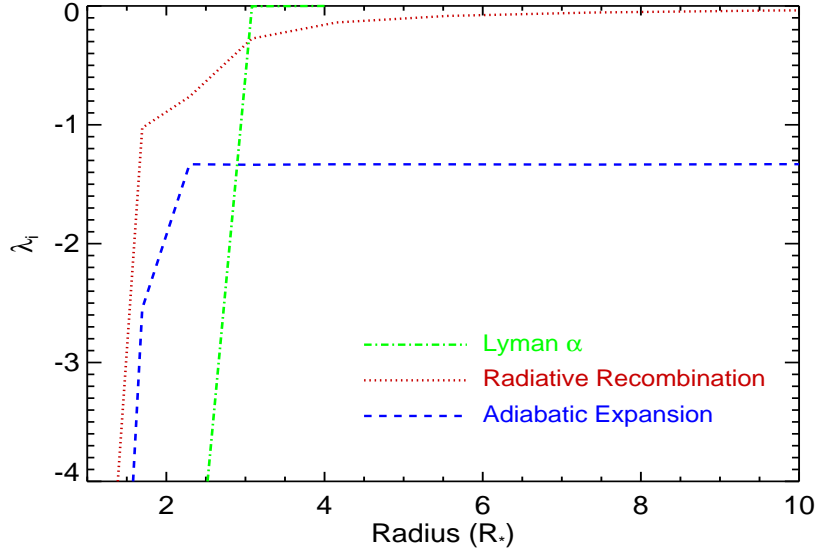


Figure 7.1: The net cooling from adiabatic expansion, radiative recombination, and Lyman α cooling in Arcturus' outflow. For adiabatic expansion cooling, the dominant term close to the photosphere is the velocity gradient term from Equation 7.8, due to the rapid wind acceleration, while further out where the wind reaches its terminal velocity, the geometric term becomes dominant. Radiative recombination is also an important cooling mechanism between $\sim 1 - 4 R_\star$. The Lyman α cooling function is very sensitive to T and is the dominant cooling process out to $2.8 R_\star$.

The radiative recombination cooling rate is

$$\Lambda = n_{HII} n_e \alpha^n \left(\frac{3}{2} kT \right) \quad \text{erg s}^{-1} \text{cm}^{-3} \quad (7.13)$$

where $3kT/2$ is the average thermal energy of a captured electron and α^n is the hydrogen recombination rate coefficient summed over n levels. The hydrogen recombination rate coefficient excluding captures to the $n = 1$ level is given as

$$\alpha_B = \frac{2.06 \times 10^{-11}}{T^{1/2}} \phi_2(\beta) \quad \text{s}^{-1} \text{cm}^3. \quad (7.14)$$

$\phi_2(\beta)$ is a function that varies with temperature and has been tabulated for various temperatures by (Spitzer, 1978). Recombination to the ground state is excluded because the process produces another ionizing photon that can be easily absorbed again, producing the net effect that the recombination had not occurred.

The radiative recombination cooling contribution can then be calculated using Equation 7.10, and as shown in Figure 7.1, its contribution is significant between $\sim 1 - 4 R_\star$.

7.3.3 Lyman-alpha Cooling

Collisions between electrons and gas atoms (or ions) causes energy to be exchanged between the thermal kinetic energy of the gas and the internal energy of the individual gas atoms (or ions). Collisional excitation cools the gas while collisional de-excitation heats the gas. At temperatures of a few thousand degrees, the excited levels in neutral hydrogen can become populated from electron collisions and thus can be a source of cooling. The analytical expression for the resulting net cooling rate per volume is

$$\Lambda_{eH} = 7.3 \times 10^{-19} n_e n_{HI} e^{-118,400/T(K)} \quad \text{erg s}^{-1} \text{ cm}^{-3} \quad (7.15)$$

Spitzer (1978). Most of the resulting radiation comes from the $n = 2$ level (Lyman α) and this is why the cooling rate is almost proportional to $\exp(-E_{12}/kT)$, where $E_{12}/k = 118319 \text{ K}$. Equation 7.15 is a very sensitive function of the gas temperature and as can be seen from Figure 7.1, is the dominant cooling process out to $2.8 R_\star$. The sharp falloff in temperature in Arcturus' outflow post $2.3 R_\star$ results in this mechanism changing from being a very efficient cooling process within $2.3 R_\star$ to having a negligible effect by $\sim 3.1 R_\star$.

7.3.4 Other Line Coolants

Due to its large abundance, hydrogen is expected to be the most efficient line cooling mechanism in the inner atmosphere of Arcturus. Nevertheless, it is also worth investigating the effects of line cooling from heavier elements which may become important at lower temperatures further out in the atmosphere, where line cooling from H has almost ceased. Line cooling from these heavy elements is due mainly to electron impact excitation of electronic levels of the neutral and ionized species at high temperatures, while at lower temperatures (i.e. farther out in the CSE) line cooling is mainly due to the electron impact excitation of fine structure levels of the neutral and ionized constituents (Dalgarno & McCray,

1972). Table 7.1 lists the most relevant heavy elements for this study based on abundance and suitable line transitions. All heavy elements with an ionization potential (IP) lower than O were assumed fully ionized, while the ionization balance of O was based on the *IUE* line profile analysis of Judge (1986).

Table 7.1: Elemental Abundance in Arcturus's Outflow.

Element	Abundance	IP (eV)	Reference
O	4.7×10^{-4}	13.6	Ramírez & Allende Prieto (2011)
C	2.1×10^{-4}	11.3	Ramírez & Allende Prieto (2011)
N ¹	6.7×10^{-5}	14.5	Asplund <i>et al.</i> (2009)
Mg	3.0×10^{-5}	7.6	Ramírez & Allende Prieto (2011)
Si	2.0×10^{-5}	8.2	Ramírez & Allende Prieto (2011)
Fe	1.0×10^{-5}	7.9	Decin <i>et al.</i> (2003)

¹ Assumed solar abundance.

The line cooling rate per unit volume due to the transition ul in a medium where the optical depth is not negligible is

$$\Lambda_{\text{line}} = \sum_{u \rightarrow l} n_u A_{ul} E_{ul} \rho(\tau) \quad \text{erg s}^{-1} \text{ cm}^{-3} \quad (7.16)$$

where n_u is the population of the upper level, A_{ul} is the spontaneous emission coefficient of the transition, and E_{ul} is the energy of the radiated photon. Here, the sum is over all possible upper to lower transitions and $\rho(\tau)$ is the probability the photon will escape the gas without being reabsorbed. This function lowers the line cooling rate and can be written as

$$\rho(\tau) = \frac{1 - \exp(-3\tau/2)}{3\tau/2}. \quad (7.17)$$

This expression reaches the correct solution in the low and high optical depth limits. It is used in the work of Rodgers & Glassgold (1991) and is an approximation of Castor (1970)'s escape probability when the logarithmic velocity gradient is zero. The level populations in Equation 7.16 were found by solving the rate

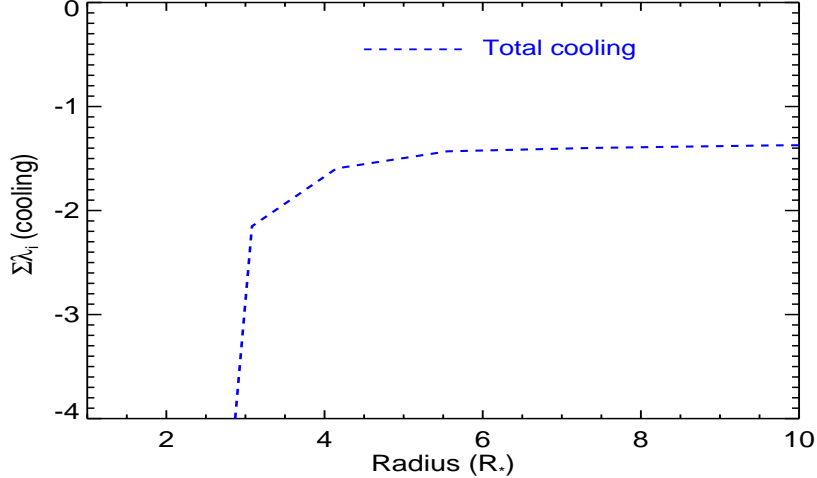


Figure 7.2: Summation of all the cooling mechanisms normalized to constant adiabatic cooling taking place in Arcturus' outflow. The cooling taking place within the first $3 R_\star$ is mainly due to Lyman Alpha, emission line while the cooling further out is from gas expansion, with a small contribution from radiative recombination.

equations, which for a two level atom can be written as,

$$\frac{n_u}{n_l} = \frac{g_u}{g_l} \exp\left(\frac{-E_{21}}{kT}\right) \left(1 + \frac{n_{\text{cr}}}{n}\right)^{-1}. \quad (7.18)$$

Here g_u and g_l are the degeneracy (the number of states with the same energy) of the levels and n is the number of collisional partners in the gas. The critical density, n_{cr} , is the ratio of the radiative and collisional de-excitation rates

$$n_{\text{cr}} = \frac{A_{ul}\rho_{ul}}{C_{ul}} \quad (7.19)$$

and determines whether the gas is effectively thin at that point in the outflow.

The line cooling from these heavy elements was found to be only significant within $1.5 R_\star$; the most efficient of which being the C II $^4P \rightarrow ^2P$ spin-forbidden permitted dipole multiplet (2326 Å). The properties of this feature, along with the next two strongest line coolants are shown in Table 7.2. As the density decreases, so too do the number of collisions, and so when atoms/ions radiate they are less likely to be re-excited. Therefore line cooling from these heavy elements is only important at high densities, i.e., close to the star. In Figure 7.2 we plot the sum of

Table 7.2: Properties of Strongest Line Coolants.

Species	Transition	E_{ul} (K)	λ (Å)	A_{ul} (s^{-1})
C II	$^4P \rightarrow ^2P$	6.2×10^4	2326	3.6
O I	$^1D \rightarrow ^3P$	2.3×10^4	6300	6.7×10^{-3}
Mg II	$^2S \rightarrow ^2P$	5.1×10^4	2796	2.6×10^8

Note: Data taken from Hollenbach & McKee (1989).

all the cooling mechanisms taking place in Arcturus' outflow. The cooling taking place within the first $3 R_\star$ is mainly due to Lyman Alpha emission line while the cooling further out is mainly due to gas expansion, with a small contribution from radiative recombination.

7.4 Heating Mechanisms

In the following sections we investigate various possible heating mechanisms taking place in Arcturus's outflow and the overall efficiency of these mechanisms at various distances from the star.

7.4.1 Photoionization Heating

The UV radiation field of Arcturus can photoionize atoms producing energetic electrons which heat the atmosphere. The energy released per second per unit volume due to the photoionization of an atom X can be written as

$$\Gamma(X) = n(X) \int_{\lambda_{min}}^{\lambda_{th}} \frac{4\pi J_\lambda}{E_\lambda} \sigma_X(\lambda) (E_\lambda - E_{\lambda_{th}}) d\lambda. \quad (7.20)$$

Here, $E_\lambda - E_{\lambda_{th}}$ is the energy added to the gas by one ionization, i.e., the energy of the incident photon minus the threshold energy for ionization, which is specific to each element. J_λ is the mean intensity of radiation at a point and so $4\pi J_\lambda/E_\lambda$ is the number of incident photons per unit area per unit time per unit wavelength interval. $\sigma_X(\lambda)$ is the ionization cross section for an atom X by photons with an energy E_λ below a threshold wavelength, λ_{th} , and is a function of wavelength.

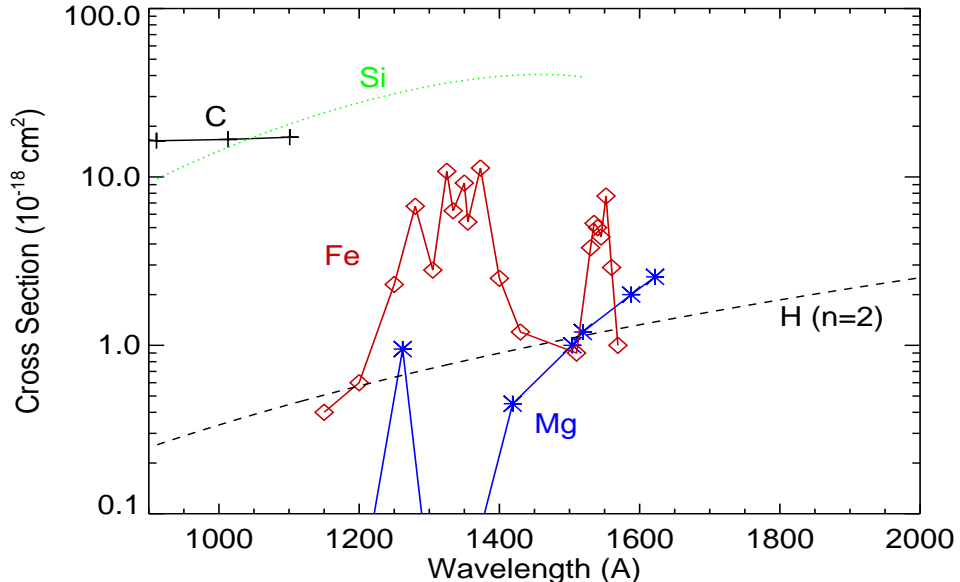


Figure 7.3: The photoionization cross section values for atoms with IPs less than 13.6 eV which were used in this study. The photoionization of H from the $n = 2$ level was also considered and its cross section is also shown. The Balmer continuum is the ionization threshold for H ($n=2$) is 3646 Å.

To calculate the mean intensity, the incident flux must be known. The flux at the stellar surface, F_* , is related to the flux observed at Earth, F_{\oplus} , by

$$F_* = \left(\frac{d}{R_*} \right)^2 F_{\oplus} = \left(\frac{2}{\phi} \right)^2 F_{\oplus} \quad (7.21)$$

where d is the distance and ϕ is the angular diameter. The mean intensity at a point in the atmosphere is then

$$J(r) = W(r) I_* = \frac{W}{\pi} \left(\frac{2}{\phi} \right)^2 F_{\oplus} \quad (7.22)$$

where I_* is the specific intensity and we have assumed the relationship, $F_* = \pi I_*$. $W(r)$ is the radiation dilution factor and is given by

$$W(r) = \frac{1}{2} \left(1 - \sqrt{1 - \left(\frac{R_*}{r} \right)^2} \right). \quad (7.23)$$

The incident flux measurements (i.e., F_{\oplus}) which vary as a function of wavelength were obtained from the online StarCAT catalog (Ayres, 2010b). Any missing data were interpolated or extrapolated upon to provide a continuous $J(r)$ between 912 Å and 3646 Å [i.e., the ionization threshold for the H ($n = 2$) level]. The photoionization cross section values for atoms with IPs less than 13.6 eV along with the values for the H ($n = 2$) level were taken from Mathisen (1984) and are shown as a function of wavelength in Figure 7.3.

The net heating due to photoionization was then found by using Equation 7.20 for each of these species resulting in significant heating inside $\sim 1.4 R_{\star}$ as shown in Figure 7.5. However, by $\sim 2 R_{\star}$ its heating ability is about one order of magnitude weaker than adiabatic cooling at the same distance and so photionization heating is not an efficient mechanism in heating Arcturus' outflow.

7.4.2 Ambipolar Diffusion Heating

If a magnetic field remains frozen to the electrons and ions in a plasma, the charged plasma and field can drift through the gas of neutral atoms. The collisions, chiefly between positive ions and neutral hydrogen atoms (Spitzer, 1978), result in an exchange of momentum between the magnetic field and the neutral gas which results in a net heating. The recent possible detection of a weak ($B < 1 G$) mean longitudinal magnetic field for Arcturus (Sennhauser & Berdyugina, 2011) suggests that ambipolar diffusion heating should be considered as a possible heating mechanism. We use the expression given by Shang *et al.* (2002) to define the volumetric rate of ambipolar diffusion

$$\Gamma = \frac{\rho_n |\mathbf{f}_L|^2}{\gamma \rho_i (\rho_n + \rho_i)^2}. \quad (7.24)$$

Here, ρ_n and ρ_i are the mass densities of the neutral and ionic species, respectively, γ is the ion-neutral momentum transfer coefficient (in units $\text{cm}^3 \text{s}^{-1} \text{g}^{-1}$), and \mathbf{f}_L is the volumetric Lorentz force

$$\mathbf{f}_L = \frac{1}{4\pi} (\nabla \times \mathbf{B}) \times \mathbf{B} \quad (7.25)$$

where \mathbf{B} is the magnetic field vector. In order to calculate the ambipolar diffusion heating, we need to find a value for γ , which depends on the collisional coefficient rates, cross sections, slip speed, and gas composition. The γ coefficient can be transformed into a quartic equation by eliminating a term known as the slip velocity, w ($w \equiv v_i - v_n$). The derivation of 7.24 assumes that the difference in acceleration in the neutrals and ions can be ignored. The radial Lorentz force is found from the equation of motion:

$$\rho_n v_n \frac{dv_n}{dr} + \rho_i v_i \frac{dv_i}{dr} = -\frac{GM_\star}{r^2}(\rho_n + \rho_i) + f_L. \quad (7.26)$$

This then allows the γ coefficient and thus the volumetric heating to be calculated. The effect of radial ambipolar diffusion heating was found to be about three orders of magnitude less than adiabatic constant velocity expansion cooling and is therefore a negligible heating mechanism. This is due to the relatively high ionization balance in Arcturus' outflow.

7.4.3 Turbulent Heating

The dissipation of turbulent fluctuations can make a significant contribution to the thermodynamic heating of a plasma, and has regularly been studied as a heating source of the solar corona and driving solar wind acceleration (e.g., Cranmer *et al.*, 2007; Lehe *et al.*, 2009). It has also been studied as a source of energy and momentum for accelerating cool evolved stellar winds (e.g., Falceta-Gonçalves *et al.*, 2006; Hartmann & MacGregor, 1980). These studies have focused on the dissipation of turbulent fluctuations from Magnetohydrodynamic (MHD) waves and we likewise make the same assumption. However, our simple phenomenological description of turbulent heating can also be explained by the dissipation of acoustic waves in an unmagnetized medium (e.g., Lighthill, 1952; Stein, 1967).

The idea of MHD turbulent heating of Arcturus' atmosphere is based on what is known to happen in the solar atmosphere. For the Sun, most of the photospheric magnetic field is located in small flux tubes (of diameter ~ 100 km) concentrated in the intergranular downflow lanes with field strengths of ~ 1400 G (Berger & Title, 2001). These flux tubes, whose geometries are shown in Figure 7.4, have relatively small photospheric filling factors of $f_\star \sim 0.1 - 1\%$ and so the

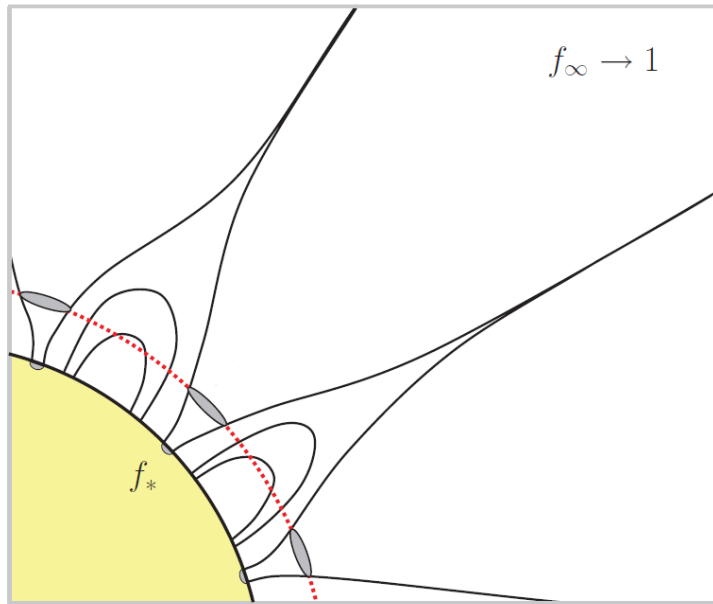


Figure 7.4: Example of diverging flux tubes in the atmosphere of a cool evolved star. The filling factor, f , of the open magnetic flux tubes grows from $f_* \ll 1$ at the photosphere to an asymptotic value of $f_\infty \rightarrow 1$ at large distances. Alfvén waves then propagate up these flux tubes and are partially reflected, resulting in an interaction causing turbulence which dissipates into heating. Image adopted from Cranmer & Saar (2011).

total magnetic flux density is much lower when spatially averaged over the entire solar disk and is in the order of $f_* B_* = 1 - 10$ G (Schrijver & Harvey, 1989). The same structures may be present in the atmosphere of Arcturus, which possibly has of a weak ($B < 1$ G) mean longitudinal magnetic field (Sennhauser & Berdyugina, 2011). Alfvén waves then propagate up these flux tubes and are partially reflected by radial gradients in the density and magnetic field strength. The counter-propagating wave packets then interact with one another along these flux tubes, developing into strong MHD turbulence (Iroshnikov, 1964). The energy flux in the cascade from large to small eddies terminates in dissipation and heating (e.g., Cranmer & van Ballegooijen, 2005; Matthaeus *et al.*, 1999).

In this study, we adopt the following phenomenological form for the MHD

turbulent heating rate per unit volume,

$$\Gamma_{turb} = \frac{1}{2} \frac{\rho U^2}{L/U} \quad \text{erg s}^{-1} \text{ cm}^{-3} \quad (7.27)$$

where U is the characteristic velocity and L is the characteristic length scale. For solar studies, the characteristic length scale at the photosphere would be the size of the granular cells that are responsible for perturbing the flux tubes (i.e., $100 - 1000$ km), which are similar in size to the solar photospheric density scale height (i.e., $H_\odot \sim 270$ km). Unlike the Sun, we cannot determine L via observations and choose L to be the local density scale height:

$$L = \rho \left(\frac{d\rho}{dr} \right)^{-1}. \quad (7.28)$$

The characteristic velocity is taken to be the local hydrogen sound speed, i.e.,

$$U = \sqrt{\frac{5}{3} \frac{P}{\rho}} = 12.85 \times 10^5 \sqrt{\frac{T_e}{10^4}} \quad \text{cm s}^{-1}. \quad (7.29)$$

Observations of optically thin chromospheric lines show that the turbulent velocity is similar to the local sound speed and we make the assumption that this remains true throughout the outflow.

This simple description of turbulent heating assumes an ideal Kolmogorov (1941) hydrodynamic cascade but such simple descriptions have already successfully reproduced many properties of coronal heating for the Sun (Cranmer, 2012). The dissipation of turbulent fluctuations in Arcturus' wind make a significant heating contribution out to many stellar radii, as can be seen in Figure 7.5. It can be shown that

$$\lambda_{turb} \propto \frac{\sqrt{T_e}}{v} \frac{d(\ln \rho)}{d(\ln r)} \quad (7.30)$$

and so when the wind has reached its terminal velocity, the turbulent heating varies as $\lambda_{turb} \propto \sqrt{T_e}$.

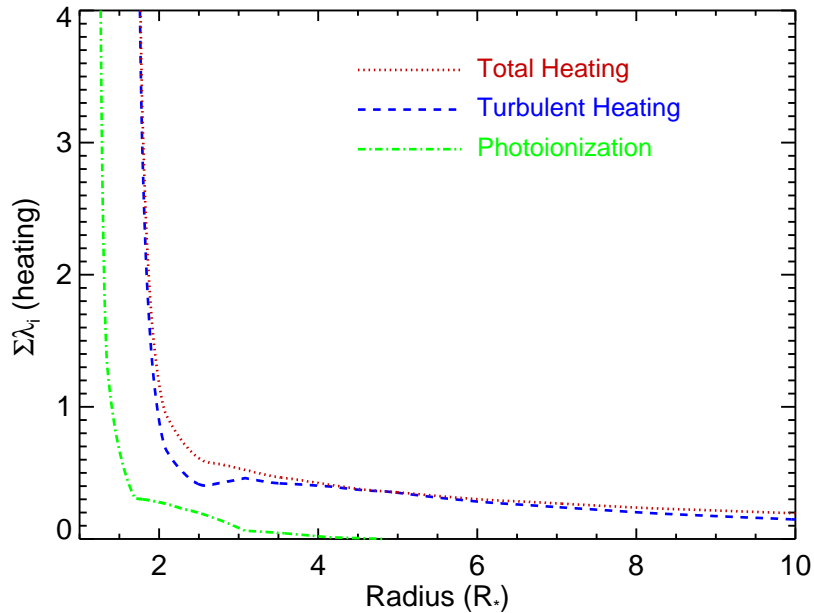


Figure 7.5: The main heating mechanism in Arcturus' wind is from the dissipation of turbulence. Photoionization of H also contributes to heating close to the star, while the heating from ambipolar diffusion is found to be negligible.

7.5 Thermal Energy Balance

We now consider the balance of heating and cooling for the reasons discussed at the end of Sections 7.1. We first find the gas kinetic temperature local power law slope, λ , for the new atmospheric model of Arcturus, which we developed in Chapter 6. To do so, we substitute the temperature profile into Equation 7.11. As the flow is isothermal between 1.2 and $2.3 R_*$, the power law slope is zero as shown in Figure 7.6. Beyond $2.3 R_*$, this model contains a temperature power-law slope of $T_e \propto r^{-1.65}$, and therefore $\lambda = -1.65$. For clarity, we have excluded the data within $1.2 R_*$ throughout this section as the density and temperature gradients within this region are very large, and can make the calculated λ many orders of magnitude greater than those beyond $1.2 R_*$. The majority of the wind acceleration occurs beyond $1.2 R_*$ so the velocity gradient is still taken into account in our analysis.

In theory, if we were able to precisely account for all of the heating and

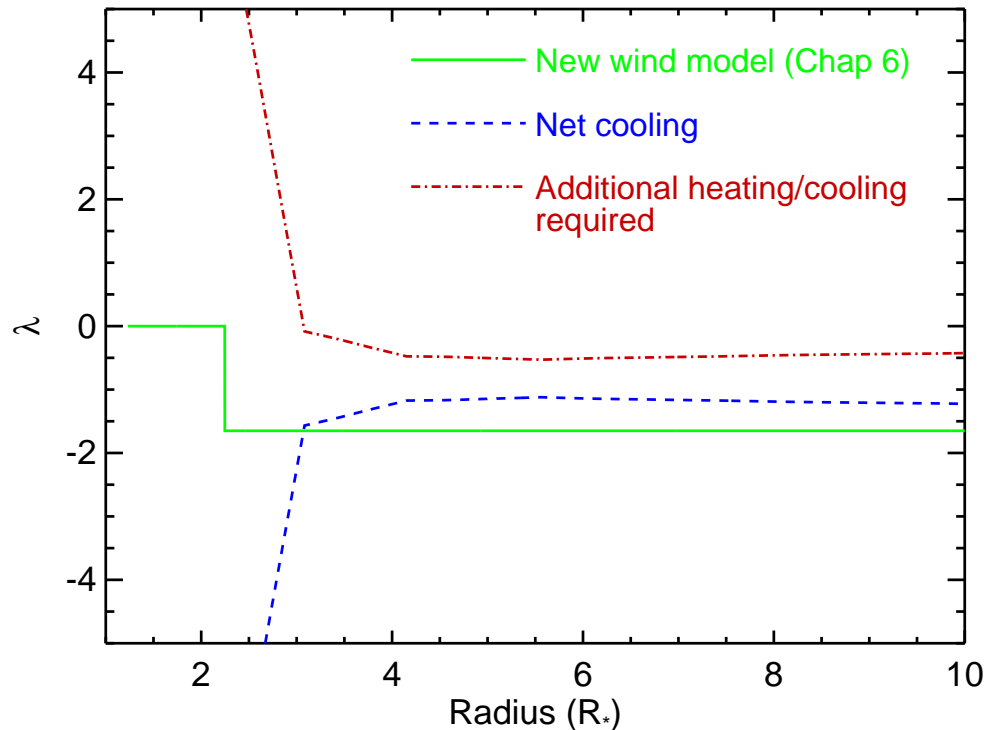


Figure 7.6: The gas kinetic temperature local power law slopes used for calculating the thermal energy balance. The green solid line is the power law slope of the new atmospheric model for Arcturus described in Chapter 6. The blue dashed line is the net cooling as a result of combining all of the cooling and heating processes described in Sections 7.3 and 7.4. The red dot-dashed line is the required additional heating/cooling to reproduce the thermal structure of our model atmosphere. A significant additional energy input is required within $3 R_{\star}$ to reproduce our model atmosphere, while some additional cooling is required beyond $3 R_{\star}$.

cooling processes taking place in Arcturus' atmosphere, then a summation of their power law slopes would reproduce the power law slope of the model atmosphere (assuming the model atmosphere to be an exact representation of the actual atmosphere). The dashed blue line in Figure 7.6 represents a summation of all the heating and cooling processes discussed in Sections 7.3 and 7.4. The result of this is a considerable net cooling at all distances from the star. Within $\sim 3 R_{\star}$, this net cooling far exceeds that predicted by the atmospheric model. This implies that one or more additional energy inputs must be acting on the

inner region of the outflow, which have not been accounted for in Section 7.4. The magnitude of this required additional heating within $\sim 3 R_\star$ is also shown in Figure 7.6 and is represented by the dot-dashed red line. Beyond, $\sim 3 R_\star$ the temperature power law slope of the model atmosphere is less than the slope of the calculated net cooling. This is because the model atmosphere of Arcturus is cooling super-adiabatically beyond $2.3 R_\star$ where $\lambda = -1.65$, while we have found that the only significant cooling process beyond $\sim 3 R_\star$ is adiabatic expansion where $\lambda = -1.33$.

7.6 Discussion

In Section 7.3 we found that the effect of Ly α line cooling becomes small beyond $\sim 3 R_\star$ and at greater distances we found that the only efficient cooling mechanism is adiabatic expansion. Since the velocity gradient is zero at these greater distances, the temperature local power law slope is $\lambda = -1.33$. The fact that we have not found any other efficient cooling mechanism beyond $\sim 3 R_\star$ does hint that the temperature power-law coefficient of -1.65 , in the new atmospheric model for Arcturus, may be too severe. The fact that we assumed a constant ionization fraction when investigating the radio spectral indices in Chapter 6 (i.e., the ionization balance was assumed to be *frozen-in*) may be a reason for this. Allowing the ionization balance to vary would have produced a smaller temperature power-law coefficient, but this approach would have given too many free parameters and no unique wind solution would have been attainable via our analytical approach.

The value of the red dot-dashed line in Figure 7.6 would be zero at all radii if our model atmosphere was a complete description of the true value and if we had accounted for all of the heating and cooling processes. It is clear from this figure that the best results (i.e., closest values to zero) are found at distances beyond $3 R_\star$ where adiabatic expansion cooling produces a power law slope of $\lambda = -1.33$ which is reasonably close to the model value of $\lambda = -1.65$. However, within $\sim 3 R_\star$, it is very clear that some major additional heating source is required to maintain the temperature profile of our model atmosphere. A more rigorous treatment (i.e., a non-phenomenological description) of heating due to

7.6 Discussion

the turbulent dissipation of Alfvén waves may be one possible route for further investigation, although one would wonder how the different descriptions of the same process could produce such vastly different results.

8

Conclusions and Future Work

The goal of the thesis was to broaden and deepen our understanding of the outflow environments of red giants and red supergiants. To achieve this goal, we observed these stars with the most sensitive radio interferometers available, allowing their atmospheres to be probed with excellent detail. The first part of the thesis described the results of our multi-wavelength high spatial resolution campaign to enhance our understanding of Betelgeuse's complex outflow environment. The second part of the thesis focused on the analysis of multi-wavelength centimeter continuum emission from Arcturus and Aldebaran, which provided a snapshot of the different stellar atmospheric layers. In this chapter, the primary findings and conclusions of these two studies are presented, along with possible directions for future work such as observing Betelgeuse's CSE with ALMA and carrying out multi-epoch observations of Betelgeuse's wind acceleration region with e-MERLIN.

8.1 Principle Results

The main findings of the thesis are discussed in the following two sections.

8.1.1 Betelgeuse's Extended Atmosphere

- The two distinct velocity components seen by Bernat *et al.* (1979) in CO absorption against the stellar spectrum at $4.6\text{ }\mu\text{m}$ were both separately detected and spatially resolved at 230 GHz for the first time. The extended CARMA C configuration resolved out almost all of the S2 emission leaving us with an approximate line profile for the S1 flow. From this profile a blueshifted outflow velocity of -9.0 km s^{-1} and a slightly greater redshifted outflow velocity of $+10.6\text{ km s}^{-1}$ was inferred; in good agreement with Bernat *et al.*'s (1979) line-of-sight expansion velocity value of -9 km s^{-1} .
- The line profiles obtained with the D and E configurations were found to be wider than the C configuration line profile, with the notable appearance of an extreme blue wing feature which was associated with the S2 flow. The high spectral resolution multi-configuration spectrum was used to determine S2 outflow velocities of -15.4 km s^{-1} and $+13.2\text{ km s}^{-1}$, which are in good agreement with Bernat *et al.*'s (1979) value of 16 km s^{-1} .
- In the blueshifted channels of the multi-configuration image cube the emission is compact at high absolute velocities and becomes more extended at lower absolute velocities, indicating that the S2 flow has a shell like structure. This is less clear in the redshifted channels, indicating an asymmetric shell. These multi-configuration maps provide the first direct measurements on the spatial extent of the S2 flow, which we derive to have a radius of $17''$; a value that is higher than most previous single dish estimates.
- A well defined outer edge for the S1 flow is not obvious. The emission at low absolute velocities is resolved out in the S1 line profile and because the resolving out scale of the C configuration is $\sim 6''$, this tells us that the spatial extent of the emission must be at least $\sim 3''$. From the intensity

8.1 Principle Results

distribution of the S1 emission, we infer that the extent of the S1 emission is between $4 - 6''$.

- Both flows were found to be inhomogeneous down to the resolution limit, with a notable clump of emission $\sim 5''$ S-W of the star, at low absolute velocities in the stellar rest frame. However, when azimuthally averaged, the intensity falloff of both flows were found to be consistent with an optically thin, spherically symmetric constant velocity outflow, similar to that found for KI at larger scales.
- Previous single dish observations of the CO line with small HPBWs do not show the classical resolved signature of high emission at large absolute velocities and low emission at low absolute velocities for two main reasons. Firstly, the S1 flow is still unresolved in these single dish observations and thus contributes emission at the lower absolute velocities. In addition, the multi-configuration CARMA maps show that the S2 emission is brighter in the higher absolute velocity maps than at lower absolute velocities and so when the emission from the fainter rings is neglected (i.e., when observed with a small HPBW), the overall line profile does not change significantly.
- The various CO rotational line profiles get narrower with increasing excitation energies, indicating that the higher excitation lines are formed mainly in the S1 flow. Therefore the high frequency bands of ALMA will preferentially trace the S1 flow.
- Assuming a mean outflow velocity of 14.3 km s^{-1} and 9.8 km s^{-1} for the S2 and S1 flows, respectively, then their ages are $\sim 1100 \text{ yr}$ and $\sim 400 - 600 \text{ yr}$. The S1 flow may be an extension of the current wind phase seen at UV and centimeter wavelengths, but higher spatial resolution data is needed to confirm this (see Section 8.2.1).
- The thermal continuum emission of Betelgeuse's inner atmosphere has been imaged at 6 cm with e-MERLIN, revealing two unresolved hotspots separated by 90 mas, with brightness temperatures 5400 ± 600 and $3800 \pm 500 \text{ K}$.

The astrometric solutions of Harper *et al.* (2001) place the optical photospheric position almost directly at the position of the weaker feature, meaning that the hotter feature is $\sim 2 R_\star$ above the optical photosphere. Existing 1-D atmospheric models are capable of almost reproducing the low resolution e-MERLIN image, but are inadequate at the highest e-MERLIN resolution. 1-D atmospheric models are probably not a realistic representation of Betelgeuse's inner atmosphere.

- High spatial resolution multi-wavelength archival VLA+Pi Town data, taken 10 yr prior to the e-MERLIN data set, were examined to look for signatures of the e-MERLIN hotspots. No evidence was found for the presence of the two hotspots at either 1.3 or 0.7 cm where the resolution was comparable or better than that of e-MERLIN's. We conclude that the hotspots are either optically thin at these high frequencies or their dynamics are time dependent on scales of just a few years.
- Multi-epoch, multi-wavelength radio continuum observations between 1996 and 2004 reveal total flux density variations between $20 \rightarrow 35\%$ at wavelengths between 0.7 and 6 cm. The 0.7 cm radio maps show a highly asymmetric source at all epochs, with dramatic changes in the radio emitting topology over a time period of only one to two years. These frequent changes in the radio emitting topology may be the cause of the flux density variations at 0.7 cm.

8.1.2 Dust-free Red Giants

- In this thesis, we have presented the most comprehensive set of multi-wavelength radio continuum observations of two luminosity class III red giants to date. A snapshot of the different stellar atmospheric layers of Arcturus and Aldebaran was obtained, independent of any long-term variability. The first detections were made at several wavelengths for each star, including a detection at 10 cm (3.0 GHz: S band) for both stars and a 20 cm (1.5 GHz: L band) detection for Arcturus, making these the first isolated luminosity class III red giants to be detected at such long wavelengths.

8.1 Principle Results

- The long-wavelength data sample the outer layers of Arcturus' atmosphere where its wind velocity is approaching its terminal value and the ionization balance is becoming frozen-in. For Aldebaran however, the long-wavelength data is still sampling its inner atmosphere where the wind is still accelerating, probably due to its lower mass loss rate.
- Little evidence for radio flux variability was found when our measurements were compared with previous observations. However, previous observations have provided only a small number of modest S/N measurements and so it is difficult to make a conclusive statement regarding the radio variability of these sources. Interestingly, prior to this study Aldebaran had been observed at 6 cm but was not detected. However, we detected the star at 6 cm with a flux density over two times greater than the previous 3σ upper limit, which could mean that its wind may have a time dependent nature.
- Our radio flux density measurements were compared with the predictions of published semi-empirical models based on UV data. The chromospheric and transition region semi-empirical model of McMurry (1999) with an optically thin wind overlain does well in reproducing our radio fluxes but we find that the chromospheric and wind semi-empirical model of Drake (1985) does not agree well with our data.
- Arcturus was found to have a spectral index of $\alpha = 1.05 \pm 0.05$ while Aldebaran's value was found to be higher at $\alpha = 1.58 \pm 0.25$. Both of these values are well above that expected for an isothermal wind with a constant velocity and ionization fraction.
- The long wavelength radio measurements of Arcturus were found to be emanating from a region of the atmosphere where its wind is close to the terminal velocity. This allowed evidence to be found for a rapidly cooling wind with a temperature radial dependence of $T(r) \propto r^{-1.65}$.
- A new wind model was developed for Arcturus which was based on the analytical advection model of Glassgold & Huggins (1986). It incorporates a rapidly cooling wind profile and was based on the new VLA long wavelength

flux measurements. This provided a new *hybrid* atmospheric model for Arcturus, which consists of the original inner atmosphere developed by Drake (1985), out to a radius of $2.3 R_\star$ and the new wind model farther out.

- The new hybrid atmospheric model for Arcturus was used to investigate the various heating and cooling processes that control the thermal structure of its mass outflow region between 1.2 and $10 R_\star$. Lyman α line cooling was found to be the main cooling mechanism within $2.8 R_\star$ while adiabatic expansion cooling was the most efficient cooling mechanism farther out. Magnetic wave heating is found to be the likely main heating mechanism throughout the atmosphere. A considerable net cooling was calculated at all distances from the star. Within $\sim 3 R_\star$, this net cooling far exceeds that predicted by the atmospheric model, implying that one or more additional energy inputs must be acting on the inner region of the outflow to maintain the thermal profile. Beyond $\sim 3 R_\star$, the only significant cooling process is adiabatic expansion, which is insufficient to account for the super-adiabatically cooling wind.

8.2 Future Work

The research presented in this thesis highlights the important and exciting science which can be carried out with red giants and red supergiants at radio wavelengths, using the latest suite of radio interferometers. The main findings presented in this thesis have been based on observations carried out with the most sensitive millimeter and centimeter interferometers available at the time. The CARMA millimeter interferometer is currently being surpassed in sensitivity, spatial and spectral resolution, and frequency coverage by the Atacama Large Millimeter/submillimeter Array (ALMA). ALMA will open up a whole new part of the millimeter and submillimeter spectrum for study with unparalleled detail, allowing the distribution of molecules and dust around M supergiants to be mapped with resolution of just a few milliarcseconds at the highest frequencies. Most of the centimeter observations discussed in this thesis were obtained with

the VLA and e-MERLIN during their commissioning phase with only a fraction of the now available bandwidth. The large bandwidth now available with these instruments will allow fast detections of historically weak or undetectable radio continuum luminosity class III red giants at both long and short wavelengths. Previous upper limits will be replaced by firm detections allowing a greater understanding of their outer atmospheric properties. In the following sections we describe some future projects which would complement and improve on the work presented in this thesis.

8.2.1 Probing the S1 flow of Betelgeuse with ALMA

In chapter 5, we outlined how the inner S1 flow around Betelgeuse was successfully imaged with sub-arcsecond spatial resolution (i.e., $0.9''$), revealing an irregular CO distribution between $40 R_\star$ ($0.9''$) and $270 R_\star$ ($\sim 6''$). Recently, Kervella *et al.* (2011) recorded a series of thermal IR images using the VLT/VISIR ($\lambda = 8\text{--}20 \mu\text{m}$) and found a ring-like structure at radius $0.5\text{--}1.0''$ (i.e., $\sim 30 R_\star$), which the author associated with the dust condensation radius. Such a spatial scale was just beyond the resolution of our CARMA data set. To build a complete and consistent picture of the mass-loss in Betelgeuse we have been awarded 5.5 hours of observing time with ALMA in the current observing cycle (i.e., ALMA Early Science Cycle 1). The goal of this scheduled study is to unravel the dynamical and chemical structure of the inner ($\lesssim 3''$) CSE, via observations of molecular line emission with a resolution of $\sim 0.09''$, an order of magnitude greater than our CARMA study. Such observations will shed light on the spatial correlation between the dust and molecules in the CSE and may identify the region where molecules condense into dust grains.

The observations will be carried out in the $B_{\max} \sim 1 \text{ km}$ configuration and the main target line will be the CO($J = 6 - 5$) line at 691 GHz. CO is a very stable molecule and does not take part in dust condensation allowing us to distinguish between different chemical and dynamics effects. Figure 8.1 displays a dust emission model based on the the VLT/VISIR image of Kervella *et al.* (2011) showing a ring like structure which may be the region of dust condensation around Betelgeuse. The CASA simulation tool was then used to create an image of the

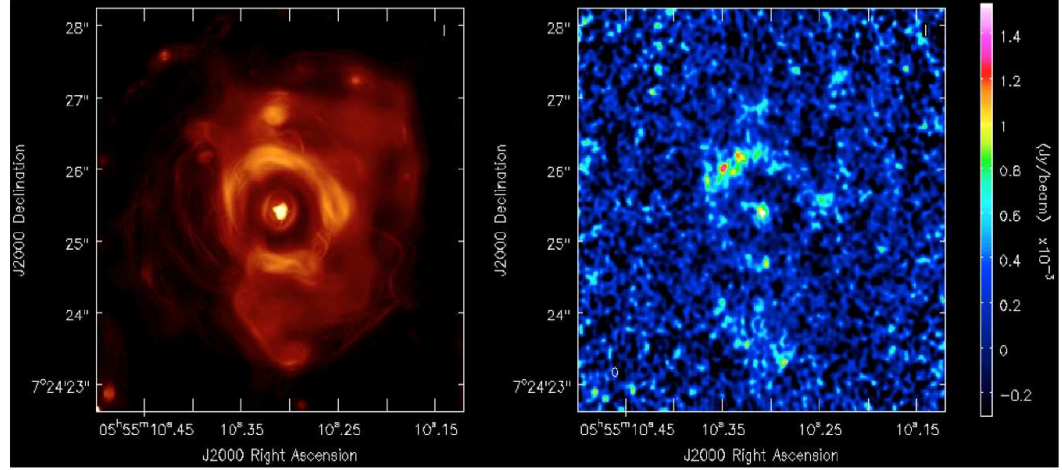


Figure 8.1: *Left:* Dust emission model based on the VLT/VISIR image of Kervella *et al.* (2011) showing a ring like structure which may be the region of dust condensation around Betelgeuse. *Right:* Simulated ALMA image of 6 GHz of continuum emission after two hours on source reveals that some of the structure should be detectable.

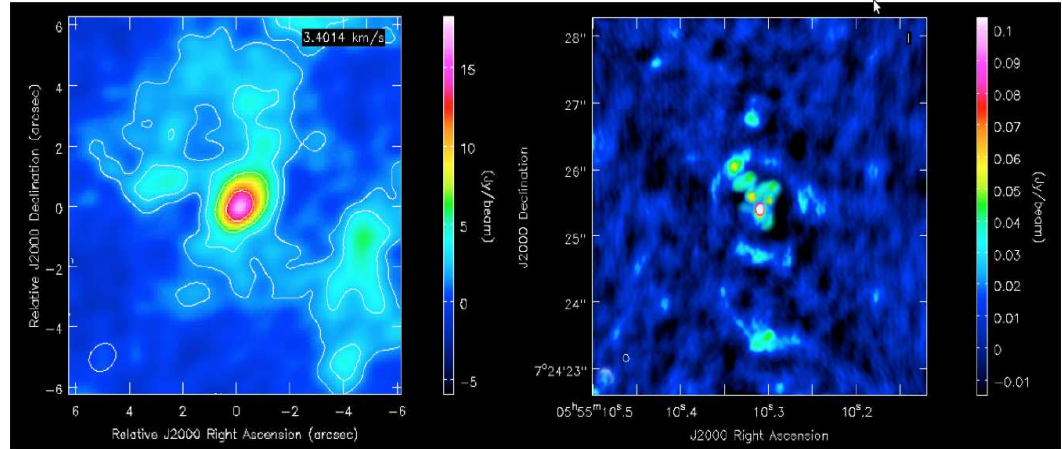


Figure 8.2: *Left:* Channel map from the CO($J = 2 - 1$) image cube of O'Gorman *et al.* (2012) using CARMA with a resolution of 0.9''. *Right:* CASA simulator tool image of the CARMA channel map scaled according to the Herschel CO($J = 6 - 5$) emission line flux (see Chapter 5) while assuming to have structure on the same scales as the dust. The scaling on the axes are different in both images.

expected ALMA dust observations, assuming 6 GHz of line-free continuum close to 690 GHz. In just 2 hours of observing time we expect to be able to detect at least some of this structure. Figure 8.2 (left) shows a channel map from our final CARMA CO($J = 2 - 1$) image cube. We scaled the intensity of this map according to the Herschel CO($J = 6 - 5$) line flux and assumed that the CO has structure on the same scales as the dust. Figure 8.2 (right) shows the simulated distribution and brightness of the CO($J = 6 - 5$) which indicates that we will be able to locate individual clump emission with a $0.09''$ beam. Even though the S1 flow is expected to extend out to $\sim 6''$, the CO($J = 6 - 5$) will be more concentrated than the CO($J = 2 - 1$) emission and so most of the CO($J = 6 - 5$) emission will be within the $9''$ ALMA primary beam. The flexibility of the ALMA correlator will also allow some other high-excitation lines to be simultaneously observed, such as SiO($v = 0, J = 16 - 15$) and SiO($v = 1, J = 16 - 15$) enabling the role of SiO in the formation of silicate dust grains to be studied.

8.2.2 Multi-epoch centimeter observations of Betelgeuse

The recent e-MERLIN 5.2 cm continuum image of Betelgeuse by Richards *et al.* (2013) has made the surprise discovery that the inner atmosphere contains two hotspots separated by 90 mas (i.e., $4 R_*$). A number of outstanding issues remain in explaining the origin of these features. The first issue is that the exact position of the optical photosphere is uncertain. While Richards *et al.* (2013) assumed this position to be at the source peak of a lower resolution image, we have shown that the astrometric solution of Harper *et al.* (2008) places the optical photosphere almost directly at the position of the less bright hotspot, which would mean that the brightest feature is located $\sim 3 R_*$ above the optical photosphere. However, this astrometric solution was based in part on lower spatial resolution and S/N radio data and so does not contain the desired level of precision. Another issue is that the time scales over which these features vary, in both brightness and position, are completely unknown. Along with the uncertainty in the photospheric position, the problem is that the velocity profile of the inner atmosphere is uncertain, due to traditional UV line diagnostics being contaminated by the large turbulent velocity.

8.2 Future Work

Our VLA–Pie Town data have revealed significant flux variations at all observed wavelengths on time scales as short as 14 months (the observing interval), while Drake *et al.* (1992) found similar variations on time scales as short as 40 days. The source of these variations will probably be strongly associated with these hot spots, at C band at least, as Richards *et al.* (2013) have shown that these contain most of the total radio flux. Ohnaka *et al.* (2011) created a 1-D aperture synthesis image of Betelgeuse using the VLTI/AMBER and concluded that “*the outer atmosphere extending to $\sim 1.3 - 1.4 R_\star$ is asymmetric and its dynamics is dominated by vigorous, inhomogeneous large-scale motions, whose overall nature changes drastically within one year*”. Could it be possible that the hotspots seen at radio wavelengths also change drastically within one year? Either way, they are likely linked to the wind-driving mechanism.

Table 8.1: Relevant capabilities of the VLA and e-MERLIN for future multi-epoch observations of Betelgeuse.

	e-MERLIN (C band)	e-MERLIN (K band)	VLA (C band)	VLA (K band)
Resolution ¹ (mas)	40	12	330	90
Frequency range (GHz)	4 – 8	22 – 24	4 – 8	18 – 26.6
Bandwidth (GHz)	2	2	4	8
Sensitivity ² (μ Jy/bm)	~ 2	~ 15	~ 2	~ 2
Maximum Scale ('')	~ 0.75	~ 0.16	~ 8.9	~ 2.4

¹ Using uniform weighting. ² Eight hour observing run.

Spatial resolution is a key requirement to understand the dynamics and evolution of these hotspots and e-MERLIN is the most suited instrument for future radio studies. e-MERLIN is expected to operate at K band by 2014 and so a future study consisting of both C and K band observations would be preferable, as each frequency would probe different layers of the atmosphere, potentially detecting other unique hotspots. Table 8.1 summarizes the relevant capabilities of e-MERLIN for such a study. The additional K band observations would provide a maximum resolution of 12 mas providing ~ 10 resolution elements across the radio disk¹. Multi-epoch observations will be required to study the evolution of

¹Based on the diameter of the fitted circular disks of our K band VLA+Pie Town data.

these features. Based on the conclusions of Ohnaka *et al.* (2011) along with the substantial flux variations we see in the radio, it would seem appropriate to carry out 3 – 4 unique observations at both C and K band in one year. Richards *et al.* (2013) C band observations were approximately 10 hr in total duration and used a total bandwidth of 0.5 GHz. Assuming the availability of the full 2 GHz of bandwidth at both C and K band then, in order to reach similar levels of sensitivity, three unique epochs each consisting of C and K band observations would amount to 30 hours of requested time with e-MERLIN.

Figure 8.3 shows a combined MERLIN and “old” VLA image of Betelgeuse at C band from 1996. Extended emission exists on scales of ~ 400 mas while the inner emission is asymmetric in the same direction as the new e-MERLIN data, although the distribution of the intensity appears to be different. Extended emission was also detected in the e-MERLIN map in the form of a S-W arc at ~ 250 mas from the star, as described in Chapter 6. The shorter baselines of the VLA would be more sensitive to this extended emission than e-MERLIN and so, combining VLA data with e-MERLIN data would surely produce the most detailed radio map of Betelgeuse ever produced. Obtaining contemporaneous observing time with both the VLA and e-MERLIN at C and K band will be a challenge, especially considering that both instruments are now dynamically scheduled. A more realistic option would be to apply for one epoch of VLA time to coincide with one of the e-MERLIN observing blocks. Besides, the extended emission evolves on slower timescales, and so one epoch would be sufficient to create a detailed map of the extended emission.

8.2.3 Semi-empirical models for Arcturus and Aldebaran

The new hybrid atmospheric model for Arcturus outlined in Chapter 6 can reproduce our VLA flux density values at long wavelengths (i.e., $\lambda \gtrsim 2$ cm) but does still not reproduce radio fluxes at shorter wavelengths. The next step of this project is to develop an entirely new atmospheric model independent of other existing models. Such a model would be based on our multi-wavelength VLA data because, unlike traditional UV diagnostics which are sensitive to localized

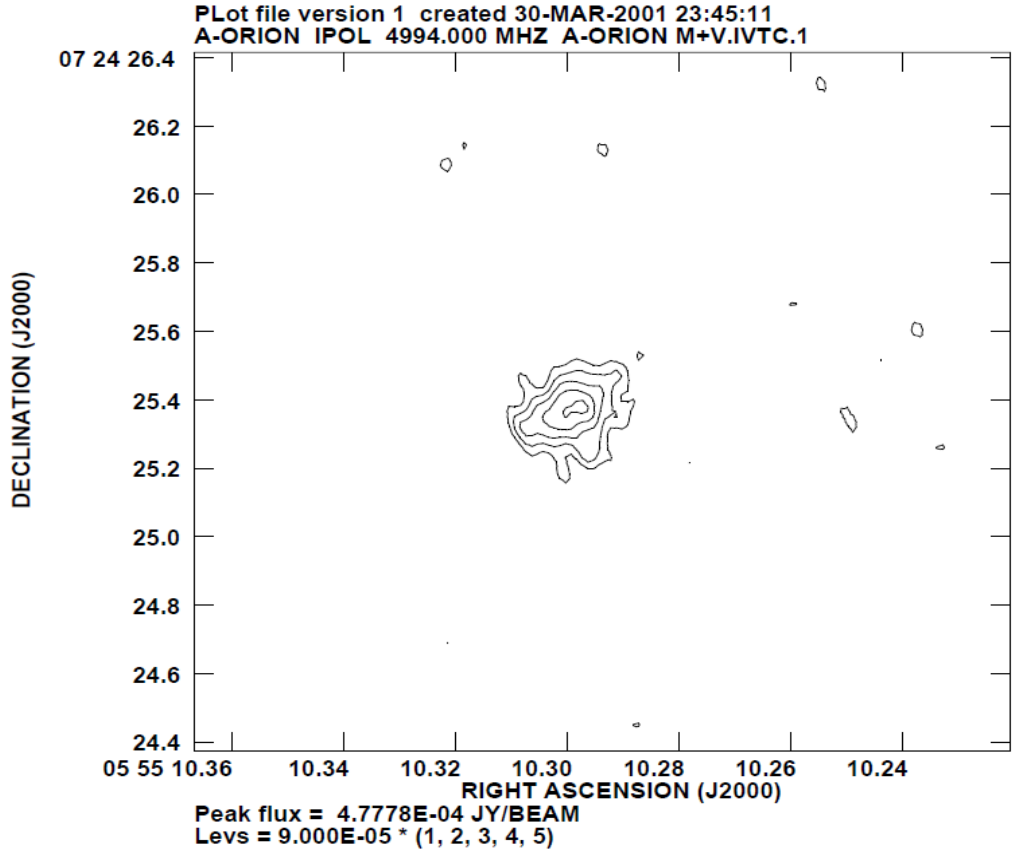


Figure 8.3: Combined MERLIN and “old” VLA image of Betelgeuse at C band. The MERLIN data were taken between 3 – 5 and 13 – 14 November 1996, while the VLA data were obtained on the 21st October, one and two weeks prior to the MERLIN data. The maximum resolution is 57 mas and the contour levels are at $(1, 2, 3, 4, 5) \times 90$ mJy. Extended emission exists on scales of ~ 400 mas while the inner emission is asymmetric in the same direction as the new e-MERLIN data, although the distribution of the intensity appears to be different. The recent upgrades to e-MERLIN and the VLA now provide ~ 20 and ~ 40 times more bandwidth, respectively, than that used in this image. Figure taken from Morris (2001).

hot plasma components, the multi-wavelength radio measurements probe many different layers and are more sensitive to the mean radial electron temperature.

We are currently developing the tools required to build these model atmospheres and our approach is outlined in Figure 8.4. A grid of wind models, with different wind acceleration profiles, mass-loss rates, and temperature pro-

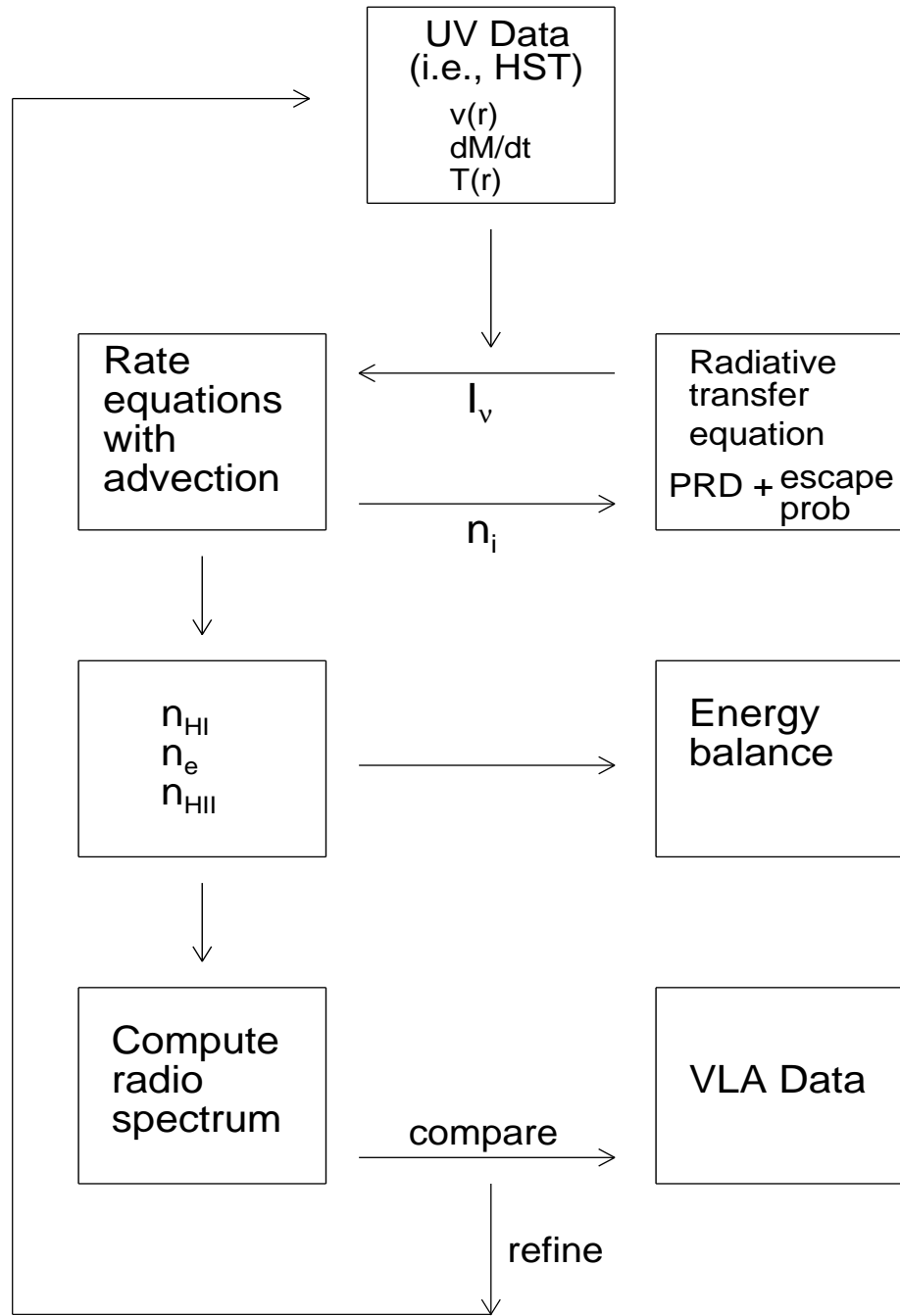


Figure 8.4: Block diagram summarizing the various stages involved in developing a new semi-empirical model for Arcturus and Aldebaran. The input model (starting guess) is mainly based on UV diagnostics. The radiative transfer equation and non-LTE atomic level populations (which include advection) are then simultaneously solved, and a radio spectrum is computed from the densities which is compared to the VLA data. The input model is adjusted until the computed radio spectrum agrees with our VLA observations. Note: PRD = “partial redistribution”.

files will be created as a starting guess, whose values will be based on our best estimates from line emission profiles in the optical and UV. The starting densities are found assuming spherical symmetry and a constant mass-loss rate. Of these input parameters, the temperature profile will be the most uncertain as there is no detectable wind emission feature in either the optical or UV. Future spatially resolved e-MERLIN observations of our two targets would be of great value as they would constrain the thermal profile. This input model is then used as a starting guess to simultaneously solve the radiative transfer equation and non-LTE atomic level populations (i.e., the rate equations) which include advection. An approximate solution for the ionization balance is then found by using escape probabilities for the optically thick lines in a six level hydrogen atom, and assuming the flow to be steady, which removes the time derivative in the rate equation. The ionization solution is non-linear and finding suitable models is a challenging computational project. Once a solution to the ionization balance has then been found, the corresponding radio spectrum is generated using the same techniques as described in Chapter 6. This radio spectrum is then compared against the actual VLA data and if it matches then this is the new atmospheric model; otherwise the process is started again with a slightly different starting guess.

8.2.4 Karl G. Jansky VLA Survey of Coronal Evolved Stars

Optically thin radio emission from coronal giants and supergiants can constrain existing atmospheric models and even provide estimates of their mass loss rates. The main survey of such stars was carried out by Drake & Linsky (1986) at 6 cm with the old VLA. Many of their sample were known x-ray sources whose observed spectra could be well fit by optically thin, thermal emission models with $T_e \sim 10^6 - 10^{7.5}$ K (Ayres *et al.*, 1981). At radio wavelengths, this thermal emission is completely dominated by free-free processes, while at x-ray wavelengths, it is the sum of many different thermal processes such as free-free, free-bound, and bound-bound. Drake & Linsky (1986) showed that the observed x-ray flux, f_x , in the soft x-ray band of the *Einstein* Observatory is theoretically related to the

8.2 Future Work

6 cm optically thin coronal radio flux, F_{cor} , by

$$F_{\text{cor}} \sim 1 \times 10^6 f_x \quad (8.1)$$

where F_{cor} has units of μJy and f_x has units $\text{erg cm}^{-2} \text{ s}^{-1}$. Using the observed x-ray values for the most nearby coronal evolved stars gives radio flux values at the μJy level, sometimes at levels similar to their expected stellar disk radio flux, F_{disk} . These low levels of radio flux were beyond the capabilities of the old VLA, and is the reason why no isolated coronal evolved stars were detected in the survey of Drake & Linsky (1986).

Table 8.2: Coronal evolved star candidates at 6 cm.

Star	Spectral Type	ϕ_* (mas)	T_{eff} (K)	f_x ($\text{erg cm}^{-2} \text{ s}^{-1}$)	F_{disk} (μJy)	F_{cor} (μJy)
β Dra	G2 Iab	4.2	5605	7.2×10^{-12}	1.5	7.2
ι Cap	G8 III	1.8	5440	8.1×10^{-12}	0.25	8.1
β Cet	K0 III	6.8	4750	2.1×10^{-11}	3	21
β Gem	K0 IIIb	8.5	4850	4.8×10^{-13}	5	0.5

Angular diameters are from Fracassini *et al.* (1981). Effective temperatures are from McWilliam (1990), Luck & Challener (1995), and Blackwell *et al.* (1986).

The increased bandwidth of the VLA now provides the required sensitivity at the μJy level to detect a number of coronal evolved stars. Four candidate coronal evolved stars are listed in Table 8.2 along with their x-ray flux values taken from Table I in Drake & Linsky (1986). Using Equation 8.1 we obtain the theoretical levels of radio flux at 6 cm, $F_{6\text{cm}}$, which should be accurate to within a factor of two. The best candidate for detection is β Cet which has a predicted 6 cm flux of $21\mu\text{Jy}$, seven times greater than its stellar disk radio flux, $F_{*6\text{cm}}$. Even though β Gem, the closest red giant to Earth, it is predicted to be a relatively weak radio emitter, we include it in Table 8.2 because it has recently been observed with the VLA at long wavelengths (Project Code: 12B-108). In Table 8.1, it can be seen that its stellar disk radio flux is predicted to be 10 times greater than its optically thin coronal flux and is still only predicted to be $5\mu\text{Jy}$. However, if a flux significantly greater than $5\mu\text{Jy}$ is detected from this new data set then this

would be in conflict with the theoretical predictions of Equation 8.1, and so it would be worthwhile to examine this new data set. Finally, Figure 8.5 provides a summary of the cool evolved star radio survey of Drake & Linsky (1986) along with two sample scaling laws. It is clear that most stars in this survey were not detected with the old VLA and their 3σ upper are plotted Figure 8.5. The recent upgrades to the VLA would make many more of these stars detectable while placing much firmer upper limits on the non-detections.

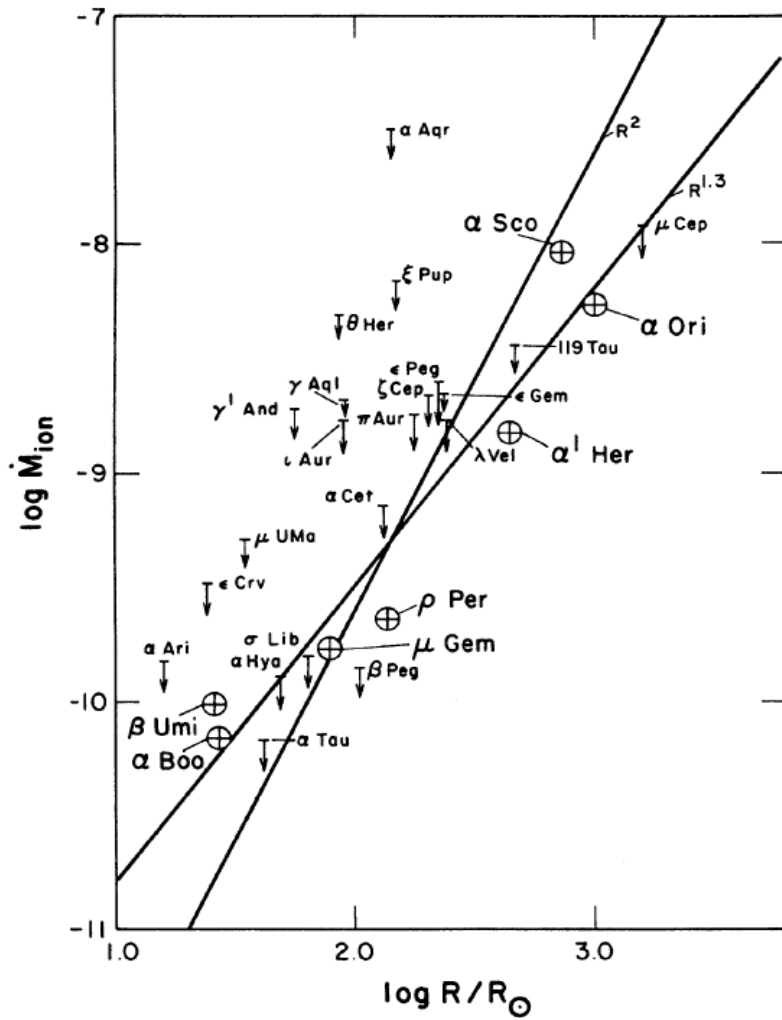


Figure 8.5: Ionized stellar mass-loss rate versus stellar radius for cool evolved stars in the radio survey of Drake & Linsky (1986) along with two sample scaling laws. Most stars have just upper limits to their flux density values. The recent upgrade to the VLA would make many more of these stars detectable.

8.3 Concluding Remarks

Radio emission has now been detected from almost all types of stars, encompassing virtually every stage of stellar evolution. This has provided breakthroughs in our understanding of stellar atmospheres and therefore the workings of stars in general. The recent and planned commissioning of a suite of new and upgraded radio interferometric facilities, operating at wavelengths spanning from the submillimeter to the meter, will ensure radio interferometry remains at the forefront of discoveries in nearly every branch of stellar astrophysics.

After decades of uncertainty, basic stellar parameters such as effective temperature, distance, and angular diameter are now becoming accurately known for a wide variety of nearby stars. Knowing these parameters to high levels of accuracy then enables reliable estimates to be made of other essential stellar parameters such as mass and age. This in turn allows these stars to be placed at reliable positions across the H-R diagram. Combing highly sensitive radio interferometric studies of stellar atmospheres with reliable stellar parameters, will ultimately allow the process of mass-loss to be understood across the entire H-R diagram.

A

List of Abbreviations Used in this Thesis.

Table A.1: List of Abbreviations

Acronym	Meaning
ALMA	The Atacama Large Millimeter/submillimeter Array
AGB	Asymptotic Giant Branch
ALC	Automatic Level Control
BIMA	Berkeley Illinois Maryland Association
CARMA	Combined Array for Research in Millimeter-wave Astronomy
CASA	Common Astronomy Software Application
CSE	Circumstellar Envelope
DDT	Director's Discretionary Time
e-MERLIN	e-Multi-Element Radio Linked Interferometer Network
FFT	Fast Fourier Transform
FITS	Flexible Image Transport System
FOV	Field of View
GBT	Robert C. Byrd Green Bank Telescope
GHRS	Goddard High-Resolution Spectrograph
GREAT	German Receiver for Astronomy at Terahertz Frequencies
HIFI	Heterodyne Instrument for the Far Infrared
HPBW	Half Power Beamwidth
H-R	Hertzsprung-Russell

Continued on next page

Table A.1 – *Continued from previous page*

Acronym	Meaning
HST	Hubble Space Telescope
IF	Intermediate Frequency
IOTA	Infrared Optical Telescope Array
IR	Infrared
IRAM	Institut de Radioastronomie Millimétrique
ISM	Interstellar Medium
IUE	International Ultraviolet Explorer
LNA	Low Noise Amplifier
LO	Local Oscillator
LSR	Local Standard of Rest
LTE	Local Thermodynamic Equilibrium
MEM	Maximum Entropy Method
MERLIN	Multi-Element Radio Linked Interferometer Network
MHD	Magnetohydrodynamic
OVRO	Owens Valley Radio Observatory
OSRO	Open Shared Risk Observing
RF	Radio Frequency
RFI	Radio Frequency Interference
RGC	Red Giant Clump
RGB	Red Giant Branch
RSG	Red Supergiant
S/N	signal-to-noise ratio
SB	Scheduling Block
SGB	Subgiant Branch
SOFIA	Stratospheric Observatory for Infrared Astronomy
SMA	Submillimeter Array
SZA	Sunyaev-Zel'dovich Array
SIS	Superconductor Insulator Superconductor
UV	Ultraviolet
VLA	Karl G. Jansky Very Large Array
VLBA	Very Long Baseline Array
VLT	Very Large Telescope
W-R	Wolf-Rayet

References

- ABIA, C., PALMERINI, S., BUSSO, M. & CRISTALLO, S. (2012). Carbon and oxygen isotopic ratios in Arcturus and Aldebaran. Constraining the parameters for non-convective mixing on the red giant branch. *Astronomy & Astrophysics*, **548**, A55. (Cited on page 78.)
- ADAMS, W.S. & MACCORMACK, E. (1935). Systematic Displacements of Lines in the Spectra of Certain Bright Stars. *Astrophysical Journal*, **81**, 119. (Cited on page 4.)
- AIRAPETIAN, V., CARPENTER, K.G. & OFMAN, L. (2010). Winds from Luminous Late-type Stars. II. Broadband Frequency Distribution of Alfvén Waves. *Astrophysical Journal*, **723**, 1210–1218. (Cited on page 170.)
- ALTENHOFF, W.J., MEZGER, P.G., WENDKER, H.J. & WESTERHOUT, G. (1960). Veröff. Sternwärte, Bonn. **59**, 48. (Cited on page 31.)
- ALTENHOFF, W.J., HUCHTMEIER, W.K., SCHMIDT, J., SCHRAML, J.B. & STUMPF, P. (1986). Radio continuum observations of comet Halley. *Astronomy & Astrophysics*, **164**, 227–230. (Cited on page 167.)
- ALTENHOFF, W.J., THUM, C. & WENDKER, H.J. (1994). Radio emission from stars: A survey at 250 GHz. *Astronomy & Astrophysics*, **281**, 161–183. (Cited on pages 137 and 167.)
- ASPLUND, M., GREVESSE, N., SAUVAL, A.J. & SCOTT, P. (2009). The Chemical Composition of the Sun. *Annual Review of Astronomy & Astrophysics*, **47**, 481–522. (Cited on page 198.)
- AYRES, T. (2010a). A stellar perspective on chromospheres. *Memorie della Società Astronomia Italiana*, **81**, 553. (Cited on page 6.)
- AYRES, T.R. (1996). Thermal bifurcation as a driver of stellar surface inhomogeneities (review). In K.G. Strassmeier & J.L. Linsky, eds., *Stellar Surface Structure*, vol. 176 of *IAU Symposium*, 371. (Cited on page 173.)
- AYRES, T.R. (2010b). StarCAT: A Catalog of Space Telescope Imaging Spectrograph Ultraviolet Echelle Spectra of Stars. *Astrophysical Journal Supplemental Series*, **187**, 149–171. (Cited on page 202.)
- AYRES, T.R. & LINSKY, J.L. (1975). Stellar model chromospheres. III - Arcturus /K2 III/. *Astrophysical Journal*, **200**, 660–674. (Cited on pages 80 and 170.)
- AYRES, T.R., LINSKY, J.L., VAIANA, G.S., GOLUB, L. & ROSNER, R. (1981). The cool half of the H-R diagram in soft X-rays. *Astrophysical Journal*, **250**, 293–299. (Cited on pages 2, 6 and 223.)

REFERENCES

- AYRES, T.R., BROWN, A., HARPER, G.M., BENNETT, P.D., LINSKY, J.L., CARPENTER, K.G. & ROBINSON, R.D. (1997). Digging Deeper in the Coronal Graveyard. *Astrophysical Journal*, **491**, 876. (Cited on page 6.)
- AYRES, T.R., BROWN, A. & HARPER, G.M. (2003). Buried Alive in the Coronal Graveyard. *Astrophysical Journal*, **598**, 610–625. (Cited on pages 83 and 84.)
- BAADE, R., KIRSCH, T., REIMERS, D., TOUSSAINT, F., BENNETT, P.D., BROWN, A. & HARPER, G.M. (1996). The Wind Outflow of zeta Aurigae: A Model Revision Using Hubble Space Telescope Spectra. *Astrophysical Journal*, **466**, 979. (Cited on page 77.)
- BEASLEY, A.J., STEWART, R.T. & CARTER, B.D. (1992). Non-thermal radio emission from post-main-sequence stars. *Monthly Notices of the Royal Astronomical Society*, **254**, 1–6. (Cited on page 166.)
- BECK, P.G., BEDDING, T.R., MOSSER, B., STELLO, D., GARCIA, R.A., KALLINGER, T., HEKKER, S., ELSWORTH, Y., FRANDSEN, S., CARRIER, F., DE RIDDER, J., AERTS, C., WHITE, T.R., HUBER, D., DUPRET, M.A., MONTALBÁN, J., MIGLIO, A., NOELS, A., CHAPLIN, W.J., KJELDSEN, H., CHRISTENSEN-DALSGAARD, J., GILLILAND, R.L., BROWN, T.M., KAWALER, S.D., MATHUR, S. & JENKINS, J.M. (2011). Kepler Detected Gravity-Mode Period Spacings in a Red Giant Star. *Science*, **332**, 205–. (Cited on page 20.)
- BECKLIN, E.E. & GEHRZ, R.D. (2009). SOFIA: Stratospheric Observatory for Infrared Astronomy. In D. C. Lis, J. E. Vaillancourt, P. F. Goldsmith, T. A. Bell, N. Z. Scoville, & J. Zmuidzinas, ed., *Submillimeter Astrophysics and Technology: a Symposium Honoring Thomas G. Phillips*, vol. 417 of *Astronomical Society of the Pacific Conference Series*, 101. (Cited on page 138.)
- BEDDING, T.R., MOSSER, B., HUBER, D., MONTALBÁN, J., BECK, P., CHRISTENSEN-DALSGAARD, J., ELSWORTH, Y.P., GARCÍA, R.A., MIGLIO, A., STELLO, D., WHITE, T.R., DE RIDDER, J., HEKKER, S., AERTS, C., BARBAN, C., BELKACEM, K., BROOMHALL, A.M., BROWN, T.M., BUZASI, D.L., CARRIER, F., CHAPLIN, W.J., DI MAURO, M.P., DUPRET, M.A., FRANDSEN, S., GILLILAND, R.L., GOUPIL, M.J., JENKINS, J.M., KALLINGER, T., KAWALER, S., KJELDSEN, H., MATHUR, S., NOELS, A., AGUIRRE, S.V. & VENTURA, P. (2011). Gravity modes as a way to distinguish between hydrogen- and helium-burning red giant stars. *Nature*, **471**, 608–611. (Cited on page 20.)
- BEDECARRAX, I., PETIT, P., AURIÈRE, M., GRUNHUT, J., WADE, G., CHIAVASSA, A., DONATI, J.F., KONSTANTINOVA-ANTOVA, R. & PERRIN, G. (2013). Long-term spectropolarimetric monitoring of the cool supergiant betelgeuse. In *EAS Publications Series*, vol. 60 of *EAS Publications Series*, 161–165. (Cited on pages 23, 68 and 69.)
- BERGER, T.E. & TITLE, A.M. (2001). On the Relation of G-Band Bright Points to the Photospheric Magnetic Field. *Astrophysical Journal*, **553**, 449–469. (Cited on page 203.)
- BERIO, P., MERLE, T., THÉVENIN, F., BONNEAU, D., MOURARD, D., CHESNEAU, O., DELLA, O., LIGI, R., NARDETTO, N., PERRAUT, K., PICHON, B., STEE, P., TALLON-BOSC, I., CLAUSSE, J.M., SPANG, A., MCALISTER, H., TEN BRUMMELAAR, T., STURMANN, J., STURMANN, L., TURNER, N., FARRINGTON, C. & GOLDFINGER, P.J. (2011). Chromosphere of K giant stars. Geometrical extent and spatial structure detection. *Astronomy & Astrophysics*, **535**, A59. (Cited on pages 7 and 78.)

REFERENCES

- BERNAT, A.P. & LAMBERT, D.L. (1976). K I 7699 Å emission from the Betelgeuse shell. *Astrophysical Journal*, **210**, 395–401. (Cited on page 4.)
- BERNAT, A.P., HALL, D.N.B., HINKLE, K.H. & RIDGWAY, S.T. (1979). Observations of CO circumstellar absorption in the 4.6 micron spectrum of Alpha Orionis. *Astrophysical Journal Letters*, **233**, L135–L139. (Cited on pages 25, 26, 69, 118, 119, 130, 141, 143 and 211.)
- BLACKWELL, D.E., BOOTH, A.J., PETFORD, A.D., LEGGETT, S.K., MOUNTAIN, C.M. & SELBY, M.J. (1986). The infrared flux method and its use for study of Alpha Boo, MU HER and Beta Dra; relation to the VEGA 1.2-5 micron infrared excess. *Monthly Notices of the Royal Astronomical Society*, **221**, 427–443. (Cited on page 224.)
- BLUNDELL, R. (2007). The Submillimeter Array. In *IEEE MTT-S International Microwave Symposium Digest*, 1857–1860. (Cited on page 138.)
- BOCK, D.C.J. (2006). CARMA: Combined Array for Research in Millimeter-Wave Astronomy. In D.C. Backer, J.M. Moran & J.L. Turner, eds., *Revealing the Molecular Universe: One Antenna is Never Enough*, vol. 356 of *Astronomical Society of the Pacific Conference Series*, 17. (Cited on pages 72 and 73.)
- BOICE, D.C., KUHN, J.R., ROBINSON, R.D. & WORDEN, S.P. (1981). Possible radio flaring activity on a late-type giant star, Alpha Ceti. *Astrophysical Journal Letters*, **245**, L71–L74. (Cited on page 166.)
- BOOKBINDER, J.A., STENCEL, R.E., DRAKE, S.A., SIMON, T., LINSKY, J.L. & FLORKOWSKI, D. (1987). VLA Observations of Rapid 6 cm Flux Variations in α Ori. In J. L. Linsky & R. E. Stencel, ed., *Cool Stars, Stellar Systems and the Sun*, vol. 291 of *Lecture Notes in Physics*, Berlin Springer Verlag, 337. (Cited on pages 136, 151 and 153.)
- BOOTHROYD, A.I. & SACKMANN, I.J. (1999). The CNO Isotopes: Deep Circulation in Red Giants and First and Second Dredge-up. *Astrophysical Journal*, **510**, 232–250. (Cited on page 118.)
- BOTTLINGER, C.F. (1911). Die Bahn des spektroskopischen Doppelsternes α Orionis. *Astronomische Nachrichten*, **187**, 33. (Cited on page 121.)
- BOWERS, P.F. & KNAPP, G.R. (1987). Detection of H I emission from the circumstellar envelope of Alpha Orionis. *Astrophysical Journal*, **315**, 305–314. (Cited on page 70.)
- BRACEWELL, R.N. (2000). *The Fourier Transform and Its Applications*. Columbus, OH: McGraw Hill, 3rd edn. (Cited on page 135.)
- BROWN, K.I.T. (2007). Long-Term Spectroscopic and Precise Radial Velocity Monitoring of Arcturus. *Publications of the Astronomical Society of the Pacific*, **119**, 237–237. (Cited on page 80.)
- BROWN, K.I.T., GRAY, D.F. & BALIUNAS, S.L. (2008). Long-Term Spectroscopic Monitoring of Arcturus. *Astrophysical Journal*, **679**, 1531–1540. (Cited on page 83.)
- BUSCHER, D.F., BALDWIN, J.E., WARNER, P.J. & HANIFF, C.A. (1990). Detection of a bright feature on the surface of Betelgeuse. *Monthly Notices of the Royal Astronomical Society*, **245**, 7P–11P. (Cited on page 158.)

REFERENCES

- CARILLI, C.L., HOLDAWAY, M.A. & SOWINSKI, K.P. (1996). Faster Switching at the VLA. In *VLA Scientific Memo. No. 169*, vol. 169 of *VLA memos*. (Cited on page 94.)
- CARLSON, B. (2001). Refined EVLA WIDAR Correlator Architecture. In *NRC-EVLA Memo 014*, vol. 14 of *NRC-EVLA Memos*. (Cited on page 85.)
- CARLSSON, M. (1986). A computer program for solving multi-level non-LTE radiative transfer problems in moving or static atmospheres. *Uppsala Astronomical Observatory Reports*, **33**. (Cited on page 172.)
- CARPENTER, K.G. & ROBINSON, R.D. (1996). HST Studies of Carbon and K-M Giant/Supergiant Stars. In P. Benvenuti, F.D. Macchettro & E.J. Schreier, eds., *Science with the Hubble Space Telescope - II*, 418. (Cited on page 84.)
- CARPENTER, K.G. & ROBINSON, R.D. (1997). GHRS Observations of Cool, Low-Gravity Stars. III. Plasma Flows and Turbulence in the Outer Atmosphere of alpha Orionis (M2 Iab). *Astrophysical Journal*, **479**, 970+. (Cited on pages 136 and 151.)
- CARPENTER, K.G., ROBINSON, R.D., HARPER, G.M., BENNETT, P.D., BROWN, A. & MULLAN, D.J. (1999). GHRS Observations of Cool, Low-Gravity Stars. V. The Outer Atmosphere and Wind of the Nearby K Supergiant lambda Velorum. *Astrophysical Journal*, **521**, 382–406. (Cited on pages 6, 7 and 78.)
- CASSINELLI, J.P. & HARTMANN, L. (1977). The effect of winds and coronae of hot stars on the infrared and radio continua. *Astrophysical Journal*, **212**, 488–493. (Cited on page 180.)
- CASTOR, J.I. (1970). Spectral line formation in Wolf-Rayet envelopes. *Monthly Notices of the Royal Astronomical Society*, **149**, 111–127. (Cited on page 198.)
- CASTOR, J.I., ABBOTT, D.C. & KLEIN, R.I. (1975). Radiation-driven winds in Of stars. *Astrophysical Journal*, **195**, 157–174. (Cited on page 11.)
- CHAPMAN, R.D. (1981). The 1979-1980 eclipse of Zeta Aurigae. I - The circumstellar envelope. *Astrophysical Journal*, **248**, 1043–1052. (Cited on page 77.)
- CHAPMAN, S. & ZIRIN, H. (1957). Notes on the Solar Corona and the Terrestrial Ionosphere. *Smithsonian Contributions to Astrophysics*, **2**, 1. (Cited on page 12.)
- CHARBONNEAU, P. & MACGREGOR, K.B. (1995). Stellar Winds with Non-WKB Alfven Waves. II. Wind Models for Cool, Evolved Stars. *Astrophysical Journal*, **454**, 901. (Cited on page 174.)
- CHARBONNEL, C. (1995). A Consistent Explanation for 12C/ 13C, 7Li and 3He Anomalies in Red Giant Stars. *Astrophysical Journal Letters*, **453**, L41. (Cited on page 118.)
- CHIAVASSA, A., HAUBOIS, X., YOUNG, J.S., PLEZ, B., JOSSELIN, E., PERRIN, G. & FREYTAG, B. (2010). Radiative hydrodynamics simulations of red supergiant stars. II. Simulations of convection on Betelgeuse match interferometric observations. *Astronomy & Astrophysics*, **515**, A12. (Cited on pages 71 and 158.)
- CHIOSI, C. & MAEDER, A. (1986). The evolution of massive stars with mass loss. *Annual Review of Astronomy & Astrophysics*, **24**, 329–375. (Cited on page 2.)

REFERENCES

- COHEN, M., CARBON, D.F., WELCH, W.J., LIM, T., SCHULZ, B., McMURRY, A.D., FORSTER, J.R. & GOORVITCH, D. (2005). Far-Infrared and Millimeter Continuum Studies of K Giants: α Bootis and α Tauri. *Astronomical Journal*, **129**, 2836–2848. (Cited on page 167.)
- CORNWELL, T., BRAUN, R. & BRIGGS, D.S. (1999). Deconvolution. In G.B. Taylor, C.L. Carilli & R.A. Perley, eds., *Synthesis Imaging in Radio Astronomy II*, vol. 180 of *Astronomical Society of the Pacific Conference Series*, 151. (Cited on page 65.)
- CORNWELL, T.J. (2008). Multiscale CLEAN Deconvolution of Radio Synthesis Images. *IEEE Journal of Selected Topics in Signal Processing*, **2**, 793–801. (Cited on page 113.)
- CRANMER, S.R. (2012). Self-Consistent Models of the Solar Wind. *Space Science Reviews*, **172**, 145–156. (Cited on page 205.)
- CRANMER, S.R. & SAAR, S.H. (2011). Testing a Predictive Theoretical Model for the Mass Loss Rates of Cool Stars. *Astrophysical Journal*, **741**, 54. (Cited on pages 13 and 204.)
- CRANMER, S.R. & VAN BALLEGOOIJEN, A.A. (2005). On the Generation, Propagation, and Reflection of Alfvén Waves from the Solar Photosphere to the Distant Heliosphere. *Astrophysical Journal Supplemental Series*, **156**, 265–293. (Cited on page 204.)
- CRANMER, S.R., VAN BALLEGOOIJEN, A.A. & EDGAR, R.J. (2007). Self-consistent Coronal Heating and Solar Wind Acceleration from Anisotropic Magnetohydrodynamic Turbulence. *Astrophysical Journal Supplemental Series*, **171**, 520–551. (Cited on page 203.)
- CROWLEY, C., ESPEY, B.R. & MCCANDLISS, S.R. (2008). EG And: Far Ultraviolet Spectroscopic Explorer and Hubble Space Telescope STIS Monitoring of an Eclipsing Symbiotic Binary. *Astrophysical Journal*, **675**, 711–722. (Cited on page 77.)
- CROWLEY, C., ESPEY, B.R., HARPER, G.M. & ROCHE, J. (2009). Winds and Chromospheres of Cool (Super-) Giants. In E. Stempels, ed., *15th Cambridge Workshop on Cool Stars, Stellar Systems, and the Sun*, vol. 1094 of *American Institute of Physics Conference Series*, 267–274. (Cited on pages 2 and 3.)
- DALGARNO, A. & LAYZER, D. (1987). *Spectroscopy of Astrophysical Plasmas*. (Cited on page 38.)
- DALGARNO, A. & MCCRAY, R.A. (1972). Heating and Ionization of HI Regions. *Annual Review of Astronomy & Astrophysics*, **10**, 375. (Cited on page 197.)
- DANCHI, W.C., BESTER, M., DEGIACOMI, C.G., GREENHILL, L.J. & TOWNES, C.H. (1994). Characteristics of dust shells around 13 late-type stars. *Astronomical Journal*, **107**, 1469–1513. (Cited on pages 14 and 117.)
- DE GRAAUW, T., HELMICHH, F.P., PHILLIPS, T.G., STUTZKI, J., CAUX, E., WHYBORN, N.D., DIELEMAN, P., ROELFSEMA, P.R., AARTS, H., ASSENDORP, R., BACHILLER, R., BAECHTOLD, W., BARCIA, A., BEINTEMA, D.A., BELITSKY, V., BENZ, A.O., BIEBER, R., BOOGERT, A., BORYS, C., BUMBLE, B., CAÏS, P., CARIS, M., CERULLI-IRELLI, P., CHATTOPADHYAY, G., CHEREDNICHENKO, S., CIECHANOWICZ, M., COEUR-JOLY, O., COMITO, C., CROS, A., DE JONGE, A., DE LANGE, G., DELFORGES, B., DELORME, Y.,

REFERENCES

- DEN BOGGENDE, T., DESBAT, J.M., DIEZ-GONZÁLEZ, C., DI GIORGIO, A.M., DUBBELDAM, L., EDWARDS, K., EGGENS, M., ERICKSON, N., EVERE, J., FICH, M., FINN, T., FRANKE, B., GAIER, T., GAL, C., GAO, J.R., GALLEG, J.D., GAUFFRE, S., GILL, J.J., GLENZ, S., GOLSTEIN, H., GOOLOOZE, H., GUNSING, T., GÜSTEN, R., HARTOGH, P., HATCH, W.A., HIGGINS, R., HONINGH, E.C., HUISMAN, R., JACKSON, B.D., JACOBS, H., JACOBS, K., JARCHOW, C., JAVADI, H., JELLEMA, W., JUSTEN, M., KARPOV, A., KASEMANN, C., KAWAMURA, J., KEIZER, G., KESTER, D., KLAPOWIJK, T.M., KLEIN, T., KOLLBERG, E., KOOI, J., KOOIMAN, P.P., KOPF, B., KRAUSE, M., KRIEG, J.M., KRAMER, C., KRUIZENGA, B., KUHN, T., LAAUWEN, W., LAI, R., LARSSON, B., LEDUC, H.G., LEINZ, C., LIN, R.H., LISEAU, R., LIU, G.S., LOOSE, A., LÓPEZ-FERNANDEZ, I., LORD, S., LUNGE, W., MARSTON, A., MARTÍN-PINTADO, J., MAESTRINI, A., MAIWALD, F.W., MCCOEY, C., MEHDI, I., MEGEJ, A., MELCHIOR, M., MEINSMA, L., MERKEL, H., MICHALSKA, M., MONSTEIN, C., MORATSCHKE, D., MORRIS, P., MULLER, H., MURPHY, J.A., NABER, A., NATALE, E., NOWOSIELSKI, W., NUZZOLO, F., OLBERG, M., OLBRICH, M., ORFEI, R., ORLEANSKI, P., OSSenkopf, V., PEACOCK, T., PEARSON, J.C., PERON, I., PHILLIP-MAY, S., PIAZZO, L., PLANESAS, P., RATAJ, M., RAVERA, L., RISACHER, C., SALEZ, M., SAMOSKA, L.A., SARACENO, P., SCHIEDER, R., SCHLECHT, E., SCHLÖDER, F., SCHMÜLLING, F., SCHULTZ, M., SCHUSTER, K., SIEBERTZ, O., SMIT, H., SZCZERBA, R., SHIPMAN, R., STEINMETZ, E., STERN, J.A., STOKROOS, M., TEIPEN, R., TEYSSIER, D., TILS, T., TRAPPE, N., VAN BAAREN, C., VAN LEEUWEN, B.J., VAN DE STADT, H., VISSER, H., WILDEMAN, K.J., WAFELBAKKER, C.K., WARD, J.S., WESSELUS, P., WILD, W., WULFF, S., WUNSCH, H.J., TIELENS, X., ZAAL, P., ZIRATH, H., ZMUIDZINAS, J. & ZWART, F. (2010). The Herschel-Heterodyne Instrument for the Far-Infrared (HIFI). *Astronomy & Astrophysics*, **518**, L6. (Cited on page 138.)
- DECIN, L., VANDENBUSSCHE, B., WAELKENS, C., DECIN, G., ERIKSSON, K., GUSTAFSSON, B., PLEZ, B. & SAUVAL, A.J. (2003). ISO-SWS calibration and the accurate modelling of cool-star atmospheres. IV. G9 to M2 stars. *Astronomy & Astrophysics*, **400**, 709–727. (Cited on pages 81, 83 and 198.)
- DECIN, L., COX, N.L.J., ROYER, P., VAN MARLE, A.J., VANDENBUSSCHE, B., LADJAL, D., KERSCHBAUM, F., OTTENSAMER, R., BARLOW, M.J., BLOMMAERT, J.A.D.L., GOMEZ, H.L., GROENEWEGEN, M.A.T., LIM, T., SWINYARD, B.M., WAELKENS, C. & TIELENS, A.G.G.M. (2012). The enigmatic nature of the circumstellar envelope and bow shock surrounding Betelgeuse as revealed by Herschel. I. Evidence of clumps, multiple arcs, and a linear bar-like structure. *Astronomy & Astrophysics*, **548**, A113. (Cited on page 72.)
- DEHAES, S., BAUWENS, E., DECIN, L., ERIKSSON, K., RASKIN, G., BUTLER, B., DOWELL, C.D., ALI, B. & BLOMMAERT, J.A.D.L. (2011). Structure of the outer layers of cool standard stars. *Astronomy & Astrophysics*, **533**, A107. (Cited on pages 166 and 167.)
- DEUTSCH, A.J. (1956). The Circumstellar Envelope of Alpha Herculis. *Astrophysical Journal*, **123**, 210. (Cited on page 4.)
- DI BENEDETTO, G.P. (1993). Empirical effective temperatures and angular diameters of stars cooler than the sun. *Astronomy & Astrophysics*, **270**, 315–334. (Cited on pages 80, 81 and 83.)
- DRAINE, B.T. (2011). *Physics of the Interstellar and Intergalactic Medium*. (Cited on page 27.)

REFERENCES

- DRAKE, S. & LINSKY, J. (1986). Radio continuum emission from winds, chromospheres, and coronae of cool giants and supergiants. *Astronomical Journal*, **91**, 602–620. (Cited on pages 5, 13, 35, 166, 167, 177, 189, 223, 224 and 225.)
- DRAKE, S.A. (1985). Modeling lines formed in the expanding chromospheres of red giants. In J.E. Beckman & L. Crivellari, eds., *Progress in stellar spectral line formation theory; Proceedings of the Advanced Research Workshop, Trieste, Italy, September 4-7, 1984 (A86-37976 17-90)*. Dordrecht, D. Reidel Publishing Co., 1985, p. 351-357., 351–357. (Cited on pages 81, 82, 168, 170, 171, 180, 184, 187, 190, 214 and 215.)
- DRAKE, S.A. & LINSKY, J.L. (1983a). First detection of winds in red giants by microwave continuum techniques. *Astrophysical Journal Letters*, **274**, L77–L81. (Cited on pages 165 and 166.)
- DRAKE, S.A. & LINSKY, J.L. (1983b). The formation of emission lines in the expanding chromospheres of luminous cool stars. I - The importance of atmospheric extension and partial redistribution effects. *Astrophysical Journal*, **273**, 299–308. (Cited on page 170.)
- DRAKE, S.A., BOOKBINDER, J.A., FLORKOWSKI, D.R., LINSKY, J.L., SIMON, T. & STENCZEL, R.E. (1992). Four Years of Monitoring a Orionis with the VLA: Where have all the Flares Gone? In M. S. Giampapa & J. A. Bookbinder, ed., *Cool Stars, Stellar Systems, and the Sun*, vol. 26 of *Astronomical Society of the Pacific Conference Series*, 455. (Cited on pages 137, 152, 153 and 219.)
- DULK, G.A. (1985). Radio emission from the sun and stars. *Annual Review of Astronomy & Astrophysics*, **23**, 169–224. (Cited on page 23.)
- DUPREE, A.K., BALIUNAS, S.L., HARTMANN, L., GUINAN, E.F. & SONNEBORN, G. (1990). Alpha ORI - Evidence for pulsation. In C. Cacciari & G. Clementini, eds., *Confrontation Between Stellar Pulsation and Evolution*, vol. 11 of *Astronomical Society of the Pacific Conference Series*, 468–471. (Cited on page 120.)
- DUPREE, A.K., LOBEL, A., YOUNG, P.R., AKE, T.B., LINSKY, J.L. & REDFIELD, S. (2005). A Far-Ultraviolet Spectroscopic Survey of Luminous Cool Stars. *Astrophysical Journal*, **622**, 629–652. (Cited on page 84.)
- DZIEMBOWSKI, W.A., GOUGH, D.O., HOODEK, G. & SIENKIEWICZ, R. (2001). Oscillations of α UMa and other red giants. *Monthly Notices of the Royal Astronomical Society*, **328**, 601–610. (Cited on page 80.)
- EATON, J.A. (2008). A Model for the Chromosphere/Wind of 31 Cygni and Its Implications for Single Stars. *Astronomical Journal*, **136**, 1964–1979. (Cited on page 77.)
- EGGEN, O.J. (1971). The Arcturus Group. *Publications of the Astronomical Society of the Pacific*, **83**, 271. (Cited on page 78.)
- EGGEN, O.J. (1996). Star Streams and Galactic Structure. *Astronomical Journal*, **112**, 1595. (Cited on page 78.)

REFERENCES

- EGGLETON, P.P., DEARBORN, D.S.P. & LATTANZIO, J.C. (2007). Compulsory Deep Mixing of ^3He and CNO Isotopes on the First Giant Branch. In R.J. Stancliffe, G. Houdek, R.G. Martin & C.A. Tout, eds., *Unsolved Problems in Stellar Physics: A Conference in Honor of Douglas Gough*, vol. 948 of *American Institute of Physics Conference Series*, 27–34. (Cited on page 118.)
- EKERS, R. (1982). Common Map Defects. In A.R. Thompson & L.R. D'Addario, eds., *Synthesis Mapping*, 12. (Cited on page 91.)
- ENGARGIOLA, G.A., NAVARRINI, A., PLAMBECK, R.L. & WADEFALK, N. (2004). Simple 1-mm receivers with fixed tuned double sideband SIS mixer and wideband InP MMIC amplifier. In C.M. Bradford, P.A.R. Ade, J.E. Aguirre, J.J. Bock, M. Dragovan, L. Duband, L. Earle, J. Glenn, H. Matsuhara, B.J. Naylor, H.T. Nguyen, M. Yun & J. Zmuidzinas, eds., *Society of Photo-Optical Instrumentation Engineers (SPIE) Conference Series*, vol. 5498 of *Society of Photo-Optical Instrumentation Engineers (SPIE) Conference Series*, 556–566. (Cited on page 74.)
- FALCETA-GONÇALVES, D., VIDOTTO, A.A. & JATENCO-PEREIRA, V. (2006). On the magnetic structure and wind parameter profiles of Alfvén wave driven winds in late-type supergiant stars. *Monthly Notices of the Royal Astronomical Society*, **368**, 1145–1150. (Cited on pages 3 and 203.)
- FAMAЕY, B., JORISSEN, A., LURI, X., MAYOR, M., UDRY, S., DEJONGHE, H. & TURON, C. (2005). Local kinematics of K and M giants from CORAVEL/Hipparcos/Tycho-2 data. Revisiting the concept of superclusters. *Astronomy & Astrophysics*, **430**, 165–186. (Cited on page 124.)
- FRACASSINI, M., PASINETTI, L.E. & MANZOLINI, F. (1981). Catalogue of apparent diameters and absolute radii of stars /CADARS/. *Astronomy & Astrophysics Supplemental*, **45**, 145–174. (Cited on page 224.)
- GEHRZ, R.D. & WOOLF, N.J. (1971). Mass Loss from M Stars. *Astrophysical Journal*, **165**, 285. (Cited on pages 4 and 14.)
- GILLILAND, R.L. & DUPREE, A.K. (1996). First Image of the Surface of a Star with the Hubble Space Telescope. *Astrophysical Journal Letters*, **463**, L29. (Cited on pages 70 and 144.)
- GLASSGOLD, A.E. & HUGGINS, P.J. (1986). The ionization structure of the circumstellar envelope of Alpha Orionis. *Astrophysical Journal*, **306**, 605–617. (Cited on pages 181, 182 and 214.)
- GOLDBERG, L. (1984). The variability of alpha Orionis. *Publications of the Astronomical Society of the Pacific*, **96**, 366–371. (Cited on pages 121 and 136.)
- GOLDBERG, L., RAMSEY, L., TESTERMAN, L. & CARBON, D. (1975). High-resolution profiles of sodium and potassium lines in alpha Orionis. *Astrophysical Journal*, **199**, 427–431. (Cited on page 119.)
- GOLDREICH, P. & SCOVILLE, N. (1976). OH-IR stars. I - Physical properties of circumstellar envelopes. *Astrophysical Journal*, **205**, 144–154. (Cited on page 194.)

REFERENCES

- GRADSHTEYN, I.S. & RYZHIK, I.M. (1994). *Table of integrals, series and products.* (Cited on page 35.)
- GRAY, R.O., CORBALLY, C.J., GARRISON, R.F., MCFADDEN, M.T., BUBAR, E.J., McGAHEE, C.E., O'DONOGHUE, A.A. & KNOX, E.R. (2006). Contributions to the Nearby Stars (NStars) Project: Spectroscopy of Stars Earlier than M0 within 40 pc-The Southern Sample. *Astronomical Journal*, **132**, 161–170. (Cited on pages 81 and 171.)
- GRIFFIN, R.E.M. (1996). Arcturus and human evolution. *The Observatory*, **116**, 404–405. (Cited on page 80.)
- GRIFFIN, R.E.M. & LYNAS-GRAY, A.E. (1999). The Effective Temperature of Arcturus. *Astronomical Journal*, **117**, 2998–3006. (Cited on page 80.)
- GUESTEN, R., HARTOOGH, P., HUEBERS, H.W., GRAF, U.U., JACOBS, K., ROESER, H.P., SCHAEFER, F., SCHIEDER, R.T., STARK, R., STUTZKI, J., VAN DER WAL, P. & WUNSCH, A. (2000). GREAT: the first-generation German heterodyne receiver for SOFIA. In R. K. Melugin & H.-P. Röser, ed., *Society of Photo-Optical Instrumentation Engineers (SPIE) Conference Series*, vol. 4014, 23–30. (Cited on page 138.)
- HABING, H.J. (1996). Circumstellar envelopes and Asymptotic Giant Branch stars. *Astronomy & Astrophysics Review*, **7**, 97–207. (Cited on page 14.)
- HAISCH, B.M., LINSKY, J.L. & BASRI, G.S. (1980). Outer atmospheres of cool stars. IV - A discussion of cool stellar wind models. *Astrophysical Journal*, **235**, 519–533. (Cited on page 2.)
- HAMAKER, J.P., BREGMAN, J.D. & SAULT, R.J. (1996). Understanding radio polarimetry. I. Mathematical foundations. *Astronomy & Astrophysics Supplemental*, **117**, 137–147. (Cited on page 104.)
- HARPER, G.M. (1988). *The outer atmospheres of hybrid giants.* Ph.D. thesis, Oxford Univ. (England). (Cited on page 2.)
- HARPER, G.M. (1994). A Computer Program for Solving Multilevel Non-Lte Radiative Transfer Problems in Spherical Geometry in Moving or Static Atmospheres. *Monthly Notices of the Royal Astronomical Society*, **268**, 894. (Cited on page 170.)
- HARPER, G.M. (2010). Betelgeuse: A Case Study of an Inhomogeneous Extended Atmosphere. In C. Leitherer, P.D. Bennett, P.W. Morris & J.T. Van Loon, eds., *Hot and Cool: Bridging Gaps in Massive Star Evolution*, vol. 425 of *Astronomical Society of the Pacific Conference Series*, 152. (Cited on page 71.)
- HARPER, G.M. (2013). Atmospheric structure and dynamics: the spatial and temporal domains. In P. Kervella, T. Le Bertre & G. Perrin, eds., *EAS Publications Series*, vol. 60 of *EAS Publications Series*, 59–68. (Cited on page 143.)
- HARPER, G.M., BROWN, A. & LIM, J. (2001). A Spatially Resolved, Semiempirical Model for the Extended Atmosphere of α Orionis (M2 Iab). *Astrophysical Journal*, **551**, 1073–1098. (Cited on pages 2, 7, 68, 69, 70, 117, 146, 147, 148, 149, 153, 155 and 213.)

REFERENCES

- HARPER, G.M., BROWN, A., BENNETT, P.D., BAADE, R., WALDER, R. & HUMMEL, C.A. (2005). VLA Observations of ζ Aurigae: Confirmation of the Slow Acceleration Wind Density Structure. *Astronomical Journal*, **129**, 1018–1034. (Cited on page 77.)
- HARPER, G.M., BROWN, A. & GUINAN, E.F. (2008). A New VLA-Hipparcos Distance to Betelgeuse and its Implications. *Astronomical Journal*, **135**, 1430–1440. (Cited on pages 68, 69, 121, 125, 147, 151 and 218.)
- HARPER, G.M., RICHTER, M.J., RYDE, N., BROWN, A., BROWN, J., GREATHOUSE, T.K. & STRONG, S. (2009). Texes Observations of M Supergiants: Dynamics and Thermodynamics of Wind Acceleration. *Astrophysical Journal*, **701**, 1464–1483. (Cited on page 70.)
- HARPER, G.M., O'RIAIN, N. & AYRES, T.R. (2013). Chromospheric thermal continuum millimetre emission from non-dusty K and M red giants. *Monthly Notices of the Royal Astronomical Society*, **428**, 2064–2073. (Cited on pages 31, 78 and 167.)
- HARRIS, M.J. & LAMBERT, D.L. (1984). Oxygen isotopes in the atmospheres of Betelgeuse and Antares. *Astrophysical Journal*, **281**, 739–745. (Cited on pages 69 and 118.)
- HARTMANN, L. & AVRETT, E.H. (1984). On the extended chromosphere of Alpha Orionis. *Astrophysical Journal*, **284**, 238–249. (Cited on pages 14, 70 and 144.)
- HARTMANN, L. & MACGREGOR, K.B. (1980). Momentum and energy deposition in late-type stellar atmospheres and winds. *Astrophysical Journal*, **242**, 260–282. (Cited on pages 2, 14, 178 and 203.)
- HARTMANN, L., AVRETT, E. & EDWARDS, S. (1982). Wave-driven winds from cool stars. II - Models for T Tauri stars. *Astrophysical Journal*, **261**, 279–292. (Cited on page 178.)
- HATZES, A.P. & COCHRAN, W.D. (1993). Long-period radial velocity variations in three K giants. *Astrophysical Journal*, **413**, 339–348. (Cited on pages 80, 81 and 83.)
- HATZES, A.P. & COCHRAN, W.D. (1998). On the nature of the radial velocity variability of Aldebaran - A search for spectral line bisector variations. *Monthly Notices of the Royal Astronomical Society*, **293**, 469. (Cited on page 83.)
- HAUBOIS, X., PERRIN, G., LACOUR, S., VERHOELST, T., MEIMON, S., MUGNIER, L., THIÉBAUT, E., BERGER, J.P., RIDGWAY, S.T., MONNIER, J.D., MILLAN-GABET, R. & TRAUB, W. (2009). Imaging the spotty surface of ζ ASTROBJ ζ Betelgeuse ζ /ASTROBJ ζ in the H band. *Astronomy & Astrophysics*, **508**, 923–932. (Cited on pages 68, 69 and 71.)
- HINKLE, K.H., LAMBERT, D.L. & SNELL, R.L. (1976). The C-12/C-13 ratio in stellar atmospheres. VI - Five luminous cool stars. *Astrophysical Journal*, **210**, 684–693. (Cited on page 118.)
- HJELLMING, R.M. & NEWELL, R.T. (1983). Radio emission from Antares and an ionized cavity in its wind. *Astrophysical Journal*, **275**, 704–708. (Cited on page 33.)
- HÖGBOM, J.A. (1974). Aperture Synthesis with a Non-Regular Distribution of Interferometer Baselines. *Astronomy & Astrophysics Supplemental*, **15**, 417. (Cited on page 65.)

REFERENCES

- HOLLENBACH, D. & MCKEE, C.F. (1989). Molecule formation and infrared emission in fast interstellar shocks. III - Results for J shocks in molecular clouds. *Astrophysical Journal*, **342**, 306–336. (Cited on page 200.)
- HOLLWEG, J.V. (1973). ALFVtN Waves in a Two-Fluid Model of the Solar Wind. *Astrophysical Journal*, **181**, 547–566. (Cited on page 13.)
- HOLZER, T.E. & MACGREGOR, K.B. (1985). Mass loss mechanisms for cool, low-gravity stars. In M. Morris & B. Zuckerman, eds., *Mass Loss from Red Giants*, vol. 117 of *Astrophysics and Space Science Library*, 229–255. (Cited on page 2.)
- HOLZER, T.E., FLA, T. & LEER, E. (1983). Alfvén waves in stellar winds. *Astrophysical Journal*, **275**, 808–835. (Cited on pages 173 and 178.)
- HOOGERWERF, R., DE BRUIJNE, J.H.J. & DE ZEEUW, P.T. (2000). The Origin of Runaway Stars. *Astrophysical Journal Letters*, **544**, L133–L136. (Cited on page 68.)
- HUBER, K.P. & HERZBERG, G. (1979). *Molecular Spectra and Molecular Structure IV. Constants of Diatomic Molecules*. New York: Van Nostrand Reinhold. (Cited on page 24.)
- HUGGINS, P.J. (1987). CO in the circumstellar envelope of Alpha Orionis. *Astrophysical Journal*, **313**, 400–407. (Cited on pages 70, 119, 120, 123, 124 and 130.)
- HUGGINS, P.J., BACHILLER, R., COX, P. & FORVEILLE, T. (1994). Neutral carbon in the circumstellar envelope of alpha Orionis. *Astrophysical Journal Letters*, **424**, L127–L130. (Cited on pages 119, 120, 128 and 130.)
- HUMMER, D.G. (1988). A fast and accurate method for evaluating the nonrelativistic free-free Gaunt factor for hydrogenic ions. *Astrophysical Journal*, **327**, 477–484. (Cited on pages 31 and 170.)
- IBEN, I., JR. (1967). Stellar Evolution Within and off the Main Sequence. *Annual Review of Astronomy & Astrophysics*, **5**, 571. (Cited on page 18.)
- IBEN, I., JR. (1993). On Why Intermediate-Mass Stars Become Giants after the Exhaustion of Hydrogen in Their Cores. *Astrophysical Journal*, **415**, 767. (Cited on page 15.)
- IROSHNIKOV, P.S. (1964). Turbulence of a Conducting Fluid in a Strong Magnetic Field. *Soviet Astronomy*, **7**, 566. (Cited on page 204.)
- JACKSON, N. (2008). Principles of Interferometry. In F. Bacciotti, L. Testi & E. Whelan, eds., *Jets from Young Stars II*, vol. 742 of *Lecture Notes in Physics*, Berlin Springer Verlag, 193. (Cited on pages 52 and 53.)
- JATENCO-PEREIRA, V. & OPHER, R. (1989). Effect of diverging magnetic fields on mass loss in late-type giant stars. *Astronomy & Astrophysics*, **209**, 327–336. (Cited on page 178.)
- JEWELL, P.R., SNYDER, L.E., WALMSLEY, C.M., WILSON, T.L. & GENSHEIMER, P.D. (1991). Observational properties of V = 1, J = 1 - 0 SiO masers. *Astronomy & Astrophysics*, **242**, 211–234. (Cited on page 70.)

REFERENCES

- JOHNSON, H.R. (1973). Cooling effect of CO in stellar atmospheres. *Astrophysical Journal*, **180**, 81–89. (Cited on page 172.)
- JONES, M.H. (2008). The incidence of mid-infrared excesses in G and K giants. *Monthly Notices of the Royal Astronomical Society*, **387**, 845–855. (Cited on pages 2 and 14.)
- JOSSELIN, E. & PLEZ, B. (2007). Atmospheric dynamics and the mass loss process in red supergiant stars. *Astronomy & Astrophysics*, **469**, 671–680. (Cited on page 14.)
- JUDGE, P.G. (1986). Constraints on the outer atmospheric structure of late-type giant stars with IUE - Methods and application to Arcturus (Alpha Boo K2III). *Monthly Notices of the Royal Astronomical Society*, **221**, 119–153. (Cited on page 198.)
- JUDGE, P.G. & CARPENTER, K.G. (1998). On Chromospheric Heating Mechanisms of “Basal Flux” Stars. *Astrophysical Journal*, **494**, 828. (Cited on pages 3 and 23.)
- KALER, J.B., IBEN, I., JR. & BECKER, S.A. (1978). On the enhancement of helium and nitrogen in planetary nebulae. *Astrophysical Journal Letters*, **224**, L63–L66. (Cited on page 118.)
- KALLINGER, T., WEISS, W.W., BARBAN, C., BAUDIN, F., CAMERON, C., CARRIER, F., DE RIDDER, J., GOUPIL, M.J., GRUBERBAUER, M., HATZES, A., HEKKER, S., SAMADI, R. & DELEUIL, M. (2010). Oscillating red giants in the CoRoT exofield: asteroseismic mass and radius determination. *Astronomy & Astrophysics*, **509**, A77. (Cited on pages 78 and 81.)
- KAMIŃSKI, T., GOTTLIEB, C.A., SCHMIDT, M.R., PATEL, N.A., YOUNG, K.H., MENTEN, K.M., BRÜNKEN, S., MÜLLER, H.S.P., WINTERS, J.M. & McCARTHY, M.C. (2013). Dust-forming molecules in VY Canis Majoris (and Betelgeuse). In *EAS Publications Series*, vol. 60 of *EAS Publications Series*, 191–198. (Cited on page 70.)
- KARZAS, W.J. & LATTER, R. (1961). Electron Radiative Transitions in a Coulomb Field. *Astrophysical Journal Supplemental Series*, **6**, 167. (Cited on page 24.)
- KELCH, W.L., CHANG, S.H., FURENLID, I., LINSKY, J.L., BASRI, G.S., CHIU, H.Y. & MARAN, S.P. (1978). Stellar model chromospheres. VII - Capella /G5 III +/, Pollux /K0 III/, and Aldebaran /K5 III/. *Astrophysical Journal*, **220**, 962–979. (Cited on page 84.)
- KERVELLA, P., VERHOELST, T., RIDGWAY, S.T., PERRIN, G., LACOUR, S., CAMI, J. & HAUBOIS, X. (2009). The close circumstellar environment of Betelgeuse. Adaptive optics spectro-imaging in the near-IR with VLT/NACO. *Astronomy & Astrophysics*, **504**, 115–125. (Cited on page 71.)
- KERVELLA, P., PERRIN, G., CHIAVASSA, A., RIDGWAY, S.T., CAMI, J., HAUBOIS, X. & VERHOELST, T. (2011). The close circumstellar environment of Betelgeuse. II. Diffraction-limited spectro-imaging from 7.76 to 19.50 μm with VLT/VISIR. *Astronomy & Astrophysics*, **531**, A117. (Cited on pages 71, 135, 216 and 217.)
- KNAPP, G.R. & MORRIS, M. (1985). Mass loss from evolved stars. III - Mass loss rates for fifty stars from CO $J = 1-0$ observations. *Astrophysical Journal*, **292**, 640–669. (Cited on page 119.)

REFERENCES

- KNAPP, G.R., PHILLIPS, T.G. & HUGGINS, P.J. (1980). Detection of CO Emission at 1.3-MILLIMETERS from the Betelgeuse Circumstellar Shell. *Astrophysical Journal Letters*, **242**, L25+. (Cited on pages 70, 119, 124 and 130.)
- KOLMOGOROV, A. (1941). The Local Structure of Turbulence in Incompressible Viscous Fluid for Very Large Reynolds' Numbers. *Akademii Nauk SSSR Doklady*, **30**, 301–305. (Cited on page 205.)
- KRAUS, J.D., TIURI, M., RAISANEN, A.V. & CARR, T.D. (1986). *Radio astronomy receivers*. (Cited on page 43.)
- KROGULEC, M. (1988). Alfven wave driven wind - Models of Alpha Boo atmosphere. *Acta Astronomica*, **38**, 107–126. (Cited on page 173.)
- KROGULEC, M. (1989). Alfven wave driven wind. II - Models of cool giant and supergiant stars. *Acta Astronomica*, **39**, 51–67. (Cited on page 173.)
- LACOUR, S., MEIMON, S., THIÉBAUT, E., PERRIN, G., VERHOELST, T., PEDRETTI, E., SCHULLER, P.A., MUGNIER, L., MONNIER, J., BERGER, J.P., HAUBOIS, X., PONCELET, A., LE BESNERAIS, G., ERIKSSON, K., MILLAN-GABET, R., RAGLAND, S., LACASSE, M. & TRAUB, W. (2008). The limb-darkened Arcturus: imaging with the IOTA/IONIC interferometer. *Astronomy & Astrophysics*, **485**, 561–570. (Cited on page 80.)
- LAMB, S.A., IBEN, I., JR. & HOWARD, W.M. (1976). On the evolution of massive stars through the core carbon-burning phase. *Astrophysical Journal*, **207**, 209–232. (Cited on page 117.)
- LAMBERT, D.L. & RIES, L.M. (1981). Carbon, nitrogen, and oxygen abundances in G and K giants. *Astrophysical Journal*, **248**, 228–248. (Cited on page 19.)
- LAMBERT, D.L. & VANDEN BOUT, P.A. (1978). Constraints on the properties of circumstellar shells from observations of thermal CO and SiO millimeter line emission. *Astrophysical Journal*, **221**, 854–860. (Cited on pages 70 and 141.)
- LAMBERT, D.L., DEARBORN, D.S. & SNEDEN, C. (1974). The C-12/C-13 ratio in stellar atmospheres. II - CN and CO in alpha Orionis. *Astrophysical Journal*, **193**, 621–630. (Cited on page 118.)
- LAMBERT, D.L., BROWN, J.A., HINKLE, K.H. & JOHNSON, H.R. (1984). Carbon, nitrogen, and oxygen abundances in Betelgeuse. *Astrophysical Journal*, **284**, 223–237. (Cited on pages 69 and 117.)
- LAMERS, H.J.G.L.M. (1998). Stellar Wind Theories. *Astrophysics & Space Science*, **260**, 81–100. (Cited on page 10.)
- LAMERS, H.J.G.L.M. & CASSINELLI, J.P. (1999). *Introduction to Stellar Winds*. (Cited on pages 8, 38, 39, 184 and 192.)
- LAMERS, H.J.G.L.M., CERRUTI-SOLA, M. & PERINOTTO, M. (1987). The 'SEI' method for accurate and efficient calculations of line profiles in spherically symmetric stellar winds. *Astrophysical Journal*, **314**, 726–738. (Cited on page 172.)

REFERENCES

- LEBZELTER, T., HEITER, U., ABIA, C., ERIKSSON, K., IRELAND, M., NEILSON, H., NOWOTNY, W., MALDONADO, J., MERLE, T., PETERSON, R., PLEZ, B., SHORT, C.I., WAHLGREN, G.M., WORLEY, C., ARINGER, B., BLADH, S., DE LAVERNY, P., GOSWAMI, A., MORA, A., NORRIS, R.P., RECIO-BLANCO, A., SCHOLZ, M., THÉVENIN, F., TSUJI, T., KORDOPATIS, G., MONTESINOS, B. & WING, R.F. (2012). Comparative modelling of the spectra of cool giants. *Astronomy & Astrophysics*, **547**, A108. (Cited on pages 81 and 83.)
- LEHE, R., PARRISH, I.J. & QUATAERT, E. (2009). The Heating of Test Particles in Numerical Simulations of Alfvénic Turbulence. *Astrophysical Journal*, **707**, 404–419. (Cited on page 203.)
- LEVESQUE, E.M. (2010). The Physical Properties of Red Supergiants. In C. Leitherer, P.D. Bennett, P.W. Morris & J.T. Van Loon, eds., *Hot and Cool: Bridging Gaps in Massive Star Evolution*, vol. 425 of *Astronomical Society of the Pacific Conference Series*, 103. (Cited on page 17.)
- LEVESQUE, E.M., MASSEY, P., OLSEN, K.A.G., PLEZ, B., JOSSELIN, E., MAEDER, A. & MEYNET, G. (2005). The Effective Temperature Scale of Galactic Red Supergiants: Cool, but Not As Cool As We Thought. *Astrophysical Journal*, **628**, 973–985. (Cited on pages 69 and 147.)
- LIGHTHILL, M.J. (1952). On Sound Generated Aerodynamically. I. General Theory. *Royal Society of London Proceedings Series A*, **211**, 564–587. (Cited on page 203.)
- LIM, J., CARILLI, C.L., WHITE, S.M., BEASLEY, A.J. & MARSON, R.G. (1998). Large convection cells as the source of Betelgeuse's extended atmosphere. *Nature*, **392**, 575–577. (Cited on pages 7, 14, 30, 69, 70, 71, 95, 136, 144, 145, 148, 152, 153, 154, 155, 157, 158 and 159.)
- LINSKY, J.L. & HAISCH, B.M. (1979). Outer atmospheres of cool stars. I - The sharp division into solar-type and non-solar-type stars. *Astrophysical Journal Letters*, **229**, L27–L32. (Cited on pages 2, 5, 80 and 84.)
- LUCK, R.E. & CHALLENER, S.L. (1995). Chemical Abundances for Very Strong-Lined Giants. *Astronomical Journal*, **110**, 2968. (Cited on page 224.)
- LUTTERMOSER, D.G., JOHNSON, H.R. & EATON, J. (1994). The chromospheric structure of the cool giant star G Herculis. *Astrophysical Journal*, **422**, 351–365. (Cited on page 8.)
- MACCHETTO, F. & PENSTON, M.V. (1978). The International Ultraviolet Explorer. *ESA Bulletin*, **13**, 9–14. (Cited on page 5.)
- MAEDER, A. & MEYNET, G. (1987). Grids of evolutionary models of massive stars with mass loss and overshooting - Properties of Wolf-Rayet stars sensitive to overshooting. *Astronomy & Astrophysics*, **182**, 243–263. (Cited on page 17.)
- MASSAROTTI, A., LATHAM, D.W., STEFANIK, R.P. & FOGL, J. (2008). Rotational and Radial Velocities for a Sample of 761 HIPPARCOS Giants and the Role of Binarity. *Astronomical Journal*, **135**, 209–231. (Cited on page 81.)

REFERENCES

- MATHISEN, R. (1984). Photo cross-sections for stellar atmosphere calculations – compilation of references and data. *Inst. Theor. Astrophys. Univ. Oslo, publ. Series No. 1.* (Cited on page 202.)
- MATTHAEUS, W.H., ZANK, G.P., OUGHTON, S., MULLAN, D.J. & DMITruk, P. (1999). Coronal Heating by Magnetohydrodynamic Turbulence Driven by Reflected Low-Frequency Waves. *Astrophysical Journal Letters*, **523**, L93–L96. (Cited on page 204.)
- MCMULLIN, J.P., WATERS, B., SCHIEBEL, D., YOUNG, W. & GOLAP, K. (2007). CASA Architecture and Applications. In R.A. Shaw, F. Hill & D.J. Bell, eds., *Astronomical Data Analysis Software and Systems XVI*, vol. 376 of *Astronomical Society of the Pacific Conference Series*, 127. (Cited on page 99.)
- McMURRY, A.D. (1999). The outer atmosphere of Tau - I. A new chromospheric model. *Monthly Notices of the Royal Astronomical Society*, **302**, 37–47. (Cited on pages 81, 84, 171, 172 and 214.)
- MCWILLIAM, A. (1990). High-resolution spectroscopic survey of 671 GK giants. I - Stellar atmosphere parameters and abundances. *Astrophysical Journal Supplemental Series*, **74**, 1075–1128. (Cited on page 224.)
- MERLINE, W.J. (1999). Precise Velocity Observation of K-Giants: Evidence for Solar-Like Oscillations in Arcturus. In J.B. Hearnshaw & C.D. Scarfe, eds., *IAU Colloq. 170: Precise Stellar Radial Velocities*, vol. 185 of *Astronomical Society of the Pacific Conference Series*, 187. (Cited on page 80.)
- MEYNET, G. & MAEDER, A. (2003). Stellar evolution with rotation. X. Wolf-Rayet star populations at solar metallicity. *Astronomy & Astrophysics*, **404**, 975–990. (Cited on pages 68, 69 and 125.)
- MICHELSON, A.A. (1890). *Phil. Mag.*, **30**, 1–21. (Cited on page 58.)
- MIHALAS, D. (1978). *Stellar atmospheres /2nd edition/*. (Cited on page 170.)
- MORAVVEJI, E., GUINAN, E.F., KHOSROSHAH, H. & WASATONIC, R. (2013). The Age and Mass of the α Herculis Triple-star System from a MESA Grid of Rotating Stars with $1.3 = M/M = 8.0$. *Astronomical Journal*, **146**, 148. (Cited on page 4.)
- MORRIS, R.A.H. (2001). Ph.D. thesis, University of Wales, Cardiff (Wales). (Cited on pages 95, 144 and 221.)
- MORTON, D.C. (1967). Mass Loss from Three OB Supergiants in Orion. *Astrophysical Journal*, **150**, 535. (Cited on page 11.)
- MUXLOW, T.W.B. (2003). e-MERLIN - a Real-Time VLBI Array. In Y.C. Minh, ed., *New technologies in VLBI*, vol. 306 of *Astronomical Society of the Pacific Conference Series*, 245. (Cited on page 144.)
- NAVARRO, J.F., HELMI, A. & FREEMAN, K.C. (2004). The Extragalactic Origin of the Arcturus Group. *Astrophysical Journal Letters*, **601**, L43–L46. (Cited on page 78.)

REFERENCES

- NEUGEBAUER, M. & SNYDER, C.W. (1962). Solar Plasma Experiment. *Science*, **138**, 1095–1097. (Cited on page 13.)
- NEWELL, R.T. & HJELLMING, R.M. (1982). Radio emission from the extended chromosphere of Alpha Orionis. *Astrophysical Journal Letters*, **263**, L85–L87. (Cited on pages 36, 70, 144, 151 and 153.)
- O'GORMAN, E. & HARPER, G.M. (2011). What is Heating Arcturus' Wind? In C. Johns-Krull, M.K. Browning & A.A. West, eds., *16th Cambridge Workshop on Cool Stars, Stellar Systems, and the Sun*, vol. 448 of *Astronomical Society of the Pacific Conference Series*, 691. (Cited on pages 181 and 191.)
- O'GORMAN, E., HARPER, G.M., BROWN, J.M., BROWN, A., REDFIELD, S., RICHTER, M.J. & REQUENA-TORRES, M.A. (2012). CARMA CO($J = 2 - 1$) Observations of the Circumstellar Envelope of Betelgeuse. *Astronomical Journal*, **144**, 36. (Cited on pages 98, 116 and 217.)
- O'GORMAN, E., HARPER, G.M., BROWN, A., DRAKE, S. & RICHARDS, A.M.S. (2013). Multi-wavelength Radio Continuum Emission Studies of Dust-free Red Giants. *Astronomical Journal*, **144**, 36. (Cited on pages 98 and 160.)
- OHNAKA, K. (2013). Spatially resolved, high-spectral resolution observation of the K giant Aldebaran in the CO first overtone lines with VLTI/AMBER. *Astronomy & Astrophysics*, **553**, A3. (Cited on pages 187 and 188.)
- OHNAKA, K., WEIGELT, G., MILLOUR, F., HOFMANN, K.H., DRIEBE, T., SCHERTL, D., CHELLI, A., MASSI, F., PETROV, R. & STEE, P. (2011). Imaging the dynamical atmosphere of the red supergiant Betelgeuse in the CO first overtone lines with VLTI/AMBER. *Astronomy & Astrophysics*, **529**, A163. (Cited on pages 219 and 220.)
- OLNON, F.M. (1975). Thermal bremsstrahlung radiospectra for inhomogeneous objects, with an application to MWC 349. *Astronomy & Astrophysics*, **39**, 217–223. (Cited on pages 172 and 174.)
- OWOCKI, S. (2004). Stellar wind mechanisms and instabilities. In M. Heydari-Malayeri, P. Stee & J.P. Zahn, eds., *EAS Publications Series*, vol. 13 of *EAS Publications Series*, 163–250. (Cited on page 11.)
- PANAGIA, N. & FELLI, M. (1975). The spectrum of the free-free radiation from extended envelopes. *Astronomy & Astrophysics*, **39**, 1–5. (Cited on pages 35, 172 and 174.)
- PARKER, E.N. (1958). Dynamics of the Interplanetary Gas and Magnetic Fields. *Astrophysical Journal*, **128**, 664. (Cited on pages 12 and 13.)
- PARKER, E.N. (1983). Magnetic Neutral Sheets in Evolving Fields - Part Two - Formation of the Solar Corona. *Astrophysical Journal*, **264**, 642. (Cited on page 13.)
- PARKER, E.N. (1988). Nanoflares and the solar X-ray corona. *Astrophysical Journal*, **330**, 474–479. (Cited on page 13.)

REFERENCES

- PAVLENKO, Y.V., JONES, H.R.A. & LONGMORE, A.J. (2003). Carbon abundances and $^{12}\text{C}/^{13}\text{C}$ from globular cluster giants. *Monthly Notices of the Royal Astronomical Society*, **345**, 311–324. (Cited on page 118.)
- PERLEY, R.A. & BUTLER, B.J. (2013). An Accurate Flux Density Scale from 1 to 50 GHz. *Astrophysical Journal Supplemental Series*, **204**, 19. (Cited on pages 106 and 162.)
- PERRIN, G., RIDGWAY, S.T., COUDÉ DU FORESTO, V., MENNESSON, B., TRAUB, W.A. & LACASSE, M.G. (2004). Interferometric observations of the supergiant stars α Orionis and α Herculis with FLUOR at IOTA. *Astronomy & Astrophysics*, **418**, 675–685. (Cited on page 69.)
- PERRIN, G., VERHOELST, T., RIDGWAY, S.T., CAMI, J., NGUYEN, Q.N., CHESNEAU, O., LOPEZ, B., LEINERT, C. & RICHICHI, A. (2007). The molecular and dusty composition of Betelgeuse's inner circumstellar environment. *Astronomy & Astrophysics*, **474**, 599–608. (Cited on page 70.)
- PERRYMAN, M.A.C., LINDEGREN, L., KOVALEVSKY, J., HOEG, E., BASTIAN, U., BERNACCA, P.L., CRÉZÉ, M., DONATI, F., GRENON, M., GREWING, M., VAN LEEUWEN, F., VAN DER MAREL, H., MIGNARD, F., MURRAY, C.A., LE POOLE, R.S., SCHRIJVER, H., TURON, C., ARENOU, F., FROESCHLÉ, M. & PETERSEN, C.S. (1997). The HIPPARCOS Catalogue. *Astronomy & Astrophysics*, **323**, L49–L52. (Cited on pages 69, 78, 80 and 81.)
- PILBRATT, G.L., RIEDINGER, J.R., PASSVOGEL, T., CRONE, G., DOYLE, D., GAGEUR, U., HERAS, A.M., JEWELL, C., METCALFE, L., OTT, S. & SCHMIDT, M. (2010). Herschel Space Observatory. An ESA facility for far-infrared and submillimetre astronomy. *Astronomy & Astrophysics*, **518**, L1. (Cited on page 139.)
- PLEZ, B. & LAMBERT, D.L. (2002). The outer atmosphere of the M-type supergiant alpha Ori: K I 7699 Åemission. *Astronomy & Astrophysics*, **386**, 1009–1018. (Cited on pages 135 and 143.)
- RAMÍREZ, I. & ALLENDE PRIETO, C. (2011). Fundamental Parameters and Chemical Composition of Arcturus. *Astrophysical Journal*, **743**, 135. (Cited on pages 80, 81 and 198.)
- RAMÍREZ, S.V., SELLGREN, K., CARR, J.S., BALACHANDRAN, S.C., BLUM, R., TERNDRUP, D.M. & STEED, A. (2000). Stellar Iron Abundances at the Galactic Center. *Astrophysical Journal*, **537**, 205–220. (Cited on page 69.)
- REIMERS, D. (1975). Circumstellar absorption lines and mass loss from red giants. *Memoires de la Societe Royale des Sciences de Liege*, **8**, 369–382. (Cited on page 4.)
- REIMERS, D. (1982). Detection of further red giants with 'hybrid' atmospheres and a possible correlation with double circumstellar MG II and CA II lines. *Astronomy & Astrophysics*, **107**, 292–299. (Cited on page 6.)
- RENZINI, A., GREGGIO, L., RITOSSA, C. & FERRARIO, L. (1992). Why stars inflate to and deflate from red giant dimensions. *Astrophysical Journal*, **400**, 280–303. (Cited on page 15.)

REFERENCES

- RETTER, A., BEDDING, T.R., BUZASI, D.L., KJELDSEN, H. & KISS, L.L. (2003). Oscillations in Arcturus from WIRE Photometry. *Astrophysical Journal Letters*, **591**, L151–L154. (Cited on page 80.)
- RICH, J.W., DE BLOK, W.J.G., CORNWELL, T.J., BRINKS, E., WALTER, F., BAGETAKOS, I. & KENNICUTT, R.C., JR. (2008). Multi-Scale CLEAN: A Comparison of its Performance Against Classical CLEAN on Galaxies Using THINGS. *Astronomical Journal*, **136**, 2897–2920. (Cited on pages 113 and 115.)
- RICHARDS, A.M.S., DAVIS, R.J., DECIN, L., ETOKA, S., HARPER, G.M., LIM, J.J., GARRINGTON, S.T., GRAY, M.D., McDONALD, I., O'GORMAN, E. & WITTKOWSKI, M. (2013). e-MERLIN resolves Betelgeuse at λ 5 cm: hotspots at 5 R. *Monthly Notices of the Royal Astronomical Society*, **432**, L61. (Cited on pages 94, 95, 116, 144, 146, 147, 151, 153, 155, 218, 219 and 220.)
- RICHICHI, A. & ROCCATAGLIATA, V. (2005). Aldebaran's angular diameter: How well do we know it? *Astronomy & Astrophysics*, **433**, 305–312. (Cited on pages 81 and 83.)
- ROBINSON, R.D., CARPENTER, K.G. & BROWN, A. (1998). Goddard High-Resolution Spectrograph Observations of Cool Low-Gravity Stars. IV. A Comparison of the K5 III Stars alpha Tauri and gamma Draconis. *Astrophysical Journal*, **503**, 396. (Cited on pages 6, 81, 84, 171, 172 and 180.)
- RODGERS, B. & GLASSGOLD, A.E. (1991). The temperature of the circumstellar envelope of Alpha Orionis. *Astrophysical Journal*, **382**, 606–616. (Cited on pages 26, 69, 194 and 198.)
- ROHLFS, K. & WILSON, T.L. (1996). *Tools of Radio Astronomy*. (Cited on page 28.)
- RYAN, S.G. & NORTON, A.J. (2010). *Stellar Evolution and Nucleosynthesis*. (Cited on page 18.)
- RYBICKI, G.B. & LIGHTMAN, A.P. (1979). *Radiative processes in astrophysics*. (Cited on page 23.)
- RYDE, N., LAMBERT, D.L., RICHTER, M.J. & LACY, J.H. (2002). Detection of Water Vapor in the Photosphere of Arcturus. *Astrophysical Journal*, **580**, 447–458. (Cited on page 83.)
- SAHA, S.K. (2011). *Aperture Synthesis*. (Cited on page 146.)
- SANFORD, R.F. (1933). No. 464. The variation in the radial velocity of alpha Orionis from 1923 to 1931. *Contributions from the Mount Wilson Observatory / Carnegie Institution of Washington*, **464**, 1–10. (Cited on pages 120 and 121.)
- SAULT, R.J., TEUBEN, P.J. & WRIGHT, M.C.H. (1995). A Retrospective View of MIRIAD. In R.A. Shaw, H.E. Payne & J.J.E. Hayes, eds., *Astronomical Data Analysis Software and Systems IV*, vol. 77 of *Astronomical Society of the Pacific Conference Series*, 433. (Cited on page 100.)
- SCHARMER, G.B. & CARLSSON, M. (1985). A new approach to multi-level non-LTE radiative transfer problems. *Journal of Computational Physics*, **59**, 56–80. (Cited on page 181.)

REFERENCES

- SCHRIJVER, C.J. & HARVEY, K.L. (1989). The distribution of solar magnetic fluxes and the nonlinearity of stellar flux-flux relations. *Astrophysical Journal*, **343**, 481–488. (Cited on page 204.)
- SCHRÖDER, K.P. & SEDLMAYR, E. (2001). The galactic mass injection from cool stellar winds of the 1 to 2.5 M_{sun} stars in the solar neighbourhood. *Astronomy & Astrophysics*, **366**, 913–922. (Cited on page 2.)
- SCHWARZ, U.J. (1978). Mathematical-statistical Description of the Iterative Beam Removing Technique (Method CLEAN). *Astronomy & Astrophysics*, **65**, 345. (Cited on page 65.)
- SCHWARZSCHILD, M. (1975). On the scale of photospheric convection in red giants and supergiants. *Astrophysical Journal*, **195**, 137–144. (Cited on page 68.)
- SCUDERI, S., PANAGIA, N., STANGHELLINI, C., TRIGILIO, C. & UMANA, G. (1998). Radio observations of stellar winds from early type stars. *Astronomy & Astrophysics*, **332**, 251–267. (Cited on page 20.)
- SEAQUIST, E.R. & TAYLOR, A.R. (1987). A detailed analysis of the radio emission from the symbiotic star RX Puppis. *Astrophysical Journal*, **312**, 813–821. (Cited on pages 174 and 175.)
- SENNHAUSER, C. & BERDYUGINA, S.V. (2011). First detection of a weak magnetic field on the giant Arcturus: remnants of a solar dynamo? *Astronomy & Astrophysics*, **529**, A100. (Cited on pages 23, 81, 83, 202 and 204.)
- SHANG, H., GLASSGOLD, A.E., SHU, F.H. & LIZANO, S. (2002). Heating and Ionization of X-Winds. *Astrophysical Journal*, **564**, 853–876. (Cited on page 202.)
- SHU, F.H. (1991). *The physics of astrophysics. Volume 1: Radiation..* (Cited on page 26.)
- SIMON, T., LINSKY, J.L. & STENCEL, R.E. (1982). On the reality of a boundary in the H-R diagram between late-type stars with and without high temperature outer atmospheres. *Astrophysical Journal*, **257**, 225–246. (Cited on page 5.)
- SKINNER, C.J., DOUGHERTY, S.M., MEIXNER, M., BODE, M.F., DAVIS, R.J., DRAKE, S.A., ARENS, J.F. & JERNIGAN, J.G. (1997). Circumstellar environments - V. The asymmetric chromosphere and dust shell of alpha Orionis. *Monthly Notices of the Royal Astronomical Society*, **288**, 295–306. (Cited on pages 70 and 144.)
- SLEE, O.B., STEWART, R.T., BUNTON, J.D., BEASLEY, A.J., CARTER, B.D. & NELSON, G.J. (1989). A microwave survey of southern red giants. *Monthly Notices of the Royal Astronomical Society*, **239**, 913–922. (Cited on page 166.)
- SMITH, M.A., PATTEN, B.M. & GOLDBERG, L. (1989). Radial-velocity variations in Alpha Ori, Alpha Sco, and Alpha HER. *Astronomical Journal*, **98**, 2233–2248. (Cited on page 120.)
- SMITH, N., HINKLE, K.H. & RYDE, N. (2009). Red Supergiants as Potential Type IIn Supernova Progenitors: Spatially Resolved 4.6 μm CO Emission Around VY CMa and Betelgeuse. *Astronomical Journal*, **137**, 3558–3573. (Cited on page 135.)

REFERENCES

- SODERHJELM, S. & MIGNARD, F. (1998). Arcturus as a double star. *The Observatory*, **118**, 365–366. (Cited on page 80.)
- SPENCER JONES, H. (1928). The radial velocity variations of a Orionis and a Scorpii. *Monthly Notices of the Royal Astronomical Society*, **88**, 660. (Cited on pages 120 and 121.)
- SPINRAD, H. & VARDYA, M.S. (1966). Approximate Abundances of the Light Elements from the Molecular Spectra of M and S Stars. *Astrophysical Journal*, **146**, 399. (Cited on page 117.)
- SPITZER, L. (1978). *Physical processes in the interstellar medium*. New York Wiley-Interscience, 1978. 333 p. (Cited on pages 185, 196, 197 and 202.)
- SPITZER, L., JR. (1939). Spectra of M Supergiant Stars. *Astrophysical Journal*, **90**, 494. (Cited on page 4.)
- STANCLIFFE, R.J., CHIEFFI, A., LATTANZIO, J.C. & CHURCH, R.P. (2009). Why Do Low-Mass Stars Become Red Giants. **26**, 203–208. (Cited on page 15.)
- STEBBINS, J. & HUFFER, C.M. (1931). Photo-electric studies of five variable stars. *Publications of the Washburn Observatory*, **15**, 178–213. (Cited on page 120.)
- STEIN, R.F. (1967). Generation of Acoustic and Gravity Waves by Turbulence in an Isothermal Stratified Atmosphere. *Solar Physics*, **2**, 385–432. (Cited on page 203.)
- STOTHERS, R. & CHIN, C.W. (1969). Advanced Phases of Evolution in Massive Red Supergiants. *Astrophysical Journal*, **158**, 1039. (Cited on page 16.)
- STOTHERS, R. & LEUNG, K.C. (1971). Luminosities, masses and periodicities of massive red supergiants. *Astronomy & Astrophysics*, **10**, 290–300. (Cited on page 120.)
- STRASSMEIER, K.G., HALL, D.S., FEKEL, F.C. & SCHECK, M. (1993). A catalog of chromospherically active binary stars (second edition). *Astronomy & Astrophysics Supplemental*, **100**, 173–225. (Cited on page 21.)
- SUGIMOTO, D. & FUJIMOTO, M.Y. (2000). Why Stars Become Red Giants. *Astrophysical Journal*, **538**, 837–853. (Cited on page 15.)
- SUTMANN, G. & CUNTZ, M. (1995). Generation of mass loss in K giants: The failure of global oscillation modes and possible implications. *Astrophysical Journal Letters*, **442**, L61–L64. (Cited on page 2.)
- SUZUKI, T.K. (2007). Structured Red Giant Winds with Magnetized Hot Bubbles and the Corona/Cool Wind Dividing Line. *Astrophysical Journal*, **659**, 1592–1610. (Cited on page 3.)
- TATEBE, K., CHANDLER, A.A., WISHNOW, E.H., HALE, D.D.S. & TOWNES, C.H. (2007). The Nonspherical Shape of Betelgeuse in the Mid-Infrared. *Astrophysical Journal Letters*, **670**, L21–L24. (Cited on page 70.)
- TAYLOR, G.B., CARILLI, C.L. & PERLEY, R.A., eds. (1999). *Synthesis Imaging in Radio Astronomy II*, vol. 180 of *Astronomical Society of the Pacific Conference Series*. (Cited on pages 47, 48, 57, 60, 65 and 162.)

REFERENCES

- TSUJI, T. (1979). A probe of optically thin dust shells around late-type stars. *Publications of the Astronomical Society of Japan*, **31**, 43–60. (Cited on page 119.)
- TSUJI, T. (2000). Water on the Early M Supergiant Stars α Orionis and μ Cephei. *Astrophysical Journal*, **538**, 801–807. (Cited on page 70.)
- TSUJI, T. (2008). Cool luminous stars: the hybrid nature of their infrared spectra. *Astronomy & Astrophysics*, **489**, 1271–1289. (Cited on page 83.)
- TSUJI, T. (2009). The K giant star Arcturus: the hybrid nature of its infrared spectrum. *Astronomy & Astrophysics*, **504**, 543–559. (Cited on page 83.)
- TURNER, N.H., TEN BRUMMELAAR, T.A. & MASON, B.D. (1999). Adaptive Optics Observations of Arcturus using the Mount Wilson 100 Inch Telescope. *Publications of the Astronomical Society of the Pacific*, **111**, 556–558. (Cited on page 80.)
- TUTHILL, P.G., HANIFF, C.A. & BALDWIN, J.E. (1997). Hotspots on late-type supergiants. *Monthly Notices of the Royal Astronomical Society*, **285**, 529–539. (Cited on page 158.)
- UITENBROEK, H., DUPREE, A.K. & GILLILAND, R.L. (1998). Spatially Resolved Hubble Space Telescope Spectra of the Chromosphere of alpha Orionis. *Astronomical Journal*, **116**, 2501–2512. (Cited on pages 68 and 69.)
- VAN CITTERT, P.H. (1934). Die Wahrscheinliche Schwingungsverteilung in Einer von Einer Lichtquelle Direkt Oder Mittels Einer Linse Beleuchteten Ebene. *Physica*, **1**, 201–210. (Cited on page 60.)
- VAN LEEUWEN, F. (2007). Validation of the new Hipparcos reduction. *Astronomy & Astrophysics*, **474**, 653–664. (Cited on pages 33, 69, 81 and 83.)
- VAN LOON, J.T. (2010). The Effects of Red Supergiant Mass Loss on Supernova Ejecta and the Circumburst Medium. In C. Leitherer, P.D. Bennett, P.W. Morris & J.T. Van Loon, eds., *Hot and Cool: Bridging Gaps in Massive Star Evolution*, vol. 425 of *Astronomical Society of the Pacific Conference Series*, 279. (Cited on page 2.)
- VAN LOON, J.T., CIONI, M.R.L., ZIJLSTRA, A.A. & LOUP, C. (2005). An empirical formula for the mass-loss rates of dust-enshrouded red supergiants and oxygen-rich Asymptotic Giant Branch stars. *Astronomy & Astrophysics*, **438**, 273–289. (Cited on page 14.)
- VERDINI, A. & VELLI, M. (2007). Alfvén Waves and Turbulence in the Solar Atmosphere and Solar Wind. *Astrophysical Journal*, **662**, 669–676. (Cited on page 13.)
- VERHOELST, T., DECIN, L., VAN MALDEREN, R., HONY, S., CAMI, J., ERIKSSON, K., PERRIN, G., DEROO, P., VANDENBUSSCHE, B. & WATERS, L.B.F.M. (2006). Amorphous alumina in the extended atmosphere of α Orionis. *Astronomy & Astrophysics*, **447**, 311–324. (Cited on page 70.)
- VIDOTTO, A.A., FALCETA-GONÇALVES, D. & JATENCO-PEREIRA, V. (2006). A Self-Consistent Determination of the Temperature Profile and The Magnetic Field Geometry in Winds of Late-Type Stars. *Space Science Reviews*, **122**, 181–188. (Cited on page 178.)

REFERENCES

- VÖGLER, A. & SCHÜSSLER, M. (2007). A solar surface dynamo. *Astronomy & Astrophysics*, **465**, L43–L46. (Cited on page 68.)
- WEI, L., WOODY, D., TEUBEN, P., LA VIGNE, M. & VOGEL, S. (2008). Bandpass Calibration for CARMA. In *CARMA Memorandum Series*, vol. 45. (Cited on page 75.)
- WEYMANN, R. (1962). Physical Conditions in the Circumstellar Envelope of α Orionis. *Astrophysical Journal*, **136**, 844–+. (Cited on pages 4, 119 and 121.)
- WHITE, S.M. (2000). The Contributions of the VLA to the Study of Radio Stars. In D.G. Finley & W.M. Goss, eds., *Radio interferometry : the saga and the science*, 86. (Cited on pages 20 and 21.)
- WHITE, S.M. (2009). Single Dish Aperture Efficiency Measurements at CARMA. In *CARMA Memorandum Series*, vol. 49 of *CARMA Memorandum Series*. (Cited on page 106.)
- WIEDEMANN, G., AYRES, T.R., JENNINGS, D.E. & SAAR, S.H. (1994). Carbon Monoxide Fundamental Bands in Late-Type Stars. III. Chromosphere or CO-mosphere? *Astrophysical Journal*, **423**, 806. (Cited on pages 83, 84 and 173.)
- WILLIAMS, M.E.K., FREEMAN, K.C., HELMI, A. & RAVE COLLABORATION (2009). The Arcturus Moving Group: Its Place in the Galaxy. In J. Andersen, Nordströara, B. m & J. Bland-Hawthorn, eds., *IAU Symposium*, vol. 254 of *IAU Symposium*, 139–144. (Cited on page 78.)
- WILSON, R.W., BALDWIN, J.E., BUSCHER, D.F. & WARNER, P.J. (1992). High-resolution imaging of Betelgeuse and Mira. *Monthly Notices of the Royal Astronomical Society*, **257**, 369–376. (Cited on page 158.)
- WOOD, B.E., HARPER, G.M., MÜLLER, H.R., HEERIKHUISEN, J. & ZANK, G.P. (2007). The Wind-ISM Interaction of α Tauri. *Astrophysical Journal*, **655**, 946–957. (Cited on pages 85, 167, 170 and 177.)
- WRIGHT, A.E. & BARLOW, M.J. (1975). The radio and infrared spectrum of early-type stars undergoing mass loss. *Monthly Notices of the Royal Astronomical Society*, **170**, 41–51. (Cited on pages 172 and 174.)
- WRIGHT, K.O. (1970). The Zeta Aurigae stars. *Vistas in Astronomy*, **12**, 147–182. (Cited on page 77.)
- WRIGHT, M. (2009). Bandpass Calibration and Stability. In *CARMA Memorandum Series*, vol. 55. (Cited on page 76.)
- WRIGHT, M.C.H. (1999). Image Fidelity. In *BIMA memo 73: Image Fidelity*, vol. 73 of *BIMA memos*. (Cited on page 72.)
- ZUCKERMAN, B., KIM, S.S. & LIU, T. (1995). Luminosity Class III Stars with Excess Far-Infrared Emission. *Astrophysical Journal Letters*, **446**, L79. (Cited on page 2.)